SEISMIC PERFORMANCE EVALUATION OF STEEL FRAME BUILDING WITH DIFFERENT COMPOSITE SLAB CONFIGURATIONS

A thesis submitted in partial fulfilment of the requirements for the degree of
Doctor of Philosophy in Civil Engineering
By

TUSHAR CHAUDHARI

Supervised by
Associate Professor Gregory MacRae

Co-supervisor
Professor Des Bull

DEPARTMENT OF CIVIL AND NATURAL RESOURCES ENGINEERING

UNIVERSITY OF CANTERBURY

CHRISTCHURCH, NEW ZEALAND

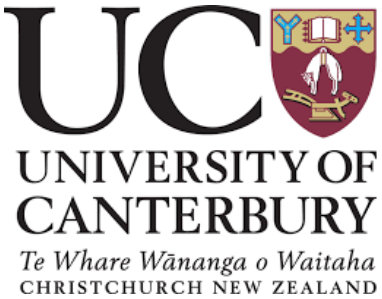

OCTOBER 2017

To my lovely wife Rachana,
Very wonderful son Neel
and
Loving Parents

Abstract

Large-scale experimental tests, detailed finite element studies, strut-and-tie studies, and hand approaches are conducted on a number of steel beam-column moment frame sub-assemblies with a composite deck slab subjected to large inelastic displacements. The four experimentally tested frame sub-assemblies were designed to have (i) full isolation of the slab from the column, (ii) a shear key within the column web but slab isolated from the outside faces of the column flanges, (iii) a modified shear key within the column web with confinement plates and slab isolated from the outside faces of the column flanges, and (iv) a full depth confined slab around the columns. The finite element and strut-and-tie numerical models were used to describe the experimental tests conducted here, as well as those by others. This information was used in the development of simple methods useful for design.

It was found that slab damage resulting from compression of the slab against the flanges could be avoided by fully isolating the column from the slab with appropriate material, and the design strength was that of the bare frame, although ductility was enhanced. By using a confined full depth slab, the strength increased by almost 50%, and the stiffness by 87% without significant strength loss. The specimens with isolation on the outside of the column flanges, and provision of shear key rebars, had enhanced the strength. However, for the configurations tested degradation of strength to that of the bare steel frame level occurred at large displacements.

The modes of slab failure and strength loss were identified. These include crushing, shear fracture at the column tips, longitudinal shear failure, slicing of concrete slab between column flange tips due to unanchored reinforcing bars, shear stud deformation, and yielding of longitudinal or transverse reinforcing steel.

The monotonic finite element study matched the envelope of the lateral force-displacement curve with deviation less than 9%. The strut-and-tie model, using simple approaches to capture all relevant mechanism described above captured the key aspects of the cyclic behaviour with deviation less than 7% on peak strength.

Finally, design methods considering all key modes of failure were provided. These are suitable for engineering use, and design examples were provided. The work conducted allows engineers to choose a slab configuration and design appropriately.

UNIVERSITY OF CANTERBURY
Te Whare Wānanga o Waitaha
CHRISTCHURCH NEW ZEALAND

Deputy Vice-Chancellor's Office
Postgraduate Office

Co-Authorship Form

This form is to accompany the submission of any thesis that contains research reported in co-authored work that has been published, accepted for publication, or submitted for publication. A copy of this form should be included for each co-authored work that is included in the thesis. Completed forms should be included at the front (after the thesis abstract) of each copy of the thesis submitted for examination and library deposit.

Please indicate the chapter/section/pages of this thesis that are extracted from co-authored work and provide details of the publication or submission from the extract comes:

Chapter 3:

Chaudhari T., MacRae G., Bull D., Chase G., Hobbs M., Clifton C., Hicks S., "Composite slab effects on beam-column subassemblies: Further development", New Zealand Society of Earthquake Engineering Conference, Aotea Centre, Auckland, 21-23 March 2014. Paper 06

Chapter 4:

Chaudhari, T. D., and MacRae, G. A. (2016). "Selection of gap infill material for structural seismic applications." *Journal of the Structural Engineering Society of New Zealand Inc (SESOC)*, 29(01).

Chapter 5:

Chaudhari, T. D., MacRae, G. A., Bull, D. K., Chase, G., Hicks, S., Clifton, G. C., and Hobbs, M. (2015). "Composite slab effects on beam-column subassembly seismic performance." *STESSA 2015*, China Architecture & Building Press, Shanghai, China

Please detail the nature and extent (%) of contribution by the candidate:

The candidate did all the work (100%) under our supervision.

Certification by Co-authors:

If there is more than one co-author then a single co-author can sign on behalf of all

The undersigned certifys that:

- The above statement correctly reflects the nature and extent of the PhD candidate's contribution to this co-authored work
- In cases where the candidate was the lead author of the co-authored work he or she wrote the text

Name:	Signature:	Date:
Gregory MacRae		30 Oct 2017

Acknowledgements

Firstly, I would like to express my sincere gratitude to my principal supervisor Associate Professor Gregory MacRae for his continuous support and guidance throughout the course of the research study at the University of Canterbury, for his patience, motivation, and immense knowledge. His guidance helped me in all the time of research and writing of this thesis. I could not have imagined having a better advisor and mentor for my PhD study. He helped to flourish my mind into what is required to become an independent researcher. I am also grateful to him for arranging the financial support for this research study. Without his immense support and motivation, completion of this study would not have been possible.

I am deeply grateful to my co-supervisor Professor Des Bull for his time and valuable feedback during experimental testing. Also, his expertise in structural concrete and floor diaphragm helped this study. His advice on the practical aspects of the research is benefited this research work. I would like to thank Associate Professor Charles Clifton (University of Auckland), who is one of the associate supervisor for this research. His insightful advice in the test configuration helps a lot in this study. I am also thankful to Dr Stephen Hicks (General Manager Structural System at HERA, New Zealand) for his valuable inputs. Another associate supervisor for this research is Distinguished Professor Geoffrey Chase; I am extremely thankful to him for his advice and time.

Completion of this research would not have been feasible without the financial support, and I would like to sincerely thank the following organisations for the financial support that was provided during this project: the MBIE Natural Hazard Research Platform, John Jones Steel scholarship, and the Heavy Engineering Educational & Research Foundation (HEERF) postgraduate scholarship. I am also indebted to Mr Steve Stickland (ComFlor New Zealand) for sponsoring the decking material along with relevant accessories. I am also thankful to him for sharing the technical information related to this research study.

I would like to thank all the technicians in the structural laboratory who have helped to accomplish the experimental phases of this research. My special thanks to Mosese Fifita (who was my main technician) for his time, technical advice and on the spot decisions. I am also grateful for the support provided by David MacPherson, John Maley, Peter Coursey, Stuart Toase, Tim Perigo, Russell McConchie, Alan Thirlwell, Gavin Keats, and Bob Wilsea-Smith.

I would like to express my appreciation to my office mates Dr Pavan Ananthaneni, Helmy Tjahjanto, Mayank Tripathi, and Saul Colunga for their friendships and social activities during my study which have made this journey an enjoyable and memorable experience. My special thanks to Dr Pavan Ananthaneni for the fruitful discussions/arguments we had on the various technical topics related to this research work. I am deeply grateful to him for motivating me time to time and helping in many ways and great friendship we have. I am also thankful to my fellow postgraduate students for their help, advice and friendship we had over the time at the University of Canterbury.

I wish to express my deepest gratitude to my extended family in Christchurch; Pawan Gautam, Monika Sharma, and Harsh for their support, motivation and unconditional love throughout the journey. The social gathering, I had with them helps me in reducing the stress and keep me focused. I would also like to thank my family friends; Dr Kiran More and family, Swapnil Patil, Dr Niteen Dubal and many more. I am indebted to my childhood friend Amol Chaudhari & family for keeping me motivated and financially supporting me during the last phase of my research study.

To my family, to whom I dedicate this thesis I would like to express my sincere thanks. I am especially grateful to my parents, brother, sister and my in-laws for providing their endless care, love and engorgement during these past years.

I am also indebted to my former supervisor Professor Devdas Menon (IIT-Madras) for inspiring me to pursue a research study and guiding me on the spiritual path.

Finally, I wish to express my utmost appreciation to my wife and son. My wife Rachana should have all credit for her sacrifice, patience, inspiration, and love for me and my work. I will never be able to thank her enough. Without her unconditional support, encouragement and motivation, I would not have even tried for this work. Most importantly to have a son like Neel is a blessing, one innocent smile and a cuddle from him would make all the stress go away and rejuvenated me. I feel very guilty for not able spend quality time with my wife and son since I was very much preoccupied with my work and for the compromise they had during this journey. I dedicate this thesis to my wife and son.

List of Publications

Journals

1. **Chaudhari, T. D**., and MacRae, G. A. (2016). "Selection of gap infill material for structural seismic applications." *Journal of the Structural Engineering Society of New Zealand Inc (SESOC)*, 29(01).
2. **Chaudhari, T. D.,** MacRae, G. A., Bull, D. K., Hicks, S., and Clifton, G. C., "Non-linear cyclic behaviour of beam-column sub-assemblies with different composite slab configurations: Experimental investigation" under preparation.
3. **Chaudhari, T. D.,** MacRae, G. A., Bull, D. K., Hicks, S., and Clifton, G. C., "Modelling non-linear cyclic behaviour of beam-column sub-assemblies with composite deck slab: Strut-and-Tie approach" under preparation.
4. **Chaudhari, T. D.,** MacRae, G. A., Bull, D. K., Hicks, S., and Clifton, G. C., "Numerical and analytical simulation to predict the lateral strength of beam-column sub-assemblies with composite deck slab" under preparation.

Conference Proceeding

1. **Chaudhari T.,** MacRae G., Bull D., Chase G., Hobbs M., Clifton C., Hicks S., "Composite slab effects on beam-column subassemblies: Further development", New Zealand Society of Earthquake Engineering Conference, Aotea Centre, Auckland, 21-23 March 2014. Paper 06
2. **Chaudhari, T. D**., MacRae, G. A., Bull, D. K., Chase, G., Hicks, S., Clifton, G. C., and Hobbs, M. (2015). "Composite slab effects on beam-column subassembly seismic performance." *STESSA 2015*, China Architecture & Building Press, Shanghai, China.
3. **Chaudhari, T. D.,** MacRae, G. A., Bull, D. K., Chase, G., Hicks, S., Clifton, G. C., and Hobbs, M. (2015). "Composite slab effects on beam-column subassembly seismic performance." Steel Innovations Conference 2015, 3-4 September 2015, Auckland, New Zealand.
4. Gregory MacRae, Michael Hobbs, Des Bull, **Tushar Chaudhari**, Roberto Leon, Charles Clifton, Geoff Chase (2016). "Slab Effects on Beam-Column Subassemblies—Beam Strength and Elongation Issues", *Composite Construction in Steel and Concrete VII*: pp. 77-92, ASCE conference proceeding.
5. **Tushar Chaudhari**, Gregory MacRae, Des Bull, George C. Clifton, and Stephen Hicks. (2018). "Analytical Methodology to Predict the Beam Overstrength Considering the Composite Slab Effects." *STESSA 2018*, Steel Construction New Zealand, Christchurch, New Zealand.

Table of Contents

Chapter 1: Introduction

1.1 Background

Present generation steel buildings are mostly built using composite slab construction, such construction consists of cold-formed steel decking beneath a reinforced concrete cast in-situ slab and is quick and easy to construct/erect, has no need of temporary formwork, and is often economical compared to the other types of slab construction (i.e. cast-in-situ concrete slabs and precast concrete slabs). The composite slab is schematically shown in Figure 1.1a and a real steel building using composite slab is shown in Figure 1.1b. In such composite construction, both the concrete and steel material are effectively utilised by taking advantage of the compressive properties of the concrete and tensile properties of the steel. This composite slab is connected to the steel beam using steel studs, which are designed to transfer the longitudinal shear between the composite slab and the steel beam. Depending on the number of the shear studs along the steel beam, the beam may be fully or partially composite [1, 2]. Because of this composite action, a steel 'I' beam acts as a 'T' shaped beam, thereby resulting in a small beam cross-section (economical design) under gravity loads. Also, depending on the orientation of the profiled deck sheeting, the sectional properties of the composite beam varies. In a conventional frame building, there is no gap between the composite slab and the column. As a result, the slab interacts with the column and increases the sub-assembly lateral strength and stiffness. The increase in lateral strength and stiffness due to the slab-column interaction can be more than 50% when compared to a bare steel frame's strength and stiffness [3].

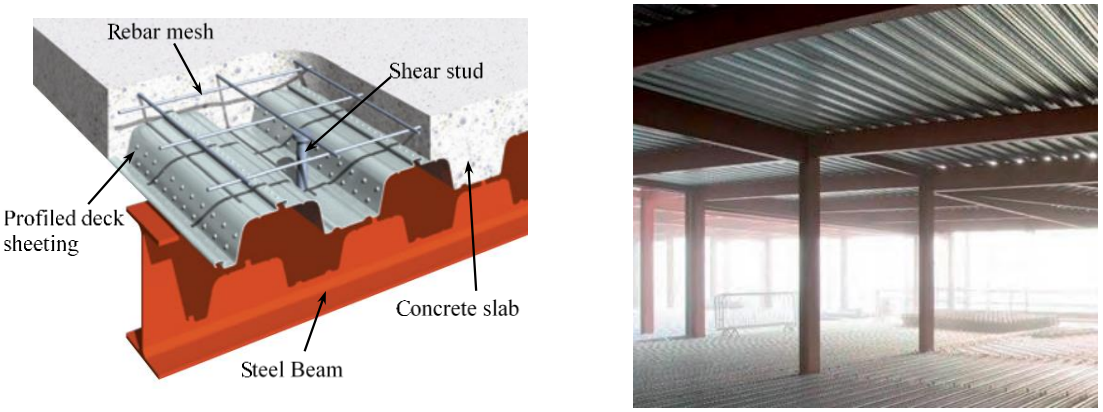

(a) Schematic representation **(b) Real building**

Figure 1.1- Schematic and real construction of the steel building using composite slab [4]

According to the NZ steel building standard [5], shear studs are not permitted in the plastic hinge regions at the beam end (CL13.4.3.2). Also, the slab-beam composite action is considered only in designing for gravity loads (i.e. dead and superimposed loads) and it is ignored while sizing the beam for lateral loads (i.e. earthquake and wind loads). This results in larger beams than when composite action is considered. Thus the benefit of composite action on beam sizing is not considered. Also, since the slab affects the column demands, the steel standard [5] requires that the slab be considered when computing beam overstrength values. Therefore, the steel standard [5] conservatively ignores the beneficial effect of the slab (for beam sizing) but considers the adverse effects of the slab (when designing the column and panel zone) [6, 7]. Method to determine the overstrength factor to estimate the demand on columns in the New Zealand steel building standard is simple and easy to use [5, 6] although they have not been verified, whereas such explicit methods are not specified in other countries building standards.

Even though there are many benefits due to composite slab construction, it was observed in past earthquakes that composite slabs have been damaged to varying extents without significant damage to the conventional steel frames. This has been verified in many experimental tests [3, 8-12]. As a result, the damaged composite slabs require repair (often with shutdown of the building) resulting in a considerable downtime-related seismic loss. The observed damage to a composite slab in a past experimental test is shown in Figure 1.2. Also, in a low damage steel frame system (e.g. sliding hinge connections, rocking frames, and etc.) the damage to the composite slab around the column may require repair. A study evaluating a range of methods to minimise such damage is not available.

Figure 1.2 Damage to the Composite Slab in Experimental Test [3]

It was experimentally and numerically verified that rapid post-peak strength degradation of a ductile steel frame building may be associated with brittle failure of the concrete slab (around the column) due to slab-column interaction [3, 11, 13]. The lateral force generated in the composite slab in a sub-assembly without transverse beams is transferred to the column through two distinct force transfer mechanisms; (i) Mechanism-1: as a bearing force from the composite slab to the column outer flanges, (ii) Mechanism-2: as a compression strut force from the composite slab to the column web and inner side of the flanges, and shearing of the concrete next to the column flange tips [14]. The rate of strength degradation associated with the mechanisms-1 and 2 depends on the strength hierarchy and deformation compatibility. It is also affected by the slab confinement on the outside and inside of the column flanges, the shear strength of the concrete between flange tips, slab reinforcement, shear connectors, and other factors [3]. In general, initial minor damage to the composite slab at lower lateral drifts is due to Mechanism-1, whereas at higher drifts the severe damage to the composite slab is because of the shearing of the slab next to the column flange tips (i.e. Mechanism-2) [15]. The seismic performance of a conventional steel frame building is partially governed by the behaviour of the composite slab under cyclic loading. The composite slabs act as the diaphragm which transfers the inertial and transfer forces to the lateral load resisting frames [16, 17]. In conventional construction practice, the composite deck slabs are usually poured up to, and against, the column flanges. However, sometimes a gap is provided to isolate the slab from the column. If a gap is left between the slab and column, it is easier to design the frame structure since the slab effects on the column, connection and panel zone are reduced [3, 13]. However, there is a greater possibility for column instability and buckling as the column restraint is reduced because of the separation [18, 19]. No research is known which considers all likely modes of behaviour to be used in design, so guidance regarding this is limited.

1.2 Need for the Research

It may be seen from the discussion above that for buildings to be designed for strong earthquakes shakes with confidence in their response, the behaviour of a typical steel frame sub-assembly with slab must be understood, modelled, and that appropriate design recommendations are to be made.

1.3 Objectives and Scope

In order to address the needs described above, beam-column sub-assemblies with composite deck slab in a moment frame were investigated; experimentally, numerically, and analytically to answer the following questions:

i) Is it possible to minimise the damage to the composite slab (around the column) in a seismic shaking by isolating the column from the slab?
ii) Is it practicable to modify the detailing in the composite slab (within the column web region) so that the rapid strength degradation associated with the shear failure in the slab next to the column flange tips can be delayed and minimized?
iii) Can the slab around the column be detailed such that strength degradation is minimised while composite strength is maintained?
iv) Does the sub-assembly's force-displacement hysteresis relationship change with different slab detailing?
v) Can the experimental behaviour be reliably predicted by numerical modelling?
vi) Can simple hand methods be used to estimate composite beam-column slab sub-assembly parameters (lateral strength and stiffness) for design?

1.4 Organisation of Thesis

The thesis consists of seven chapters including the "Introduction," "Conclusions" and a brief outline of each chapter is given below.

Chapter 2 presents the literature summary of past experimental investigation on moment resisting frames with composite slabs followed by numerical methods. Finally, the codal approaches of different countries are discussed.

Chapter 3 presents an overview of the experimental test programme. The methodology adopted for the selection of the different test configurations is explained. Thereafter the design and details of the tested frame sub-assemblies are presented. Details of the tests carried out on the material (steel and concrete) to evaluate the mechanical properties, and the corresponding test results are reported. Further, the details of the construction of the specimens, test setup, and instrumentation are summarised. Finally, the methodology of interpretation of test results is presented.

Chapter 4 discusses situations where isolation gaps in construction may limit the damage during earthquake shaking. These are (i) concrete slab isolation from a steel column, and (ii)

non-structural element separation from a seismic frame. The development of performance criteria for the gapping material is firstly described. Then different materials are tested to evaluate their ability to match the performance criteria. The evaluation of appropriate material for a given situation is performed using the Subjective Quantitative Assessment (SQA) considering the different characteristics related to the material. Finally, design methodology on the determination of isolation gaps were provided.

Chapter 5 presents the experimental findings of the tested frame sub-assemblies with different composite slab configurations. The key failure modes observed in the steel beam and the composite slab are reported and discussed. Further, the contribution of individual frame component deformation to the overall lateral displacement is evaluated and discussed. The key hysteretic parameters (i.e. peak strength, initial stiffness, energy dissipation, equivalent viscous damping, and stiffness degradation) are evaluated and compared.

Chapter 6 presents the details of the numerical simulation using the micro and macro model approaches. A frame model with the strut-and-tie formation is proposed to simulate the cyclic behaviour of the tested sub-assemblies. Finally, a simple analytical methodology was developed to evaluate the lateral strength of the frame sub-assembly considering the strength hierarchy of the different force transfer modes. Further, the lateral stiffness of the tested frame sub-assemblies is calculated and compared with experimental results.

Chapter 7 summarises the overall conclusions of the research study with reference to the objectives set out in Section 1.3. Further, the scope for future research work related to the beam column sub-assembly with a composite slab is discussed.

Chapter 2: Literature review

2.1 Introduction

This chapter provides a literature review related to the composite deck slab effects on the moment resisting frames. It begins with literature related to previous experimental investigations followed by analytical study and finally summarises with the codal approaches. Since, the current research work is preliminary done by Hobbs [3] at the University of Canterbury to study the effect of the different slab configurations and it was extended further to investigate the slab effects on the moment resisting frames. The finding of Hobbs [3] research work is cited herein which act as a stepping stone for the current research study.

2.2 Previous Experimental Investigation on Moment Frame with Composite Slabs

DuPlessis and Daniels [20] tested four composite steel-concrete T-beams specimens subjected to a concentrated positive end moment with different slab width and thickness. The noted observed failure sequence was yielding of the steel beam followed by cracking and spalling of the concrete slab at the column face occurred. The major finding was, the ultimate strength of the test beams was independent of slab width. However, it depends on the column face width, slab thickness, concrete strength and yield strength of steel. It was noted that the compressive stress acting at the slab-column interaction on column flange width is around $1.3f'_c$.

Lee and Lu [8] has tested three full scaled joint sub-assemblages with composite deck slab under cyclic loading to investigate drift characteristics of the structural elements like (i) column, (ii) beam, and (iii) panel zone. The test specimens were categorised as EJ-FC (Exterior Joint – Flange Connection), IJ-FC (Interior Joint – Flange Connection), and EJ-WC (Exterior Joint – Welded Connection). In all test sub-assemblies, it was observed that the beam bottom flange started yielding followed by column web panel yielding and crushing of concrete near the column flange. The panel zone was the weakest element and went under large shear distortions. The presence of the composite deck slab substantially increases the strength and stiffness of steel beam when subjected to positive loading. Figure 2.1, below shows the deflection components of the EJ-FC test specimen and it can be seen that there is much more demand on panel zone during composite action under cyclic loadings. The slab-column interaction causes significant panel zone deformation in case of the weak panel.

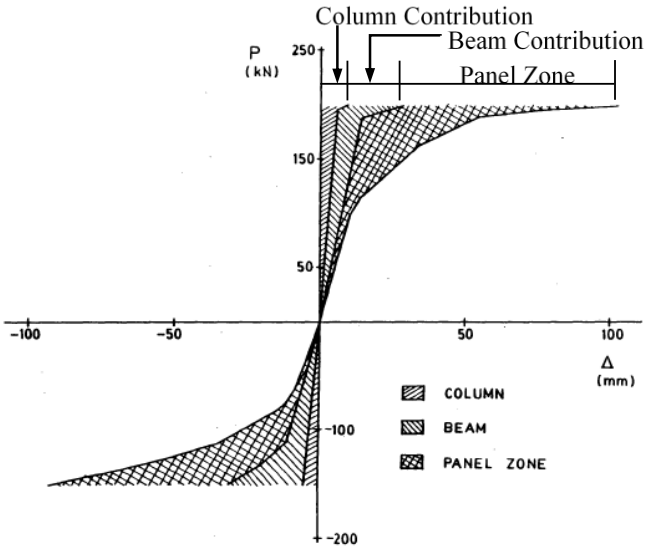

Figure 2.1 - Components of Total Deflection Composite Test Specimens
(Adopted from Lee and Lu [8])

Hysteresis curves were stable and repetitive, however they showed a slight pinching at large deformations and it was primarily due to the opening and closing of the cracks in the concrete slab. It was stated that for weak-beam and strong column concept, it might be beneficial to allow some yielding of panel zone to lessen the ductility demand on the beams and connecting elements.

Doneux and Parung [10] tested three specimens with different connection configurations wherein the reinforcement arrangement around the column is varied as shown in Figure 2.2. In BF-X (Bolted Flexible) specimen, the omission of transverse reinforcement and studs around column caused splitting of slab along the stud line. The observed crack pattern shows less cracking in the slab for BR-X (Bolted Rigid) specimen due to the provision of both transverse and longitudinal reinforce. In case of WR-X (Welded Rigid) specimen, provision of only transverse reinforcement was not sufficient to avoid splitting in concrete. Severe cracks observed due to lack of confinement reinforcement. The bolted flexible specimen was detailed to deactivate the slab-column interaction using the Styrofoam strips (isolation material) and expected to achieve the strength of bare steel section, however, the test results show increase in moment resistance by 16% for a positive moment and 29 % for a negative moment because of resistance offered by the transverse beam. This reveals that, it will be unsafe to consider only bare steel section in the design of composite structure if the transverse beam is connected to the slab through the shear studs.

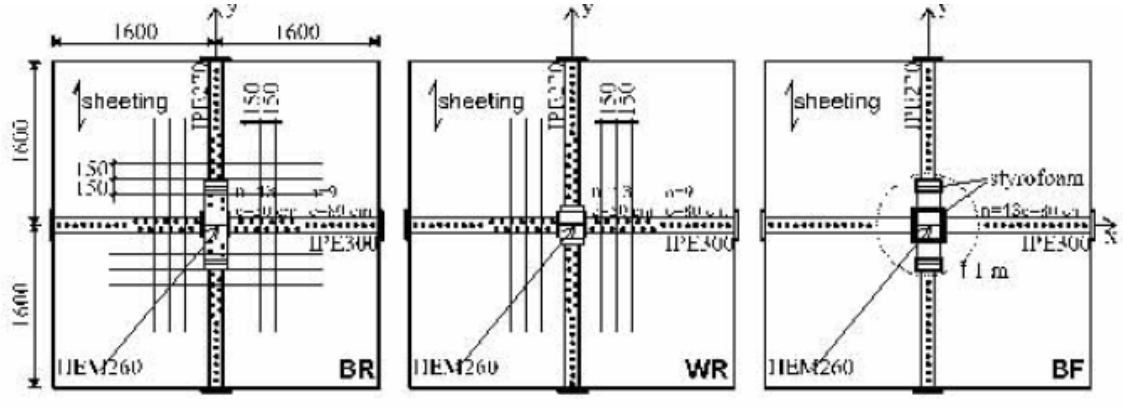

a) Rebar and Shear Stud Arrangement

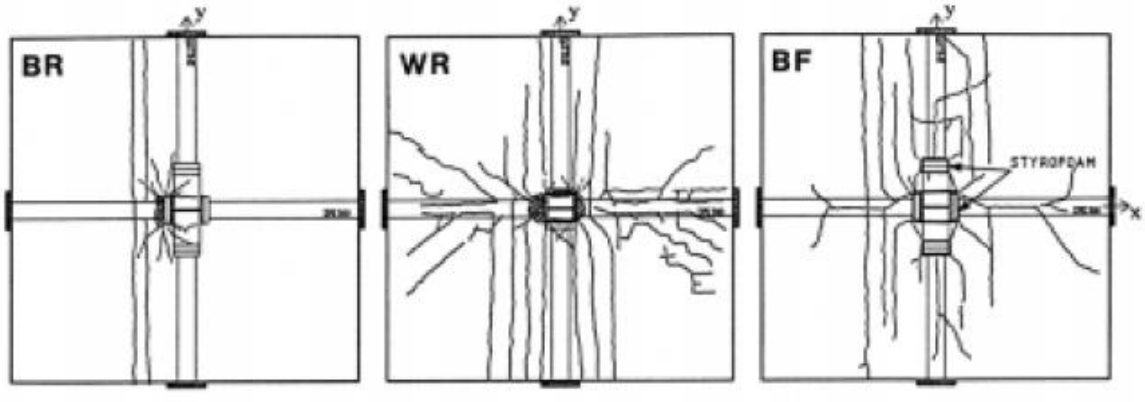

b) Details of Slab Crack Pattern

Figure 2.2 - Slab Details and Crack Patten of Test Specimens
(Adopted from Doneux and Parung [10])

Following the 1994 Northridge earthquake (California), connection failures in the girders of the moment resisting frames have been observed especially weld fracture in the beam bottom flanges. It was theories that the slab participation has changed the local behaviour of the connection. Leon, Hajjar and Gustafson [9, 13] worked extensively on composite moment connections to investigate the effect of the slab on the steel frame and its behaviour under seismic loading after Northridge earthquake. They tested three full-scale different types of test configurations, two with partial composite action (35% and 55%) and one with bare steel frame. The test specimens were designed based on the capacity design criteria of the strong column/weak beam philosophy with rigid panel zone, however it is not clear whether the slab participation was considered. The experimental investigation showed that, the composite connections exceeded the plastic moment strength of the bare steel section, which signifies the potential of an unexpected strong beam / weak column mechanism if the effect of the composite slab is neglected. Also observe that, strains near the bottom flange of the specimen with slab were larger than strain near top flange indicating the stress concentrations causing failure of connection due to fracture and this nonsymmetrical strain distribution in the top and bottom

connection implies that the neutral axis shifted upward due to the presence of the slab. The contribution of the tensile resistance of slab and rebars in the moment resistance was minimal. In addition, it shows inadequate ductility under a positive bending moment. Further investigation was carried on connection behaviour using finite element simulation and found that strains near CJP welds at girder bottom flange is 5 times higher than the strains in top flange as shown in Figure 2.3

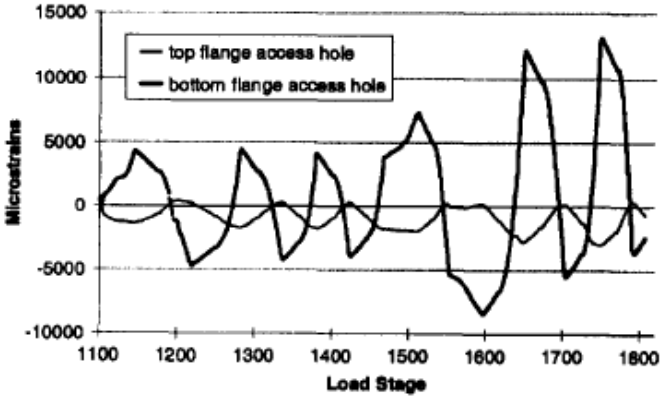

Figure 2.3 - Strains at Bottom and Top Access Holes ([9], Leon et al. [13])

Similarly, after failures of welded moment connections in the Northridge earthquake, Liu and Astaneh-Asl [21] studied the contribution of simple shear connections to the lateral moment resistance considering the composite slab action to develop partially rigid connections [22]. For this purpose sixteen full-scale tests carried out in two series and it was found that the presence of slab in test specimen resulted roughly twice the maximum lateral load resistance as shown in Figure 2.4. Loss of composite action took place due to concrete damage as well as bucking of the metal deck at 0.04 radians drift (approx.).

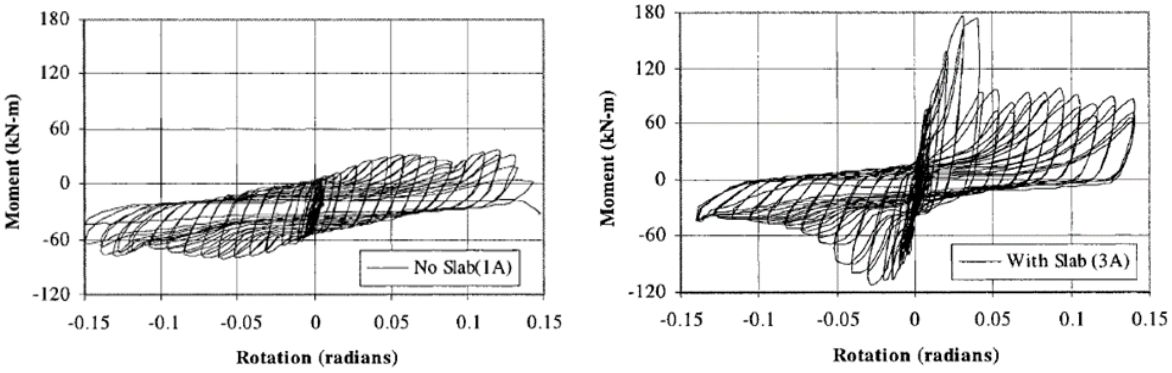

a) Bare Steel Frame **b) Steel Frame with Slab**

Figure 2.4 - Comparison of Moment vs Rotation Response for Specimens with and without slab (Liu and Astaneh-Asl [21])

The provision of additional grid reinforcement around column helps to increase in negative moment capacity. The presence of floor slab in shear tab connections attributed to 30 to 45%

increase in beam plastic moment or 2.5 times the plastic capacity of the shear tabs. In Phase 2 testing, Liu and Astaneh-Asl [23] have studied the effect of various parameters like, numbers of bolts, different concrete strength, use of additional reinforcement, the presence of a column web cavity and shear tab thickness to develop guidelines for estimating moment and rotation capacity of shear tab connection. The provision of column web cavity reduces the lateral load resistance by 20% and it suggests that the sub-assembly strength depends on a number of force active transfer mechanism arises from the slab-column interaction.

Civjan et al. [11] tested six full-scale specimens to investigate the performance of dogbone (i.e. RBS: reduced beam section) and haunch connections used for retrofits of pre-Northridge steel moment connections. The ratio of plastic flexure strengths (M_{ecr}) to the actual maximum moment (M_a) during testing shows 20 to 35% higher values for composite dogbone specimen as compared to bare steel specimen. For the composite hunch connections, the maximum positive moment was 10 to 27% higher than the bare steel frame because of composite action of the slab as well as the stabilising effect of the slab. It was also noted that, the slab compression zone at column face is wider than the column flange and initiated at the column internal flange. From the recorded flange strains, it was observed that the neutral axis was shifted upwards nearer the top of the section for positive bending, however in negative bending, it was located close to the bare steel frame. It was also found that the column face is wider than the column flange and it is initiated at the column internal flange spreading approximately at 15° to 30° as shown in Figure 2.5. The composite slab helps to reduce the top flange stresses and delay the local and lateral torsional buckling of the beam.

Figure 2.5 - Crack Pattern at Column Face (Civjan et al. [11])

In continuation with previous research on the partially restrained connections, Green, Leon and Rassati [24] tested a full-scale specimen with simple connection subjected to bidirectional loading in order to study the slab effect on the column subjected to lateral loading in weak direction. The test specimen was provided with two additional bars placed diagonally (inclined at 45°) on each side of column (Figure 2.6) to prevent the diagonal cracks initiated from the column flange. Under cyclic loading, the connections showed elastic behaviour up to 1% drift followed by significant yielding and damage occurred at 1.5% drift. The additional strength and stiffness provided by composite slab were effective up to 2-3% drift and it decreased after crushing of concrete against the column face. A localized panel zone yielding was observed primarily due to out plane distortion of the column web due to loading in the column weak axis and resulted in a punch-through failure of the column web due to force transfer from the shear tab connection provided in the weak axis of the column. In order avoid this kind of failure, special detailing required around the column. Author's suggested to provide a full depth slab at least of 150mm wide around the joint.

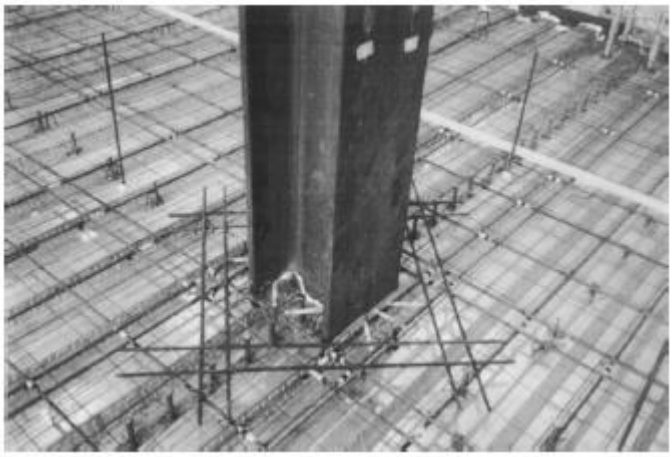

Figure 2.6 - Details of Slab around the Column (Green et al. [24])

Gil and Bayo [25] tested two external and one internal semi-rigid composite joints with flush end plates. Conventionally, the external joint configuration requires an additional cantilever slab to facilitate the sufficient anchorage for the rebars, however authors proposed alternative detailing wherein the two central longitudinal rebars are inserted through the column flanges and anchored on outer column flange as shown in Figure 2.7 (a). The test results show that the provision of the rebars passing through the column flange improved the joint stiffness as well as the rotation capacity of the internal joint. However, the improvement in the rotational capacity of the external joint was less and can be further enhanced by the increasing the diameter of central rebars. The specimens were tested under negative bending (i.e. hogging)

focusing on the behaviour tie reinforcement, however, the effect of positive loading (i.e. sagging) is not investigated and further research needed to study the behaviour of the test specimens with proposed detailing under cyclic loading regime. Nevertheless, the proposed detailing for the external joint will help the architectures and structural engineers to avoid the provision of the additional cantilever head for the rebar anchorage.

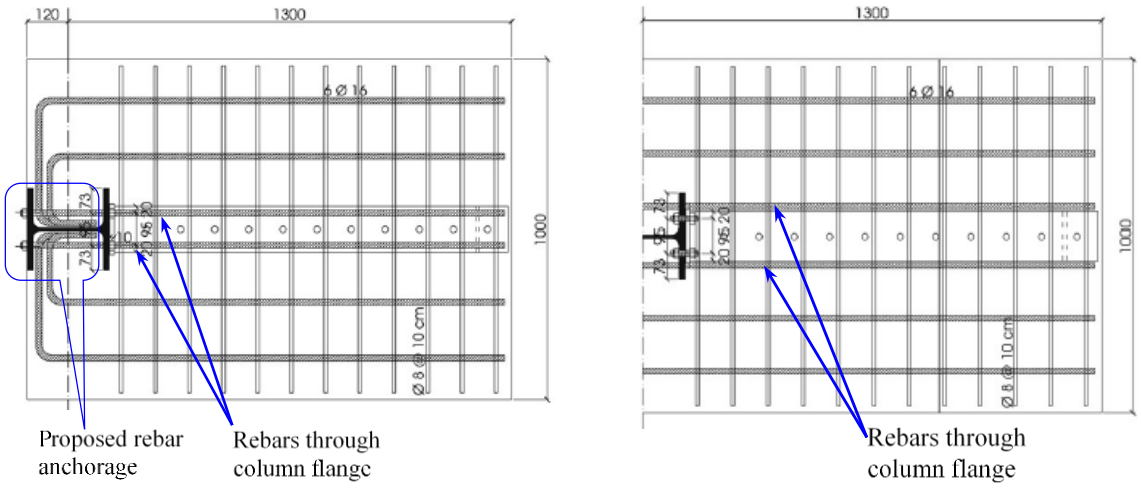

a) External Joint **b) Internal Joint**

Figure 2.7 - Details of Reinforcement around the Column (Gil and Bayo [25])

[12], Braconi et al. [26] performed tests on partial strength connections to investigate the energy dissipation characteristics of ductile components like beam end-plate as well as shear yielding of panel zone in beam-column joints. For a better understanding of other force transfer mechanisms, no shear connection (i.e. shear studs) was provided between the slab and the secondary beams (i.e. transverse beams) to suppress the contribution of the secondary beam in lateral load resistance (i.e. mechanism 3 as per EC8 [14]). Pseudo-dynamic testing showed that damage to the frame was limited to cracking in the concrete and localised crushing of the concrete against the column faces. In addition, a fracture of the weld between lower beam flange and end plate was noted as shown in Figure 2.8. The hysteresis curves show pinching response due to the crushing of concrete and yielding of the longitudinal reinforcement. It was also found that, one of the strut and tie mechanisms suggested by Eurocode 8 for transferring forces to the column could not achieve because of the discontinuity between the slab and the concrete encasing the column, which resulted in excessive direct bearing stresses at the column outer flanges and leads to concrete crushing at the slab-column interaction.

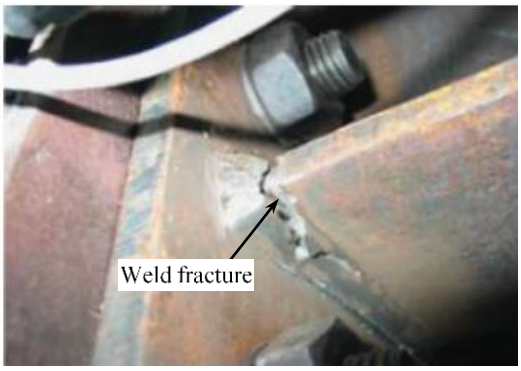

Figure 2.8 – Weld fracture between the end plate and lower beam flange (Braconi et al. [12])

Braconi, Elamary and Salvatore [27] carried out further investigations by performing a series of tests on ten composite beam-column joint assemblies with bolted endplate connections. Their prime focus was on to investigate the seismic performance of beam to column joint under different slab types (i.e. composite deck slab and precast slab), different connection system between slab and column, the effect of the type of column panel zone (i.e. strong or weak panel), and different concrete strengths. At the slab-column interaction zone, different construction details were adopted. First one is the provision of steel wings for compression force transfer through the direct bearing (i.e. force transfer mechnism1 as per EC8 [14]) as shown in Figure 2.9 (a) and another one is provision of stirrups fastening for shear force transfer in column web (i.e. force transfer mechanism2 as per EC8 [14]) as shown in Figure 2.9 (b).

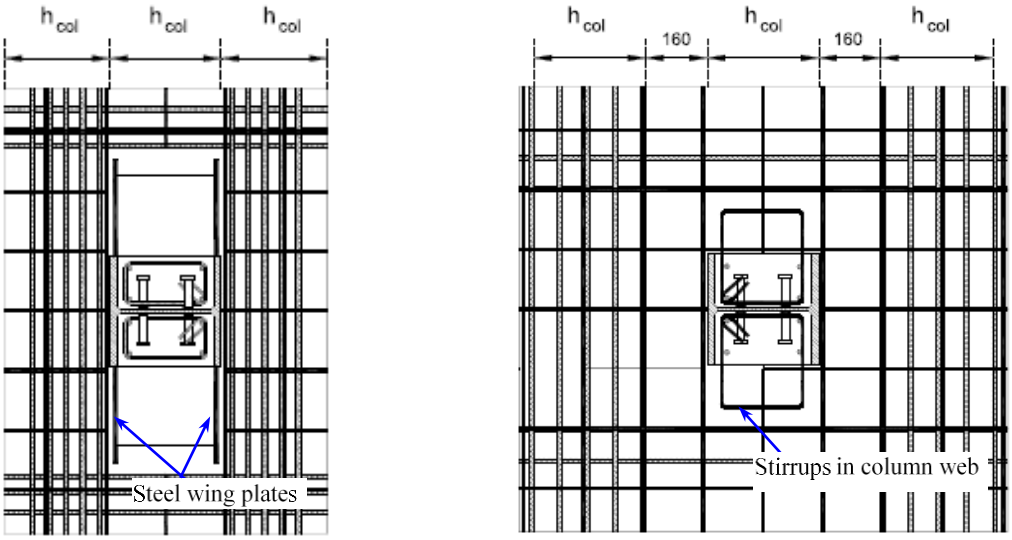

a) Specimen with Steel Wing Plates **b) Specimen with Stirrups**

Figure 2.9 - Concept of Steel Wings and Stirrups in Column Web (Braconi et al. [27])

Shear stirrups system showed better performance than the steel wings and assured a ductile behaviour under sagging as well as hogging bending moments. Metal deck exhibits more strength degradation as compared to full depth precast slab when subjected to sagging

moments, whereas under hogging moments the effect of slab type was not so influential. Results from these tests show that the high strength concrete negatively influenced the behaviour of the beam-column joint causing lowering of the maximum resistance and witnessed the rapid strength degradation after the sub-assembly peak strength and. The strength of panel zone governed by plastic deformation between connection and web panel and it was independent of slab type. The metal deck slab shows higher values of ductility as compared to full depth slab. The noted overstrength factor of the tested specimen was in the range of 1.40 to 1.85 and the specimens with strong column web panel and full depth slab possess high overstrength values compared to other test specimens.

In a recent study conducted at the University of Canterbury, Hobbs [3], [28, 29] tested five specimens with different tray directions (transverse and longitudinal), slab isolation, full depth slab around the column and sliding hinge joint. All specimens were tested for varying drift levels from 0.2% to 5.0% drift as per ACI testing protocol. In the isolated test, a 25mm thick polystyrene block was used to separate the slab from the column, however due to improper isolation at the bolted end plate connection, part of the connection was still in contact with the slab as shown in Figure 2.10. This results in partial isolation as a bearing force are developed on the exposed portion of the connection and the test result shows that some interaction between the slab and column had occurred which was not desired.

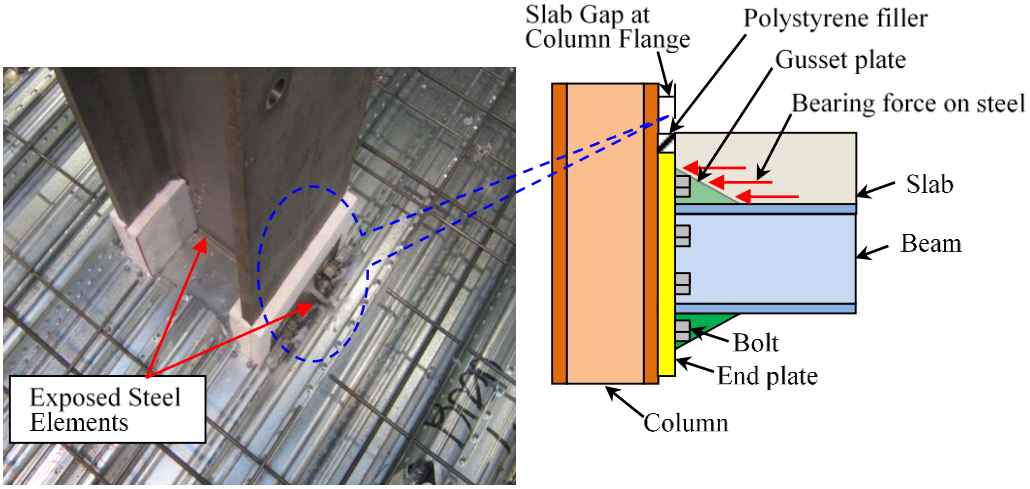

Figure 2.10 – Partial Isolation Details [3, 29]

The hysteretic behaviour of various tests shows that the partially isolated specimen had around 40% lesser lateral load resistance compared to slabs in contact as shown in Figure 2.11.

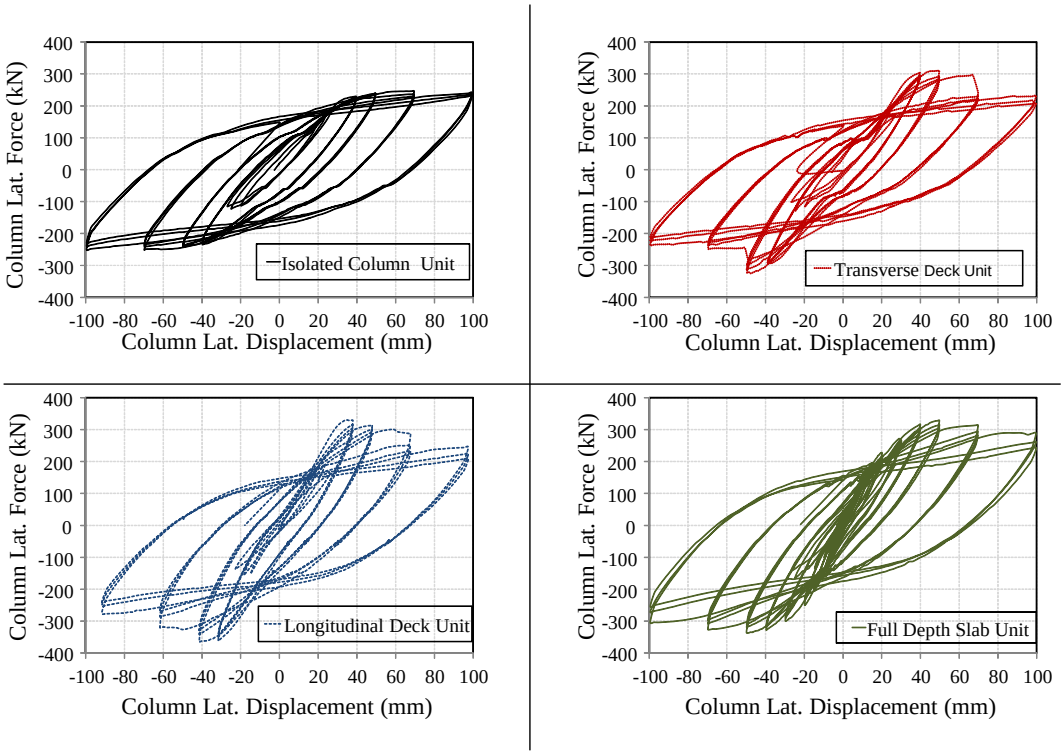

Figure 2.11 – Sub-assembly hysteresis behaviour [3, 29]

The specimen with longitudinal deck shows more resistance to the lateral load than a specimen with transverse deck because of increase in bearing depth at the slab-column interaction. It was observed that the deck orientation (i.e. transverse or longitudinal) has an effect on the sub-assembly lateral strength and longitudinal deck sub-assembly shows 10% higher lateral strength as compared to the transverse deck assembly. This is because of the increase in bearing area at the slab-column interaction zone. The noted failure sequence was buckling of the beam bottom flanges beyond, followed by the shearing of the concrete between column flanges and a reminder of the slab, and finally spalling of the slab at column faces. At 5% drift, all specimens had strength similar to that of the partially isolated specimen. During experimental testing, it was observed that, the concrete between the column flanges sheared away from the rest of a slab in all test specimens except in full depth slab. In case of deck running parallel to the primary beam (i.e. longitudinal unit), a longitudinal shear failure of the concrete at both edges of the trough of the profiled floor (that was centred in the column) was noted, which resulted in delamination of the slab as shown in Figure 2.12.

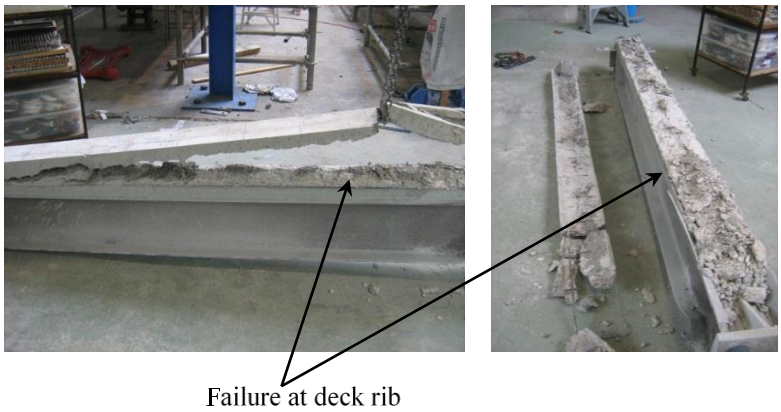

Figure 2.12 – Delamination of slab surface in longitudinal deck subassembly [28]

In case of the partially isolated slab unit, there was minimal damage to the slab due to separation from the column. The provision of the full depth slab around the column shows improved strength stiffness as compared to the transverse deck sub-assembly and exhibits less strength degradation at the larger drift cycles as compared to the other test frame sub-assemblies. No significant cracking near the column was noted as well as the shear failure of the concrete between the column flanges does not observe in the full depth slab sub-assembly. In all the tests, the column, panel zone and beam end connections remained elastic. In addition, the testing on sliding hinge joint (SHJ) shows that the extent of both the longitudinal and diagonal cracks was greater than that observed in partially isolated specimen but less than the transverse and longitudinal subassemblies. The SHJ connections sustained large drifts and primarily losses its strength due to spalling and shearing of concrete. The beam elongation measurement demonstrations that all sub-assemblies beams show around 2-4mm of residual elongation and with the realistic boundary condition, this effect will further reduce.

2.3 Finite Element Simulation

Hajjar et al. [9] simulated a steel frame with and without the composite slab in Abaqus (version 5.6) nonlinear finite element model. Both the beam and the column were modelled with eight noded continuum elements (i.e. element C3D8I). The column was a model in two segments, the expected elastic segment was modelled as a beam element (i.e. element B33) and the portion close to connection was modelled using eight nodded elements as shown in Figure 2.13. Multipoint constraints were invoked to connect the solid elements with the beam elements to ensure the geometrical compatibility of the column. The concrete slab is connected to the steel beam using slide line elements (i.e. element ISL31) with high stiffness to ensure the full composite action. The elastic-perfectly plastic material was used for steel. The concrete material model considers the nonlinear stress-strain up to peak compression stress and instead

of modelling the concrete softening behaviour, a concrete stress-strain behaviour retained small negative modulus. The concrete tension model was simulated using the elastic-plastic behaviour. The simulated model shows a strain concentration at the tip of the bottom flange spreading across the weld-column interface suggesting a potential damage to the bottom flange weld and similar observation were noted by authors during the experimental tests. Both the numerical and experimental investigation shows that the longitudinal strain in girder bottom flange was five times higher than the strain in top flange especially closer to welding regions.

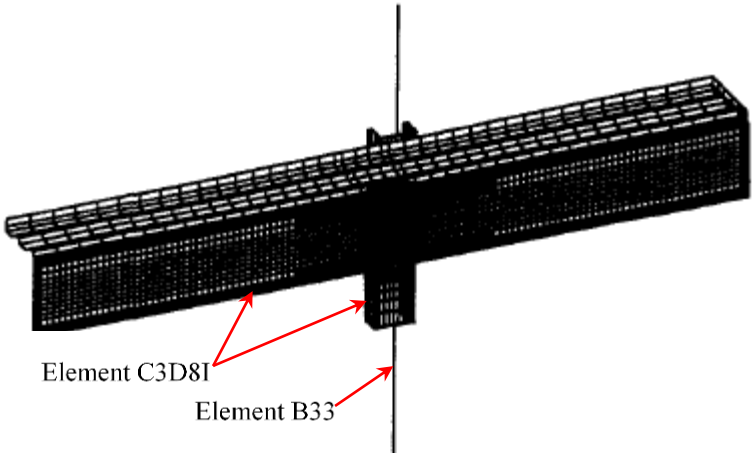

Figure 2.13 – Composite Specimen Finite Element Discretization [9]

To study the effect of the transverse beam on the sub-assembly strength and stiffness, Doneux C. [30] simulated an interior beam-column joint of the frame sub-assembly using a finite element program 'CASTEM 2000'. A four noded shell element was used to model the beam, column and the concrete slab. An elasto-plastic material with isotropic hardening is used for the steel element. The concrete material model consists of an elasto-plastic law with Drucker-Präger criteria for compression behaviour and for tension a Rankine fixed crack model was used. The concrete slab was simulated using multi-layered thin shells and shear studs were represented by beam elements with force-displacement law obtained from theoretical equations available in the literature. At the slab-column interaction, the separation was allowed under negative bending and contact allowed under positive bending. The simulated model was calibrated by comparing the test results of the WR-X test ([10]) and the parametric study was conducted to investigate the effect of the transverse beam. The influence of percentage of reinforcement, shear connectors, beam size and ratio of slab thickness to beam depth were investigated. Author found that the transverse beam connected with shear studs exhibits a force transfer mechanism 3 (based on EC8 [14]) however its contribution in load resistance is less (which was found to be 4.4% in the simulated specimens) as compared with other force transfer

mechanisms (i.e mechanism 1: direct compression of the slab on the column flange and mechanism 2: the inclined compressive struts at the sides of the column). Need for additional research to investigate a role of transverse beam was advocated by author and suggested further modelling of the sub-assembly with only activating the force transfer mechanism 3 (i.e. participation of the transverse beam) and suppressing the other force transfer mechanisms (i.e. mechanism 1 and mechanism 2).

El-Lobody and Lam [31] performed a finite element analysis on a composite girder with different types of slabs (i.e. precast slab and solid slab). The prime objective of this study to simulate the structural behaviour of the composite girder, which considers the non-linear behaviour of the concrete, steel beam and shear connectors. Eight noded (C3D8) solid elements were used in both the models. Considering the symmetry, only half of the beam is model and load is applied using the RIKS method. The steel beam was a model using elastic-plastic material and concrete was model considering the tension stiffening effect. The shear studs were modelled using the spring element with nonlinear load-slip characteristics based on the push-off tests and the REBAR option available in ABAQUS was used to simulate the reinforcement. After comparing the results of the numerical model with experimental result, the author finds the adopted modelling approach could able to predict the load-deflection of beam considering the material nonlinearity as well as captures the longitudinal slip of the shear studs.

Salvatore et al. [15] carried out a numerical analysis to study the behaviour of the partial strength joints. For this purpose a three-dimensional simulation was carried out using ABAQUS and ADINA software for the exterior and interior joint of the frame sub-assembly respectively. Two noded beam element (B31) was used to simulate the rebars with elasto-plastic material and eight noded (C3D8R) solid elements with reduced integration was used to simulate the beam, column and the concrete slab. A non-linear spring element (SPRING2) was employed to represent the shear studs and the metal deck was assumed to be fully connected with the concrete. The slab-column interaction was based on the ‘Hard’ contact in the normal direction and ‘Tangential’ contact with friction coefficient equal to 0.2 was assumed in the tangential direction. Authors find good agreement between the numerical simulation and the experimental test results under monotonic loading. However further numerical investigation with cyclic loading and specimen different tray direction (i.e. longitudinal deck) is needed. The finding of a parametric study on the force transfer mechanism is discussed in subsequent section.

To study the effect of the composite slab in moment resisting frame and the associated increase in demand on the column was numerically investigated by Mago and Clifton [32]. For this purpose one bare frame model and two with composite slab were simulated using ABAQUS. Four noded shell elements (S4R) with reduced integration was used to model the sub-assembly's beams, column, doubler plates and the metal deck, whereas the concrete slab was modelled using eight noded solid elements (C3D8R). The rebar mesh was stimulated suing beam element and embedded in slab assuming no slip between the rebar and concrete. Here the shear studs were modelled using the solid elements and embedded into the concrete. Frictionless contact was modelled between the beam flange and steel deck, and between the steel deck and concrete face. The material for the concrete slab was based on the 'concrete damaged plasticity' model. Authors find that the slab interaction with column increases the demand on the column. Also find that the slab was in contact with both the column flanges (outer and inner) and contributed more bearing resistance on column outer flange (associated with force transfer mechanism 1) and lower compression on the column inner flange (associated with force transfer mechanism 2) as shown in Figure 2.14.

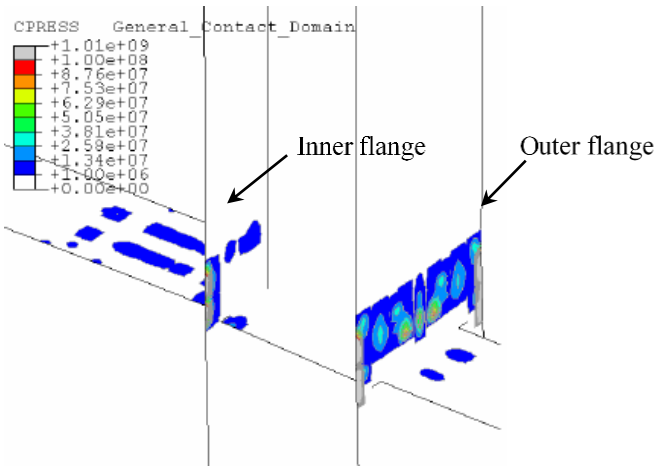

Figure 2.14 – Contact Pressure Distribution on Column Flanges [32]

Zhou et al. [33] performed a finite element analysis steel-concrete composite frame under cyclic loading using DIANA. This study involves modelling of two frame structure with composite slab and for this purpose the authors simplified the geometric details of the deck slab, which was a simulated using shell element as shown in Figure 2.15. The steel beam and columns were modelled using two noded beam elements with the elastic-plastic bilinear material. The shear studs were simulated using the spring elements and elasto-plastic material properties were assigned based on the elastic stiffness and maximum shear force in stud.

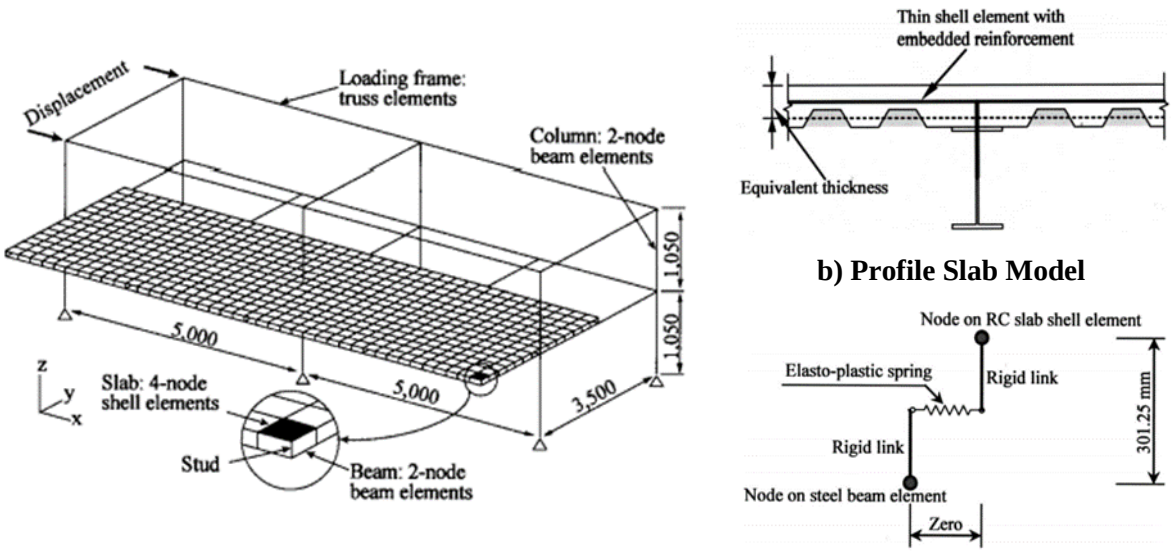

b) Profile Slab Model

a) Simplified Test Frame **c) Shear Stud Spring Model**

Figure 2.15 – Detail of FE Model of Test Frame. [33]

The results of the simulated test frame was calibrated using the results of experimental test carried by Nakashima et al. [34] and authors found that the total strain crack model of DIANA could able to provide a stable numerical solution to evaluate the hysteretic behaviour of concrete as well as the simulated model could bale to capture the similar strength and stiffness that of the experimental tests.

Mirza and Uy [35] studied the behaviour of the composite beam-column flush end connections using blind bolts under seismic loading. A numerical simulation was conducted using ABAQUS software. The various component of the sub-assembly was modelled using eight noded solid elements (C3D8R), whereas the shear studs and the blind bolts were modelled using the thirty-node quadratic brick element (C3D20R). The metal deck was represented by four noded shell elements (S4R) and two-noded truss element (T3D2) used for the rebars. The simulated model was calibrated by comparing with the experimental test and the further parametric study was conducted to study the effect of slab depth, stud spacing, reinforcement spacing, and effect of distance of stud from column surface. Based on the parametric study, the authors concluded that the increase in slab thickness would help in reducing the concrete cracking. They also found that the most suitable stud spacing is between 150 and 300 mm and the spacing beyond the 300mm will lead to stud fracture. The recommended location of the first shear stud from the column face was around 200-350mm and if the shear stud is located the bound 350mm, they suggested that the additional reinforcement required around the column to prevent severe cracking.

2.4 Macro Model Simulation

This section focuses on the literature related to the non-linear analysis of steel-concrete composite structures using the macro model simulation approach.

Kattner and Crisinel [36] developed a two-dimensional model using DIANA software to study the behaviour of semi-rigid composite joints wherein the beam elements are used to represent the steel beam, column and the concrete slab. Shear studs were modelled using the translational springs. The slab-column interaction was realised through the horizontal springs with compression only property. Linear kinematic conditions were used to link a slab with column and load-displacement behaviour of the translation springs was obtained from experiments and codes. Authors concluded that the proposed model of the composite joint with flush end plates could able to numerically simulate the global behaviour (i.e. moment-rotation) of the semi-rigid joint.

Rassati et al. [37] proposed a component-based modelling approach to simulate the partially restrained/semi-rigid composite connections. This model is formulated using eight different springs to account the influence of the various deformation components, including a slip in the bolts, partial interaction between the concrete slab and steel girder, shear deformation of the panel zone, and cracking and crushing of the slab. The connection spring stiffness and force-displacement properties were calculated based on the equations in Annex J of the EC3 [38]. A user-defined element was developed in ABAQUS software to implement the proposed component model. To incorporate the slab interaction with column face especially under positive moment (i.e. slab in compression) a concrete spring with length equal to 1.5 times column depth was used. The constitutive law used by authors for the concrete spring has linear behaviour up to its tensile strength, followed by a softening branch (i.e. tension stiffening effect) in tension, and elastic-perfectly plastic in compression, with no degradation in either stiffness or strength. The validation of the proposed model was carried out by comparing the simulated results with the previously developed model as well as with the experimental tests and it was found that after crushing of the concrete slab, the model could able to track both the strength and stiffness of sub-assembly under positive and negative loading. Authors concluded that the proposed model is capable of simulating the cyclic behaviour of the semi-rigid joints however it is too complicated for everyday professional practice and requires special user-defined element in ABAQUS. Therefore, there is also need to develop a simple model to simulate the rigid joint of the moment resisting frame as well as the formulation should be easily incorporated into any software.

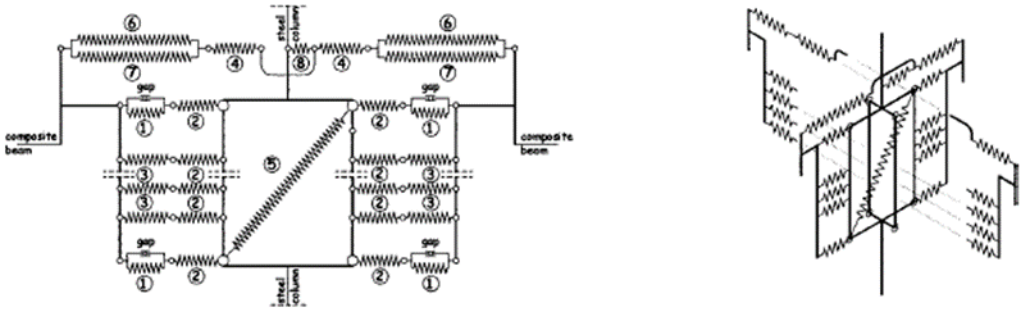

Figure 2.16 – Component Model for Composite Joint [37]

MacRae and Gunasekaran [39] proposed a beam-column joint model to study the slab effect on the moment resting frames considering the beam growth caused by the gap opening as well as to study the effect on beam overstrength. The proposed model was an extension of the model developed by Kim et al. [40] and to consider the slab effect a 'slab element' has been added as shown in Figure 2.17. This element is modelled as a strut element with bilinear hysteretic behaviour and the beam-column joint was treated as rigid joint, hence the shear deformation was ignored. Here, the slab element had some limitations like bending effect of the slab is ignored as well as the interaction of the column sides is ignored as the slab is not connected with the column node. The proposed model was developed using the computer program Ruaumoko–2D and calibrated with the experimental results. Authors observed that the model could able to capture the initial trends of the experiments, especially the strength on the loading part of the load-displacement curve. It was also observed that the sub-assembly strength was increased by 21% due to the presence of the slab.

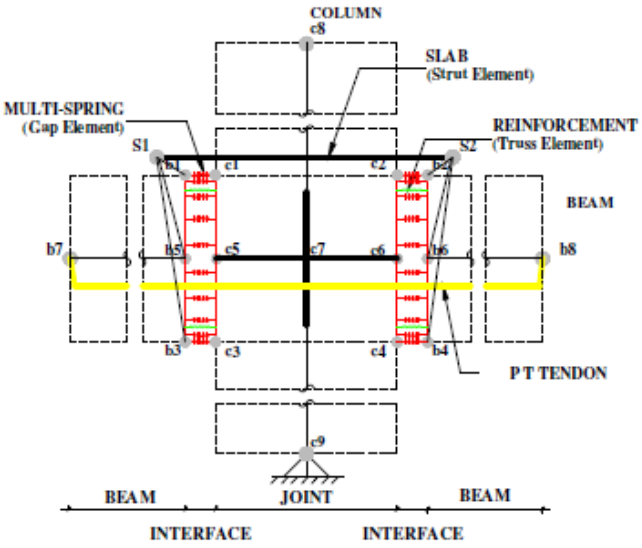

Figure 2.17 – Beam-Column Joint Model [39]

Elghazouli et al. [41] studied the seismic performance of the composite moment frame designed as per the provisions of EC8 [14]. For this purpose author used a nonlinear finite element program ADAPTEC. The frame elements like beam and column were modelled using the four cubic elasto-plastic elements (cbp2), which is based on the spread plasticity across the section and link elements (lnk2) were used to represent the composite action between the slab and steel beam. The panel zone was modelled into two parts, first part represents the main panel zone of the steel frame and the second part comprises the column portion which is in touch with the slab as shown in Figure 2.18. To consider the slab-column interaction, a contact behaviour was incorporated through the joint element with a rigid-plastic constitutive law. The capacity under positive bending was based on the maximum axial force developed in the slab through the composite action and the capacity under negative bending was based on the yield strength of the rebars. Authors carried out several time history analysis to study the influence of the loading, geometric and design parameters on the performance of composite moment frames and concluded that the structural configuration, choice of behaviour factor in relation to the seismic intensity and the panel zone effect influence the behaviour of the moment resisting frames.

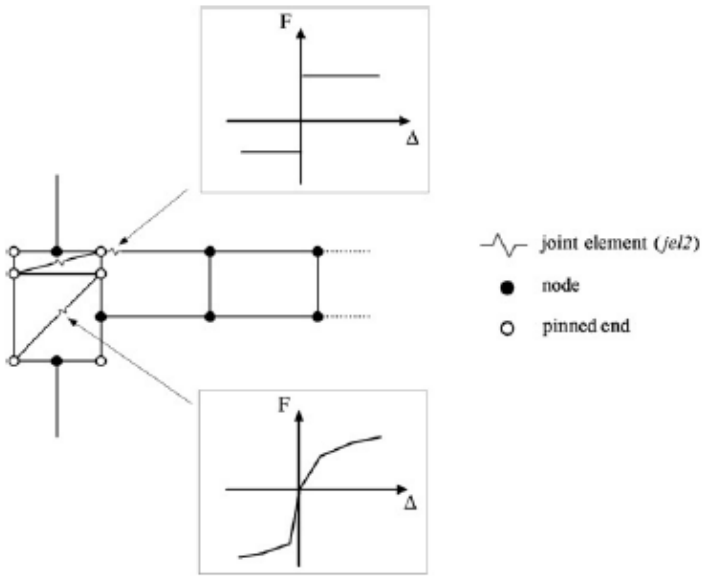

Figure 2.18 – Proposed Numerical Model of Composite Joint [41]

2.5 Strut-and-Tie Mechanism

The past research studies [15, 27, 30] shows that slab interaction with steel column resulted in the formation of the strut-and-tie mechanism to transfer the interaction forces. The unbalanced negative moment under gravity loads leads to developed of the additional tension on the one side of the column and which is balanced by the compression on the other side of the column through the formation of strut-and-tie mechanism as shown in Figure 2.19 [30].

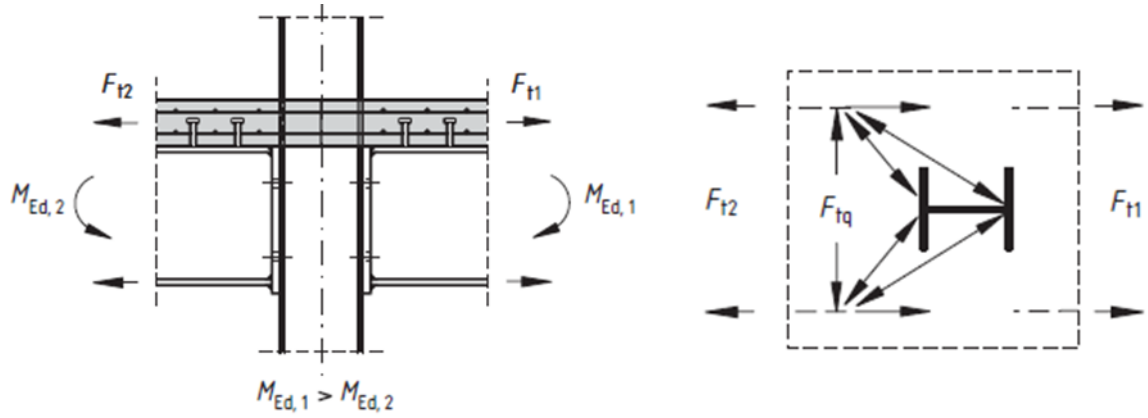

a) External Forces on Composite Joint **b) Internal Force Distribution**

Figure 2.19 – Strut-and-Tie Model for Unbalanced Loading (adopted from EC4 [42])

As per EC4 [42], the longitudinal rebars are designed such that the yielding of the transverse rebars and failure in concrete should be avoided. However, in case of the seismic loading, the frame sub-assembly developed positive (sagging) bending moment in one beam and negative (hogging) bending moment in another beam. Plumier and Doneux [30] argued that "*it is not certain that the EC4 proposed mechanism provides enough resistance to achieve at one side a ductile negative moment and at the same time at the other side a ductile positive moment without crushing of concrete*" and to minimise the damage in the slab they proposed that the yielding of the beam bottom flange should take place prior to crushing failure in slab under the sagging moment. To satisfy this condition, the concrete stains (ε_c) in the concrete slab top should be smaller than 0.002 under the cyclic loading condition. Authors suggested that raising the natural axis by maximising the effective width may suffice this objective. In case of the seismic loading, when no transverse beam is present, the slab-column interaction leads to the development of the two force transfer mechanisms; Mechanism-1(i.e. direct compression on the column flange) and Mechanism-2 (i.e. compressed concrete struts inclined at 45° to the column sides). If the transverse beam is present and it connected with slab using shear studs, then an additional force transfer Mechanism-3 (i.e. compression on the connectors of the transverse beam) is developed as shown in Figure 2.20.

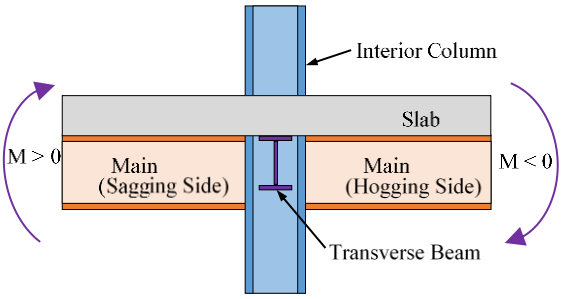

a) External Forces on Interior Composite Joint

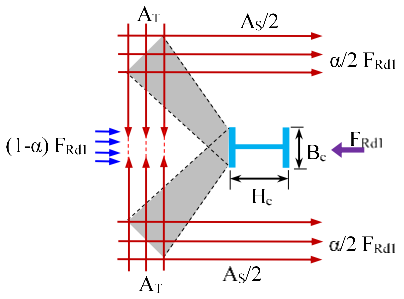

b) Mechanism-1 (direct compression on the column outer flange)

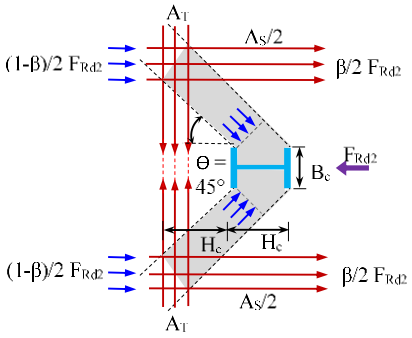

c) Mechanism-2 (compressed concrete struts inclined at 45° to the column sides)

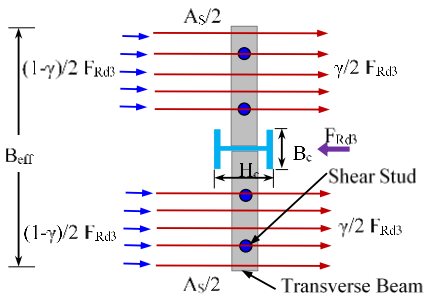

d) Mechanism-3 (compression on the connectors of transverse beam)

Figure 2.20 – Force Transfer Mechanisms in an Interior Composite Beam-to-Column Joint (adopted from EC8 [14])

The design capacity of these mechanisms can be calculated using the expressions provided in EC8 (Annex C) [14] as given below:

$$F_{Rd1} = B_c\, d_{eff} f_{cd} \tag{2.1}$$

$$F_{Rd2} = 0.7 H_c\, d_{eff} f_{cd} \tag{2.2}$$

$$F_{Rd3} = n P_{Rd} \tag{2.3}$$

where:

B_c	=	Column flange width
H_c	=	Column depth
d_{eff}	=	Topping slab thickness
n	=	Number of connectors in effective width
P_{Rd}	=	Design resistance of one connector

Salvatore et al. [15] carried out a 3D finite element analysis to study the effect of the strut-and-tie mechanisms. To activate Mechanism-1, authors removed the friction of contact surfaces between the concrete of the slab and the partially encased column. However, to activate Mechanism-2, the nodes between the concrete of the slab and concrete of the column have been connected. The hard contact between the column flange and concrete slab was established as well as the connection of the nodes between the concrete of the slab and the concrete of

composite column was reestablished to activate the mechanisms-1 and 2. The distribution of the minimum principal stresses in concrete slab corresponding to different force transfer mechanisms is shown in Figure 2.21. As per a study conducted both on the exterior and interior joints of the frame subassembly, authors concluded that the full activation of Mechanism-1 and 2 in the concrete slab causes stiffening and strengthening of joints. It was observed that, the Mechanism-1 and Mechanism-2 do not have same stiffness, wherein Mechanism-1 exhibits greater stiffness than Mechanism-2.

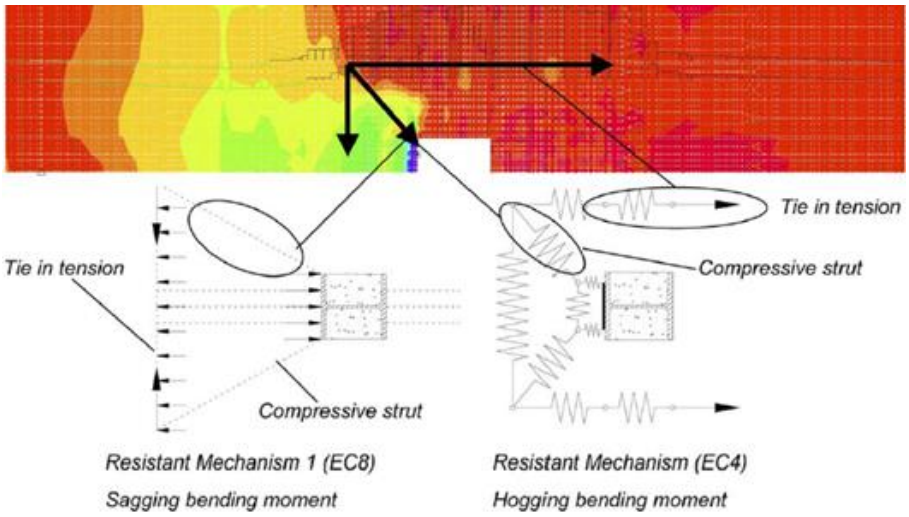

a) Minimum Principal Stresses in Concrete Slab with Activation of Mechanism-1

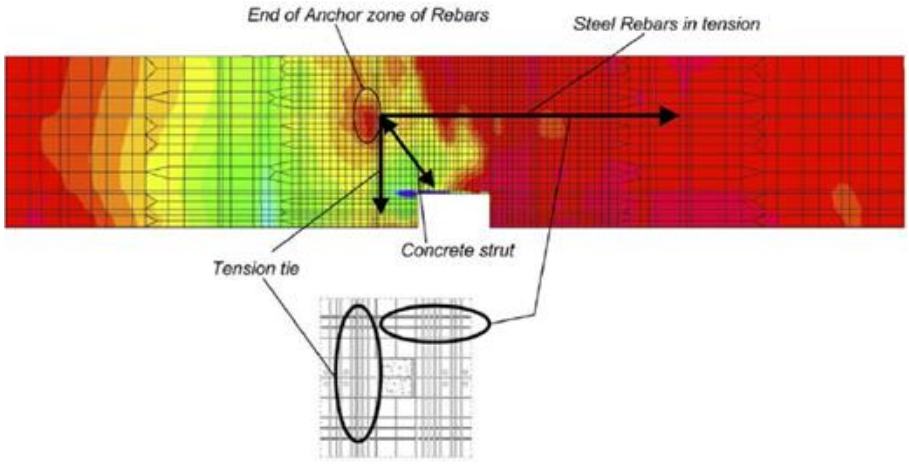

b) Minimum Principal Stresses in Concrete Slab with Activation of Mechanism-2

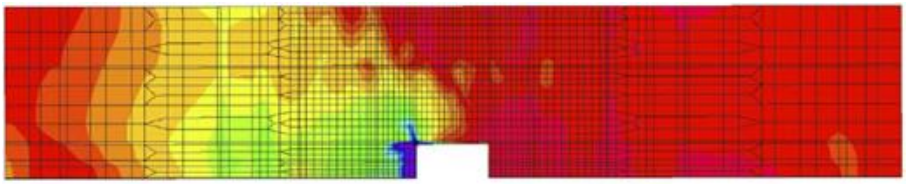

c) Minimum Principal Stresses in Concrete Slab with Activation of Mechanism-1and 2

Figure 2.21 – Minimum Principal Stresses in Concrete Slab of an Interior Joint at 3.0% Lateral Drift (adopted from Salvatore et al. [15])

2.6 Slab Confinement

MacRae et al. [29] discusses on the confinement of the concrete slab in the slab-column interaction zone. Also, the possible methods to improve the state of concrete in this zone to avoid concrete spalling failure has been proposed. As noted by Hobbs et al. [28], when the column pushes against the composite deck slab, the slab only carries the load if the concrete does not lose strength through an axial stress, shear stress or spalling failure. Considering the composite slab configuration in the vicinity of the column, the slab portion which bears against the column is typically confined on three sides (i.e. below and on the two sides two sides) and the slab is not confined from the top. The stress and strain associated with the initiation of spalling can be conservatively considered to be the unconfined concrete crushing strength f'_c and ε_c = 0.002 respectively. The current NZS3404:1 [5] code specified the location of first shear stud/connector should be at 1.5 times the depth of beam (to avoid any stress concentration in the beam-yielding zone). As mentioned before in Section 2.5, the strain in concrete interaction zone should be less than 0.002 in order avoid/minimise the concrete spalling [30]. If the concrete strain in this zone is less than 0.002, then only spalling can be avoided, however in reality to maintain a strain below 0.002 is a big challenge. Whereas the strain capacity within the concrete slab in this zone (1.5 times beam depth) can be increased by achieving the confinement of top of the slab. Authors suggested that the confinement can be done by two ways; (i) slab confinement with steel top plate, and (ii) slab confinement with rebar cage as shown in Figures 2.22 and 2.23.

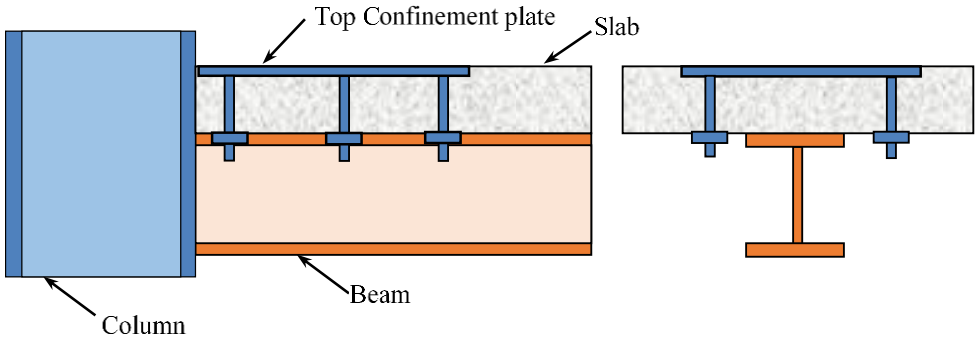

a) Side View **b) End View**

Figure 2.22 – Slab Confinement with Top Plate (adopted from MacRae et al. [29])

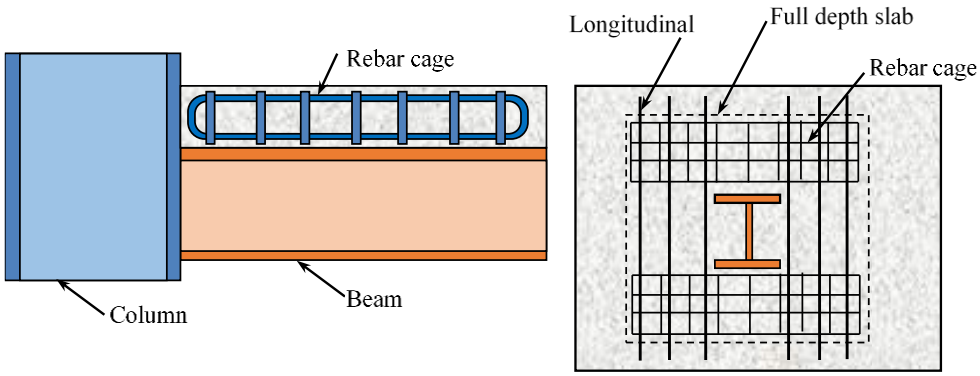

a) Side View **b) Plan View**

Figure 2.23 – Slab Confinement with Rebar Cage (adopted from MacRae et al. [29])

2.7 Current Code Provisions for Seismic Design of Composite Frames

2.7.1 New Zealand Code

The slab-column interaction in the New Zealand steel code is considered in the design, to calculate the over strength moments arising from the composite action of the slab. The overstrength moments acting at the column face is calculated as the sum of overstrength moment capacities of the composite beam's framing in to the column and the moment associated with the slab axial force acting at the centroid of the slab as shown in Figure 2.24(a). Currently, in NZS3404:1 [5] the overstrength moment capacities of the composite beam is calculated by using an overstrength factor of 1.25 applied to the nominal moment capacities of the bare steel beam and then multiplying by a factor to represent the contribution of the composite slab to the overstrength moment capacity of the beam. The beam's framing in to the joint along with the composite deck slab shares a horizontal equilibrium resulting in the development of axial forces in the beam, which results in a reduction of the moment capacity of the beams. The amount and level of reduction can be calculated using the axial force-moment interaction diagram shown in Figure 2.24(b).

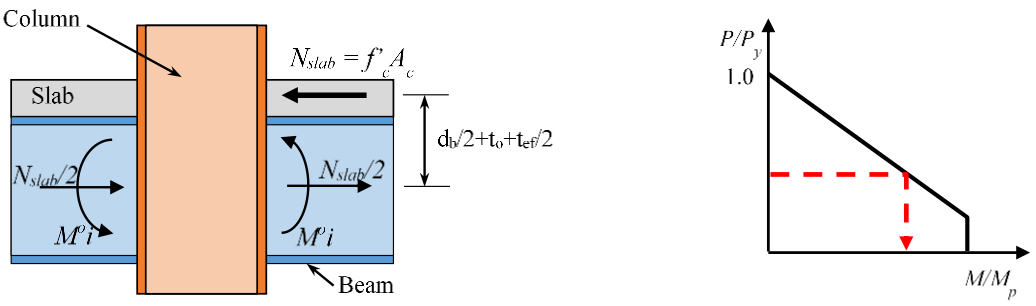

a) Axial and Flexural Forces imposed by Beams **b) Axial Force- Moment interaction**

Figure 2.24 – Axial and Flexural Force imposed by Beam on the Sub-assembly Composite Joint (adopted from MacRae et al. [6])

NZS 3404 steel code defines the process for determining the overstrength moments of moment resisting frames with different ductility levels (i.e. ductile, limited ductile and nominally ductile). The overstrength moment capacity of the beam (M^o_{bi}) is calculated by applying an overstrength factor (ϕ_{oms}) to the nominal moment capacity of the beams as shown in Equation 2.4. Further, the overstrength moment capacities of the beams are reduced to take in to account the axial forces arising due to the composite slab as shown above in Figure 2.24. The modified moment capacity of the beam considering the axial force-moment diagram can be calculated using Equation 2.5.

$$M^O_{bi} = \varphi_{oms} M_{bi} \tag{2.4}$$

The steel beam moment-axial force interaction is shown in Equation 2.5.

$$\sum M^o_i = min\left\{1.18 \times \left(1 - {N_{slab}}/{\sum(A_g f_y)_i}\right) \times \sum M^O_{bi}; \sum M^O_{bi}\right\} \tag{2.5}$$

The slab axial force (N_{slab}) is calculated considering the compressive strength capacity of the concrete (f'_c) and the contact area with the column, provided that the axial force calculated is limited by the axial capacity of the beams. The slab axial force can be calculated using Equation 2.6, where the effective contact width (b_{sef}) and the effective thickness (t_{ef}) depend on the size, type and orientation of the column, and type and layout of the deack slab respectively. The effect of short and long term increment in the concrete strength is considered by using a factor f'_{cos} and is usually taken as 10 MPa.

$$N_{slab} = min\left\{1.3 t_{ef} b_{sef} (f'_c + f'_{cos}); \sum (A_g f_y)_i\right\} \tag{2.6}$$

The overstrength moment demand acting at the column face (M^O) is calculated by summing up the overstrength moment capacities of the beams framing into the column and the moment arising due to the axial forces in the slab acting over a lever arm between the slab and beam centroid ($d_b/2+t_o-t_{ef}/2$) and is shown in Figure 2.24 (a). The overstrength moment demand at the column face is calculated using Equation 2.7. Where, d_b is the depth of the beam and t_o is the thickness of the slab.

$$M^o = \sum M^o_i + N_{slab}\left({d_b}/{2} + t_o - {t_{ef}}/{2}\right) \tag{2.7}$$

The New Zealand steel code also prescribes a simplified methodology to calculate the overstrength moment demand at the column face for I section beams framing into the flanges

on I section columns. In such scenarios, the overstrength moment demand can be calculated by multiplying section capacity of the beam (M_s) with a modified overstrength factor (φ_{omss}) which inherently taken into account the effect of the slab. The overstrength moment demand at the column face can be calculated using Equation 2.8 and Equation 2.9 and is derived based on the empirical data and has shown to have at most 3% loss of accuracy within the practical range of t_{ef}/d_b.

$$M^o = \varphi_{omss} M_s \tag{2.8}$$

$$\varphi_{omss} = \varphi_{oms}\left(1.0 + 1.08\, {}^{t_{ef}}/_{d_b}\right) \tag{2.9}$$

The method of accounting slab participation in the joint overstrength moment is based on the assumption that the slab is infinitely rigid and strong axially and carries the force through the concrete bearing against the outer column flange and the effect of inner column flange is ignored. However, in reality the slab interaction forces are developed on both columns outer and inner flange as shown in Figure 2.25.

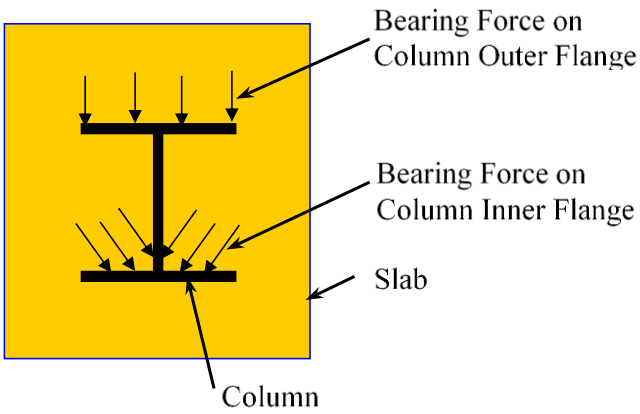

Figure 2.25 – Bearing Force Distribution on Column from the Concrete Slab (adopted from MacRae et al. [6])

2.7.2 American code

In ANSI/AISC:341-10 [43], no specific methods are given to determine the effect of slab-column interactions on the column. It acknowledges the fact that the force transfer can occur between the concrete slab and the adjoining steel members through the bearing and the slab effects were considered under capacity design where the resisting moment of the column must be greater than the sum of the resisting moments of the composite beams framing into it or the sum of the resisting moments of the connections if partial strength connections are used (particularly in composite partially restrained moment frames C-PRMF). As per code: *"The*

system should be designed to enforce a strong column-weak beam mechanism except for the roof level. ASCE TC (1998) suggests using the following equation to achieve this beahviour, where M_{cu}^{+} and M_{cu}^{-} *refer to the connection moment strength in positive and negative bending respectively:"*

$$\sum M_{p,col}\left(1-\frac{P_u}{P_0}\right) > 1.25\left(M_{cu}^{+} + M_{cu}^{-}\right) \tag{2.7}$$

where:

$M_{p,col}$	=	Nominal plastic flexural strength of the column
M_{cu}	=	Connection moment strength
P_u	=	Required axial strength
P_o	=	Nominal axial strength

Since the force transfer from the slab to the column relies on the bearing, the code specified to provide a full depth slab from the column flange at least for a distance of 305mm (i.e.12inch) as shown in Figure 2.26 (a) or provision of alternative arrangement of reinforcement in the column flange width as shown in Figure 2.26 (b)

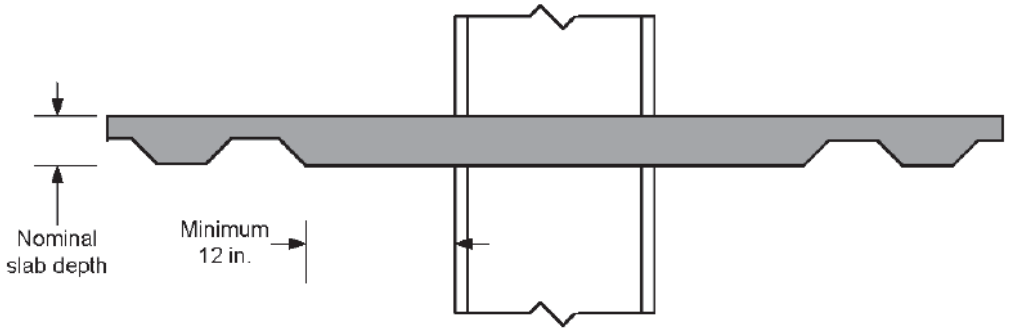

a) Provision of Solid Slab around Column

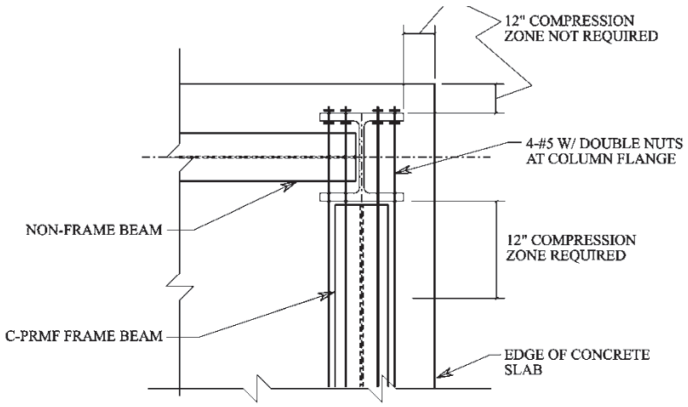

b) Alternate means of Providing Slab Force Transfer

Figure 2.26 – Provision of Solid Slab around Column and Alternate means of Force Transfer (adopted from ANSI/AISC:341-10 [43])

2.7.3 Eurocode

Section 7 of the Eurocode 8:1 [14] covers the seismic design of composite moment resisting frames. The code provides detailing requirements for the slab surrounding a column as shown in Figure 2.27 and these are mainly to ensure the development of the force transfer Mechanism-1 and 2 shown in Figure 2.20. Annex C discusses the design of the slab and its connection to the steel frame in moment resting frame. To ensure high ductility in bending, it specifies following two requirements;

i) Early buckling of the steel part shall be avoided
ii) Early crushing of the concrete of the slab shall be avoided

The above mentioned ductility requirement was fulfilled by imposing an upper limit on the cross-sectional area of the longitudinal reinforcement (A_s) and lower limit of the cross-sectional area of the transverse reinforcement (A_T) as shown in Figure 2.27. It also discusses the details of the different force transfer mechanisms (i.e. Mechanism-1, 2 and 3). To achieve yielding in the bottom flange of the steel section without crushing of the slab concrete, the code specified that the the total compressive force developed in these force transfer mechanisms should be 1.2 times higher than the total slab force developed in the slab (due to positive and negative bending of the beams on either side of the column) which is given as:

$$F_{Rd1} + F_{Rd2} + F_{Rd3} \geq 1.2(F_{sc} + F_{st}) \tag{2.8}$$

where:

F_{Rd1}, F_{Rd2} & F_{Rd3}	=	Resistance of mechnasim-1,2 and 3 respectively (refer Equations 2.1 to 2.3)
F_{sc}	=	Compression force in concrete in positive bending = $b_{\text{eff}}\, d_{\text{eff}}\, f_{\text{cd}}$
F_{st}	=	Tension force in the reinforcing bars parallel to the beam
b_{eff}	=	Effective width in positive bending

The explicit method for the design of the column considering the effect of slab-column effects is not specified.

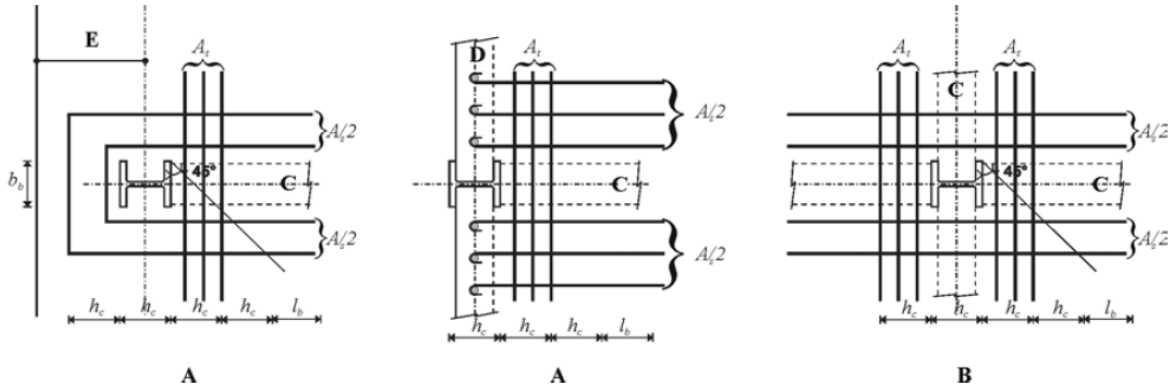

Figure 2.27 – Provision of Seismic Rebars according to Eurocode 8 (adopted from EC8 [14])

Chapter 3: Experimental Test Program

This chapter describes the selection of five different test configurations of the beam-column sub-assembly, test configurations details, test setup details and construction, material properties, loading protocol, instrumentation and interpretation of test results.

3.1 Selection of Test Configurations

In order to study the slab effects on the beam-column sub-assembly, five different test configurations were selected based on the literature and research study conducted by Hobbs [3]. Several different options for specimen configuration were assessed at the conceptual level, and the decision was made on the basis of subjective quantitative assessment (SQA). The selection was conducted using the following criteria:

i) Interaction between the slab and the column (i.e. force transfer mechanism).
ii) State of concrete (confinement or unconfined) around the column.
iii) Prevention of shearing of concrete in between the column flanges.
iv) The orientation of the deck.
v) Architectural Considerations.
vi) Cost-effectiveness and ease of application.

Details of the SQA are included in Appendix B. The test configurations selected for further investigation resulting from the SQA are summarised in Table 3.1.

Table 3.1: Summary of Test Configurations

Test	Specimen Designation	Deck Orientation	Detail around the Column	Active Force Transfer Mechanism
1	Bare Steel Frame **(BSF)**	-	-	-
2	Fully Isolated Slab Unit **(FI-SU)**	Transverse Deck	All around isolation of slab from the column	none
3	Shear Key Slab Unit **(SK-SU)**	Longitudinal Deck	Slab isolated on the column outer flange	Mechanism-2
4	Modified Shear Key Slab Unit **(MSK-SU)**	Longitudinal Deck	Slab isolated on the column outer flange	Mechanism-2
5	Full Depth Slab Unit **(FD-SU)**	Transverse Deck	Slab casted touching to the column on full depth	Mechanism-1 and Mechanism-2

3.2 Test Specimen Design

The test specimens represent the internal beam-column joint of a fictitious building with a moment resisting frame supporting a composite deck slab. The sub-assembly details (beam, column, panel zone and the deck slab) are similar to that from a previous experimental study

conducted at the University of Canterbury by Hobbs [3]. The design calculations are included in Appendix A. Test specimens were 3.0 m wide and 6.0 m long with a 150 mm deep ComFlor80 [4] deck slab. It was supported by two Grade 300 310UB32 primary beams. The column was a Grade 300 310UC158. The deck slab was provided with two shear studs (ϕ19 mm x 125mm long) per trough with a spacing of 300 mm. No shear studs were provided within 1.5 times the depth of the beam from the column face in accordance to NZS3404 Clause 13.4.11.3.3 [5]. The SE82 (Grade 500E Steel, ϕ8 mm round bar in a 200 mm x 200 mm grid) [44] anti-crack rebar mesh was placed 35 mm below the slab surface as recommended in NZS3404:1 [5]. Based on the ComFlor 80 design guide [4], additional reinforcing was provided around the column, in the form of 2-ϕ12 mm (deformed) Grade 500E rebars on each side of the column. Deformed ϕ10 mm Grade 500E rebars were tied to the mesh from the bottom side in each deck trough. The concrete had set to a target strength of 30 MPa at 28 days.

3.3 Details of Test Configurations

3.3.1 Bare Steel Frame (BSF)

In the BSF test configuration, the column and beams were connected through extended end plate connections as shown in Figure 3.1. This test configuration was considered as a benchmark/control for comparison with other test configurations with composite deck slab.

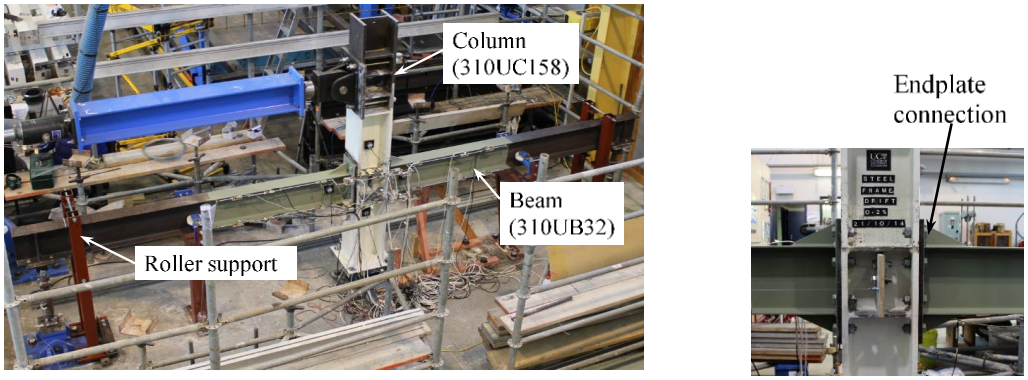

a) Test Configuration Setup **b) Connection Details**

Figure 3.1 – Bare Steel Frame (BSF) Test Sub-assembly.

Roller supports were provided at the beam ends to limit lateral displacement of the beam at the ends and to limit the possibility of significant lateral torsional buckling as shown in Figure 3.2. These rollers allowed free movement along the beam length (X-axis) as well as in vertical direction (Z-axis) and arrested the out-of-plane movement (Y-axis). The grease was applied in between the beam flange tips and the rollers to minimise frictional effects.

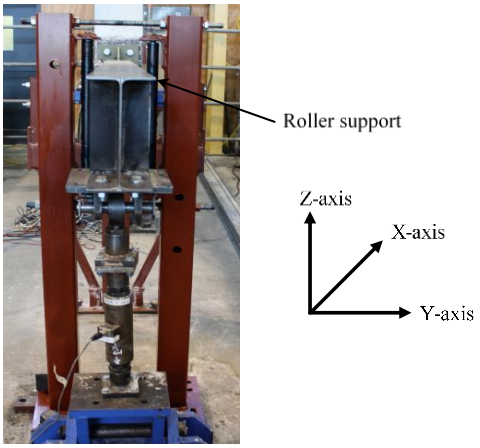

Figure 3.2 – Rolled Supports at Beam End.

3.3.2 Fully Isolated Slab Unit (FI-SU)

The fully isolated test configuration comprised a steel beam-column sub-assembly with a composite deck slab, and the slab was fully isolated around the column using infill material (Actifoam) as shown in Figure 3.3. The infill material has been selected based on subjective quantitative assessment (SQA), and details of the material selection process have provided in Section 4.4. The main salient feature of this test configuration is the deactivation of both the force transfer Mechanism-1 and Mechanism-2 as per EC8 [14], in order to study the effect of slab isolation on the beam-column sub-assembly and system overstrength.

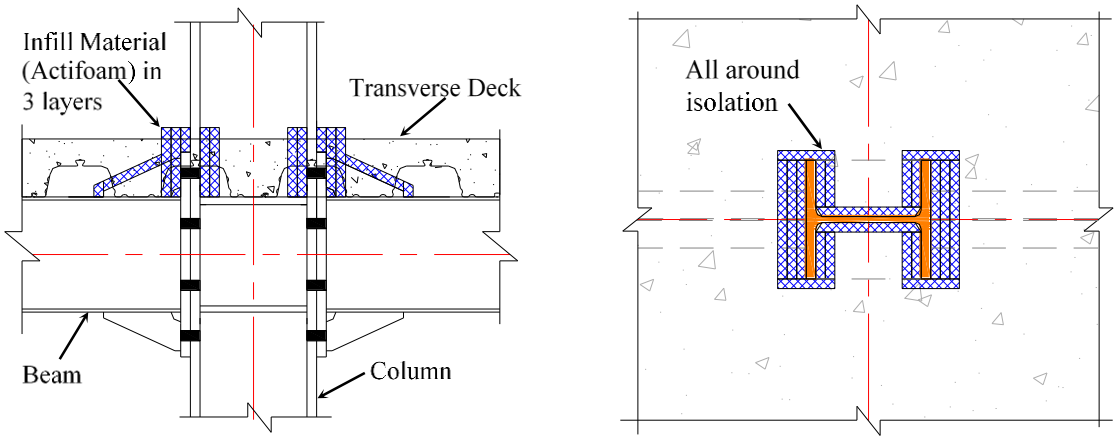

a) Front View **b) Plan**

Figure 3.3 – Fully Isolated Slab Unit (FI-SU) Test Sub-assembly.

The actifoam (25 mm thick) as an infill material was applied in three layers to cover the extended end plate (layer 1), bolt head/nut (layer 2), and the actual isolation gap (layer 3). Isolation of the gusset plates was also provided as shown in Figure 3.4. It is important to note that, the isolation detail around the column may vary according to the type of beam-column connection (e.g. Bolted flange plate connection or a welded connection) [45].

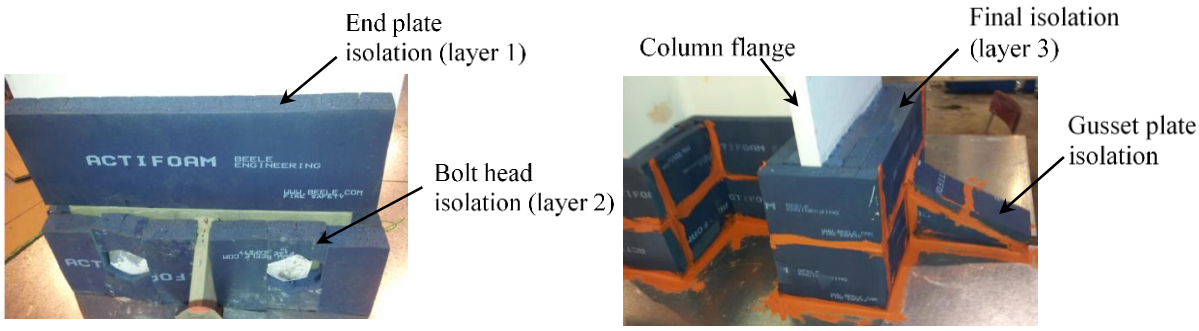

a) Isolation in layers **b) All around isolation**

Figure 3.4 – Slab Isolation details for Bolted End Plate Connection.

As noted by Hobbs [3], any exposure of steel material leads to partial isolation and an interaction force starts bearing on the exposed steel component as shown in Figure 3.5. The utmost care has been taken in the current test configuration, in order to achieve full isolation.

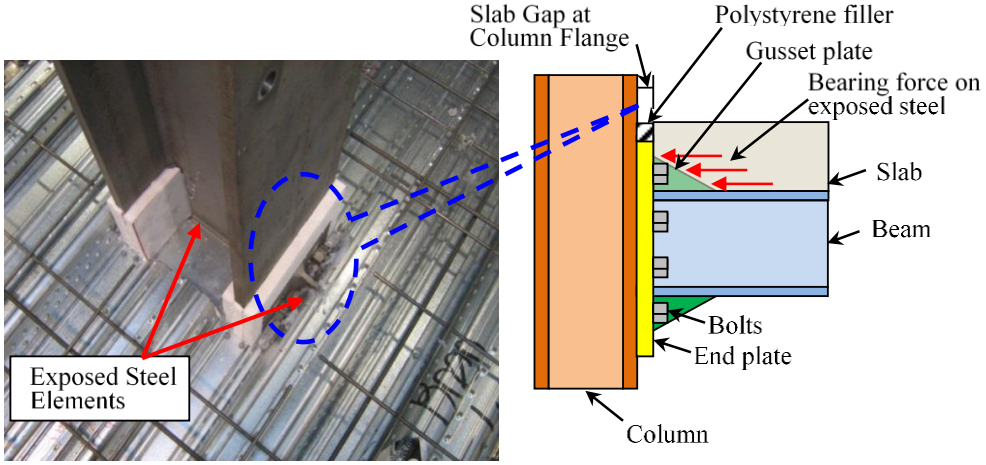

Figure 3.5 – Partial Isolation: Exposed steel connection [46].

3.3.3 Shear Key Slab Unit (SK-SU)

In this test configuration, a shear key has been introduced by providing the reinforcement in the form of the U-shape rebar (Hair Pin). This arrangement was based on the analogy of the concrete corbel. The slab bearing occurs on the internal surface of the column flanges. In order to avoid concrete crushing/spalling, the slab was isolated on the external surface of the column flanges as shown in Figure 3.6. The composite deck was oriented in the longitudinal direction. The shear key was provided in the form of 4-ϕ16 mm (deformed) Grade 500E rebars with a bend of 5 times bar diameter as recommended in NZS3101:1 [47]. The spacing between two shear key rebars was 50 mm, and a cover of 30 mm was provided from the column internal flange. The details of the reinforcement layout around the column has been provided in Appendix A.

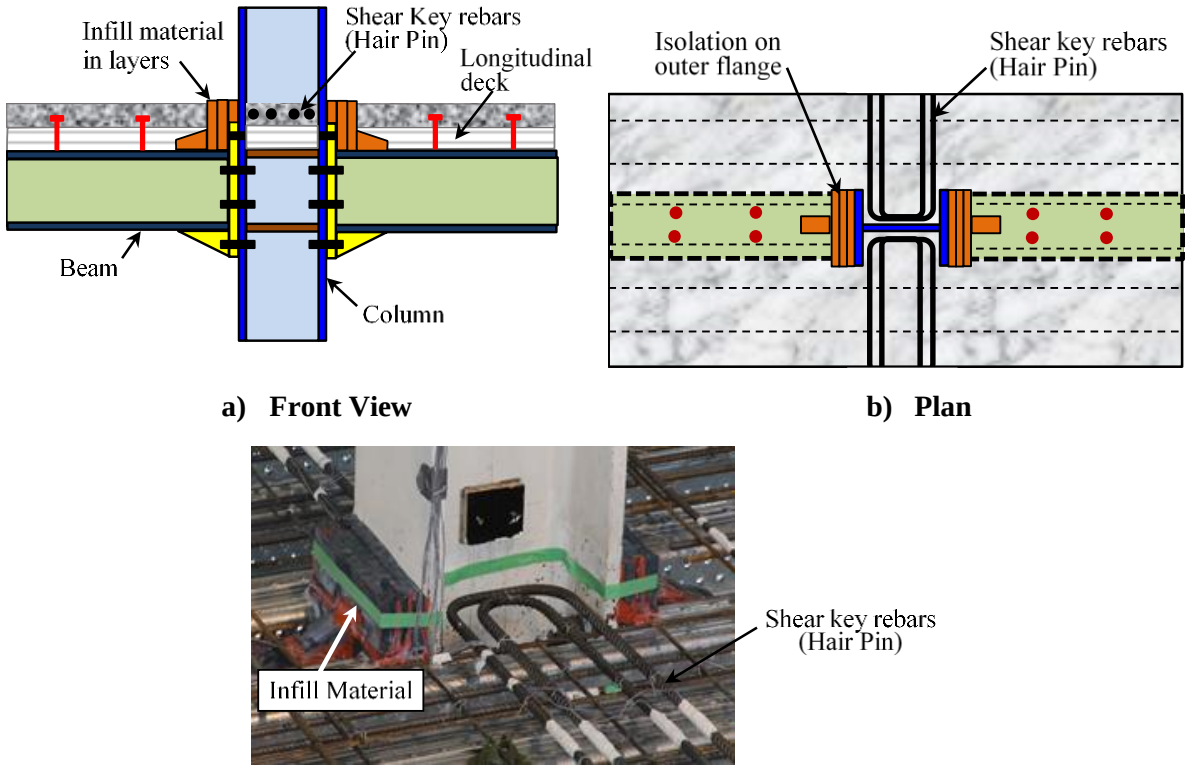

a) Front View **b) Plan**

c) Construction detail before concreting

Figure 3.6 – Shear Key Slab Unit (SK-SU) Test Sub-assembly

The main salient feature of this arrangement was the activation of the only one force transfer mechanism, which was Mechanism-2 (compression on the column sides) and deactivation of the Mechanism-1 (compression of the column flanges). An additional force transfer mechanism (Mechanism-3), caused by force applied through the transverse (secondary) beam was prevented (no shear studs on secondary beam). The shear key was designed based on the shear friction concept as per New Zealand code [5], and an adequate development length was provided beyond the column flange tips. The objective of this test configuration was to evaluate the contribution of the Mechanism-2 to the system strength.

3.3.4 Modified Shear Key Slab Unit (MSK-SU)

The modified shear key slab test configuration (MSK-SU) is conceptually similar to the shear key test configuration (SK-SU); wherein the shear key rebars are anchored to the slab with the help of welded threaded rods. Two centrally located, vertical threaded rods (M16 - Class 4.6) were welded to the continuity plate in the panel zone to facilitate the rebar anchorages as shown in Figure 3.7c. Instead of the hairpin shape rebars, V-shape rebars have been used for the construction ease, as the limited space was available. The shear key was provided in the form of 4-ϕ12 mm (deformed) Grade 500E rebars with a bend of 5 times bar diameter as recommended in NZS3101:1 [47]. The spacing between two shear key rebars was 30 mm. The

V-shape rebars were provided at 60° inclination with column web. The details of the reinforcement layout around the column have been provided in Appendix A. In order to achieve confinement from the slab top; the steel plate was bolted to the slab before the commencement of the experimental test. For this purpose, two additional threaded rods (M24 - Class 4.6) located near to column flanges were welded to the continuity plate. The PVC sleeves were provided to the threaded rods to achieve debonding between the concrete and threaded rod as shown in Figure 3.7c. A thin layer of dental plaster was applied between the slab and confinement plate, to achieve a level surface as well as to provide a uniform stress distribution.

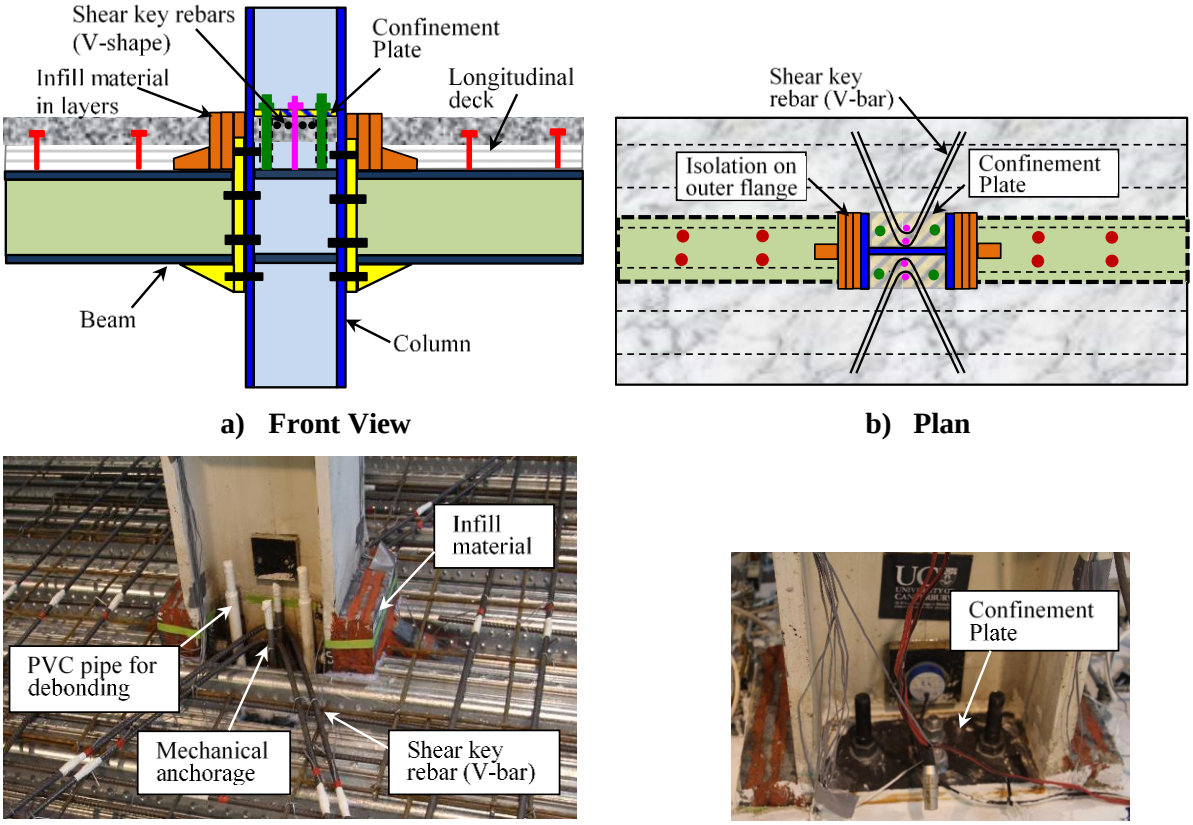

a) Front View **b) Plan**

c) Construction detail before concreting **d) Confinement plate in place**

Figure 3.7 – Modified Shear Key Slab Unit (MSK-SU) Test Sub-assembly

Similar to the SK-SU test configuration, the slab was isolated on the external surface of the column flanges by using actifoam as an infill material, in order to deactivate the force transfer Mechanism-1. In this test configuration, Mechanism-2 was the only active force transfer mechanism.

3.3.5 Full Depth Slab Unit (FD-SU)

In the full depth slab test configuration (FD-SU), a square size (3 times column depth) cut-out in a decking sheet was provided around the column as shown in Figures 3.8a and 3.8b. The concrete in full depth portion was confined using a reinforced cage made out of plain 8 mm diameter rebars of Grade 300E placed at 100 mm spacing. Other details like those of shear key rebars and provision of the confinement plate in between the column flanges, were kept similar to the MSK-SU test configuration as shown in Figure 3.8c. The details of the reinforcement layout around the column have been provided in Appendix A. A plain galvanized sheet of 1.5 mm steel was used to support the concrete in the full depth portion. It was connected to the surrounding decking sheet using self-tapping screws. Additional propping was provided at the junction of the decking and the sheet at the time of the concrete pour. The composite deck was oriented in the transverse direction.

The main aim of the FD-SU test configuration was to evaluate the effect of force transfer Mechanism-1 and Mechanism-2 [14] on the system strength as well as to assess the effect of confinement on the strength and stiffness at the larger storey drifts.

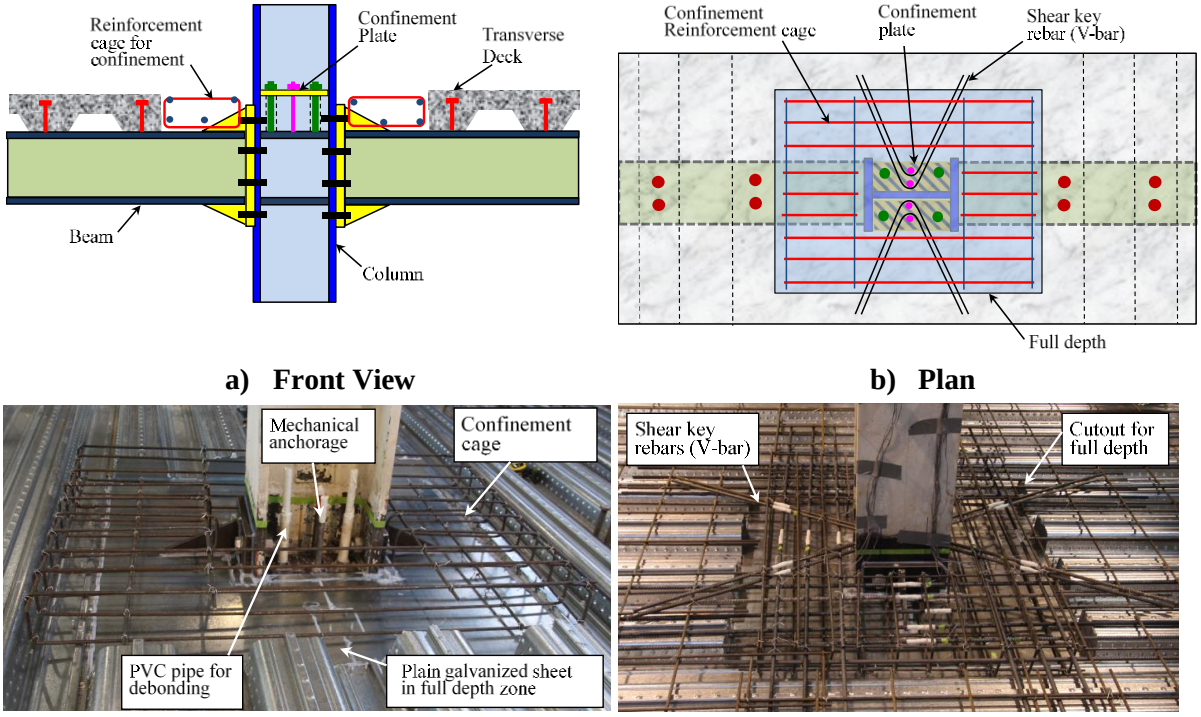

a) Front View **b) Plan**

c) Construction detail before concreting

Figure 3.8 – Full Depth Slab Unit (FD-SU) Test Sub-assembly.

3.4 Material Properties

3.4.1 Steel Properties

Section Dimensions and Tolerances

The steel sections used in the experimental test were obtained through the steel supplier (Vulcan Steel Ltd.) and were produced/supplied by OneSteel, Australia [48]. The standard dimensions of the hot-rolled steel beam section 310UB32 (Grade 300) and 310UC158 (Grade 300) column are presented in Table 3.2 along with measured dimension (average of three values). These dimensions were found to be within accepted tolerances set by the AS/NZS 3679.1 standard [49].

Table 3.2: Section Sizes and Dimension Tolerances

Designation	Beam (310UB32)			Column (310UC158)		
	Standard (mm)	Measured (mm)	Permissible Variation (mm)	Standard (mm)	Measured (mm)	Permissible Variation (mm)
Depth (d)	298	297.98	± 3.0	327.2	327.17	± 3.0
Flange Width (b_f)	149	149.52	+6 to -5	311	308.67	+6 to -5
Web Thickness (t_w)	5.5	5.72	± 0.7	15.7	15.44	± 1.0
Flange Thickness (t_f)	8.0	7.88	± 1.0	25	26.19	± 1.5

Tensile testing

The mechanical properties of the Beam (310UB32, Grade 300), Column (310UC158, Grade 300) were obtained through monotonic tensile testing. The test coupon was prepared based on the AS1391[50] procedure, and the test specimens were taken from the steel section before testing (for this purpose, extra lengths were ordered for each specimen). The cut-out location for the test coupon was selected as suggested by the AS/NZS 3679.1[49]. The tensile coupon dimensions are shown in Figure 3.9. The test coupons were tested using universal testing machine available at the structural laboratory of the University of Canterbury.

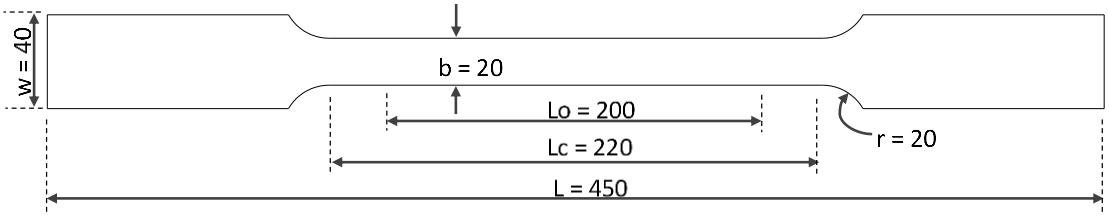

Figure 3.9 – Tension Coupon Details

Three test pieces were fabricated and tested for each section, and average values of the test results are shown in Table 3.3 below in comparison with mill certified values and code values.

An average area of the test specimen was calculated by measuring the width and thickness at the three different locations, and the stress was calculated as the applied load divided by the average specimen area. Whereas, the strain was obtained by using epsilon extensometer of 50 mm gauge length. The extensometer was used up to the necking formation and to avoid damage to the instrument; it was removed before specimen breaking. From the stress-strain curve, the yield stress (σ_y) and yield strain (ε_y) were noted down. The ultimate strength (σ_u) and ultimate strain (ε_u) were also noted. The detail test data of the tension test and mill certificates are presented in Appendix C.

Table 3.3: Tensile Test Results & Mill Certified Test Values

Section		Tensile Test (average values)		Mill Certified Test		AS/NZS 3679.1 :2010	
		Yield Stress (MPa)	Ultimate Strength (MPa)	Yield Stress (MPa)	Ultimate Strength (MPa)	Yield Strength (MPa)	Ultimate Strength (MPa)
Main Beam 310UB32	Flange	342.83	502.06	347.5	485	320	440
	Web	365.32	505.93			320	440
Column 310UC158	Flange	287.01	474.54	322.5	490	280	440
	Web	309.05	477.37			300	440
***Secondary Beam 200UB29.8**	Flange	-	-	351.67	503.33	320	440
	Web	-	-			320	440

Note: *Tension coupon test for the secondary beams (200UB29.8) was not carried out since they were not a part of the load resisting systems and designed to carry very small load arising from the slab self-weight.

The primary beam, 310UB32 had a minimum specified yield stress of 320 MPa and an ultimate stress of 440 MPa (for both the flange and the web). The ratio of the values obtained through tension coupon test to the minimum specified values by AS/NZS 3679.1, falls within the range of 1.07 to 1.14 for the yield strength. Similarly, for the ultimate strength, it varies from 1.14 to 1.15.

3.4.2 Concrete Properties

The concrete needed for the experimental testing was set to a minimum compressive strength of 30 MPa at 28 days and a maximum aggregate size of 19 mm with 100 mm slump. The concrete was ordered from the ready-mix concrete supplier "Allied Concrete" in batches of 2.3 m^3 to 2.5 m^3 for each slab configuration, considering the quantity needed for the test cylinders and wastages. The batch records obtained from the supplier is presented in Appendix C.

The test cylinders of 100 mm diameter and 200 mm length were cast on the day of a slab pour.

The test specimen was filled in three equal layers and compacted using the vibrating table as suggested in NZS3112.2 [51] and cured at 20° temperature in the fog room. The end-capping was provided to the cylinders using a thin layer of the dental plaster in order to get an even surface and uniform force distribution. The average values of the three compression cylinder tests are presented in Table 3.4 below.

Table 3.4: Concrete Compressive Strengths (N/mm^2)

Test Specimen	Compressive Cylinder Strength		
	21 Days	**28 Days**	**Test Day**
Fully Isolated Slab Unit **(FI-SU)**	39.91	43.42	45.27
Shear Key Slab Unit **(SK-SU)**	34.0	39.0	41.16
Modified Shear Key Slab Unit **(MSK-SU)**	34.0	39.61	*39.61
Full Depth Slab Unit **(FD-SU)**	33.89	39.61	*39.61

***** The testing of the slab carried on the 28th day of cast

3.4.3 Fastener/Stud Properties

The moment frame connection was constructed using bolted endplate connections to connect the beams to the column. The bolts used for the endplate connection were M24 structural Class 8.8 with the appropriate washers. The Blacks fasteners supplied all bolts used in the experimental testing and complying to the AS/NZS 1252 [52]. Before installation of the bolts, the steel section surface was cleaned using the wire brush to remove the rust and loose particles followed by the cleaning using acetone. Initially, the bolts were tightened by using a hand wrench to a snug tight level followed by tightening using the torque wrench with 661 Nm torque value to obtain the proof strength of 211.8 kN and tensile strength of 293 kN as specified by BlacksFasteners [53].

The standard shear studs were supplied by Comflor, New Zealand. They were 19 mm diameter x 125 mm (after weld height 120mm) with a specified minimum tensile strength of 415 MPa as per NZS3404:1 [5]. The stud welding was carried out by 'Studwelders Composite Floor Ltd' as per the standard procedure in AS/NZS:1554.2 [54]. Ringing sound testing was performed to check the welding quality. Improperly welded studs were removed and replaced with the new ones. The bending test was conducted randomly on the studs to ensure the weld quality.

3.5 Experimental Test setup

A full-scale internal beam-column-joint sub-assembly was constructed at the University of Canterbury. The column and beam were pin supported at the mid-span representing the points of contraflexure in a moment resistant frame subjected to the lateral loads. A displacement controlled loading ram with 1000 kN capacity was provided at the column top as shown in Figure 3.10. Horizontal roller supports were provided at the beam end to control out-of-plane movement. The beam-ends were connected to 150 kN load cells through universal joints. The test specimen was subjected to the lateral load.

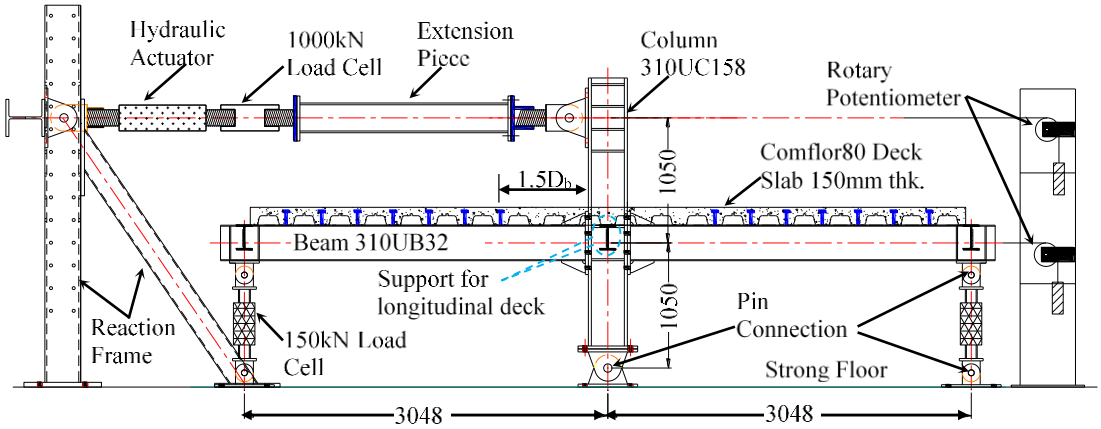

Figure 3.10 – Test Setup

3.6 Construction of the test specimens

The beam – column sub-assembly was fabricated in the structural engineering laboratory at the University of Canterbury. The received steel members were wire brushed followed by acetone cleaning to remove the loose parts and grease/oil if any. The welding of the specimen was carried by the certified welder as specified by AS/NZS:1554.1 [55]. The column was supported on the hinge base and initially provided with the wooden props at the hinge base so that, the column stayed vertical. The steel beam was connected to the column, which was temporarily supported by the steel saddles as shown in Figure 3.11.

Figure 3.11 – Beam- column sub-assembly construction

The laying of deck sheets was started from the midspan so that they were equally distributed on all sides to maintain the symmetry. To accommodate the column, gussets, and endplates, the decking sheet was cut-to-suit as shown in Figure 3.12a. The deck sheets were connected with each other at the regular interval with the help of self-tapping screws. Before commencement of the stud welding, the deck sheets were nailed down to the beam flange using nailing gun at regular intervals (preferably close to shear stud location) to minimize the gap between the decking and the beam flange. Any air gaps result in improper welding as the air gets entrapped with the moisture released from the zinc coating. This leads to porous welding as shown in Figure 3.12b. Due care is therefore required while carrying out the stud welding. The edge trims were added using self-tapping screws, and the restraint traps were provided to secure the edge trim top to avoid it being pushed out by the wet concrete while pouring and curing. At the junction of the two edge trims meeting at the corner, a splice plate bent into 90 degrees were used. For connecting two straight pieces, flat plate was used as shown in Figure 3.12c. Silicon sealant was used to fill up the small gaps. This made the decking waterproof and avoided any concrete leakage.

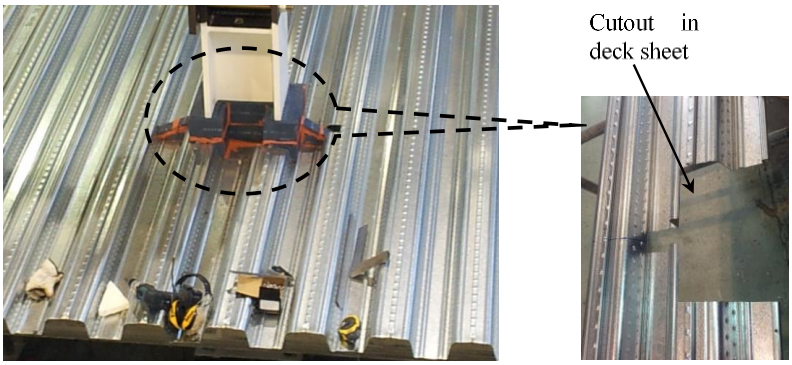

a) Deck cut-out details

b) Stud welding

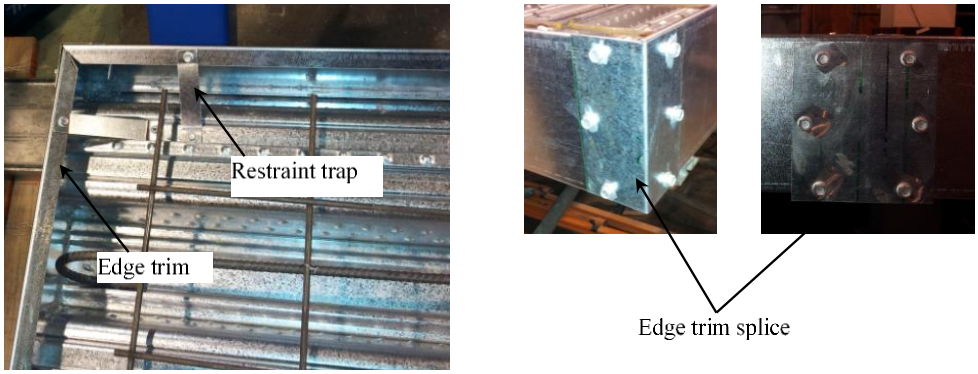

c) Edge trim and splice

Figure 3.12 – Steel deck construction details

The anti-crack mesh, SE82 (8 mm Dia x 200 mm spacing) of grade 500E was provided as recommended by clause 13.2.2 of NZS3404:1 [5], with 35mm cover from the slab top. The SE82 mesh was available to 2440 mm x 6100 mm. Since an available the width of SE82 was lesser than the specimen slab width (3000 mm), splicing of the rebar mesh was essential. In this regards, several splicing options worked out were considered. SQA (refer Annexure C for the further details) was conducted following splice option in Figure 3.13 for all test specimens with a slab. The lap splice was at least of 225 mm as per recommendations of Steel and Tube [44].

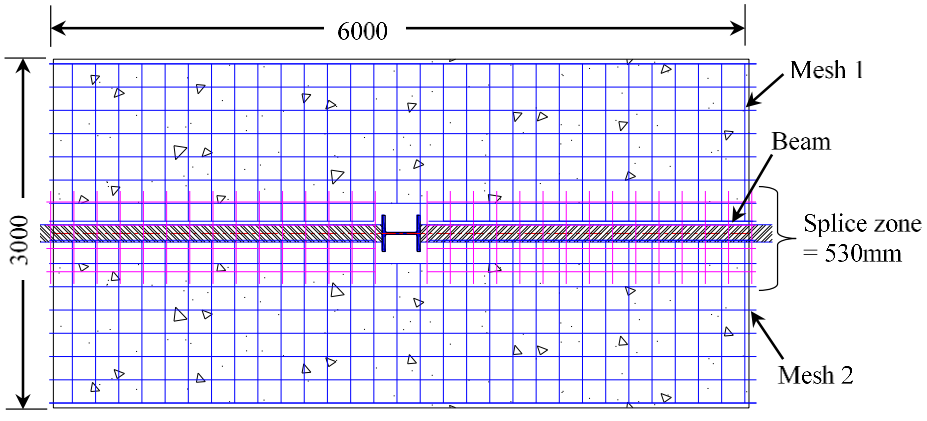

Figure 3.13 – Rebar Mesh Splice details

The slab was cast in a single pour with ready-mix concrete of Grade M30 which was supplied by ‘Allied Concrete.' Before commencement of pouring, all the dust and loose particles were removed with the help of an air blower. It was made sure that the rebar chairs were at in place. A small tipping bucket was used to pour the concrete in place since the pumping of concrete to the slab location was difficult due to space availability inside the structural laboratory. The concrete was vibrated using a needle vibrator and screeded to the top of the edge trim with the help of a 4.0 m long screed as shown in Figure 3.14. A bull float was used to achieve the final finish to the concrete after 2-3 hours of the concrete pour. A thin layer of acrylic based concrete curing compound “Antisol A” [56] was sprayed on the concrete surface to slow down the rate of water evaporation from the concrete slab.

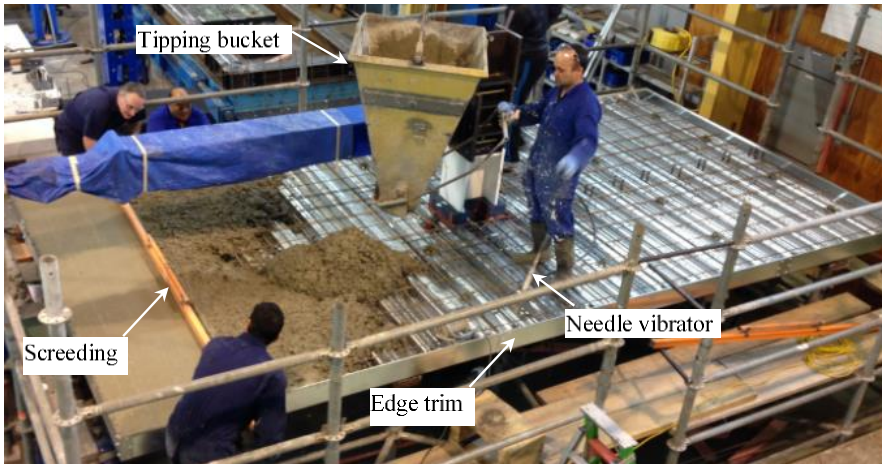

Figure 3.14 – Slab casting in progress

3.7 Instrumentation

The test setup was instrumented to capture the deformation/rotation at various locations. Instruments like linear potentiometers, rotary potentiometers, and load cells were installed at the regions of expected inelastic deformations and slip. All the load cells and potentiometer were calibrated to obtain the calibration factor, which was incorporated into the data logger.

3.7.1 Load and Displacement Measurement

The main actuator was connected with a 1000 kN load cell to measure the load at the column top whereas the vertical supports of the beam-ends were provided with a 150 kN load cell to capture the reaction at the beam supports. A rotary potentiometer with a range of ± 250 mm displacement was installed at the column top in line with the loading ram centre to record the total displacement of the frame as well as to control the loading. Another rotary potentiometer was used to capture displacement at the centre of the panel zone as shown in Figure 3.10.

3.7.2 Panel Zone Deformation and Beam Axial Deformation Measurement

In order to capture the panel zone deformation for the transverse deck sub-assembly, linear potentiometers ‘C1’ to ‘C6’ were used as shown in Figure 3.15. Potentiometer ‘C5’ and ‘C6’ were positioned in a diagonal direction to measure the panel zone shear deformation. However in the case of the longitudinal deck sub-assembly, potentiometer ‘C1’ along the top continuity plate as well the two diagonal potentiometers ‘C5’ and ‘C6’ were removed to clear the infringement with the secondary beam framing into the column web, which was provided to support the longitudinal deck. To measure the beam axial deformation, a series of linear potentiometer ‘C7’ – ‘C16’ and ‘D1’-‘D6’ were also installed at the top and bottom flange of the main beam as shown in Figure 3.15.

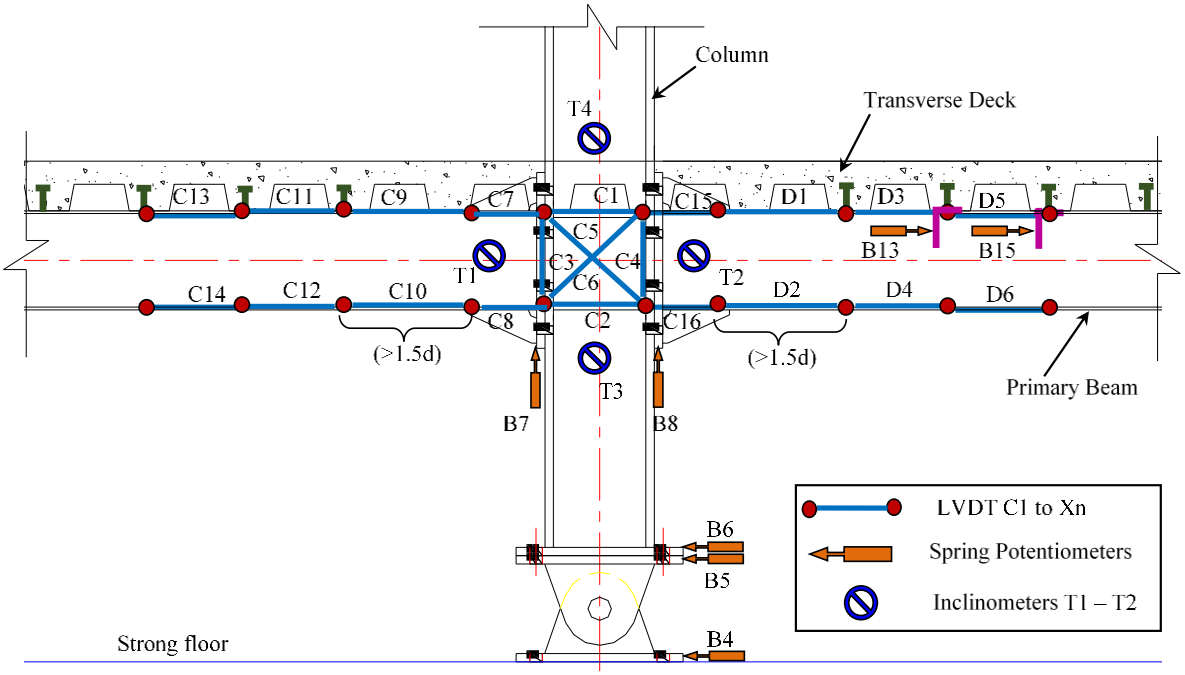

Figure 3.15 – Instrumentation on the beam-column sub-assembly

3.7.3 Base Slip and Deck Slip Measurement

The spring potentiometers ‘B4’ to ‘B6’ were installed at the column base to monitor a slippage between the different components. In order to capture the relative slip of beam end plate on the column flange to check the slippage of bolt clamping in the vertical direction, linear potentiometers ‘B7’ and ‘B8’were installed.

The relative slip between the primary beam and the composite deck was obtained by installing the spring potentiometers ‘B13’ to ‘B16’ on the beam web in line with the location of the 2nd and 3rd shear stud from the column outer flange. These were installed two on each side of beam

web. A small piece of an aluminium angle was connected to the soffit of the composite deck slab with the help of self-drilling screws in order to receive the potentiometer as shown in Figure 3.16.

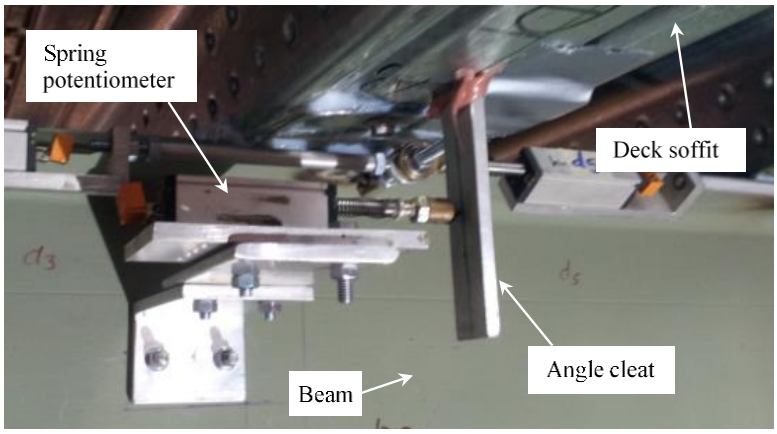

Figure 3.16 – Deck slip instrumentation details

3.7.4 End Plate Lift-off Measurement

In order to capture the end plate lift-off, spring potentiometers (B9 – B12) were installed between the beam end plate, and column flange in line with column continuity plates and an aluminium bracket was used to mount them as shown in Figure 3.17.

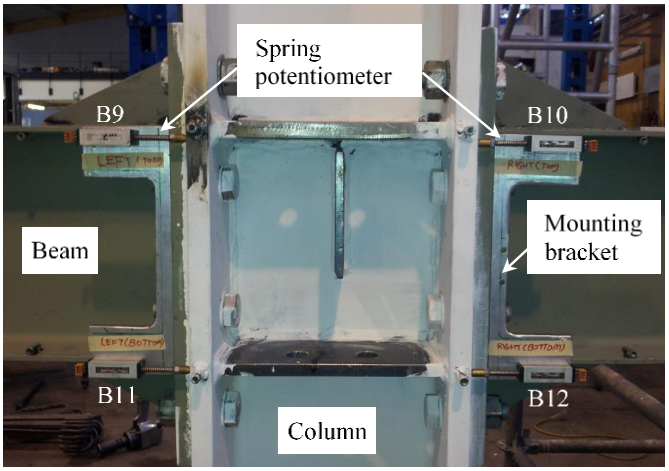

Figure 3.17 – Instrumentation for end plate lift off

3.7.5 Slab Instrumentation

Linear potentiometers were installed in a grid format covering the half of the slab to measure the slab horizontal deformation on the top surface of the slab as shown in Figure 3.18. A grid of 250 mm by 250 mm was used near the column zone and for the remainder portion; the instruments were placed in a 500 mm by 500 mm grid.

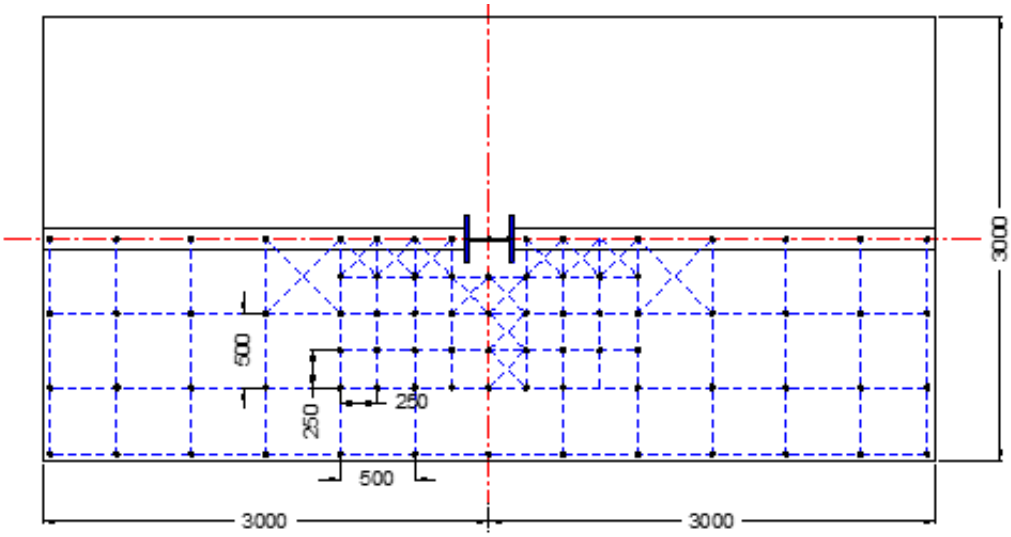

Figure 3.18 – Grid layout of potentiometer of the slab top

3.8 Loading Protocol

Testing of each sub-assembly was carried out using displacement control loading regime of ACI report T1.1-01 [57] as per Figure 3.19.

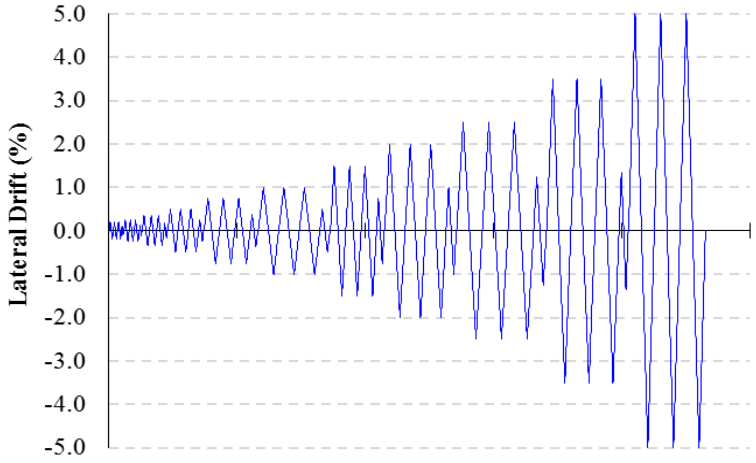

Figure 3.19 – Displacement Control Loading Regime

The starting drift for each test was set to 0.2% drift (4.2 mm displacement) at the column top, followed by the gradual increment up to 5% drift (105 mm displacement) as shown in Table 3.5. Each drift level was subjected to the three full cycles followed by one cycle of half drift for a corresponding previous drift level in order to observe the residual stiffness of the structure.

Table 3.5: Target Displacement and No. of Cycles

Drift %	Target Displacement (mm)	No. of Cycles
0.2	4.2	3
0.25	5.25	3
0.35	7.35	3
0.5	10.5	3
0.75	15.75	3
1.0	21	3
1.5	31.5	3
2.0	42	3
2.5	52.5	3
3.5	73.5	3
5.0	105	3

3.9 Interpretation of Test Results

This section describes the test data interpretation of the different beam column sub-assemblies. The specimen behaviour was presented by the various parameters like applied load, column top displacement, panel zone deformation, connection rotation, beam rotation, beam axial deformation, deck/shear stud slip, slab deformation, and energy dissipation.

3.9.1 Hysteresis

The total displacement of the beam column sub-assembly was obtained by the rotary string potentiometer aligned in line with loading ram load. The global hysteretic behaviour was represented by a plot of the load applied (P) at the column tip versus the interstorey total displacement (Δ_{tot}) measured experimentally. The recorded measurements were zeroed to the first recorded readings. To remove the displacement caused by base slip, the data obtained from the string potentiometer mounted at the top of the column were corrected by subtracting the displacement data of spring potentiometer situated at the column base.

3.9.2 Interstorey Displacement Components

The total interstorey displacement (Δ_{tot}) comprises of five different displacement components as follows: panel zone deformation (Δ_{pz}), beam deformation ($\Delta_{beam} = \Delta_{b(el)}+\Delta_{b(ph)}$), connection deformation (Δ_{con}), column deformation (Δ_{col}) and unaccounted deformation ($\Delta_{unaccounted}$). Total interstorey displacement (Δ_{tot}) is expressed as a sum of the four components as per Equation 3.1.

$$\Delta_{tot} = \Delta_{pz} + \Delta_{beam} + \Delta_{con} + \Delta_{col} + \Delta_{unaccounted} \quad (3.1)$$

The last term in the above equation is for the deformation unaccounted due to lack of instrumentation for the measurement of shear deformation in beam and cracking in concrete. It is calculated as the difference between total deformation and other four deformation components. Since, no instrumentation was installed to capture the inelastic shear deformation in the beam, this deformation was considered in the "unaccounted" part of the Equation 3.1. The schematic representation of the different deformation components of the beam-column test sub-assembly is illustrated in Figure 3.20.

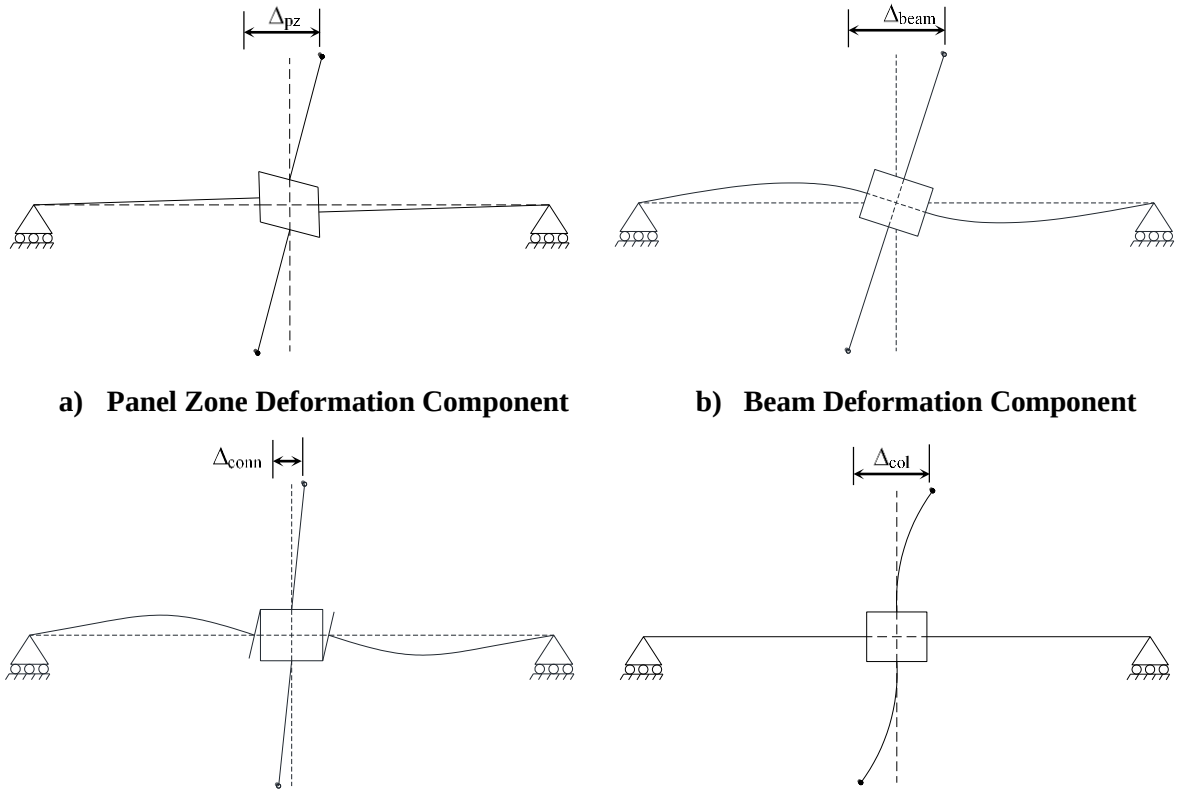

a) Panel Zone Deformation Component **b) Beam Deformation Component**

c) Connection Deformation Component **d) Column Deformation Component**

Figure 3.20 – Schematic of Storey Displacement Components

Panel Zone Deformation Component

The beam column sub-assembly was designed with relatively rigid panel zone to ensure the column to remain elastic throughout the test so that the same column section can be reused for the different test configurations. The expected contribution of the panel zone deformation in overall system deformation is assumed to be relatively small. The panel zone shear deformation was calculated from the two diagonal LVDT's (C5 & C6) placed in the panel zone as shown in Figure 3.15. The panel zone shear deformation "γ_{pz}" for the SK-SU and MSK-SU test frame sub-assemblies with the deck oriented in longitudinal direction (i.e. deck ribs parallel to the

main beam), not measured due to the lack of space availability to install the instrumentation in the panel zone as they were infringing with the secondary beam framing into the column web, which was provided to support the longitudinal deck. To calculate the contribution of the panel zone shear deformation component to the overall lateral displacement of the SK-SU and MSK-SU frame sub-assembly, the panel zone deformation obtained from the FD-SU frame sub-assembly is used in the absence of the relevant data. The panel zone deformation was shown in Figure 3.21.

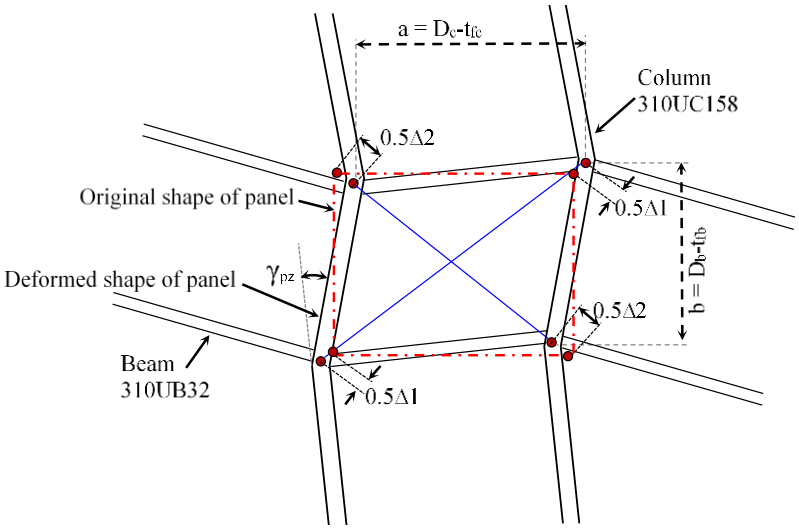

Figure 3.21 – Panel Zone Deformation Measurement.

The panel zone deformation was calculated [58]:

$$\gamma_{pz} = (\Delta 1 - \Delta 2)\frac{\sqrt{a^2+b^2}}{2ab} \tag{3.2}$$

where:

$\Delta 1$ and $\Delta 2$	=	Displacements of diagonal LVDTs
$a = D_c - t_{fc}$	=	Width of panel zone between LVDT connection points
$b = D_b - t_{fb}$	=	Height of panel zone between LVDT connection points
D_c and D_b	=	Depth of column and beam respectively
t_{fc} and t_{fb}	=	Flange thickness of column and beam respectively

The effect of the panel zone deformation to the column tip deflection is determined by considering the beam end restraints. Initially, when there is no restraint, the panel zone deformation would rotate the entire specimen as shown in Figure 3.22a. However, in reality, the beam tip displacement should be zero due the beam end restrains and the entire system has to be re-rotate as shown in Figure 3.22b to satisfy this boundary condition.

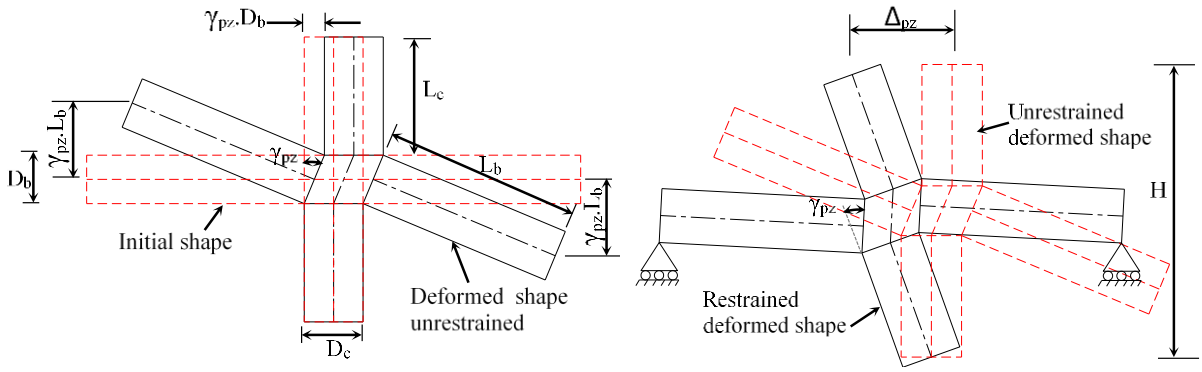

a) Unrestrained Beams Deformation **b) Restrained Beams Deformation**

Figure 3.22 – Panel Zone Deformation at Column Tip.

From the geometry, the column tip displacement component caused by panel zone deformation is calculated as [59]:

$$\Delta_{pz} = \gamma_{pz} D_b - \left[\left(\frac{\gamma_{pz} L_b}{L_b + (D_c/2)}\right).H\right] \qquad (3.3)$$

where:

γ_{pz}	=	Panel zone deformation
L_b	=	Distance from beam end to column face
L_c	=	Distance from column end to beam face
H	=	Storey height

The panel zone demand is a function of the beam moments and the shear in the column. The various forces acting at the panel zone boundary as depicted in Figure 3.23

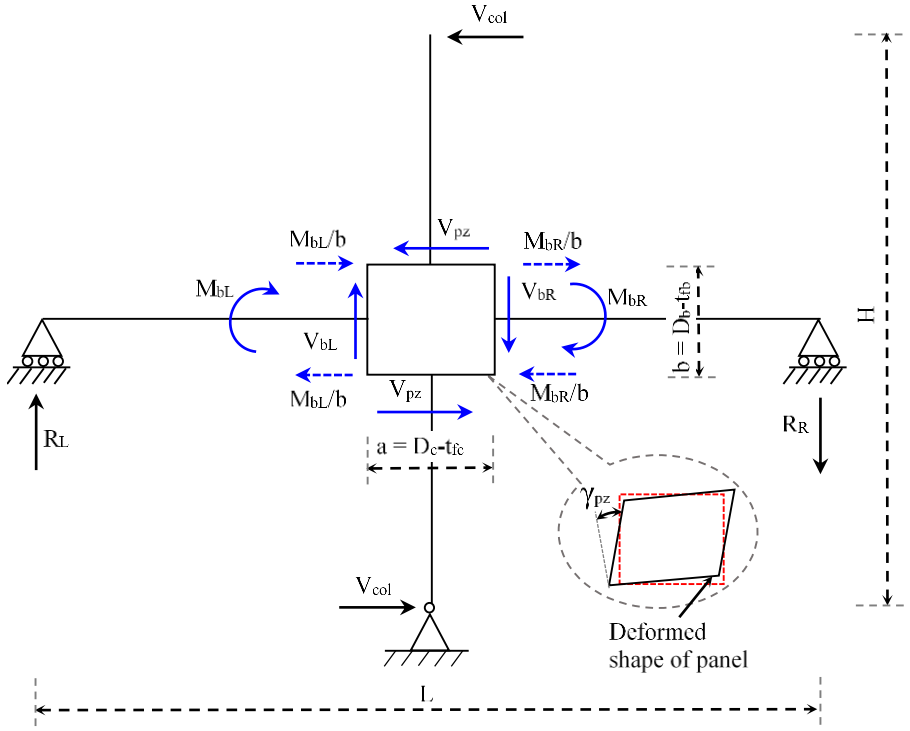

Figure 3.23 – Forces in Panel Zone.

The shear forces acting on the panel boundary influence the panel zone deformation and the panel zone shear force is expressed as:

$$V_{pz} = \frac{M_{bL}}{b} + \frac{M_{bR}}{b} - V_{col} \quad (3.4)$$

where:

V_{pz}	=	Panel zone shear force
M_{bL} and M_{bR}	=	Moment in beam at panel zone in left and right beam respectively
V_{bL} and V_{bR}	=	Beam shear force in left and right beam respectively
V_{col}	=	Column shear force
L	=	Beam span
H	=	Storey height

Connection Deformation Component

The connection rotation was obtained through the spring potentiometer installed between the connection end plate and the column outer flange as shown in Figure 3.17. The endplate lift-off on the left side was captured by the spring potentiometer "B9 (top)" and "B11 (bottom)" and that of right side by "B10 (top)" and "B12 (bottom)" as shown in Figure 3.24. The connection rotation on each side is calculated as per equation 3.5 and 3.6.

$$\theta_{con.Left} = \frac{\Delta_{B11} - \Delta_{B9}}{d1} \quad (3.5)$$

$$\theta_{con.Right} = \frac{\Delta_{B10} - \Delta_{B12}}{d1} \quad (3.6)$$

where:

$\theta_{con.Left}$	=	Connection rotation on left beam
$\theta_{con.Right}$	=	Connection rotation on right beam
d_1	=	Distance between top and bottom spring potentiometer
Δ_{B9} to Δ_{B12}	=	Displacement of spring potentiometer

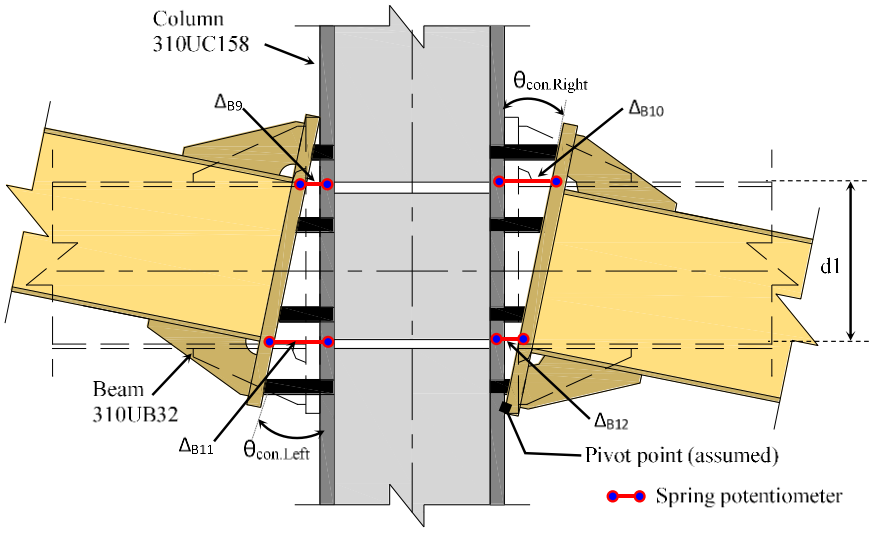

Figure 3.24 – Connection Deformation Measurement.

Once the connection rotation was calculated, based on the geometry, it was converted to the column tip displacement at the column centre as:

$$\Delta_{conn} = \left(\frac{\theta_{con} L_b}{L_b + (D_c/2)}\right) . H \qquad (3.7)$$

Beam Plastic Deformation Component

The beam plastic rotation was calculated from the LVDTs installed on the top and bottom beam flanges at the plastic hinge zone as shown in Figure 3.25. The expected plastic hinge region assumed to be of 1.5 times the beam depth starting from the tip of gusset plate. The beam rotation obtained from LVDT readings comprises of both the elastic and plastic rotation. The beam plastic rotation was obtained by subtracting the rotation component of beam elastic flexural deformation in beam plastic hinge zone (X_2).

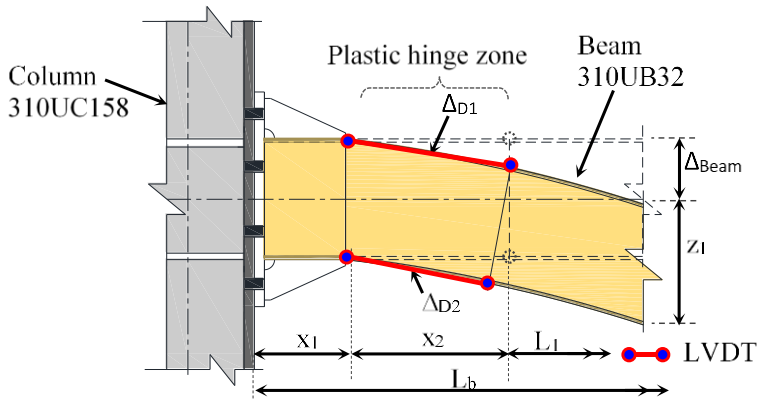

Figure 3.25 – Beam Deformation Measurement.

Referring to Figure 3.25 and from the geometry, the beam plastic rotation and the column tip displacement caused by beam plastic deformation at the column centre was calculated as:

$$\theta_{b(ph)} = \left(\frac{\Delta_{D1} - \Delta_{D2}}{z_1}\right) - \frac{1}{2} . \left[\left(\frac{R.L_1}{E.I_{eff1}}\right) - \left(\frac{R.(L_1 + x_2)}{E.I_{eff2}}\right)\right] . x_2 \qquad (3.8)$$

$$\Delta_{b(ph)} = \left[\theta_{b(ph)} . \left(\frac{L_b - (0.5x_2 + x_1)}{L_b + (D_c/2)}\right) . H\right] \qquad (3.9)$$

where:

$\theta_{b\,(ph)}$	=	Beam plastic rotation in PH zone
$\Delta_{b\,(ph)}$	=	Column tip displacement due to beam deformation in PH zone
L_b	=	Distance from beam end to column face
L_1	=	Distance from beam end to 1st shear stud = $(L_b - x_1 - x_2)$
H	=	Storey height
z_1	=	Distance between top and bottom LVDT
$\Delta_{D1,\,D2}$	=	Displacement of LVDTs
R	=	Reaction at beam end
E	=	Young's Modulus of steel
I_{eff1}	=	Effective moment of inertia of composite beam in mid-span region including partial composite action, for Be = Span/4 (Refer Appendix E)

I_{eff2} = Effective moment of inertia of composite beam in support region including partial composite action, for Be = Width of column or width of spreader plate (Refer Appendix E)

The effective width of the composite section in support region for a positive moment was calculated based on the clause 13.4.2.3 of NZS3404:1 [5]. For the bare steel frame test sub-assembly, the effective moment of inertia is equal to the major axis moment of inertia of the steel section used for the beam (310UB32).

Beam Elastic Deformation Component

The contribution of the beam elastic flexure and elastic shear deformation was calculated and converted relative to the column centreline as per equation 3.10.

$$\Delta_{b(el)} = \left[\left(\frac{R.{L_1}^3}{3.E.I_{eff1}}\right) + \left(\frac{1}{2}.\left(\left(\frac{R.L_b}{E.I_{eff2}}\right) - \left(\frac{R.L_1}{E.I_{eff1}}\right)\right).(L_b - L_1)\right).\left(L_1 + \frac{2}{3}.(L_b - L_1)\right) + \left(\frac{R.{L_1}^3}{E.I_{eff1}}\right).(L_b - L_1).\left(L_1 + \frac{1}{2}.(L_b - L_1)\right)\right].\left(\frac{H}{L_b + (D_c/2)}\right) + \left(\frac{RL1\alpha b}{GA_b}\right)\left(\frac{H}{L_b + (D_c/2)}\right) \quad (3.10)$$

where:

$\Delta_{b(el)}$ = Column tip displacement due to beam elastic deformation
A_b = Area of beam
I_b = Moment of inertia of bare steel beam
α_b = Beam form factor was calculated based on Blodgett [60]
= $\frac{A_b}{8I_b t}(bd^2 - bd_1^2 + td_1^2)$
b = Flange width of section
d = Total depth of section
d_1 = Web depth of section
t = Web thickness of section

Column Elastic Deformation Component

The column was designed to remain elastic throughout the test, and the contribution of the column elastic flexure and shear deformation was calculated as:

$$\Delta_{col} = 2\left[\left(\frac{P{L_c}^3}{3EI_c}\right) + \left(\frac{PLc\alpha_c}{GAc}\right)\right] \quad (3.11)$$

where:

Δ_{col} = Column tip displacement due to column elastic deformation
P = Applied load at column tip
E = Young's Modulus of steel
A_c = Area of column section
I_c = Moment of inertia of column
L_c = Distance form column end to beam face
α_c = Column form factor was calculated based on Blodgett [60]

$$= \frac{A_c}{8I_c t}(bd^2 - bd_1^2 + td_1^2)$$

b = Flange width of section
d = Total depth of section
d_1 = Web depth of section
t = Web thickness of section

3.9.3 Beam Axial Deformation

The beam axial deformation/elongation is predominately observed in the reinforced concrete structure under cyclic loading, but has also been observed in steel structures by MacRae [61, 62]. The beam axial elongation is mainly caused due to the accumulation of inelastic deformations in the beam because of alternate yielding of the beam flanges. Considering a beam subjected to cyclic moments, yielding of beam flanges and web occurs with neutral axis being located close to the compression flange due to the strain hardening. When this load is reversed, the natural axis tends to shift to the opposite side resulting in tension yielding of the previously compressed flange. This alternate cyclic yielding of beam flanges results in the accumulation of residual deformations contributing to the beam axial deformation as shown in Figure 3.26. The magnitude of beam axial elongation expected in the steel structures is relatively small and is dependent on the material non-linearity and type/number of inelastic cycles. The beam elongation was calculated up to the initiation of the beam flange buckling.

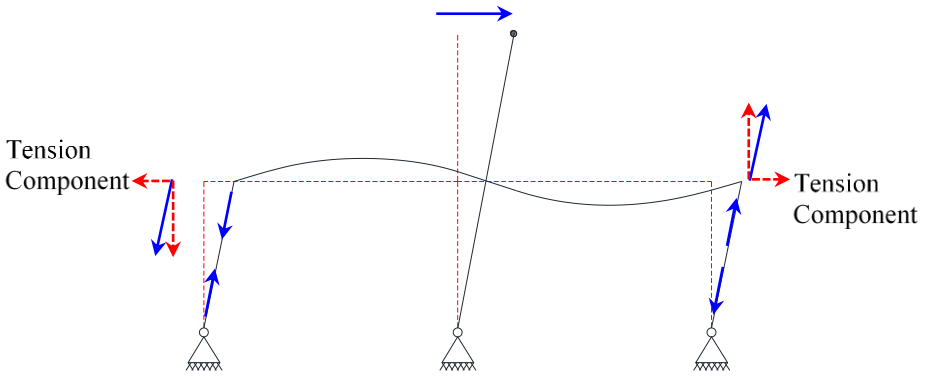

(a) Beam-Column Test Subassembly with Lateral Loading

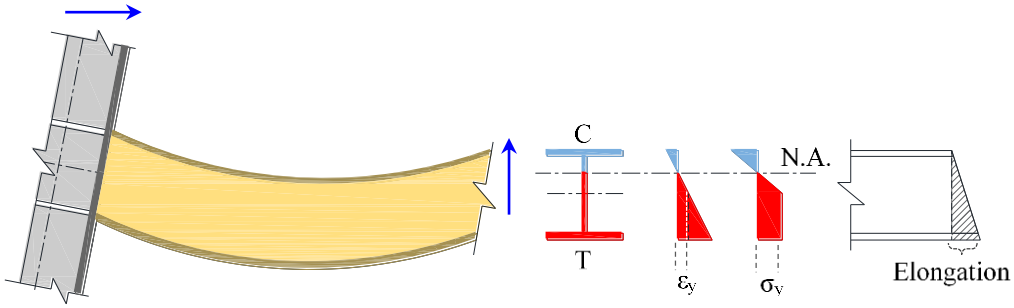

(b)

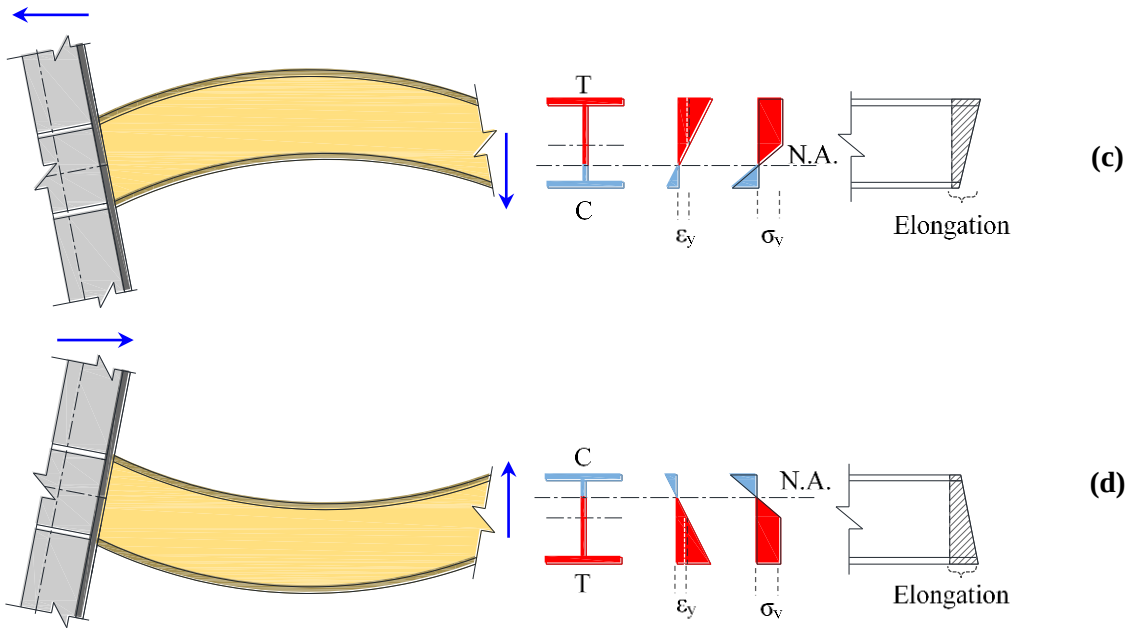

Figure 3.26 – Beam Axial Deformation Mechanism[61].

The increase in beam axial deformation in the plastic hinge zone of the beam was captured through the LVDT installed at the beam top and bottom flanges. The beam axial deformation was determined as:

$$\Delta_{b\ axial} = \frac{\Delta_{top} + \Delta_{bottom}}{2} \tag{3.12}$$

where:

$\Delta_{b\ axial}$ = Beam axial deformation in plastic hinge zone
Δ_{top} and Δ_{bottom} = Absolute displacement of top and bottom LVDT on beam flange installed in beam plastic hinge zone

3.9.4 Slab Surface Deformation

The slab surface deformation was plotted as a two-dimensional contour plot using Matlab code developed by Hobbs [3]. As only half of the slab was instrumented in a grid pattern, the slab surface deformation plot is mirrored along the main beam (X-axis). A small portion of the slab quadrant is depicted in Figure 3.27 and the column centre considered as a starting point of X-axis (along the main beam) and Y-axis (along the secondary beam). All points along the main beam centerline were set to zero Y displacement whereas all points along the secondary beam line were set to zero X displacement. Then the movement of each point was calculated relative to the nearest zero point (on the reference axis) by subtracting the movement of the other points in-between the point of interest and nearest zero points on the axis as shown in Figure 3.27. The total displacement, relative to the column centreline, is obtained by summing the individual point displacements between the column and the point of interest. Following this, the net

displacement was obtained by taking the square root of the sum of the squared x and y data and these points are plotted by using Matlab code.

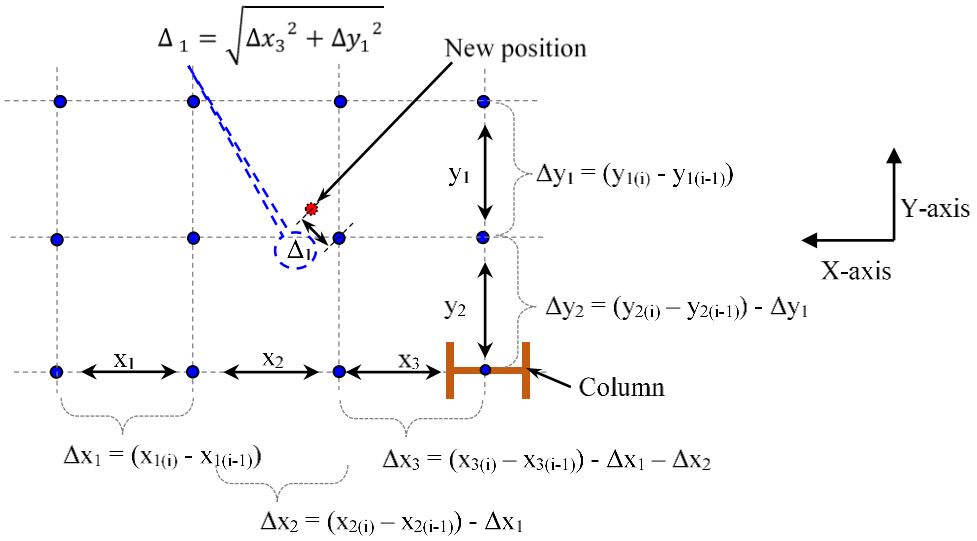

Figure 3.27 – Slab Surface Deformation Measurement[3].

3.9.5 Energy Dissipation, Equivalent Viscous Damping, Initial Stiffness, and Average Secant Stiffness

The energy dissipation (E_{Diss}) of the beam column sub-assembly was calculated by summing up the area under the load-displacement hysteresis curve and converted into the equivalent viscous damping (ξ_{eq}). The equivalent viscous damping is the ratio of the energy dissipated per cycle (E_{Diss}) to the elastic strain energy (E_{sto}) stored in the corresponding cycle. The initial stiffness (K_0) is calculated as the ratio of the average of the positive and negative force to the average of the positive and negative displacement at the first cycle of 0.2% lateral drift. In addition, the peak-to-peak secant stiffness (K_{eff}) was also calculated, and it is defined as the ratio of the average of the peak positive and negative forces to the peak positive and negative displacement of the particular lateral drift cycle as shown in Figure 3.28.

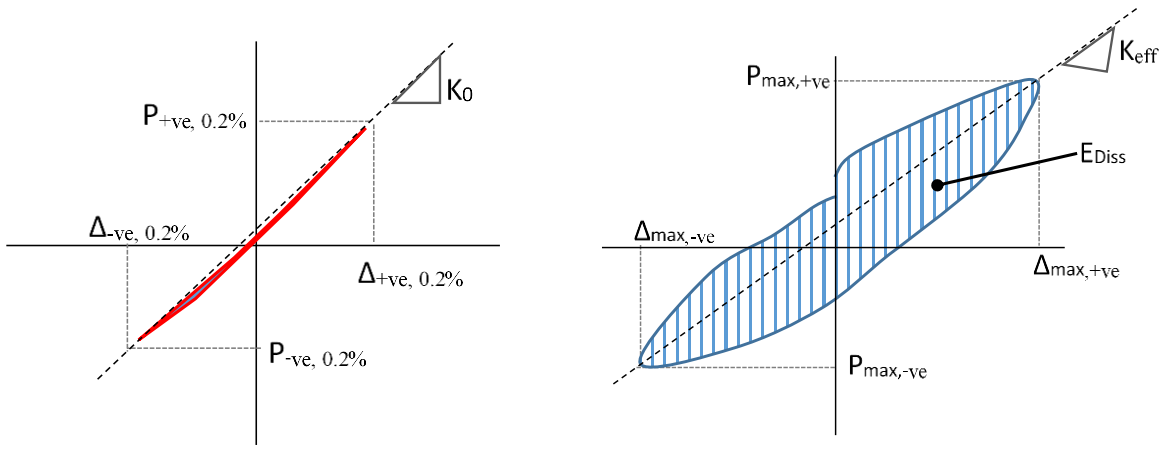

Figure 3.28 – Initial stiffness, Secant stiffness, and Energy Dissipated for Hysteresis Curve.

The energy dissipated, equivalent viscous damping and the secant stiffness is calculated as:

$$E_{Diss} = \sum_{i=1}^{n} \frac{P_{(i+1)}+P_{(i)}}{2}\left(\Delta_{(i+1)} + \Delta_{(i)}\right) \quad (3.13)$$

$$E_{sto} = \left(\frac{P_{max(+ve)}\Delta_{max(+ve)}}{2}\right) + \left(\frac{P_{max(-ve)}\Delta_{max(-ve)}}{2}\right) \quad (3.14)$$

$$\xi_{eq} = \frac{1}{4\pi}\frac{E_{Diss}}{E_{sto}} \quad (3.15)$$

$$K_0 = \frac{1}{2}\left[\frac{P_{(+ve,0.2\%)}}{\Delta_{(+ve,0.2\%)}} + \frac{P_{(-ve,0.2\%)}}{\Delta_{(-ve,0.2\%)}}\right] \quad (3.16)$$

$$K_{eff} = \frac{1}{2}\left[\frac{P_{max(+ve)}}{\Delta_{max(+ve)}} + \frac{P_{max(-ve)}}{\Delta_{max(-ve)}}\right] \quad (3.17)$$

where:

E_{Diss}	=	Energy dissipated per cycle
E_{sto}	=	Elastic energy stored per cycle
ξ_{eq}	=	Equivalent viscous damping
$P_{(i)}$	=	Load at each step (i)
$\Delta_{(i)}$	=	Displacement at each step (i)
K_{eff}	=	Average effective stiffness
$P_{max(+ve)}$ and $P_{max(-ve)}$	=	Peak load at indented cycle
$\Delta_{max(+ve)}$ and $\Delta_{max(-ve)}$	=	Peak displacement at indented cycle
K_o	=	Initial stiffness
$P_{(+ve,0.2\%)}$ and $P_{(-ve,0.2\%)}$	=	Load at first cycle of 0.2% lateral drift
$\Delta_{(+ve,0.2\%)}$ and $\Delta_{(-ve,0.2\%)}$	=	Displacement at first cycle of 0.2% lateral drift

Chapter 4: Experimental Investigation and Design Calculation of the Infill Material between the Composite Slab and the Column

4.1 Introduction

In the 2010 & 2011 Canterbury earthquakes, major damage has been observed in brittle elements within buildings as a result of frame displacements. When structural elements/items were in close proximity to, or contact with, other structural or non-structural elements within a structure, then damage can occur to one of these elements. The cost of replacement/repair of these elements may be substantial. If these elements were stopped from interacting with the structural elements, then this damage and loss could be avoided. This damage may be undesirable, or it may result in an unacceptable structural response. In such cases, gaps may be placed between the elements to avoid or limit the significant transfer of force. This may be accomplished by providing a gap in between the structural & non- structural elements to avoid them impacting with each other as shown in Figure 4.3b. Such a gap should be filled with a suitable infill material. The required properties of the infill will depend on the specific application, two such applications were considered here; (i) floor slabs in steel frames, and (ii) non-structural elements.

Floor slabs in steel frames

As mentioned before in the Section 1.1, in conventional construction practice, composite deck slabs are usually poured up to, and against, the column flanges. For slabs in contact with the column, horizontal forces may enter the floor diaphragm due to inertial forces, bearing forces, compatibility forces, and transfer forces. When a moment frame structure is subjected to lateral loads, the slabs interact with the column and transfer bearing forces on the column outer and inner flanges as shown in Figure 4.1.

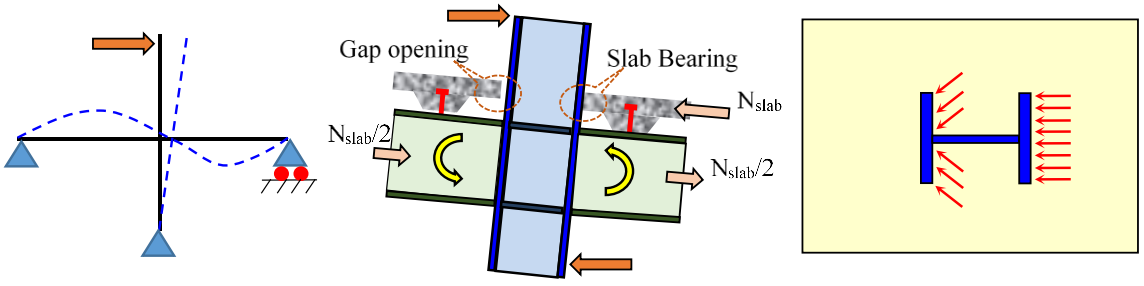

(a) Deflected shape **(b) Slab Interaction** **(c) Bearing force on column flanges**

Figure 4.1- Interaction of Structural System with other Elements[6]

Over the past few years, a number of slabs in NZ buildings have been constructed with a gap between the slab and column as shown in Figure 4.2 to reduce the bearing and compatibility forces, resulting in smaller column and beam axial demands. The disadvantages this are; (i) an increased likelihood of column buckling due to decreased restraint, (ii) a cost associated with placing the gap and, (iii) isolation material cost. To construct the gap, an infill material is often used to form the gap, and it may be left in the gap after construction. Most commonly, the infilled material is either polystyrene or foam (spray) is used to provide a gap of the required thickness. Sometimes a gap is provided only on the outside of the column flanges resulting in partial isolation as shown in Figure 4.2a. To provide full isolation of the slab the gap should be provided all around the column and all structural elements such as the column (external and internal flange surfaces), connection end plate, gusset plate, and bolt surfaces should be isolated as shown in Figure 4.2b and Figure 4.10 to prevent any bearing.

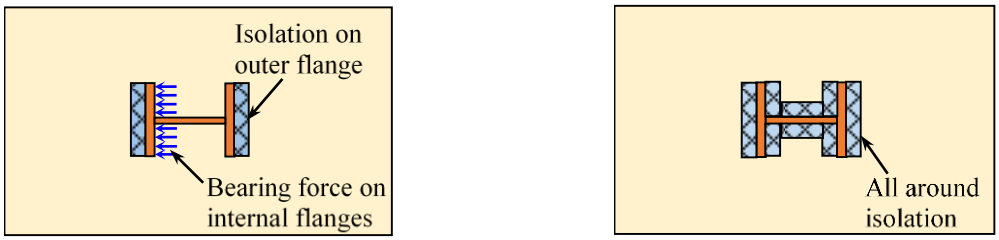

(a) Partial Isolation Details **(b) Fully Isolation Details**

Figure 4.2- Interaction of Structural System with other Elements

Non-Structural Elements

Non-structural elements like partition walls, false ceilings, facades and canopies have been damaged in the past [63]. These components often not engineered for the seismic performance. While low-damage structural systems using techniques such as; (i) base isolation, (ii) rocking frames/walls, (iii) friction connections and, (iv) supplemental damping systems were implemented to protect structural elements in a seismic event, there still a possibility that damage may occur in non-structural elements as shown in Figure 4.3a. A gap of the sort shown above the partition and below the beam generally required to avoid damage as a result of beam deflections. This gap, together with gaps on the sides of the partition may be used to isolate the partition from the structural elements to avoid the potential damage.

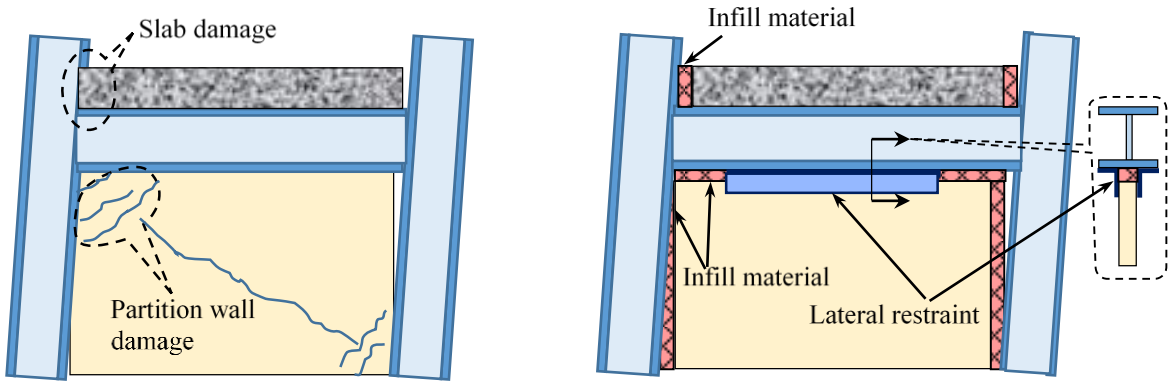

(a) Non-isolated structural system **(b) Isolated structural system**

Figure 4.3- Interaction of Structural System with other Elements [64]

For a number of reasons, including fireproofing, soundproofing, and others, leaving an air gap is unacceptable, so infill suitable material is needed in the gap. While polystyrene has been used in the past [3], it's had a poor fire performance, so there is need; to determine what infill material may be useful for a given scenario, to evaluate different infill materials against performance criteria, and to select the most appropriate infill material for some common applications.

This chapter aims to address this need by seeking answers to the following questions:

1) When may infill material be needed in a seismic gap?
2) What should infill material performance criteria is appropriate for different cases?
3) How do a range of materials rate against such performance criteria?
4) What are some possible design details for some seismic gaps?

4.2 Performance Criteria

To select infill material for a particular construction type the following seven different performance criteria were used: (i) compressibility under seismic deformation, (ii) construction compressibility, (iii) fire rating, (iv) water resistance, (v) elasticity, (vi) cost/ease of application, and (vii) sound resistance. It is assumed that the gap is of sufficient size not to close under the expected frame deformations.

4.2.1 Compressibility under Seismic Deformation

Selection Criterion: $\Delta_{infill\ (comp^n)} > \Delta_{gap\ (required)}$

This criterion requires that the distance between the brittle element and the structural frame at

the frame drift considered, $\Delta_{gap\ (required)}$, should not cause significant compression forces on the infill material over this distance. That is, infill material should be compressible over a distance, $\Delta_{infill\ (comp^n)}$, which must be greater than $\Delta_{gap\ (required)}$. These compressive forces should be less than 10% (assumed) of that which would cause failure of the brittle element to experience damage, as this will not only protect the element, but will also limit the possibility of the frame deformation mode changing to something less acceptable which is not considered in the design.

4.2.2 Construction Compressibility

Selection Criterion: $f_{comp(infill)\ @\ 1.0mm\ displacement} > f_{wet\ conc}$

For a composite deck slab, where the concrete is cast-in-situ, the gapping material should have enough strength ($f_{comp(infill)\ @\ 1.0mm\ displacement}$) against the wet concrete pressure ($f_{wet\ conc.}$) so that the concrete does not fill-in the gap. A displacement of about 1.0 mm may be selected as displacement at which the strength is reached. This implies that the material should have sufficient stiffness.

4.2.3 Fire Rating

Selection Criterion: $FR_{infill} > FR_{building}$

This criterion is applicable to situations where the gapping material may be subjected to fire. An unfilled isolation gap may allow fire/smoke to spread. In order to prevent the spread of the fire as well as to protect the structural elements, the gapping material should be fire rated and it should be not noxious in the fire. The infill material should have the minimum fire rating (FR_{infill}) equal to that required in that vicinity of the building ($FR_{building}$) as shown in Figure 4.4.

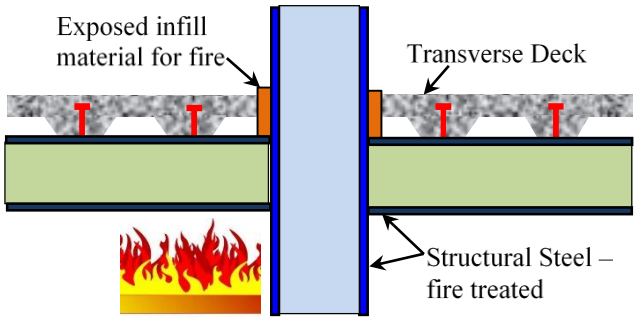

Figure 4.4 - Fire Issue of Infill Material

4.2.4 Water Resistance

The infill material should be waterproof and should not absorb moisture. In the where the wet concrete is cast directly against the infill material, absorption of moisture may alter the

water/cement ratio of freshly laid concrete. Also, it may become a location of mildew growth.

4.2.5 Elasticity

Selection Criteria: $\Delta_{infill\ (permanent)}$ is small

The infill material should have a small permanent displacement so it can refill the gap after a seismic event. Otherwise, the unfilled gap will act as a weak link to transfer fire, smoke and sound.

4.2.6 Cost/Ease of Practical Application

The time and ease of installation will affect its use. For example, mineral wool needs an additional formwork/wrapping to protect it from the wet concrete. In other cases, it may require special attachment on one side to not fall out during large gap openings. The 25 mm thick, polystyrene material cost NZ$ 5.2 per m^2 [Trade Me]. This was significantly less than the 20mm thick spiralite cost NZ$ 43.88 per m^2 [Firepro Centabuild Ltd], whereas 25 mm thick actifoam was expensive, costing NZ$ 1361 per m^2 [CSD Sealing Systems]. In the current study, more emphasis was given on the material performance than the material cost.

4.2.7 Sound Resistance

This criterion is majorly applicable to places where acoustic resistance is one of the functional requirements of the non-structural elements. For example, near partition walls and ceilings the infill material should have a high level of sound resistance in order to avoid transfer of noise from one room to another (especially in case of the conference/meeting rooms).

4.3 Methodology

4.3.1 Materials Selected

In order to demonstrate the process of quantifying the most promising infill material type, the following materials were selected; (i) polystyrene (EPS) [65], (ii) spiralite - B400 [66], (iii) actifoam [67]. The polystyrene was expanded polystyrene sheet (EPS) used in building insulation/packaging. It is made from lightweight plastic material to form a microcellular closed cell foam and its characteristics such as lightweight, compressive strength (70kPa @ 10% deformation), moisture resistance and ease of use were considered [65]. Spiralite B400, was a resin bonded mineral fibreboard, extensively used as fire protection for steelwork. It also exhibits a good sound absorption property (Sound reduction index 27dB for 20mm thick) [66].

Actifoam was foam rubber available in different thickness and widely used to fill cavities or gaps in construction. It had good thermal insulation properties (K = 12.3mk/W @ 10°) and was easy to use. It does not absorb water when tested at 2.5 bar water pressure during 24 hours [67].

4.3.2 Compressive Properties

In order to investigate the compression properties of the various material listed above, a compression testing was carried out in displacement-controlled compression machine in the University of Canterbury mechanical engineering laboratory. The specimen dimensions are summarised in Table 4.1 and they were tested at a loading rate of 1mm/min. The test specimens were free to move in or out on the sides.

Table 4.1: Test Specimen Dimensions

Sr. No	Material Description		Length (L) mm	Width (B) mm	Thickness (T) mm
01	Spiralite **(SP)**	**SP1**	101	100	19
		SP2	100	100	20
		SP3	100	99	20
02	Actifoam **(A)**	**A1**	99	98	28
		A2	98	98	28
		A3	98	97	27
03	Polystyrene **(P)**	**P1**	100	100	24.6
		P2	110	99.5	24.6
		P3	99.5	98.3	24.7

The stress-displacement plot in Figure 4.5 shows that polystyrene possessed a high initial stiffness up to a displacement of about 1 mm. The stiffness then decreased as the cells started collapsing at greater displacements, but gradually increased again as the thickness became very small. Spiralite was stiffer than the actifoam and showed a similar trend of increasing strength and stiffness with displacement.

Permanent deformation was computed after the load was removed from the specimen. The 24.6 mm thick polystyrene material, when unloaded from a force of 5.08kN and displacement of 19.5 mm had a deformation of 9.4 mm at zero loads. This was significantly greater than the 2.2 mm for 27.0 mm thick actifoam, unloaded from a force of 4.88 kN and displacement of 18.2 mm, and the 1.3 mm for 20 mm thick spiralite unloaded from a force of 5.11 kN and displacement of 11.8 mm. Since polystyrene shows larger residual deformation, there is greater

possibility that the gap remains open after the structure is subjected to large displacements. A water absorption test was also conducted on the actifoam and spiralite by keeping the material submerged in water for 24 hours. In order to determine the percentage of water absorption, specimen weights (before & after the test) were measured. It was found that, the spiralite absorbed more water (21% by weight) as compared to actifoam (0.65% by weight).

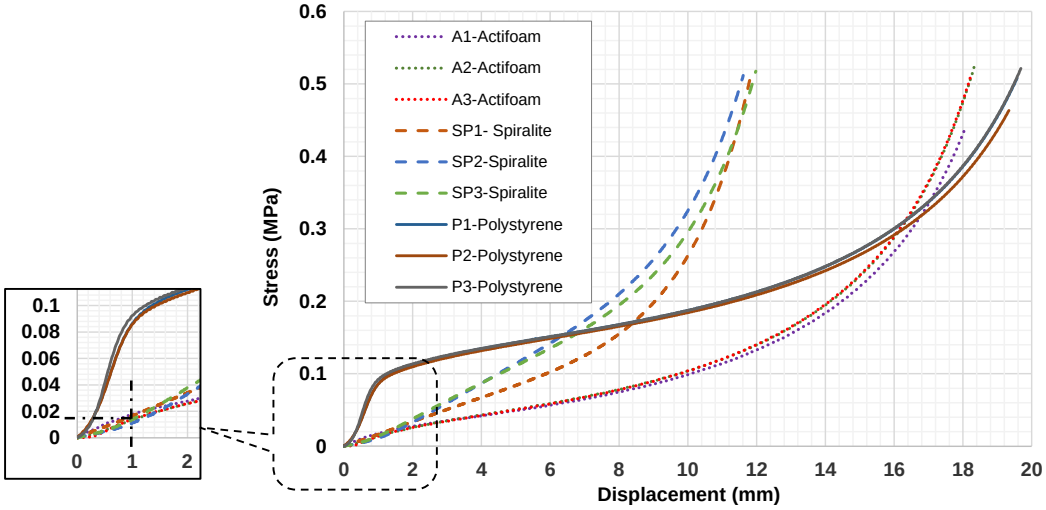

Figure 4.5 – Compression Behaviour of Infill Material (Actifoam, Spiralite, & Polystyrene)

4.4 Subjective Quantitative Assessment (SQA)

Subjective quantitative analysis (SQA) is a tool to help in decision making [68]. In this process, different parameters were identified and they were rated on a scale. In the example below the scale goes from '1' (which indicates 'poor' performance) to '10' (which indicates 'good'). The ranking was based on material specifications, test results and the impression of material for particular performance criteria on a subjective basis. For example, consider a 'fire rating' as performance criteria, polystyrene was ranked lowest (scale =1) since it was very poor in fire resistance, whereas actifoam was ranked highest (scale = 10) based on its technical specifications. Moreover, the weighing percentage was based on the subjective importance of particular criteria. This depends on the value system of the decision made. The results of the subjective quantitative analysis (SQA) on different infill materials (i.e. polystyrene, actifoam, and spiralite) are reported in Table 4.2.

Table 4.2: SQA Scores (S) on Infill Material

Material Type	Compressibility under Seismic Deformation	Construction Compressibility	Fire Rating	Water Resistance	Elasticity	Low Cost	Sound Resistance	Rank ∑S* W
Weights (W)	**25%**	**15%**	**20%**	**10%**	**10%**	**10%**	**10%**	
Polystyrene	7	8	1	8	3	9	2	5.35
Actifoam	9	7	10	9	9	1	8	**8.0**
Spiralite	5	7	7	3	6	8	8	6.2

Scale 'S' =1 to 10 (Poor to Good)

Based on the above SQA, with the rating and weighing scales used in this particular example, the actifoam material is found to be the most suitable infill material for the seismic gaps. Other rating/weighing scales could result in different outcomes.

4.5 Design Example

4.5.1 Design of Gapping Material for Slab Isolation

In this section, an example of slab isolation in composite deck construction is presented. In order to design the infill material, the first step was to calculate the gap required in particular construction situation. For this purpose, an internal joint of a steel building with 6.0 m x 6.0 m bay size having 150 mm thick composite deck slab (ComFlor80) was considered. The column was 310UC158 and beam was 310UB32. The structure was designed to follow the strong-column and weak-beam philosophy. The ultimate limit state inter-storey drift of 2.5% was considered to calculate the required gap (Δ_{gap}) as shown in Figure 4.6.

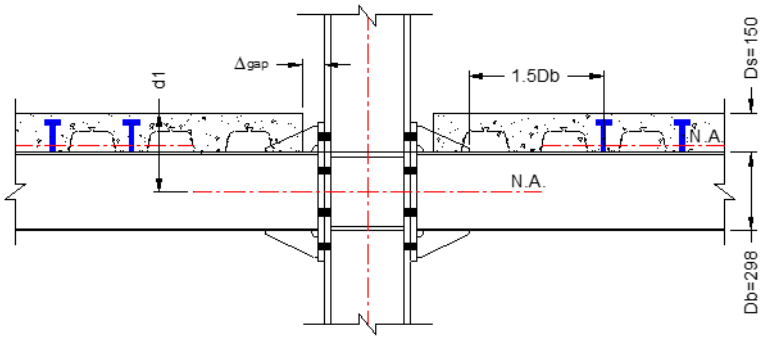

Figure 4.6 – Details of Selected Isolated Slab

The isolation gap (Δ_{gap}) is a function of inter-story drift and depth of bare beam neutral axis from the slab top (d_1). As per Clause 13.4.11.3.3 of NZS3404:1 [5], the first shear stud should be welded at 1.5 times the beam depth ($1.5D_b$) from the column face so that large beam yielding

deformations may occur in this zone. Since the beam is not connected to the slab in this yielding zone, and the slab is isolated from the column flange, beam end plates, bolts and gusset plates, there are no bearing forces entering the columns. It is assumed that the neutral axis is at the centroid of the bare steel beam (ignoring the slab).

4.5.1.1 Design Steps

(i). Calculate the ultimate limit state (ULS) inter-story drift, *D*, using standard code procedures

(ii). Calculate depth of bare beam neutral axis from slab top, d1, where D_s is the slab depth and D_b is the beam depth.

$$d1 = (D_s + D_b/2) \tag{4.1}$$

(iii). Determine the minimum gap required for the isolation,

$\Delta_{gap\ (required).}$ $\Delta_{gap\ (required)} = D.d1$ (4.2)

(iv). Check that the compression of the infill material ($\Delta_{infill\ (comp.^{n})}$) is more than $\Delta_{gap\ (required)}$ without a stress of greater than $0.1f'_{c.}$

(v). Calculate lateral pressure of wet concrete, $f_{wet\ conc.}$, where ρ is the concrete density, D_s is the slab depth, and g is the acceleration of gravity.

$$f_{wet\ conc.} = \rho.g.D_s \tag{4.3}$$

(vi). Check construction stiffness. That is, the strength of infill material at 1.0 mm displacement ($f_{comp(infill)\ @\ 1.0mm\ displacement}$) is more than the lateral pressure of the wet concrete ($f_{wet\ conc}$).

(vii). Check that the fire rating of the infill material, FR_{infill}, is more than the fire rating, $FR_{building}$

(viii). Ensure gap provided, $\Delta_{gap\ (provided)}$ is more than $\Delta_{gap\ (required)}$.

4.5.1.2 Example

(i). Assume ultimate limit state inter-story drift of the structure = *D* = 2.5%

(ii). Depth of neutral axis from slab top ($d1$)

$$d1 = (D_s + D_b/2) = (150 + 298/2) = 299\ mm$$

(iii). Minimum gap required for the isolation $\Delta_{gap\ (required)}$

$$\Delta_{gap\ (required)} = D.(d1) = 2.5\%\ x\ 299mm = 7.5mm$$

(iv). Referring to stress-displacement plot of different infill materials in Figure 4.5, it may be seen that the maximum stress is less than 0.6MPa which is much less than $0.1f'_c$ (3.0MPa) and the noted compression of the infill material ($\Delta_{infill\ (comp.}{}^{n}{}_{)}$) is listed below;

a) for 27mm thick actifoam, $\Delta_{infill\ (comp.}{}^{n}{}_{)}$ (= 18.0mm) > $\Delta_{gap\ (required)}$ (= 7.5mm)

b) for 20mm thick spiralite, $\Delta_{infill\ (comp.}{}^{n}{}_{)}$ (= 12.0mm) > $\Delta_{gap\ (required)}$ (= 7.5mm)

c) for 24.6mm thick polystyrene, $\Delta_{infill\ (comp.}{}^{n}{}_{)}$ (= 19.0mm) > $\Delta_{gap\ (required)}$ (= 7.5mm)

(v). Lateral pressure of wet concrete ($f_{wet\ conc.}$)

$$f_{wet\ conc} = \rho.g.D_s = 2400\ x\ 9.81\ x\ 0.15 = 3532\ N/m^2 = 0.0036MPa$$

(vi). Check that construction stiffness (i.e. the strength of infill material at 1.0 mm displacement ($f_{comp(infill)\ @\ 1.0mm\ displacement}$) is more than lateral pressure of wet concrete ($f_{wet\ conc}$)

a) For actifoam, $f_{comp(infill)\ @\ 1.0mm}$ (= 0.018 MPa) > $f_{wet\ conc}$ (= 0.0036 MPa)----- Ok

b) For spiralite, $f_{comp(infill)\ @\ 1.0mm}$ (= 0.016 MPa) > $f_{wet\ conc}$ (= 0.0036 MPa)------ Ok

c) For polystyrene, $f_{comp(infill)\ @\ 1.0mm}$ (= 0.095 MPa) > $f_{wet\ conc}$ (= 0.0036 MPa)--Ok

(vii). Check that fire rating of infill material (FR_{infill}) is more than fire rating of building ($FR_{building}$)

Consider that, the building is designed for 2.0 hours of fire rating.

a) For actifoam, FR_{infill} = 3 Hrs > $FR_{building}$ = 2 Hrs ----------Ok

b) For spiralite, FR_{infill} = 2 Hrs ≥ $FR_{building}$ = 2 Hrs ----------Ok

c) For polystyrene, FR_{infill} = 0 Hrs < $FR_{building}$ = 2 Hrs -----Not Ok

The actifoam is the most suitable infill material to isolate the slab in the example above. Therefore, a gap equal to the thickness of the actifoam material, $\Delta_{gap(provided)}$, of 27.0mm should be provided. This is satisfactory because it is greater than $\Delta_{gap(required)}$ of = 7.5mm. This is also the most expensive option.

4.5.2 Design of Gapping Material for Partition Wall Isolation

This section presents an example of determination of isolation gap in case of the partition wall. The required performance criteria for this case are different from section 4.5.1. Here a steel frame building with 3.0 m x 3.0 m bay size and floor-to-floor height of 3.3 m was considered. The ultimate limit state inter-storey drift of 2.0% is assumed to calculate the required gap (Δ_{gap}) as shown in Figure 4.7.

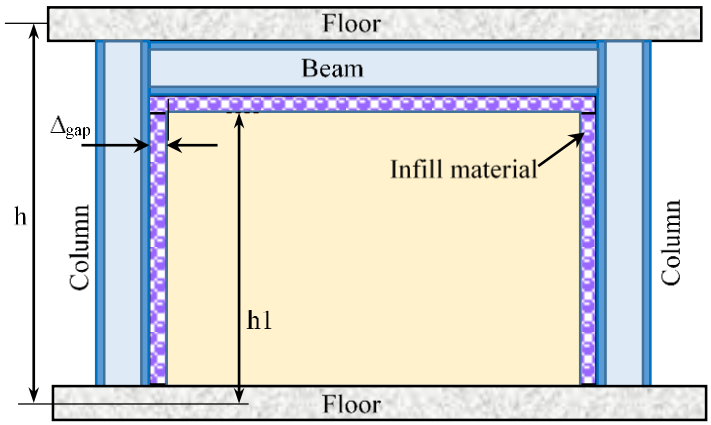

Figure 4.7 – Details of Selected Isolated Slab [69]

4.5.2.1 Design Steps

(i). Calculate the ultimate limit state (ULS) inter-story drift, *D*, using standard code procedures

(ii). Calculate height of partition wall from the centre of bottom floor (*h1*)

(iii). Determine minimum gap required for the isolation $\Delta_{gap\ (required)}$

$$\Delta_{gap\ (required)} = D.h1 \tag{4.4}$$

(iv). Check for the compression of infill material ($\Delta_{infill\ (comp.}{}^{n}$)) is more than gap required ($\Delta_{gap\ (required)}$)

(v). Check for fire rating of infill material (FR_{infill}) is more than fire rating of building ($FR_{building}$)

(vi). Ensure gap provided, $\Delta_{gap\ (provided)}$ is more than $\Delta_{gap\ (required)}$

4.5.2.2 Example

(i). Assume ultimate limit state inter-story drift of the structure = *D* = 2.0%

(ii). Height of partition wall from the centre of bottom floor = *h1* = 3000mm (assumed)

(iii). Minimum gap required for the isolation ($\Delta_{gap\ (required)}$)

$$\Delta_{gap\ (required)} = D.h1 = 2.0\% \ x\ 3000mm = 60mm$$

(iv). Check for the compression of infill material ($\Delta_{infill\ (comp.^{n})}$) is more than gap required ($\Delta_{gap\ (required)}$), Referring to the stress-displacement plot of different infill material (Figure 4.5).

a) For actifoam, $\Delta_{\text{infill (comp}^{n})} = 18.0\text{mm} < \Delta_{\text{gap (required)}} = 60\text{mm}$ -----Not Ok

Consider that, the infill material is provided in 4 layers,

$\Delta_{\text{infill (comp}^{n})}$ for four layers = 72mm > $\Delta_{\text{gap (required)}}$ = 60mm ------ Ok

b) For spiralite, $\Delta_{\text{infill (comp}^{n})}$.= 12.0mm < $\Delta_{\text{gap (required)}}$ = 60mm ----Not Ok

Consider that, the infill material is provided in 5 layers,

$\Delta_{\text{infill (comp}^{n})}$ for five layers = 60mm ≥ $\Delta_{\text{gap (required)}}$ = 60mm ------ Ok

c) For polystyrene, $\Delta_{\text{infill (comp}^{n})} = 19.0\text{mm} < \Delta_{\text{gap (required)}} = 60\text{mm}$ ----Not Ok

Consider that, the infill material is provided in 4 layers,

$\Delta_{\text{infill (comp}^{n})}$ for four layers = 76.0mm > $\Delta_{\text{gap (required)}}$ = 60mm ----- Ok

(v). Check for fire rating of infill material (FR_{infill}) is more than fire rating of building ($FR_{building}$)

Consider that, the building is designed for 2.0 hours of fire rating.

a) Check for actifoam, FR_{infill} = 3 Hrs > $FR_{building}$ = 2 Hrs ----------Ok

b) Check for spiralite, FR_{infill} = 2 Hrs ≥ $FR_{building}$ = 2 Hrs ----------Ok

c) Check for polystyrene, FR_{infill} = 0 Hrs < $FR_{building}$ = 2 Hrs -----Not Ok

From above, the four layers of actifoam was the most suitable infill material to isolate the partition wall. Therefore, provide a gap equal to four times thickness of actifoam material, $\Delta_{gap\ (provided).}$ = 108mm > $\Delta_{gap\ (required).}$ = 60mm. Note that, if cost were a more significant parameter, other options might be more desirable.

4.6 Recommended Conceptual Detailing

This section provides conceptual details for slab isolation as well as for isolation of non-structural elements (partition walls and ceilings).

4.6.1 Slab Isolation Details

In case of isolation of the welded connection, wherein the beams are directly welded to the column, the infill material need to provide all around the column (i.e. isolation of external and internal flange surfaces and web surfaces) as shown in Figure 4.8.

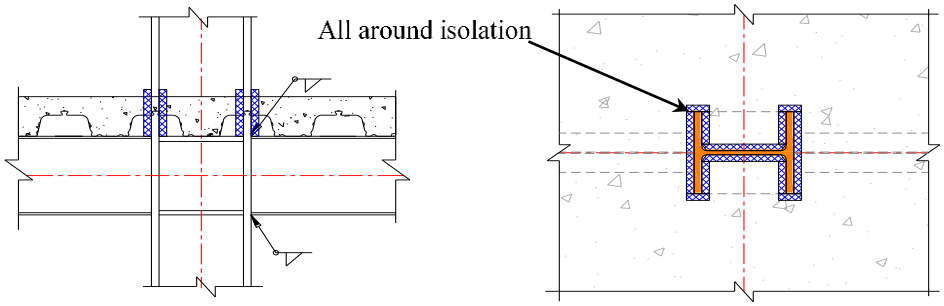

(a) Front View **(b) Plan**

Figure 4.8 – Welded Connection – Slab Isolation Details

For isolating the bolted flange plate connection, the isolation should be provided all around the column as well as all connection components like flange plates and bolts should be isolated as shown in Figure 4.9.

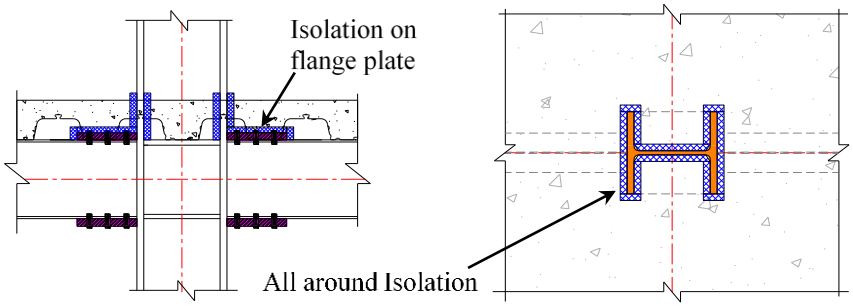

(a) Front View **(b) Plan**
(flange plates are not shown for clarity)

Figure 4.9 – Bolted Flange Plate Connection – Slab Isolation Details

For bolted end-plate connections with gusset plates, in addition to the isolation above, the gusset plate should also be isolated as shown in Figure 4.10.

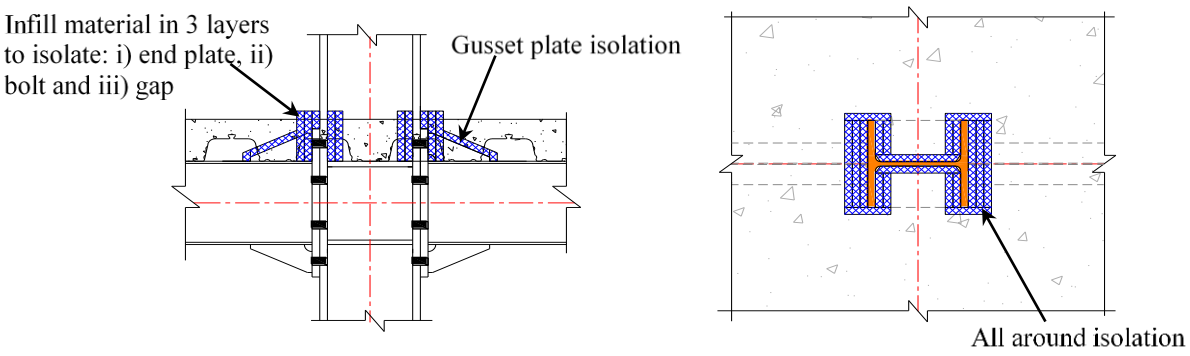

(a) Front View **(b) Plan**

Figure 4.10 – Bolted End Plate Connection – Slab Isolation Details

The isolation can also be done in the diamond format as shown in Figure 4.11, wherein the infill material is placed diagonally to form a diamond shape. This type of construction is applicable to both the bolted and welded moment connection and multiple layers of infill material can be avoided. However, the infill material needs to be cut in to form a shape of the decking sheet. Such construction has also been used in NZ.

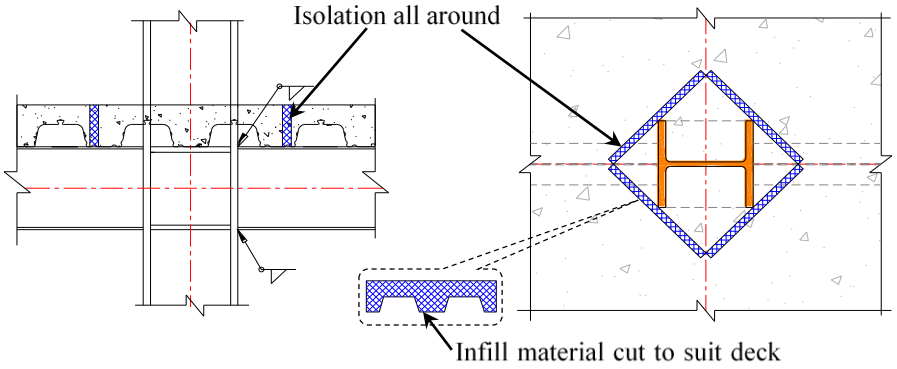

(a) Front View **(b) Plan**

Figure 4.11 – Diamond Type – Slab Isolation (adopted from Dave Anderson –John Jones Steel)

4.6.2 Non-Structural Element Isolation Details

Possible conceptual details for partition walls and ceilings are shown in Figure 4.12 thereby allowing two-way action without damage.

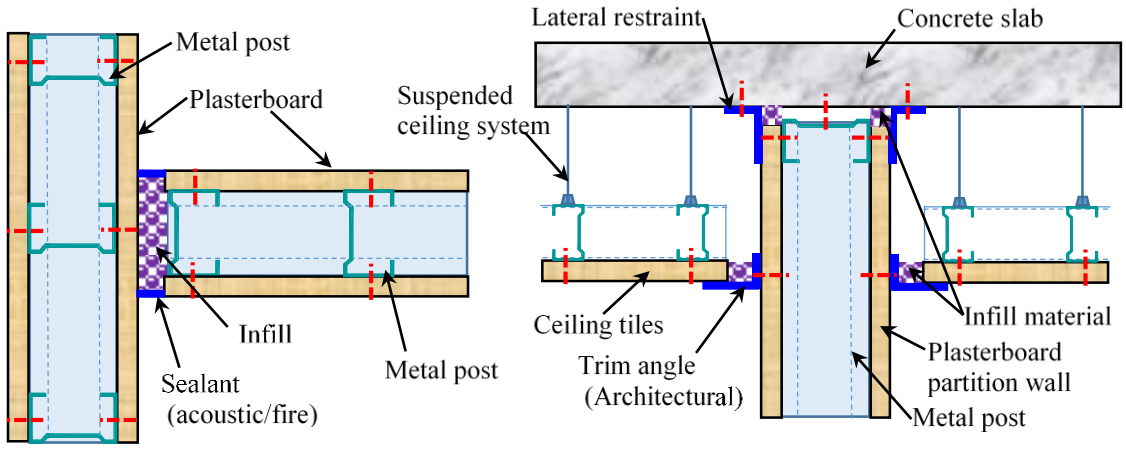

(a) Junction of partition wall to partition wall (plan)

(b) Junction of partition to ceiling (elevation)

Figure 4.12 – Conceptual Details – Isolation of non-structural elements (based on USG [70] & Rondo [71])

4.7 Conclusions

This paper presents a process to select infill material for gaps in some structural applications. It is shown that:

i) Seismic gaps may be placed between structural and other elements in a building system to decrease the possibility of damage. Infill material is often required in these gaps for practical reasons, such as for sound or fire resistance.

ii) For the cases of gaps between the floor slab and column, or between non-structural partition walls and seismic frames, the following performance criteria were considered: (a) Compressibility under seismic deformation, (b) Construction stiffness, (c) Fire rating, (d) Water resistance, (e) Elasticity, (f) Cost/Ease of application, and (g) Sound resistance.

iii) Polystyrene, spiralite and actifoam were selected as candidate materials for gap infill. Subjective quantitative analysis, based on information provided by the manufacturer, tests and reputation was used to rate these materials for the different cases. For the rating and weighing criteria chosen, the actifoam was a most promising infill material in structural applications due to its better compressibility, elasticity, fire resistance, and water resistance than the other materials. However, it

is significantly more expensive than the other materials. As a result, criteria, which emphasize cost, may result in a different outcome. The framework developed for infill material assessment may also be used for other possible gap infill materials.

iv) Some possible conceptual gap details for the structural as well as non-structural applications, which allow freedom of movement and reduce the possibility of seismic damage in brittle elements are also provided.

Chapter 5: Experimental Investigation on Frame Sub-assemblies with different Composite Slab Configurations

5.1 Introduction

This chapter presents the cyclic behaviour of the beam-column sub-assemblies with different composite slab configurations and observed modes of failure in the steel beam and the composite slab under quasi-static cyclic loading history. The four types of tested composite slab configurations are: (i) Fully Isolated Slab Unit (FI-SU), (ii) Shear Key Slab Unit (SK-SU), (iii) Modified Shear Key Unit (MSK-SU), and (iv) Full Depth Slab Unit (FD-SU). To investigate the contribution of the composite slab to the over-strength capacity of the beam, a bare steel frame (BSF) sub-assembly is also tested. The geometrical and cross-sectional details, and the applied loading protocol to evaluate the structural performance of the frame sub-assemblies is reported in the previous chapter. The methodology to evaluate/calculate the initial lateral stiffness, contribution of individual frame component (i.e. beam, column, panel zone, and connection) deformation to the overall lateral displacement of frame sub-assembly, beam axial deformation, energy dissipation, and slab surface deformation are detailed in Section 3.9. Also, the deformation contributions of the sub-assembly frame components to the overall lateral displacement are reported. Finally, the comparison of structural performance parameters of the tested frame sub-assemblies and the derived conclusion based on the test findings are reported.

5.2 Bare Steel Frame (BSF) Sub-assembly

The bare steel frame (BSF) sub-assembly was made of steel I shape column and I shape beams and connected using bolted end-plate connections. The layout of the tested BSF frame sub-assembly is reported in Chapter 3 (refer Figure 3.1). The 310UB32 beam is a non-compact section according to the New Zealand steel code NZS3404:1 [5] (close to compact section as section slenderness, λ_e=10.15 ≈ λ_{ep}=10), however, it is a compact section as per EC3 [38] and ANSI/AISC:360-10 [72]. The beam-ends were restrained with the vertical roller support to avoid the lateral torsional buckling. As mentioned before, the primary objective of testing the bare frame sub-assembly is to identify modes of failure in the beam (with and without a composite slab). The test results of the BSF sub-assembly were used to: (i) evaluate the overstrength capacity of the beam, (ii) investigate the effect of tested different composite slab configurations on the structural performance parameters; such as initial lateral stiffness,

nominal lateral strength, etc.

5.2.1 Hysteresis Behaviour

The recorded load to push the frame sub-assembly to the specified input column top displacement was used to construct the hysteresis loop of the BSF frame sub-assembly. The experimentally obtained hysteresis plot for BSF frame sub-assembly is shown in Figure 5.1.

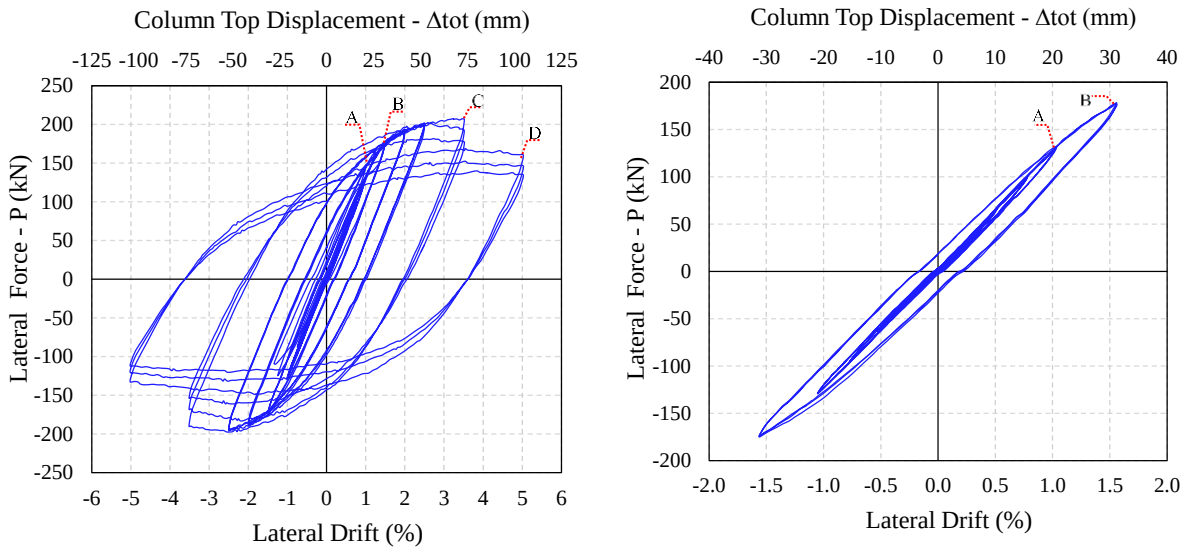

a) Overall Hysteresis Plot **b) Hysteresis Plot up to 1.5% Lateral Drift**

Figure 5.1 –Hysteresis Behaviour of BSF Frame Sub-assembly

It is evident from Figure 5.1 that the hysteresis behaviour of the BSF frame sub-assembly is ductile due to predominant flexural deformation and associated yielding in the beam. The strength degradation at 5% lateral drift was due to the buckling of the beam in front of the gusset as shown in Figure 5.2. The calculated initial lateral stiffness of the BSF frame sub-assembly was 6156 kN/m. The BSF frame sub-assembly achieved the maximum lateral strength of 206 kN at 3.5% lateral drift. The load-displacement curve was linear and elastic up to the 1.0% lateral drift as shown by point 'A' in Figures 5.1a and 5.1b. Shear deformation of the beam web was observed (this conclusion was arrived because the coated brittle paint started to flake off) in the first cycle of 1.5% lateral drift (point 'B' in Figure 5.1b). The location of the shear deformation was approximately 25 to 50 mm away from the tip of the gusset plates (i.e. in the beam plastic hinge zone) as shown in Figure 5.2. Yielding of the beam flanges was also observed at the same lateral drift level. As the beam falls into the non-compact category, the bucking of the flanges and web is expected. In this test, the buckling of the beam flanges was observed in the second cycle of 2.5% lateral drift. The BSF frame sub-assembly achieved its maximum lateral strength of 206 kN in the first cycle of 3.5% lateral drift (i.e. point 'C' in

Figure 5.1a). At the same drift level, substantial buckling in the beam flanges and the web was also observed as shown in Figure 5.2. The noted magnitude of the bucking in the beam flanges was in the order of 7 mm to 12 mm at the peak of the first cycle of 3.5% lateral drift and the buckling half wavelength of approximately 60 mm from the end of the gusset plate as shown in Figure 5.3d.

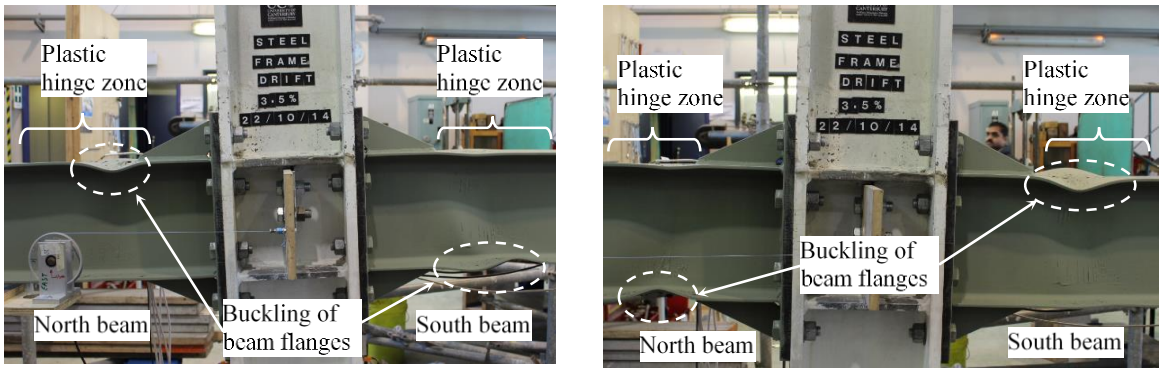

a) Positive Drift Direction **b) Negative Drift Direction**

Figure 5.2 – Beam Bucking in the First Cycle of 3.5% lateral drift : BSF Sub-assembly

The strength degradation of the BSF frame sub-assembly started in the second cycle of 3.5% lateral drift, and further strength degradation was observed in the subsequent cycles. The reduction in lateral strength from the first cycle to the third cycle was 15%. The observed residual buckling magnitude of the beam flanges at the end of 3.5% lateral drift was approximately 17 mm in both the beams of the BSF frame sub-assembly. The lateral force of the BSF frame sub-assembly in the first cycle of 5.0% lateral drift was 159.7 kN (i.e. point 'D' in Figure 5.1a), which indicates a strength degradation of 23% when compared to the sub-assembly peak strength at 3.5% lateral drift. The strength degradation in the last cycle of 5% lateral drift was approximately 35% (i.e. lateral force is 65% of peak lateral force at 3.5% lateral drift). The beam flange buckling was more prominent at the same drift. At the end of the test, the residual buckling magnitude in the beam flanges was 37 mm, and the buckling modes were symmetrical on both the beams as shown in Figure 5.3c.

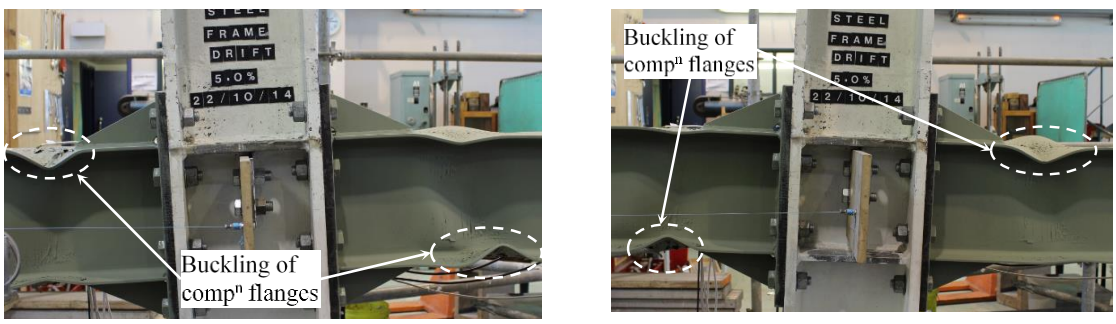

a) Positive Drift Direction **b) Negative Drift Direction**

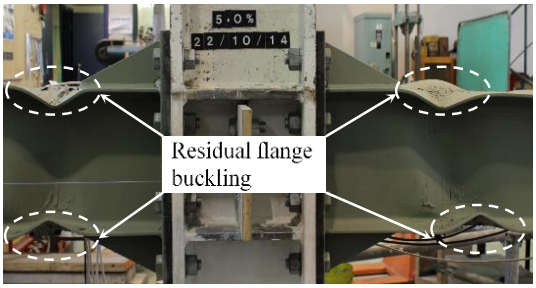

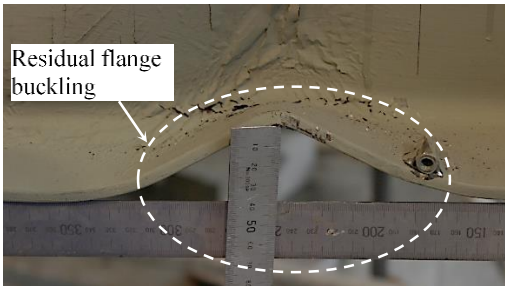

c) Residual Buckling in the Beam Flanges

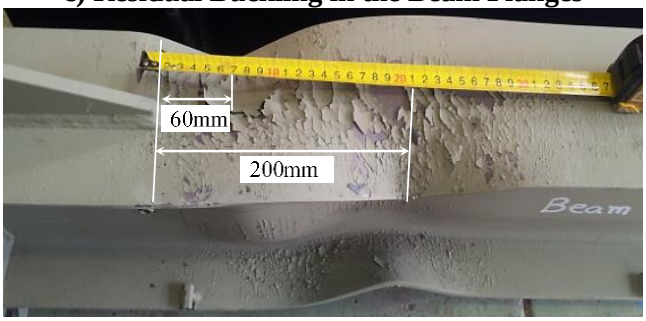

d) Location and Wavelength of Beam Flange Buckling

Figure 5.3 – Beam Bucking after 5.0% Drift : BSF Sub-assembly

5.2.2 Cyclic Behaviour of the Panel Zone and End-plate Connection

As the BSF frame sub-assembly was designed by applying the capacity design principles (i.e. strong column/connection-weak beam), the nonlinearity is expected to be limited to the beam only, and the column, panel zone, and connections are expected to be linear and elastic. In this section, the cyclic behaviour of the panel zone and the end-plate connection are evaluated based on the experimentally obtained results. The cyclic shear force vs shear deformation/distortion of the panel zone of the BSF frame sub-assembly under quasi-static cyclic loading is shown in Figure 5.4. Based on the cyclic behaviour of the panel zone reported in Figure 5.4, it can be concluded that the panel zone is elastic (as expected), the maximum panel zone shear deformation at a lateral drift of 3.5% was approximately 0.0013 rad, which is less than the yield shear deformation of 0.0022 rad computed using the formulae reported in FEMA451 [73] considering the sub-assembly peak lateral strength. As the panel zone was rigid, the contribution of the panel zone deformation to the overall lateral displacement is very limited (which will be verified in the later section). Therefore, in the numerical model, the panel zone can be treated as a rigid and elastic element without significant error in the prediction of overall hysteresis behaviour.

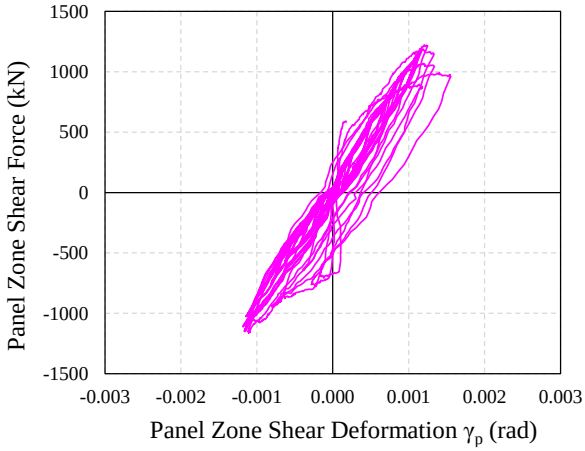

Figure 5.4 – Panel Zone Shear Deformation : BSF Sub-assembly

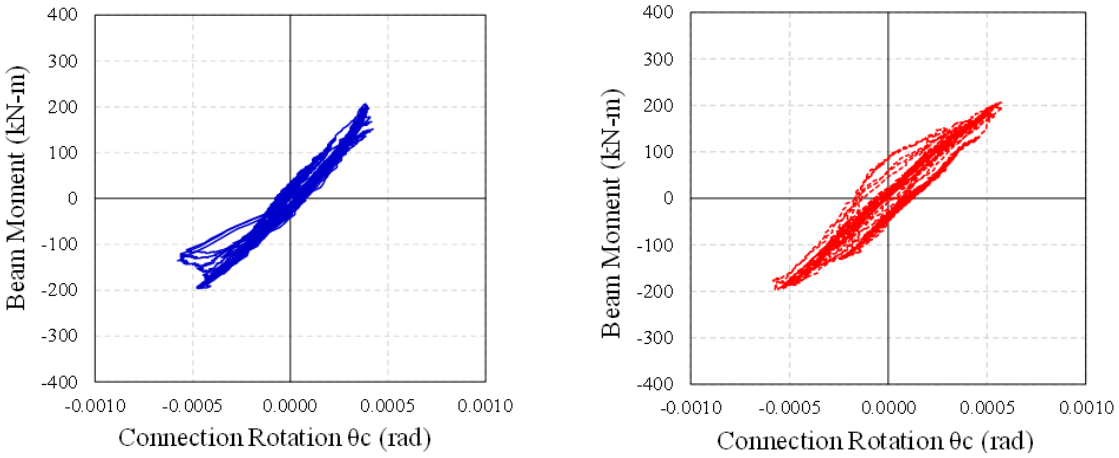

a) South Beam **b) North Beam**

Figure 5.5 – Connection Rotation : BSF Sub-assembly

As the end-plate connection was designed to be in elastic state by increasing its stiffness and strength by using the gusset plates, this is verified here by utilizing the experimentally obtained moment versus rotation plot. The moment versus rotation cyclic plot of the end-plate connection under quasi-static cyclic load is shown in Figure 5.5. The maximum rotation of the end-plate was approximately 0.0005 rad, which is considerably less than the yield rotation of the beam. Therefore it can be concluded that the end-plate connection can be classified as rigid and elastic. Also, the lift-off of the end-plate connection (i.e. separation between the end-plate and column flange) was obtained from the spring potentiometer mounted on the end-plate as shown in Figure 3.22. The maximum lift-off of the end-plate was 0.15 mm, this can be ignored in the numerical modelling, and the lift-off plot as a function of time step is reported in Appendix D. As the connection found to be rigid, its deformation contribution to the overall lateral displacement of the frame sub-assembly is minimal, and is explicitly addressed and verified in the next section.

5.2.3 Decomposition of the BSF Frame Sub-assembly Overall Lateral Displacement

The lateral displacement of the BSF frame sub-assembly at the column top under a given lateral load is due to the deformation of the individual frame components, namely; panel zone shear distortion (Δ_{pz}), end-plate connection rotational deformation (Δ_{conn}), column elastic flexural deformation ($\Delta_{col(el)}$), and beam elastic ($\Delta_{b(el)}$) and inelastic ($\Delta_{b(ph)}$) deformation. The plots of the individual frame components deformation as a function of lateral drift/column top displacement is shown in Figure 5.6. At 1.0% lateral drift, the cumulative contribution of panel zone shear deformation, end-plate connection rotational deformation, and the column elastic flexural deformation to the overall lateral displacement of the frame sub-assembly was approximately 17%, which is considerably less, whereas the contribution of the beam's elastic flexural deformation was 77%. This is mainly because of the adopted capacity design methodology in the designing the BSF frame sub-assembly. At 3.5% lateral drift, the contribution of the panel zone, endplate connection, and the column deformation remains more or less same, and the beam's overall deformation can be further divided in to elastic and plastic deformation, which was 34% and 45% respectively to the overall lateral displacement of the frame sub-assembly.

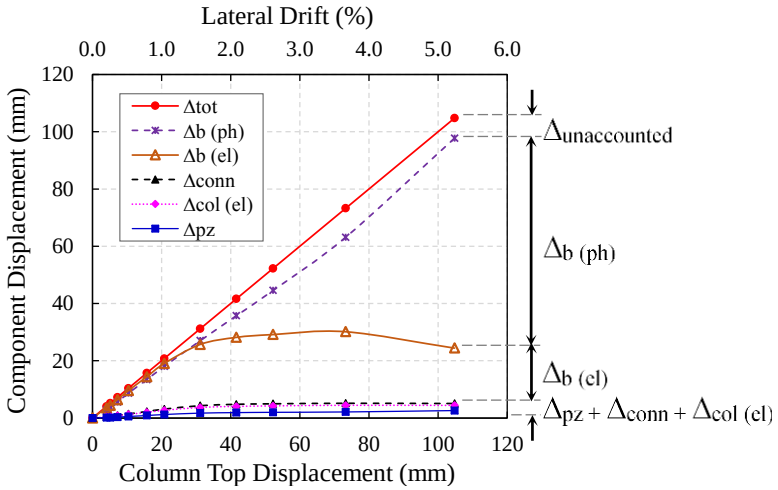

Figure 5.6 – Contribution of Frame Components Deformation to the Overall Lateral Displacement : BSF Sub-assembly

5.2.4 Beam Axial Deformation

The beam axial deformation is computed as the average of absolute deformation of beam's top and bottom flange in the plastic hinge zone. The residual beam axial deformation at un-deformed position (i.e. at zero column top displacement) of the frame sub-assembly approximately represents the beam elongation under cyclic loading (i.e. accumulation of plastic strain in a beam under cyclic bending). The cyclic beam axial deformation plots of the north

and south beams as a function of the lateral drift is shown in Figure 5.7. The measured average beam axial deformation of the north and south beams was 2.2 mm at the initiation of beam flange buckling (i.e. 2.5% lateral drift), whereas the average residual deformation (i.e. beam elongation) was 0.72 mm. The residual beam axial deformation/elongation is negligible and is in line with the observations reported in the literature [61]. In real frame buildings, the columns in the subsequent bays could offer an additional restraint to the beams, as a result, the overall elongation of the beams may further reduce when compared to the beam residual deformation observed in the test specimen.

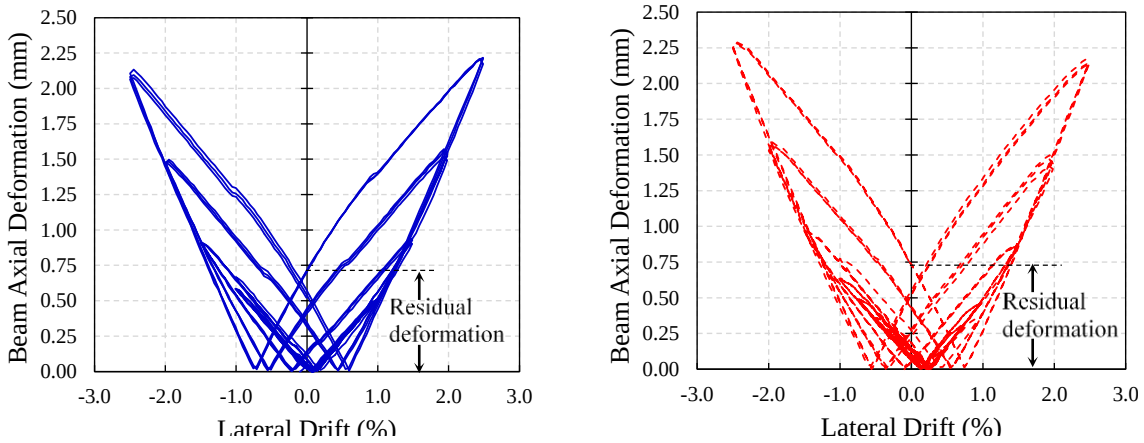

a) South Beam Axial Deformation **b) North Beam Axial Deformation**

Figure 5.7 – Beam Axial Deformation : BSF Sub-assembly

5.3 Frame Sub-assembly with Fully Isolated Slab Unit (FI-SU)

The steel beams and column of the frame sub-assembly with isolated slab unit (i.e. no interaction between the slab and the column) were same as that of the bare steel frame sub-assembly. The isolation is achieved by filling the gap between the column and the slab by using highly compressible and fireproof Actifoam infill material (the details of the infill material is reported in Chapter 3). The primary objective of this test are: (i) to avoid the damage to the slab around the column caused by slab-column interaction, (ii) to investigate the contribution of composite action of the slab with the beam alone (eliminating the slab-column interaction mechanisms [14]) to the lateral strength and initial lateral stiffness of the frame sub-assembly.

5.3.1 Hysteresis Behaviour

The experimentally obtained hysteresis behaviour of the frame sub-assembly with fully isolated slab under quasi-static cyclic loading is shown in Figure 5.8a. The close-up view of the hysteresis loop up to 1.5% lateral drift is shown in Figure 5.8b. The overall hysteresis plot of the frame sub-assembly with an isolated slab is very much similar to the hysteresis plot of the bare steel frame sub-assembly up to 3.5% drift (i.e. peak strength). This is due to the similar behaviour of beams in both the test sub-assemblies i.e. yielding and buckling of the beam.

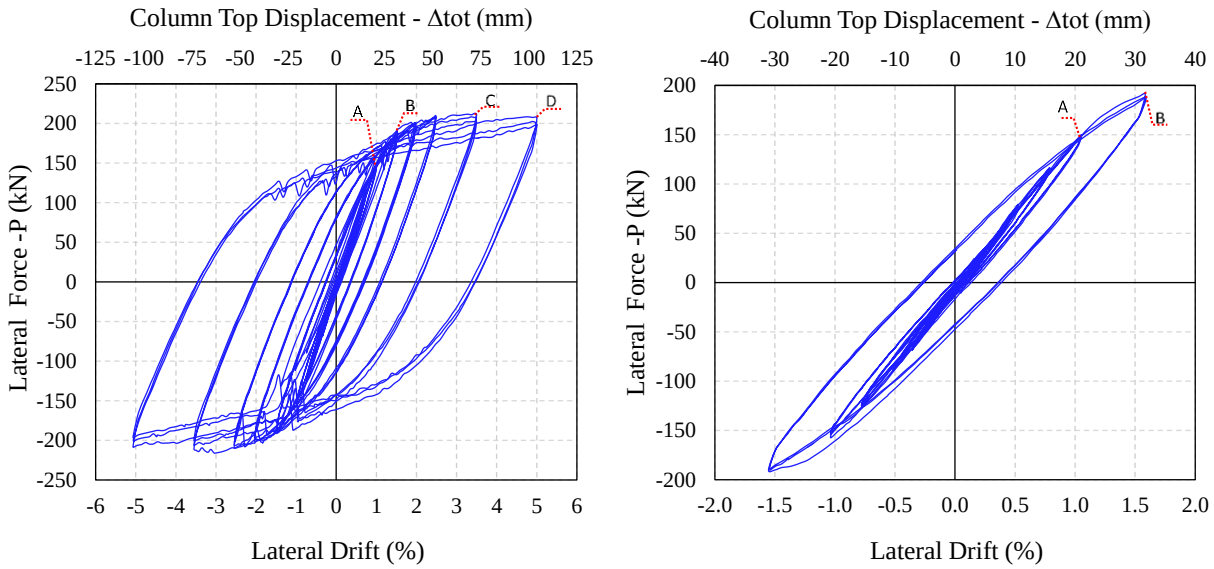

a) Overall Hysteresis Plot **b) Hysteresis Plot up to 1.5% Lateral Drift**

Figure 5.8 –Hysteresis Behaviour of FI-SU Frame Sub-assembly

The initial lateral stiffness of the frame sub-assembly with the fully isolated slab is 8747 kN/m, which is 43% higher than the lateral stiffness of the BSF frame sub-assembly. This increment in lateral stiffness is due to the composite action of the slab with the beam. The FI-SU frame sub-assembly hysteresis behaviour was linear up to 1.0% lateral drift (i.e. point 'A' in Figure

5.8). Yielding in the beam was observed at the first cycle of 1.5% lateral drift (i.e. point 'B' in Figure 5.8) in the beam plastic hinge region. Similar to the BSF frame sub-assembly, shear distortion of the beam web was observed in the plastic hinge region (approximately 25 to 50 mm away from the tip of gusset plate as shown in Figure 5.2) at the same drift. Buckling of the beam flanges was started in the first cycle of 2.5% lateral drift. Similar to the BSF frame sub-assembly, the frame sub-assembly with the fully isolated slab configuration achieved a peak strength of 211.4 kN in the first cycle of 3.5% lateral drift (i.e. point 'C' in Figure 5.8), at the same drift level substantial buckling in the beam flanges and the web was also observed. The peak lateral strength of FI-SU frame sub-assembly is approximately same as the peak lateral strength of the BSF frame sub-assembly. This is because, in both the cases, the lateral strength of the frame sub-assemblies is limited by the strength of the beam. The magnitude of buckling in the beam flanges was 12 mm in the first cycle of 3.5% lateral drift. The residual buckling magnitude of the beam top and bottom flanges after the completion of three cycles of the 3.5% lateral drift was 13.7 mm and 22 mm respectively. The lower buckling magnitude in the beam top flanges as compared to beam bottom flanges was due to the lateral restraint offered by the slab unit to the beam top flanges. The strength degradation from the first to the third cycle of 3.5% lateral drift was 4%, which is significantly less as compared to the strength degradation observed in BSF frame sub-assembly. The strength degradation at the end of 5% lateral drift was 6.3% when compared to the peak lateral strength achieved at 3.5% lateral drift, whereas in the BSF frame sub-assembly it was 35%. The significant reduction in the strength degradation of FI-SU frame sub-assembly is due to the composite action of the slab unit with beams, which restrained the buckling in the beam top flanges, whereas it is not the case in BSF frame sub-assembly. At the end of 5% lateral drift, the residual buckling magnitude of the beam top and bottom flanges was 26 mm and 30 mm respectively as shown in Figure 5.9.

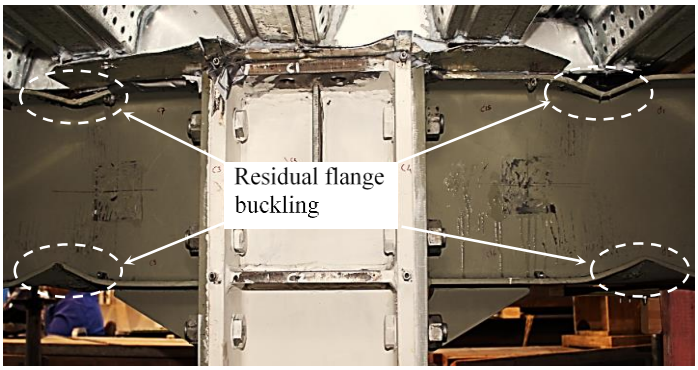

a) Residual Buckling in the Beam Flanges

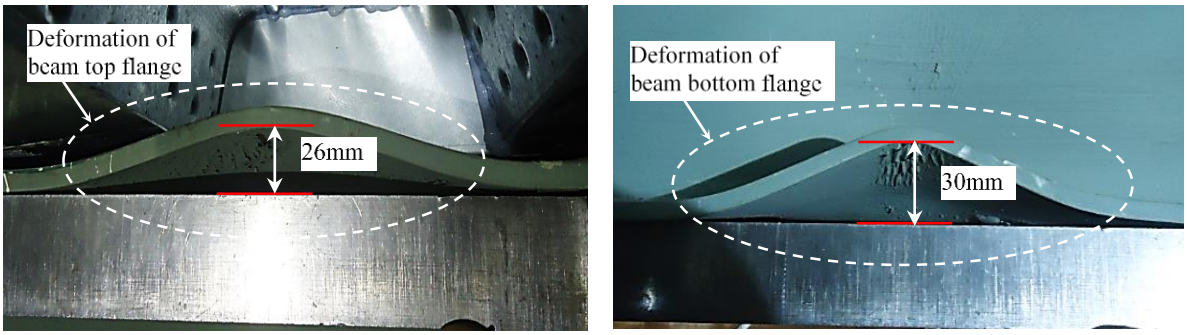

b) Buckling Magnitude of Top Flange **c) Buckling Magnitude of Bottom Flange**

Figure 5.9 – Beam Bucking after 5.0% Lateral Drift : FI-SU Sub-assembly

5.3.2 Cyclic Behaviour of the Panel Zone and End-plate Connection

The beam, column and the end-plate connections of the FI-SU frame sub-assembly were same as that of the BSF frame sub-assembly. As it was already found in the previous section (Section 5.2.2), the panel zone and the end-plate connection behaviour is linear and elastic, the same is expected in the FI-SU frame sub-assembly test. This is because the hysteresis behaviour in both the frame sub-assemblies (i.e. FI-SU and BSF) were similar, which indicates the similar magnitude of demand on the end-plate connection and panel zone. The cyclic panel zone shear force versus distortion obtained from the test data is shown in Figure 5.10. The panel zone shear deformation at 3.5% lateral drift (corresponding to a peak lateral force of 211.4 kN) was 0.002 rad, which is less than the yield panel zone shear deformation of 0.0022 rad. The cyclic moment versus rotation of the end-plate connection under quasi-static cyclic loading is shown in Figure 5.11. The maximum end-plate connection rotation for the south and north beam was 0.00012 rad and 0.00029 rad respectively at 3.5% lateral drift. It is clear that the maximum rotation that the connection experienced is considerably less than the yield rotation of the beam. Based on the results plotted in Figure 5.10 and Figure 5.11, it is further verified that the panel zone and the end-plate connection behaviour is linear and elastic. The maximum lift-off for the south and north beam was 0.05 mm and 0.1 mm respectively and the plots for connection lift-off as a function of the time step is provided in Appendix D. As the panel zone and the end-plate connection are rigid, the contribution of these components to the overall lateral displacement is very much limited.

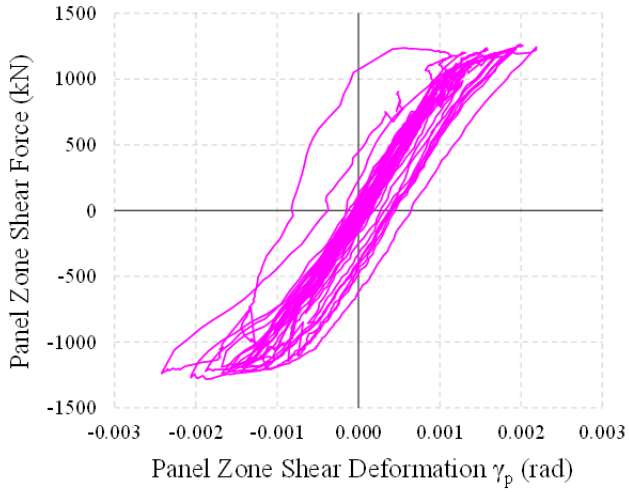

Figure 5.10 – Panel Zone Shear Deformation: FI-SU Sub-assembly

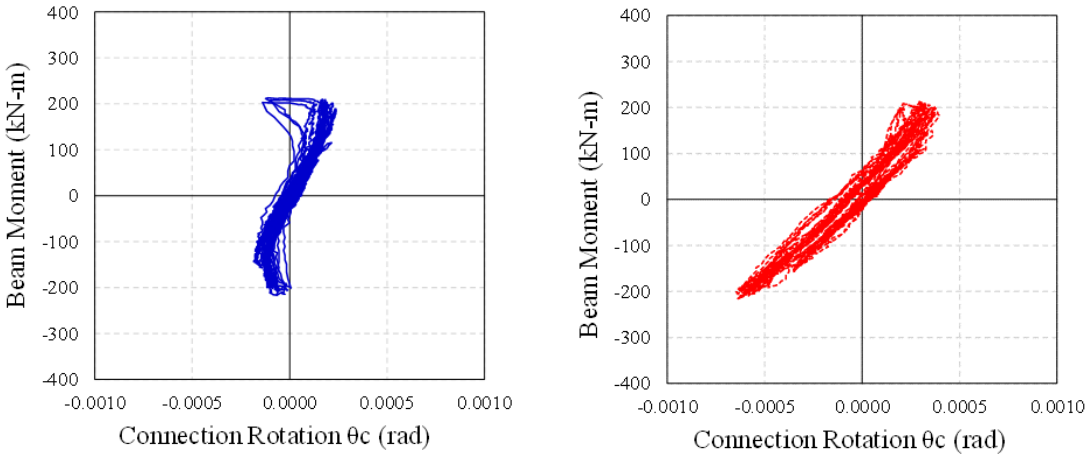

a) South Beam **b) North Beam**

Figure 5.11 – Connection Rotation: FI-SU Sub-assembly

5.3.3 Decomposition of the FI-SU Frame Sub-assembly Overall Lateral Displacement

The overall lateral displacement of the frame sub-assembly with the fully isolated slab is due to the deformation of its frame components such as; panel zone shear distortion (Δ_{pz}), end-plate connection rotational deformation (Δ_{conn}), column elastic flexural deformation ($\Delta_{col(el)}$), and beam elastic ($\Delta_{b(el)}$) and inelastic ($\Delta_{b(ph)}$) deformation. As there is no interaction of the composite slab with the column, its contribution to the overall lateral displacement can be neglected without inducing significant error. The plots of the individual frame components deformation to the overall lateral column displacement/drift is shown in Figure 5.12. At 1.0% lateral drift, the cumulative contribution of the panel zone shear deformation, end-plate connection rotational deformation, and the column elastic flexural deformation was 20%, and the beam's elastic flexural deformation contribution was 76% to the overall lateral

displacement of the frame sub-assembly with the fully isolated slab. At 3.5% lateral drift, the contribution of the panel zone, endplate connection, and the column deformation remains more or less same, and the beam's overall deformation can be further divided in to elastic and plastic deformation, which was 29% and 48% respectively to the overall lateral displacement of the frame sub-assembly. It is clear from the Figure 5.12 that the frame sub-assembly displacement is predominantly due to the elastic and inelastic deformation of the beams. This is expected because the beams were designed to be much weaker than the column.

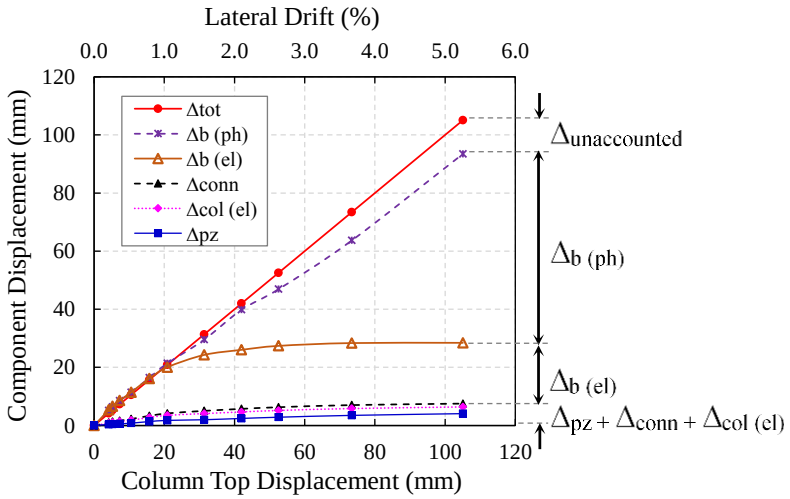

Figure 5.12 – Contribution of Frame Components Deformation to the Overall Lateral Displacement : FI-SU Sub-assembly

5.3.4 Beam Axial Deformation

The cyclic variation of the axial deformation of the beams within the plastic hinge region is depicted in Figure 5.13. Also, in the same figure, the residual axial deformation (i.e. beam elongation) is noted. Based on the cyclic beam axial deformation plots shown in Figure 5.13, the maximum axial deformation of the south and north beams was 1.1 mm and 1.15 mm respectively at 1.5% lateral drift. It is also clear that at this drift level negligible residual axial deformation was present (0.25 mm), which indicated that there is no significant accumulation of plastic axial strains due to cyclic bending. At the initiation of the beam flange buckling (i.e. 2.5% lateral drift), the beam axial deformation of the south and north beams was 2.56 mm and 2.44 mm respectively, whereas the residual axial deformation (i.e. beam elongation) at the end of the 2.5% lateral drift cycle was approximately 0.75 mm. As the residual axial deformation of the frame sub-assembly with the isolate slab unit is negligible, this has been ignored in the numerical macro-modelling/simulation reported in the next chapter.

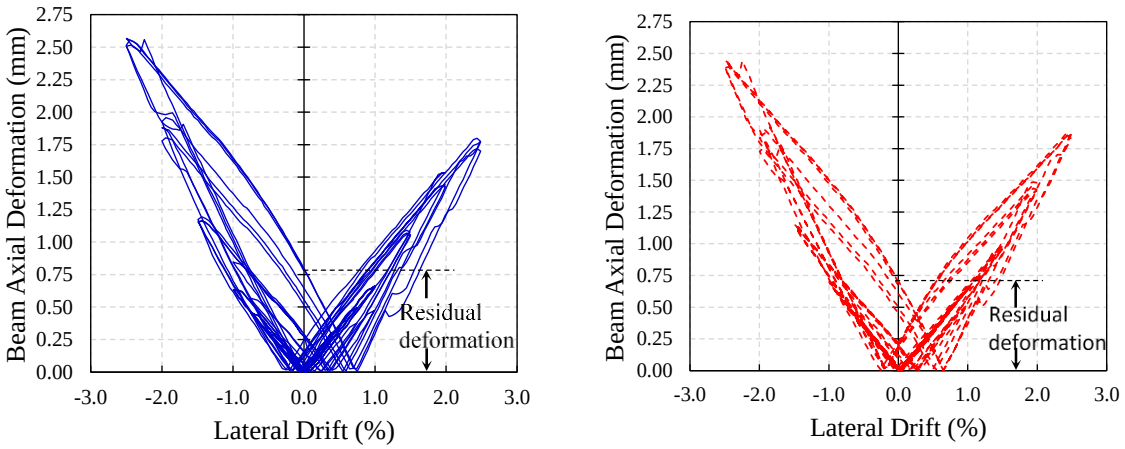

a) South Beam Axial Deformation **b) North Beam Axial Deformation**

Figure 5.13 – Beam Axial Deformation: FI-SU Sub-assembly

5.3.5 Observed Damages in the Fully Isolated Slab Unit

The deck of the FI-SU frame sub-assembly was oriented in the transverse direction (i.e. deck ribs were perpendicular to the main beam). As mentioned before, the slab was isolated from the column in order to switch off the two force transfer mechanisms [14] i.e. Mechanism-1 (concrete bearing on column outer flanges) and Mechanism-2 (concrete bearing on the column internal flanges) between the column and the slab. The first transverse crack of 0.03 mm width appeared on both the sides of the slab in the beam plastic hinge zone (i.e. 850mm from the column centre line) at 0.25% lateral drift which is shown as dotted line in Figure 5.14a. The width and length of the first transverse crack was increased in subsequent lateral drift levels. At 1.0% lateral drift, many transverse cracks spaced at an interval of 300 mm parallel to the first transverse crack were formed along the beam length, these cracks are schematically reproduced in Figure 5.14a. It is clear by comparing the sectional elevation view of the slab and the observed crack pattern that these transverse cracks were formed at the location of the deck ribs were the slab depth is minimum. The actual cracks observed during the test in south and north side of the slab are shown in Figure 5.14b and Figure 5.14c respectively.

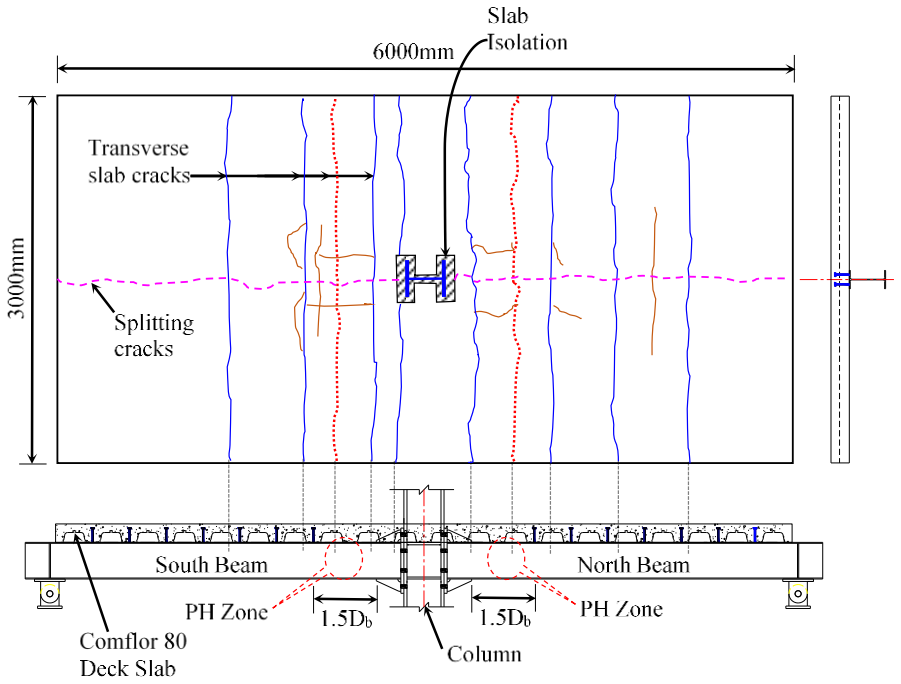

(a) Schematic Representation of Observed Cracks in FI-SU Frame Sub-assembly

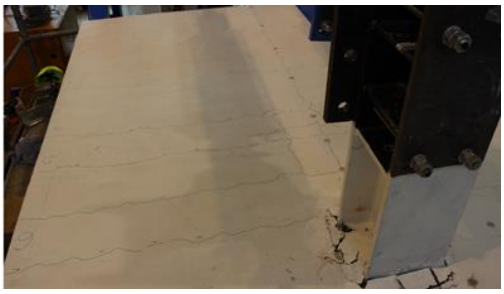

(b) Observed Cracks in South Side of the Slab

(c) Observed Cracks in South Side of the Slab

Figure 5.14 – Observed Crack Pattern in Fully Isolated Slab Unit

In addition to the transverse cracks, at 1.5% lateral drift splitting cracks parallel to the beam were observed along the beam centre line. The splitting crack initiated at second shear stud and extended along the beam at higher lateral drift. The width of the splitting cracks was increased from 0.03 mm to 0.15 mm when the lateral drift was increased from 1.5% to 3.5% respectively. As the deformation of the frame sub-assembly increased, more transverse cracks appeared in the non-composite section of the slab (i.e. slab between the column and the first shear stud). The transverse and longitudinal crack widths were less than 0.75 mm at the 3.5% lateral drift and were between 1.0 mm and 1.2 mm at the end of 5% lateral drift. To summarize, two major types of cracks were observed in the fully isolated slab; (i) transverse cracks (due to flexural deformation of the slab), (ii) splitting cracks due to the bearing of shear studs on the slab. As the slab was fully isolated around the column, no spalling of the concrete was observed around the column even after removing the infill material which is shown in Figure 5.15b.

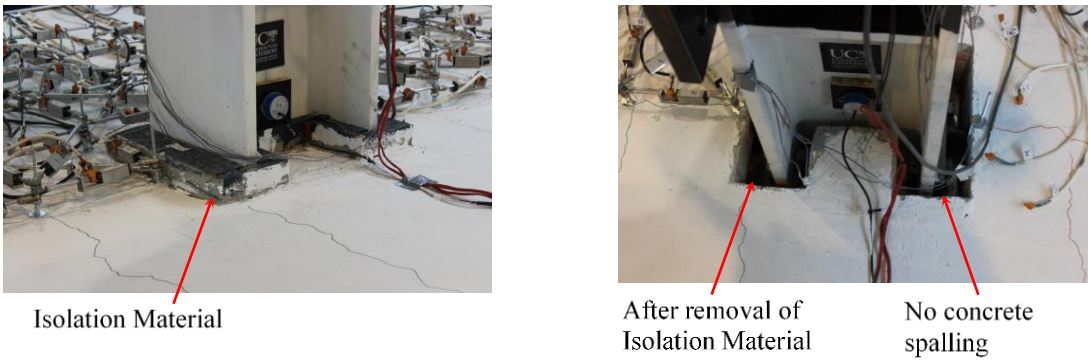

a) With Isolation Material **b) After Removal of Isolation Material**

Figure 5.15 – Slab Damage at Column Interaction: FI-SU Test Sub-assembly.

Spatial Variation of Slab Surface Deformation

The spatial variation of fully isolated slab surface deformation at each lateral drift level is computed using the readings from linear potentiometers mounted on the slab in a rectangular grid pattern. The absolute maximum spatial surface deformation (i.e. compression/stretch of a particular point on the surface) at the end of 5% lateral drift is shown in Figure 5.16. This plot can be used to identify maximum stress zones in the slab under a given lateral deformation. The surface deformation plots at 1.0%, 1.5%, 3.5% and 5.0% lateral drifts are reported in Appendix D. It is clear from the Figure 5.16 that the maximum stress zone in the slab was located between 750 mm to 1000 mm from the column centre line (i.e. the location of first shear stud). The absolute maximum obtained surface deformation at the end of 5% drift was approximately 3.0 mm.

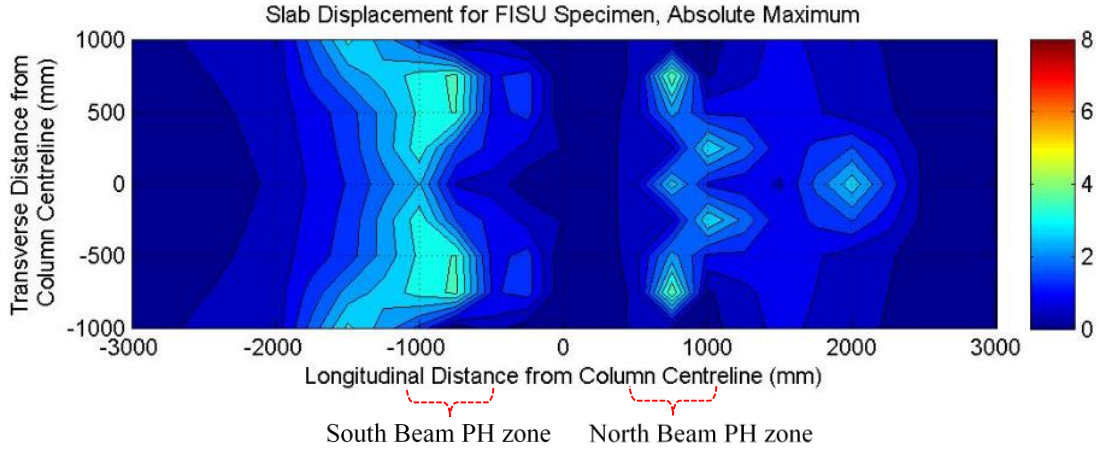

Figure 5.16 – Absolute Maximum Slab Surface Displacements at the end of 5% Lateral Drift : FI-SU Sub-assembly

5.4 Frame Sub-assembly with Shear Key Slab Unit (SK-SU)

In this frame sub-assembly, the composite slab was isolated at the outer column flanges and U-shaped shear key rebars were provided within the column web. The main objective of this test was to improve the shear capacity of the composite slab enclosed between the inner column flanges by providing the U-shaped rebars, which acts as dowels in resisting the shear demand. To quantify the increase in the shear capacity associated with Mechanism-2 (i.e. the bearing of concrete on internal flanges of the column), the load transfer mechanism associated with Mechanism-1 (i.e. the bearing of concrete on column outer flanges) was eliminated by providing isolation using an infill material. Note that in the fully isolated slab frame sub-assembly, both the mechanisms (1 and 2) were deactivated. This conclusion was drawn as the hysteresis behaviour of both FI-SU and BSF frame sub-assembly were very much similar. In addition, to avoid the development of the force transfer Mechanism-3 [14] (i.e. transfer of torsion forces in the secondary beams to the column web), the secondary beams framing into the column web were provided with no shear studs. In this test, the increase in the lateral stiffness and strength of the frame sub-assembly by enhancing the shear capacity of the concrete (in Mechanism-2) as compared to the BSF frame sub-assembly is evaluated.

5.4.1 Hysteresis Behaviour

The hysteresis behaviour of SK-SU frame sub-assembly under quasi-static loading is shown in Figure 5.17. The cyclic behaviour of SK-SU frame sub-assembly was linear up to 1.0% lateral drift (i.e. point 'A' in Figure 5.17a). The initial lateral stiffness of the shear key slab (SK-SU) frame sub-assembly was 15031 kN/m. Due to the composite action of the slab with beam and activation of the Mechanism-2 (i.e. the bearing of concrete on internal flanges of the column) resulted in substantial increase in the initial lateral stiffness of the SK-SU frame sub-assembly. Which was 71% and 144% higher compared to the FI-SU and BSF frame sub-assemblies initial lateral stiffness respectively.

At 1.5% lateral drift (i.e. point 'B' in Figure 5.17a), yielding of the beam was observed and the SK-SU frame sub-assembly achieved its peak strength of 263kN, unlike the FI-SU and BSF frame sub-assemblies which achieved its peak strength at 3.5% lateral drift. This early peak strength of the frame sub-assembly is due to activation of Mechanism-2. It is evident from Figure 5.17 that the strength degradation was also observed in the second cycle of 1.5% lateral drift; this degradation is associated with the shear failure of concrete next to the column flange tips. The provided U-shaped shear key rebars were able to increase the nominal lateral strength

at 1.5% lateral drift, whereas at the higher lateral drift, the shear key rebars were ineffective in providing additional shear resistance. This is due to inadequate anchorage to the shear key rebars. The peak lateral strength of SK-SU frame sub-assembly was 28% higher than the peak strength of BSF frame sub-assemblies, and it confirms that the slab interaction (i.e. activation of the Mechanism-2) with column plays a vital role in increasing the strength and stiffness of the frame sub-assembly.

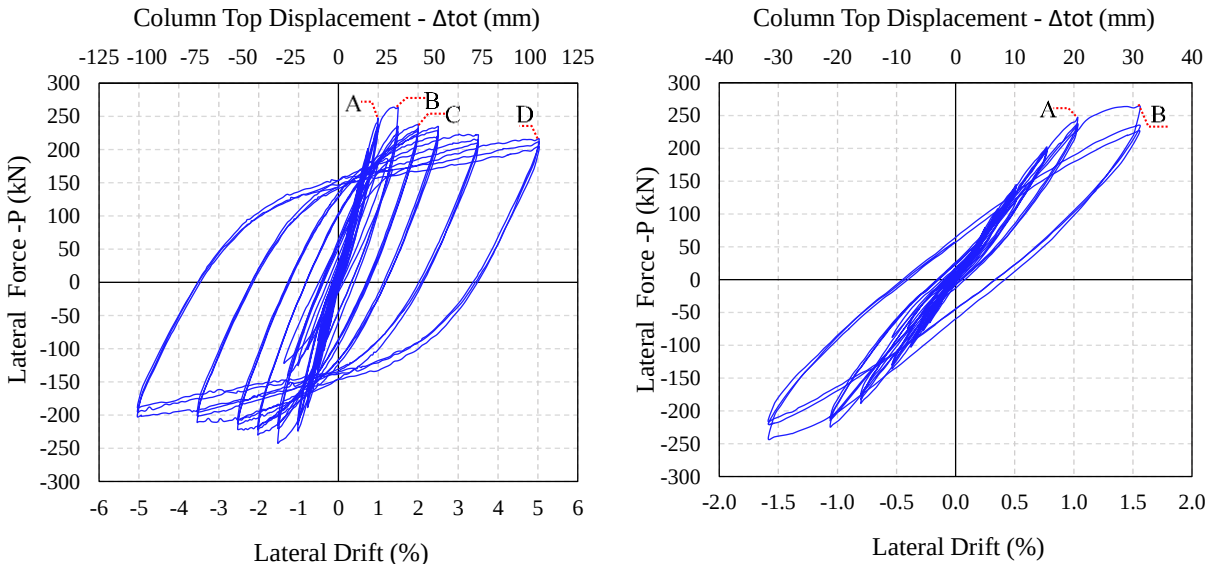

a) Overall Hysteresis Plot **b) Hysteresis Plot up to 1.5% Lateral Drift**

Figure 5.17 –Hysteresis Behaviour of SK-SU Frame Sub-assembly

In the first cycle of 2.0% lateral drift, bottom flanges of the beam started to buckle and the frame sub-assembly experienced 10% strength degradation (i.e. point 'C' in Figure 5.17). The buckling of the top flanges of the beam initiated in the first cycle of 2.5% lateral drift. Substantial buckling of the beam flanges was observed in the first cycle of 3.5% lateral drift. The residual buckling magnitude of the beam top and bottom flanges at the end of 3.5% lateral was between 12 mm and 14 mm, and 33 mm and 35 mm respectively. The less buckling in the beam top flanges was due to the presence of the composite slab, which restrains the lateral torsional buckling and top flange buckling.

The peak lateral force in the first cycle of 5.0% lateral drift was 215.44 kN (i.e. point 'D' in Figure 5.17a), which is around 82% of the frame sub-assembly peak strength (i.e. point 'B' in Figure 5.17a). The strength degradation in the last cycle of 5.0% lateral drift was 22 %, which is lower than the BSF frame sub-assembly's final strength degradation. This less strength degradation is due to the restraint offered by the slab to the beam top flanges.

At the end of the test, the residual buckling magnitude of the beam top and bottom flanges was between 18 mm and 42 mm respectively and is shown in Figure 5.18.

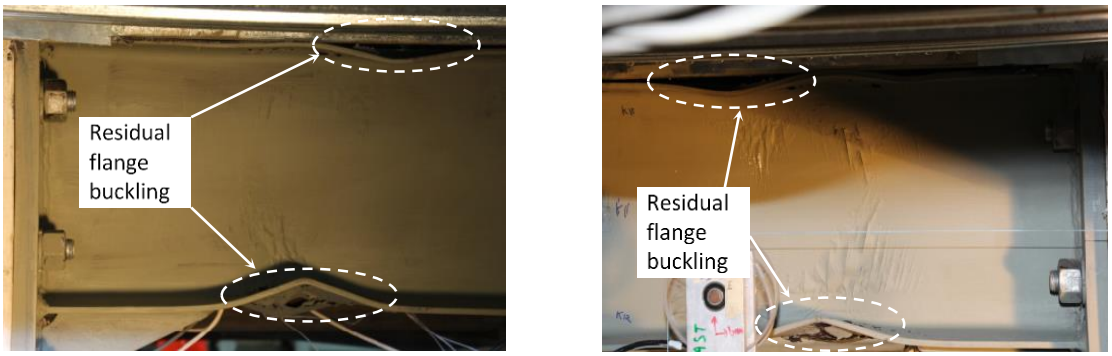

a) Residual Buckling in South Beam **b)) Residual Buckling in North Beam**

Figure 5.18 – Residual Beam Bucking after 5.0% Drift : SK-SU Sub-assembly

5.4.2 Cyclic Behaviour of the End-plate Connection

The end-plate connection behaviour in SK-SU frame sub-assembly was expected to be linear and elastic since the end-plate connection was designed based on the strong column/connection-weak beam philosophy as explained previously in Section 5.2.2. The cyclic moment versus rotation plot of the end-plate connection under quasi-static cyclic loading is shown in Figure 5.19. The maximum end-plate connection rotation for the south and north beam was 0.0007 rad and 0.0006 rad respectively at 3.5% lateral drift. Based on the results plotted in Figure 5.19, it is further verified that the end-plate connection behaviour is linear and elastic. The maximum lift-off for the south and north beam was 0.16 mm and 0.12 mm respectively and the plots for connection lift-off as a function of the time step is provided in Appendix D. As the end-plate connection is rigid, the contribution of this component to the overall lateral displacement is very much limited.

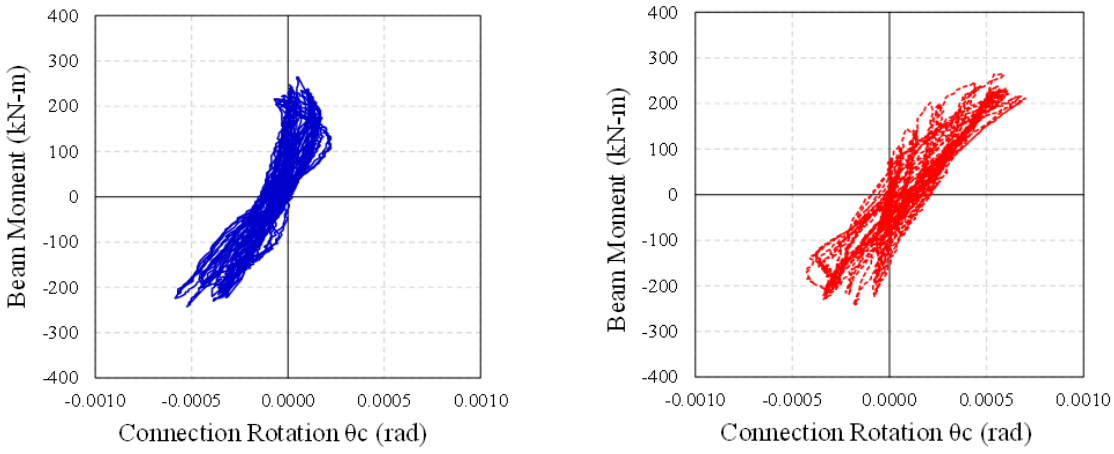

a) South Beam **b) North Beam**

Figure 5.19 – Connection Rotation: SK-SU Sub-assembly

5.4.3 Decomposition of the SK-SU Frame Sub-assembly Overall Lateral Displacement

The overall lateral displacement of the SK-SU frame sub-assembly is due to the deformation of its frame components such as; panel zone shear distortion (Δ_{pz}), end-plate connection rotational deformation (Δ_{conn}), column elastic flexural deformation ($\Delta_{col(el)}$), and beam elastic ($\Delta_{b(el)}$) and inelastic ($\Delta_{b(ph)}$) deformation. As already discussed in Chapter 3, panel zone shear deformation was not measured for SK-SU frame sub-assembly. Therefore, the panel zone shear deformation obtained from the test on full depth slab unit frame sub-assembly (discussed in Section 5.6) is used to evaluate the contribution of panel zone shear deformation to the overall lateral displacement of the SK-SU frame sub-assembly. The plots of the individual frame components deformation to the overall lateral column displacement/drift is shown in Figure 5.20. At 1.0% lateral drift, the cumulative contribution of the panel zone shear deformation, end-plate connection rotational deformation, and the column elastic flexural deformation was 26%, and the beam's elastic flexural deformation contribution was 64% to the overall lateral displacement of the SK-SU frame sub-assembly. At 3.5% lateral drift, the contribution of the panel zone, endplate connection, and the column deformation remains constant, and beam's deformation (elastic and plastic) majorly contributed to the overall deformation of the frame sub-assembly. The contribution of beam's elastic and plastic deformation to the overall deformation of the frame sub-assembly was 15% and 54% respectively. It is clear from the Figure 5.20 that the frame sub-assembly displacement is predominantly due to the elastic and inelastic deformation of the beams. This is expected because the beams were designed to be much weaker than the column.

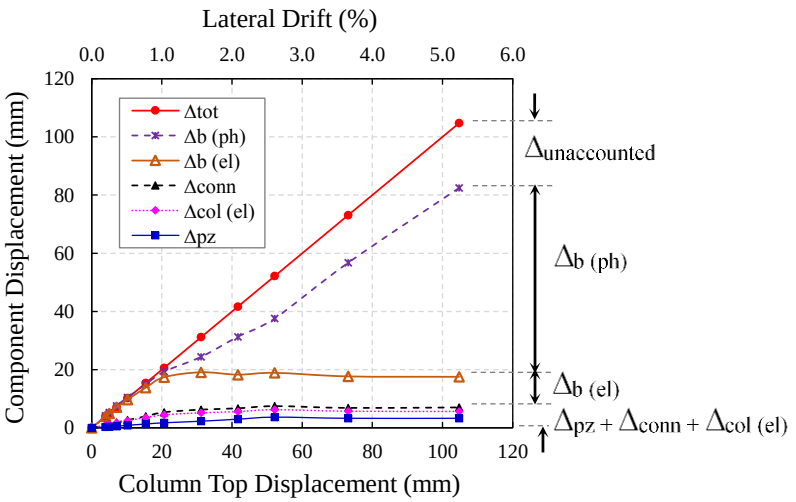

Figure 5.20 – Contribution of Frame Components Deformation to the Overall Lateral Displacement : SK-SU Sub-assembly

5.4.4 Beam Axial Deformation

The cyclic beam axial deformation plots of the north and south beams as a function of lateral drift is shown in Figure 5.21. Also, in the same figure, the maximum residual axial deformation (i.e. beam elongation) is noted. Based on the cyclic beam axial deformation plots shown in Figure 5.21, the maximum average axial deformation of the south and north beams was 1.68 mm, whereas the average residual deformation (i.e. beam elongation) was 0.4 mm at 2.0 % lateral drift (i.e. drift level corresponding to the initiation of beam flange buckling). The residual beam axial deformation/elongation is negligible and is in line with the observations reported in previous sections.

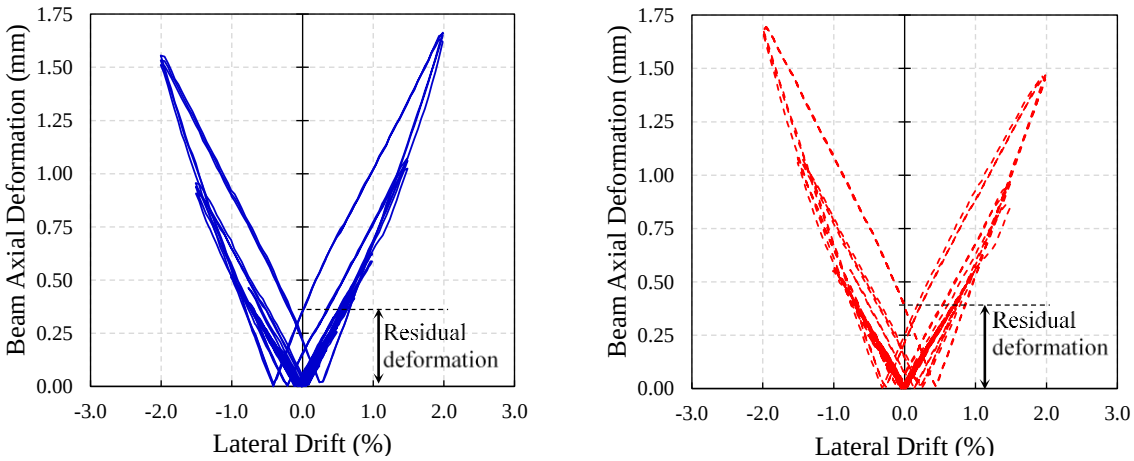

a) South Beam Axial Deformation **b) North Beam Axial Deformation**

Figure 5.21 – Beam Axial Deformation: SK-SU Sub-assembly

5.4.5 Observed Damages in the Shear Key Slab Unit

The deck flutes of the SK-SU frame sub-assembly were oriented parallel to the main beam. Because of the parallel deck orientation, the first longitudinal crack was observed along the main beam in the first cycle of 0.5% lateral drift, which is shown by dashed line in Figure 5.22a. Due to the interaction of the shear key with the column and the shear studs with the concrete, splitting cracks were observed in the slab along the main beam. These splitting cracks were located at the edge of the deck ribs where the slab depth is minimum. Transverse cracks were also observed along the slab width (shown as red dotted lines in Figure 5.22a) in the subsequent cycles of 0.5% lateral drift. The first transverse crack appeared close to the first shear stud from the column, which falls into the plastic hinge zone (located 850 mm from column centre line) as shown in the sectional elevation view of the slab in Figure 5.22a.

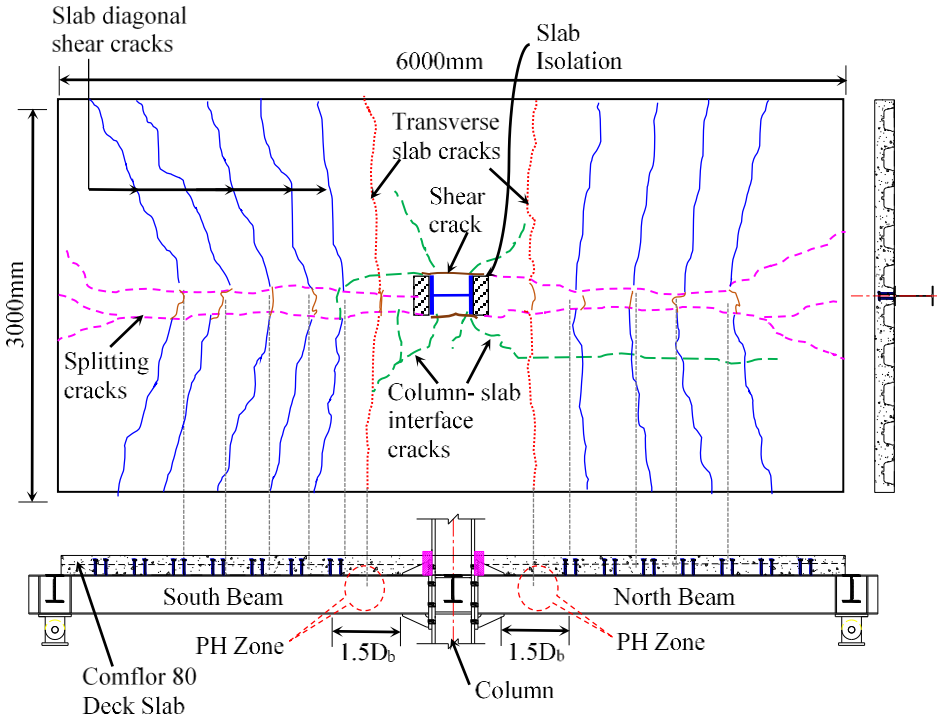

a) Schematic Representation of Observed Cracks in SK-SU Frame Sub-assembly

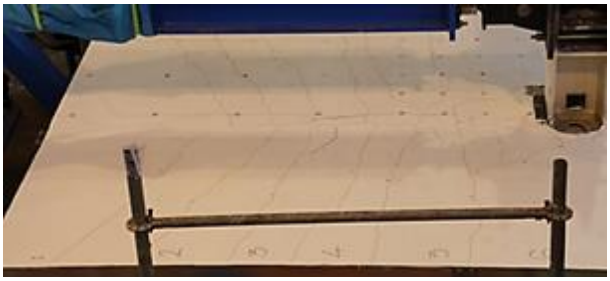

b) Observed Cracks in South Side of the Slab

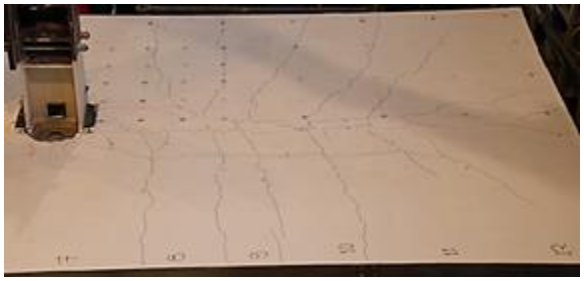

c) Observed Cracks in North Side of the Slab

Figure 5.22 – Observed Crack Pattern in Shear Key Slab Unit.

At 1.0% lateral drift, diagonal cracks (i.e. column-slab interface cracks) were observed at the column flange tips as shown in Figure 5.23a. These cracks were formed due to the stress concentration associated with the force transfer Mechanism-2. Due to the inadequate anchorage of the shear key rebars and lack of confinement within the column web, the concrete above the shear key rebars was delaminated, which is shown in Figure 5.23b. At higher drift levels, additional diagonal shear cracks were observed in the slab along the beam (shown as blue lines in Figure 5.22a). These cracks start from the shear studs and propagate diagonally towards the slab edges. At 3.5% lateral drift, concrete in between the column flanges spalled/crushed, followed by a complete concrete lift-off, thereby exposing the shear key rebars as shown in Figure 5.23c and Figure 5.23d. The width of the transverse and diagonal shear cracks was less than 0.75 mm at 3.5% lateral drift, whereas the width of the splitting crack was about 1.2 mm. The splitting crack width was between 1.3 mm and 1.5 mm at the end of 5% lateral drift. To summarize, the following major cracks were observed in the shear key slab unit (SK-SU) with isolation in front of the column flanges; transverse cracks, diagonal shear cracks, and the splitting cracks. As the slab was isolated, no spalling of the concrete was observed in front of the column flanges. However, the crushing/spalling within the column web was observed due to the slab-column interaction as shown in Figure 5.23e.

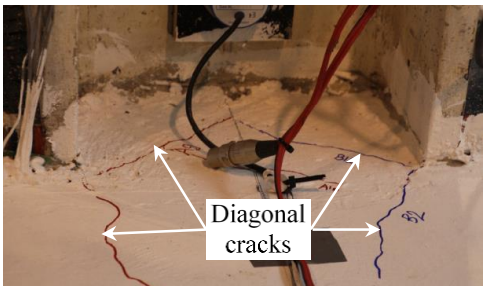

a) Diagonal Crack at 1.0% Drift

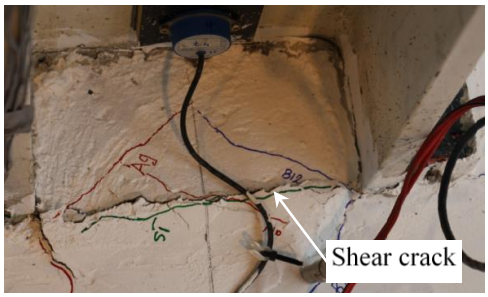

b) Shear Crack at 1.5% Drift

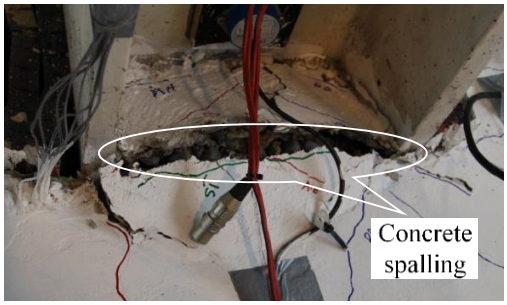

c) Spalling at 3.5% Drift (1st Cycle)

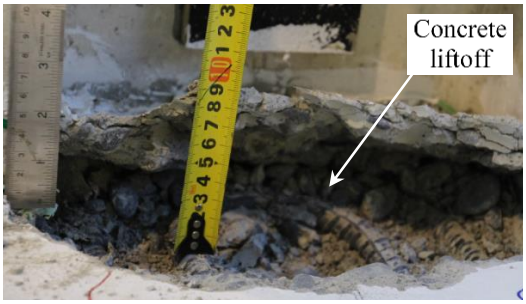

d) Concrete Lift-off after 3.5% Drift

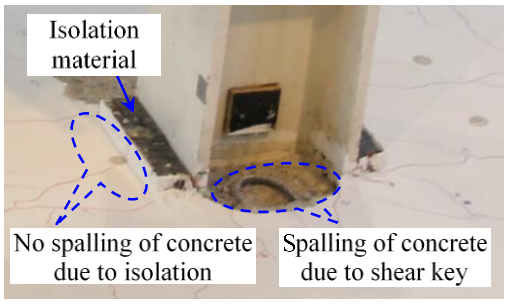

e) Slab Damage around Column

f) Undamaged Concrete below Shearkey

Figure 5.23 – Slab Damage at Column Interaction: SK-SU Test Sub-assembly.

After the completion of the test, the slab next to the beams was saw cut and removed, and a delamination crack between the topping slab and the deck rib was observed. This delamination crack further continued through the column web as shown in Figure 5.24a and Figure 5.24b. The concrete portion (in between the column flanges) below the shear key does not show any crushing/spalling, which is shown in Figure 5.23f. After dismantling of the slab, the concrete around the shear studs was chipped off and it was observed that all the shear studs were intact without any bending deformation as shown in Figure 5.24c.

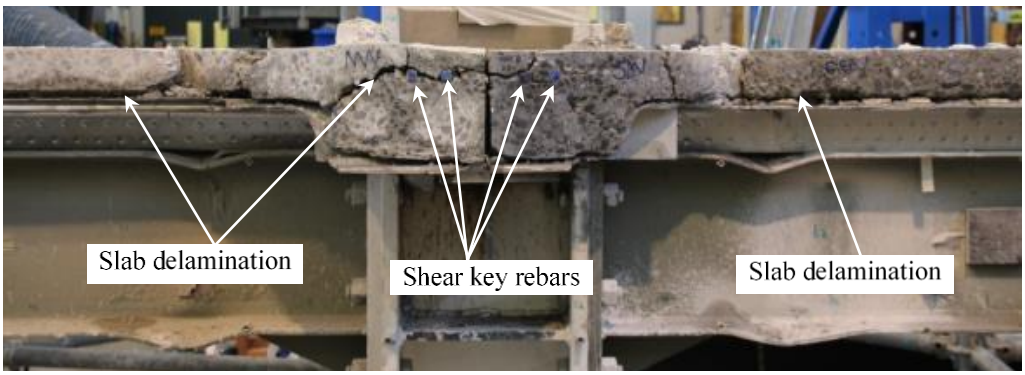

a) Slab Delamination along the Main Beam

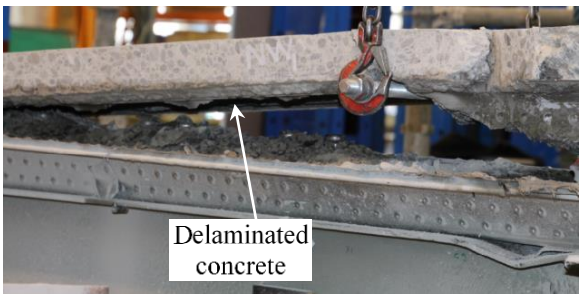

b) Dismantling of Delaminated Portion

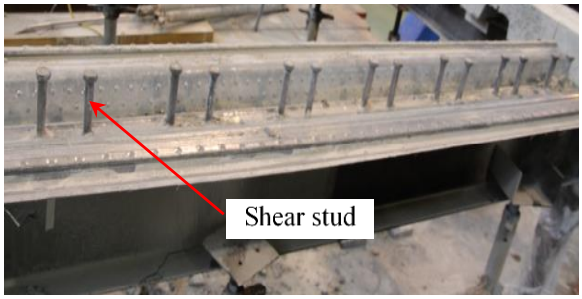

c) Shear Studs Position after Testing

Figure 5.24 – Details of Slab Delamination and Shear Stud: SK-SU Sub-assembly

Spatial Variation of Slab Surface Deformation

The spatial variation of the shear key slab surface deformation was obtained from the potentiometers mounted on the slab in a grid pattern. The absolute maximum spatial surface deformation (i.e. compression/stretch of a particular point on the surface) at the end of 5% lateral drift was approximately 7.0 mm as shown in Figure 5.25, which is higher than the FI-SU absolute maximum spatial slab surface deformation. This increase in deformation was primarily due to the spalling/crushing of the concrete in between the column flanges as the slab interacted with the column internal flanges. The surface deformation plots at 1.0%, 1.5%, 3.5% and 5.0% lateral drifts are reported in Appendix D.

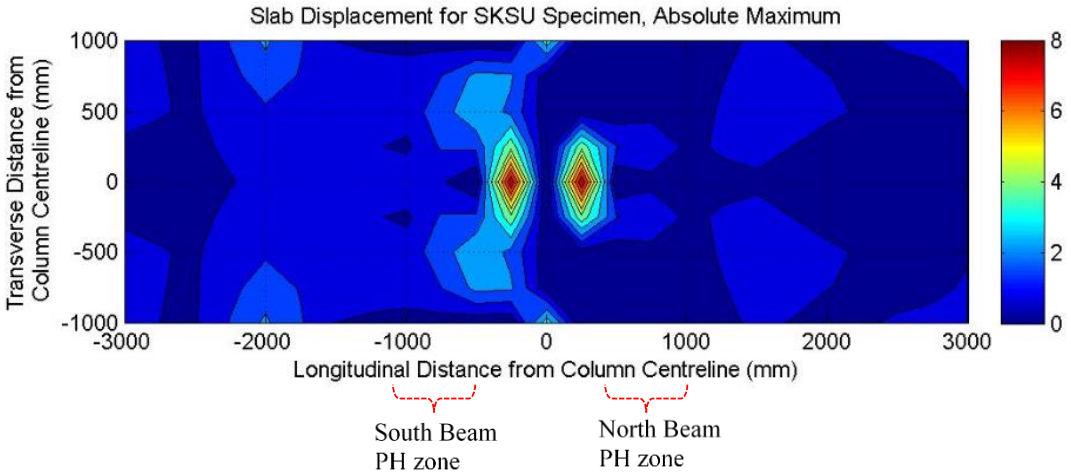

Figure 5.25 – Absolute Maximum Slab Surface Displacements at the end of 5% Drift : SK-SU Sub-assembly

5.5 Frame Sub-assembly with Modified Shear Key Slab Unit (MSK-SU)

As it was found with U-shaped shear key rebars in SK-SU frame sub-assembly the initial stiffness and nominal lateral strength was increased compared to BSF/FI-SU frame sub-assembly, but after 1.5% lateral drift the strength degradation was rapid (which means low ductility compared to BSF/FI-SU frame sub-assembly). The aim of this test is to improve the structural performance of the frame sub-assembly at higher drift levels.

The frame sub-assembly with the modified shear key slab has same test configuration as that of SK-SU frame sub-assembly except the detailing within the column web was modified. Instead of unanchored U-shaped rebars, anchored V-shaped rebars along with the active confinement plate were used in the MSK-SU frame sub-assembly. The V-shaped rebars were anchored to the bolts which were welded to the continuity plate at the bottom of the deck and clamped to the plate at the top of the slab. The presence of top plate within the web provides the confinement to the concrete within the web and the concrete lift-off observed in SK-SU frame sub-assembly can be avoided. Similar to the SK-SU frame sub-assembly, the slab was isolated on outer column flanges by using infill material. The primary objective of this test was to (i) improve the structural performance at higher drift levels, and (ii) delay the shear failure next to the columns flanges associated with force transfer Mechanism-2.

5.5.1 Hysteresis Behaviour

The overall hysteresis behaviour of the modified shear key slab unit (MSK-SU) frame sub-assembly under quasi-static cyclic loading is shown in Figure 5.26a, and the hysteresis behaviour plot up to 1.5% lateral drift for better interpretation of the initial lateral stiffness is shown in Figure 5.26b.

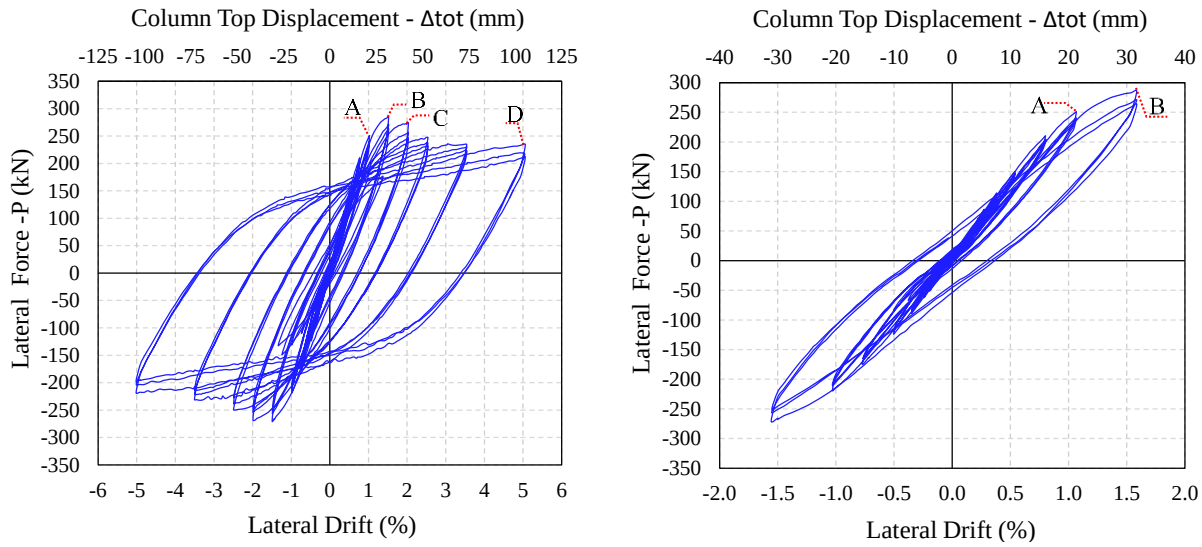

a) Overall Hysteresis Plot **b) Hysteresis Plot up to 1.5% Lateral Drift**

Figure 5.26 –Hysteresis Behaviour of MSK-SU Frame Sub-assembly

The modified shear key slab (MSK-SU) frame sub-assembly has an initial lateral stiffness of 14506 kN/m, and it is 65% and 136% higher compared to the FI-SU and BSF frame sub-assemblies stiffness respectively. The cyclic behaviour of MSK-SU frame sub-assembly was linear up to 1.0% lateral drift (i.e. point 'A' in Figure 5.26a).

The beam yielding was observed in the first cycle of 1.5% lateral drift (i.e. point 'B' in Figure 5.26a) and the lateral load capacity of the MSK-SU frame sub-assembly at this drift was 285.2 kN. Also, the frame sub-assembly achieved its peak strength at this drift, unlike in BSF and FI-SU sub-assemblies, where peak strength was achieved at 3.5% lateral drift. The confinement of the concrete within the column flanges enhanced the slab performance, and the peak strength of MSK-SU sub-assembly was 10% higher compared to the SK-SU frame sub-assembly's peak strength. The MSK-SU frame sub-assembly's peak strength was 38% higher compared to BSF sub-assembly's peak strength, and it confirms that the slab interaction (Mechanism- 2) with the column inner flanges along with the concrete confinement plays a vital role in strength enhancement of the frame sub-assembly. At the second cycle of the 1.5% lateral drift, the MSK-SU frame sub-assembly exhibited 4% strength degradation compared to the peak strength, whereas the SK-SU sub-assembly experienced 10% strength degradation. The less strength degradation is due to the active confinement and proper anchorage of the V-shaped shear key rebars. In the first cycle of the 2.0% lateral drift (i.e. point 'C' in Figure 5.26a), buckling of the beam bottom flanges was observed. The buckling of the beam top flanges initiated in the second cycle of 2.5% lateral drift.

Further buckling of the flanges and the strength degradation was observed in the first cycle of 3.5% lateral drift. The average residual buckling magnitude of the beam top and bottom flanges after the completion of 3.5% lateral drift was 13 mm and 31 mm respectively. The less buckling in the top flanges is due to the presence of the composite slab, which helps in restraining the lateral torsional and flange buckling.

The peak lateral force in the first cycle of 5.0% lateral drift was 234.1 kN (i.e. point 'D' in Figure 5.26a), which is around 82% of the peak strength (i.e. point 'B'), indicating 18% of the strength degradation. The strength degradation in the last cycle of 5.0% lateral drift was 26%, which is 35% less than the BSF frame sub-assembly strength degradation. At the end of the test, the average residual buckling magnitude of the beam top and bottom flanges was 17 mm and 28 mm respectively as shown in Figure 5.27.

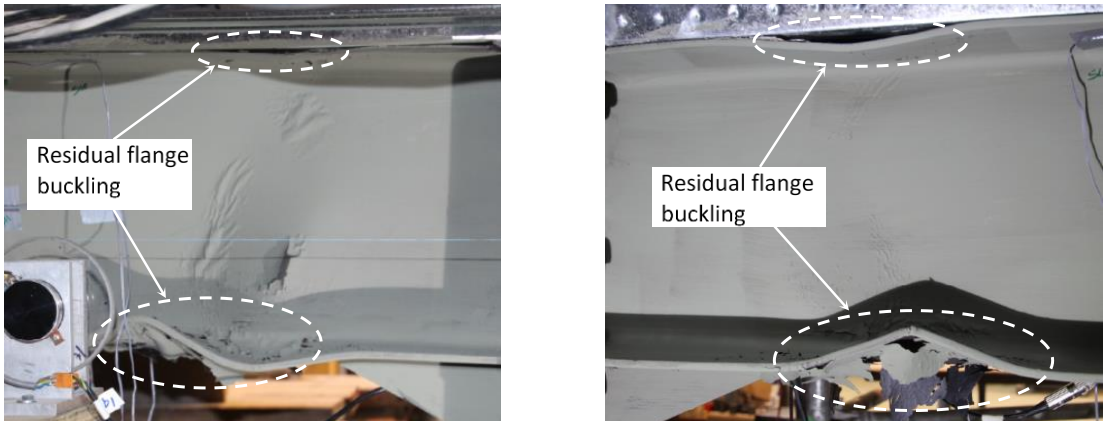

a) Residual Buckling in South Beam **b) Residual Buckling in North Beam**

Figure 5.27 – Residual Beam Bucking after 5.0% Drift : MSK-SU Sub-assembly

5.5.2 Cyclic Behaviour of the End-plate Connection

The end-plate connections of the MSK-SU frame sub-assembly was same as that of the BSF/FI-SU/SK-SU frame sub-assembly and was designed to remain linear and elastic. The cyclic moment versus rotation plot of the end-plate connection as a function of lateral drift is shown in Figure 5.28. The average maximum end-plate connection rotation for the south and north beam was 0.0001 rad at 3.5% lateral drift. Based on the results plotted in Figure 5.28, it is clear that the end-plate connection behaviour is linear and elastic. The average maximum lift-off for the south and north beam was 0.15 mm and the detailed plots for connection lift-off as a function of time step are provided in Appendix D.

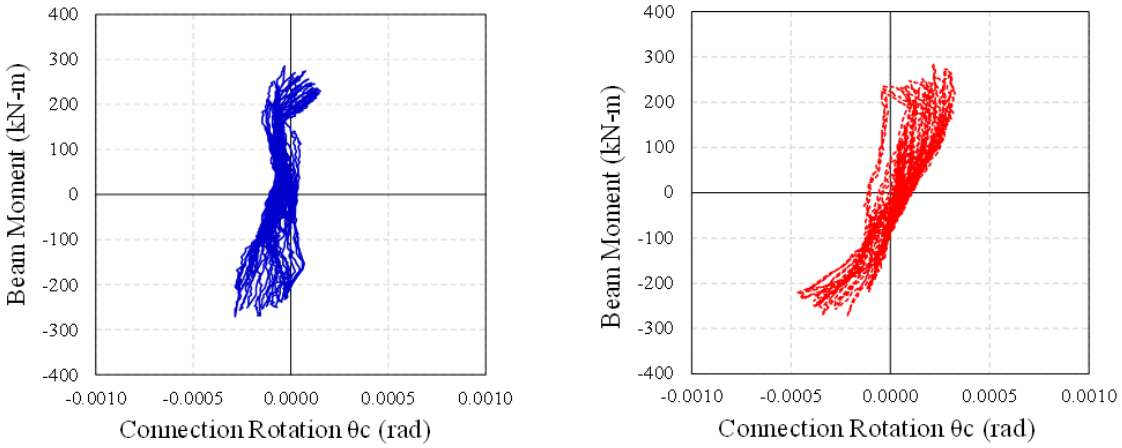

a) South Beam **b) North Beam**

Figure 5.28 – Connection Rotation: MSK-SU Sub-assembly

5.5.3 Decomposition of the MSK-SU Frame Sub-assembly Overall Lateral Displacement

The overall lateral displacement of the MSK-SU frame sub-assembly is due to the deformation of its frame components such as; panel zone shear distortion (Δ_{pz}), end-plate connection rotational deformation (Δ_{conn}), column elastic flexural deformation ($\Delta_{col(el)}$), and beam elastic ($\Delta_{b(el)}$) and inelastic ($\Delta_{b(ph)}$) deformation. As already discussed in Chapter 3, due to the presence of secondary beams, panel zone shear deformation was not measured in MSK-SU frame sub-assembly. Therefore, to calculate the contribution of panel zone shear deformation to the overall lateral displacement of the MSK-SU frame sub-assembly, the panel zone shear deformation obtained from the test on full depth slab frame sub-assembly (FD-SU) is used. The plots of the individual frame components deformation to the overall lateral column displacement/drift is shown in Figure 5.29. At 1.0% lateral drift, the cumulative contribution of the panel zone shear deformation, end-plate connection rotational deformation, and the column elastic flexural deformation was 24%, and the beam's elastic flexural deformation contribution was 63% to the overall lateral displacement of the MSK-SU frame sub-assembly. At 3.5% lateral drift, the contribution of the panel zone, endplate connection, and the column deformation remains the same, and the beam's overall deformation can be further divided into elastic and plastic deformation, which was 15% and 51% respectively to the overall lateral displacement of the frame sub-assembly. It is clear from the Figure 5.29 that the frame sub-assembly's displacement is predominantly due to the elastic and inelastic deformation of the beams.

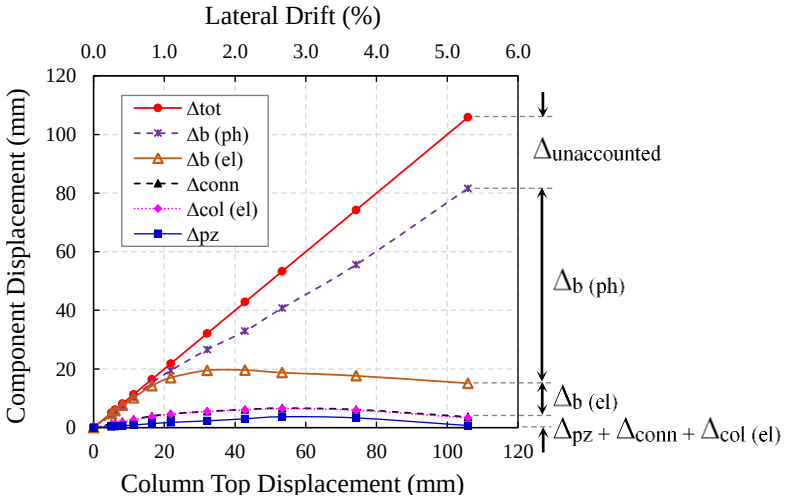

Figure 5.29 – Contribution of Frame Components Deformation to the Overall Lateral Displacement : MSK-SU Sub-assembly

5.5.4 Beam Axial Deformation

The cyclic beam axial deformation plots of the north and south beams along with the maximum residual deformation (i.e. beam elongation) is shown in Figure 5.30. Based on the cyclic beam axial deformation plots shown in Figure 5.30, the average maximum beam axial deformation, and the average residual deformation (i.e. beam elongation) for both the beams (north and south) was 1.60 mm and 0.46 mm respectively in 2.0% lateral drift (i.e. the drift corresponding to the initiation of beam flange buckling). As expected, the residual beam axial deformation/elongation is negligible and can be ignored for practical purpose.

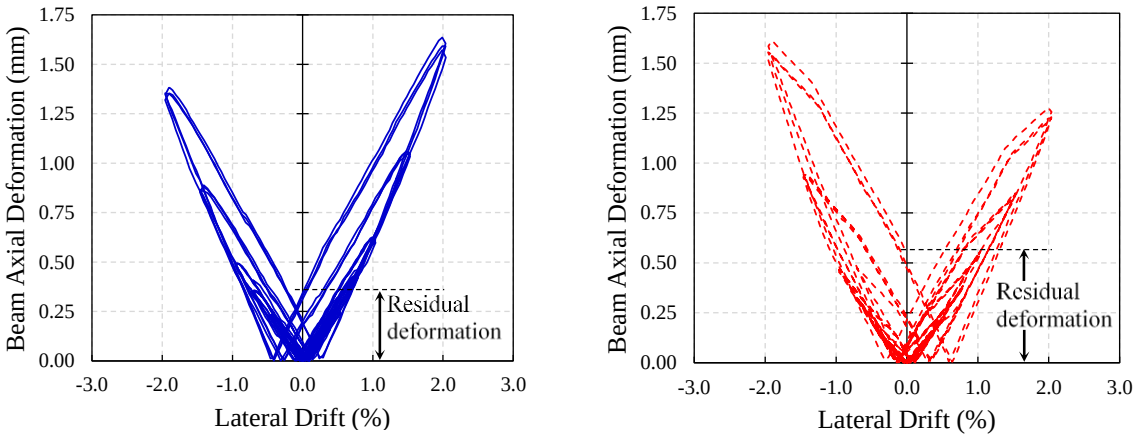

a) South Beam Axial Deformation **b) North Beam Axial Deformation**

Figure 5.30 – Beam Axial Deformation: MSK-SU Sub-assembly

5.5.5 Observed Damages in the Modified Shear Key Slab Unit

The deck flutes orientation of MSK-SU frame sub-assembly is same as that of SK-SU frame sub-assembly; parallel to the main beams. Because of the longitudinal deck orientation, the

first crack on the slab appeared along the main beam in the first cycle of 0.25% lateral drift, shown by dashed line (magenta colour) in Figure 5.31a. Due to the interaction of the V-shaped shear key rebars with the column and activation of the force transfer Mechanism-2, along with the interaction of the shear studs with the concrete, splitting of the concrete along the main beam next to the edges of the deck flute was observed. Transverse cracks were also observed as shown by the red dotted line in Figure 5.31a in the subsequent cycles of 0.25% lateral drift. These cracks start from the first shear stud and propagate diagonally toward slab edges.

In the first cycle of 0.5% lateral drift, diagonal cracks (i.e. column-slab interface cracks) were observed at the column flange tips due to the interaction of slab with the inner column flanges as shown in Figure 5.32a. When the MSK-SU frame sub-assembly reached its peak strength in the first cycle of 1.5% lateral drift, the shear cracks next to the column flange tips was observed as shown in Figure 5.32b; this leads to the strength degradation at higher drift levels. In the subsequent lateral drift cycles, additional diagonal cracks were developed along the slab (blue lines in Figure 5.31a). These cracks start from the shear studs and propagate diagonally towards the slab edges. The width of the shear cracks in front of the confinement plate continued to grow along with the concrete spalling when the sub-assembly reached 2.0% lateral drift and concrete lift-off was noted in front of the confinement plate in 3.5% lateral drift as shown in Figure 5.32c and Figure 5.32d.

The width of transverse and diagonal shear cracks was less than 0.72 mm at 3.5% lateral drift, whereas the width of splitting cracks was about 1.1 mm. The splitting cracks width was between 1.2 mm and 1.5 mm at the end of 5% lateral drift. To summarize, the following major cracks were observed in the modified shear key slab unit (MSK-SU) with isolation in front of the column flanges; transverse cracks, diagonal shear cracks, and the splitting cracks. As the slab was isolated to the outer flanges of the column, no spalling of the concrete was observed, but crushing/spalling of the concrete within the column web has been noted, where the slab is interacting with the column as shown in Figure 5.32e.

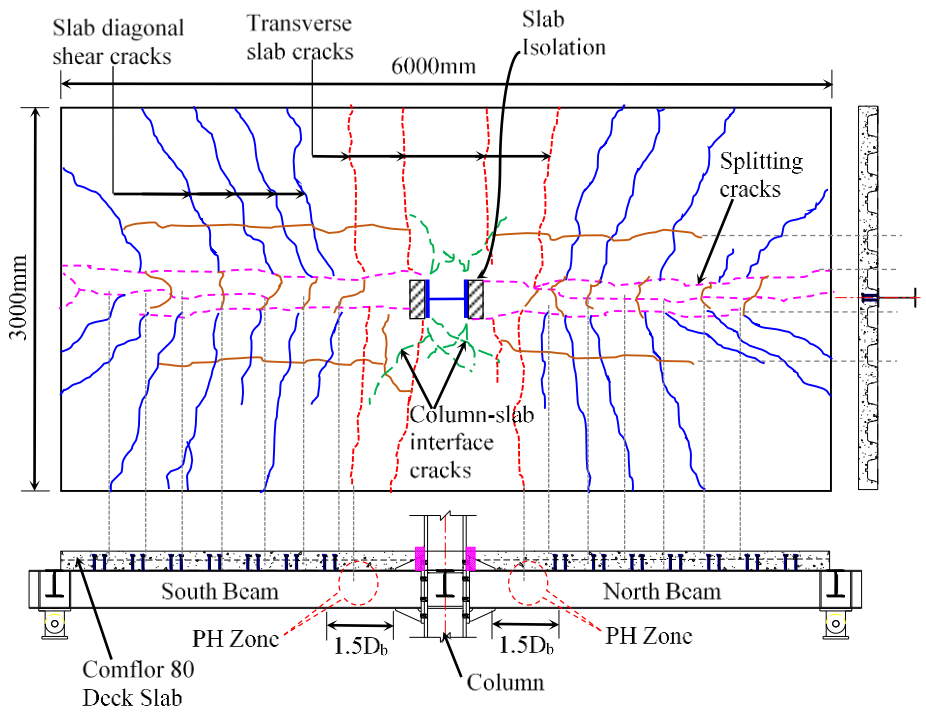

a) Schematic Representation of Observed Cracks in MSK-SU Frame Sub-assembly

b) Observed Cracks in South Side of the Slab

c) Observed Cracks in North Side of the Slab

Figure 5.31 – Observed Crack Pattern in Modified Shear Key Slab Unit

After the completion of the test, the slab next to the beams was saw cut and removed, and a delamination crack between the topping slab and the deck rib was observed. These cracks further extended through the column web, as shown in Figure 5.33a and Figure 5.33b. The concrete portion within the column web does not show any crushing/spalling as shown in Figure 5.33c, due to the active confinement.

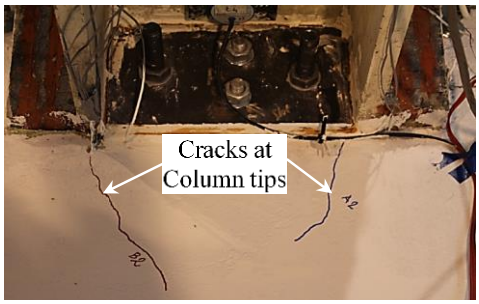

a) **Cracks Column Tips at 0.5% Drift**

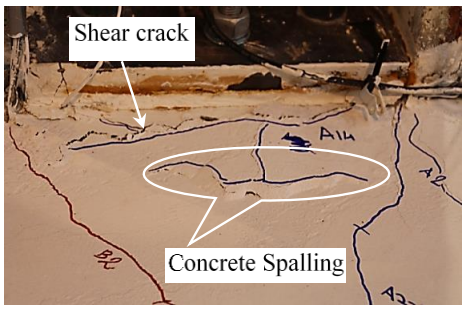

b) **Shear Crack at 1.5% Drift**

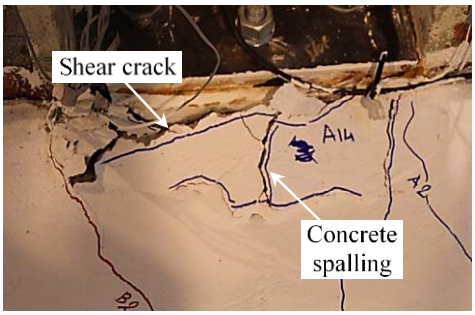

c) **Spalling at 2.0% Drift**

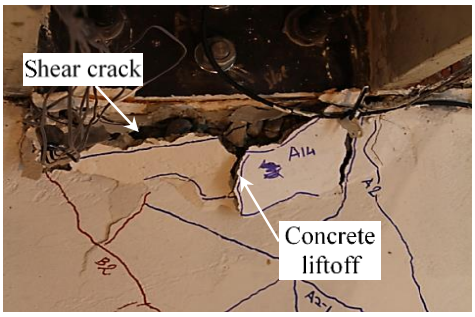

d) **Concrete Lift-off at 3.5% Drift**

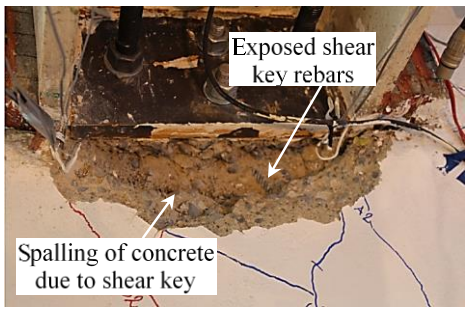

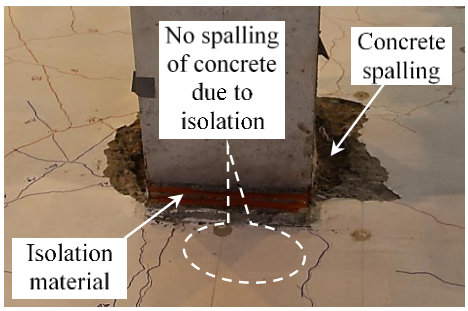

e) **Slab Damage around Column**

Figure 5.32 – Slab Damage at Column Interaction: MSK-SU Test Sub-assembly.

After dismantling of the slab, the concrete around the shear studs was chipped off, and it was observed that all the shear studs were intact without any deformation as shown in Figure 5.33d.

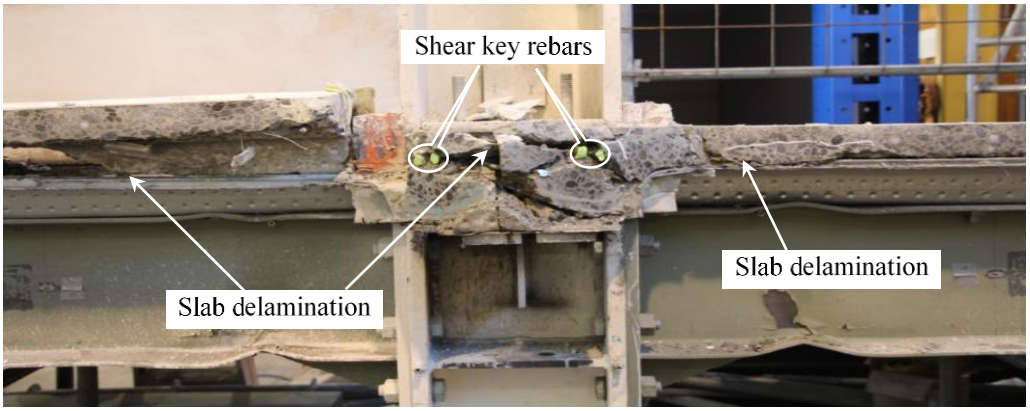

a) **Slab Delamination along the Main Beam**

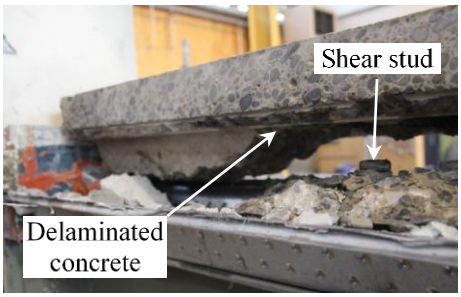

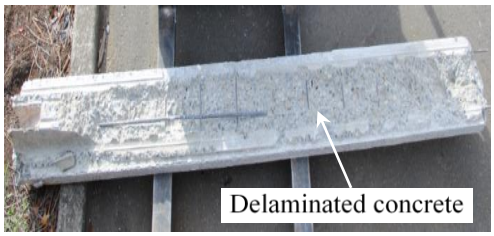

b) Dismantling of Delaminated Portion

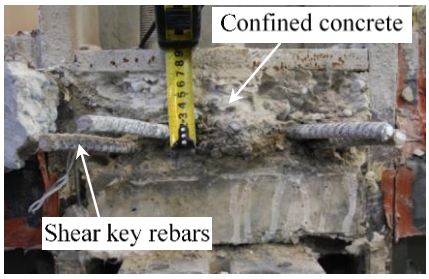

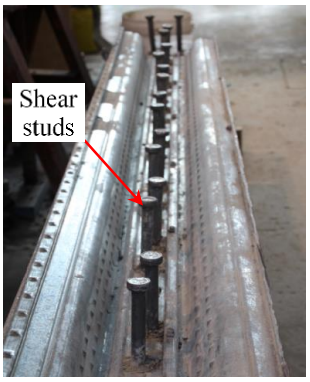

c) Undamaged Concrete below Shearkey **d) Shear Studs Position after Testing**

Figure 5.33 – Details of Slab Delamination and Shear Stud: MSK-SU Sub-assembly

Spatial Variation of Slab Surface Deformation

The spatial variation of the modified shear key slab surface deformation was obtained from the potentiometers mounted on the slab in a grid pattern. The absolute maximum spatial surface deformation (i.e. compression/stretch of a particular point on the surface) at the end of 5% lateral drift was approximately 5.5 mm as shown in Figure 5.34, which is higher than the FI-SU absolute maximum spatial slab surface deformation. This increase in deformation was primarily due to the spalling/crushing of the concrete in between the column flanges as the slab interacted with the column internal flanges. The surface deformation plots at 1.0%, 1.5%, 3.5% and 5.0% lateral drifts are reported in Appendix D.

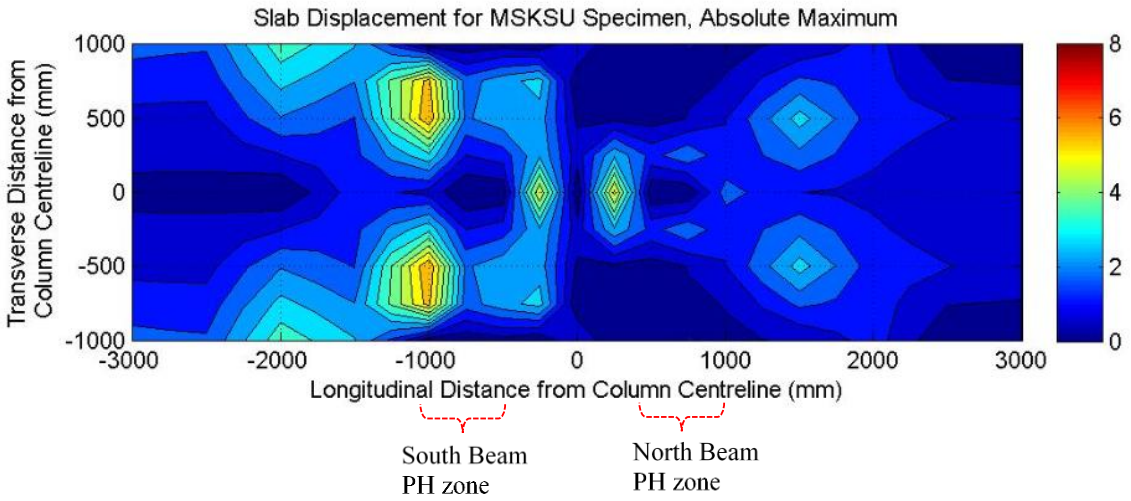

Figure 5.34 – Absolute Maximum Slab Surface Displacements: MSK-SU Test Sub-assembly

5.6 Frame Sub-assembly with Full Depth Slab Unit (FD-SU)

In the conventional composite slab construction, the concrete around the column is not confined. As a result, due to the force transfer Mechanism-1 (i.e. the bearing of concrete on column outer flanges) and Mechanism-2 (i.e. the bearing of concrete on internal flanges of the column), the concrete gets crushed at low drift levels, this was observed by previous researchers in the literature [3]. Also in the conventional composite slab construction, the effective concrete bearing area is less and varies with the deck orientation. Because of the less bearing area, high compressive stresses are induced. In order to improve the overall structural performance of the composite slab; in this test the following modifications were made when compared to the conventional composite slab construction: (i) full depth slab is provided around the column to increase the bearing area, (ii) the concrete within the full depth slab was confined to increase its compressive strength and ductility, and (iii) the detailing within the column web is same as that of MSK-SU frame sub-assembly; anchored V-shaped shear key rebars with top confinement plate. This detailing was adopted because it was proved in the previous test (i.e. MSK-SU) that the strength and ductility are considerably improved when compared to BSF frame sub-assembly. By providing the full depth slab around the column, the same area of the bearing is ensured with any deck orientation (i.e. either longitudinal or transverse). In this test, following important structural performance parameters of the frame sub-assembly with the developed full depth slab configuration are assessed: (i) overall hysteresis behaviour, (ii) damage in the slab around the column, and (iii) slab surface deformation.

5.6.1 Hysteresis Behaviour

The hysteresis behaviour of the frame sub-assembly with the full depth composite slab around the column under the applied quasi-static cyclic loading is shown in Figure 5.35a. The close view of the hysteresis behaviour up to 1.5% lateral drift is shown in Figure 5.35b.

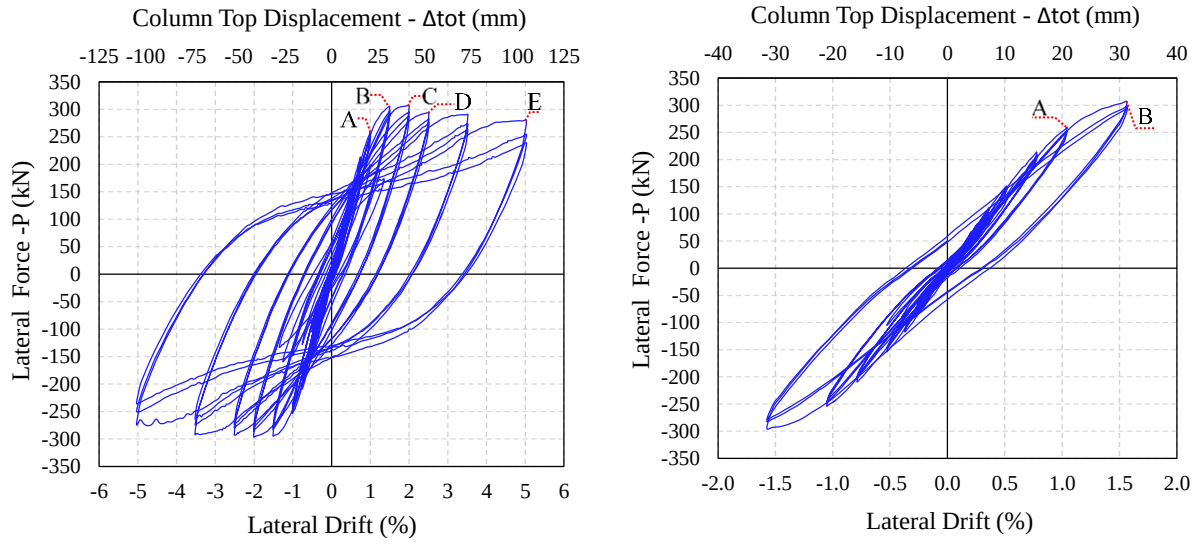

a) Overall Hysteresis Plot **b) Hysteresis Plot up to 1.5% Lateral Drift**

Figure 5.35 –Hysteresis Behaviour of FD-SU Frame Sub-assembly

The initial lateral stiffness of the full depth slab frame sub-assembly (FD-SU) was 16402 kN/m. This is 87% and 166% higher than that of the FI-SU and BSF frame sub-assembly respectively. The beam yielding was initiated in the first cycle of 1.0% lateral drift (i.e. point 'A' in Figure 5.35a). The flacking of the paint was observed in the beam bottom flanges in the plastic hinge zone, which indicates yielding in the beam. The buckling of the beam bottom flanges was observed in the first cycle of 1.5% lateral drift (i.e. point 'B' in Figure 5.35a) and the lateral force was 305.3 kN at this drift. Splitting cracks were formed in the slab centre along the main beams. The FD-SU frame sub-assembly achieved the peak strength of 306.3 kN (i.e. point 'C' in Figure 5.35) in the first cycle of 2.0% lateral drift, unlike the BSF and FI-SU sub-assemblies, where peak strength was achieved at the 3.5% lateral drift. The confinement reinforcement all around the column in full depth slab and additional confinement plates in between the column flanges increased strength and stiffness, and ductility of the FD-SU frame sub-assembly significantly. The peak strength of the FD-SU frame sub-assembly was increased by 7.5% as compared to the MSK-SU sub-assembly. This additional strength increment is predominantly due to the activation of Mechanism-1. The FD-SU sub-assembly strength was 48% higher as compared to BSF sub-assembly's peak strength, and it confirms that the slab-column interaction (i.e. activation of both the Mechanism- 1 & 2) with the column and increased bearing area (due to full depth slab) along with the confinement within the slab plays a vital role in improving the hysteretic behaviour of FD-SU frame sub-assembly.

The buckling of the beam bottom flanges was prominent along with the web buckling, in the subsequent cycles of 2.0% lateral drift and no spalling of the concrete was observed at this drift level. The strength degradation of the frame sub-assembly was observed in the first cycle of 2.5% lateral drift (i.e. point 'D' in Figure 5.35a). The frame sub-assembly exhibited only 3.8% strength degradation at this drift level, which confirms that the state of the concrete (i.e. confined or unconfined) in the interaction zone plays a significant role in sub-assembly's structural performance. The buckling of the beam top flanges was observed in the first cycle of 3.5% lateral drift and frame sub-assembly exhibited less degradation in strength due to full confinement. The residual buckling magnitude of the beam bottom flanges at the end of 3.5% lateral drift was 24 mm, whereas no residual buckling in beam top flanges was observed. The full depth composite slab (i.e. activation of both the force transfer Mechanism - 1 and 2) restrains the lateral torsional and top flange buckling of the beam. The peak force in the first cycle of 5.0% lateral drift was 279.4 kN (i.e. point 'E' in Figure 5.35a), which is around 92% of the peak strength (i.e. point 'C' in Figure 5.35a), which means the sub-assembly experiences 8.0 % strength degradation from 2.0% lateral drift to 5.0% lateral drift. The strength degradation between the last cycle of 5.0% lateral drift was 22.2%, which is less compares to the BSF frame sub-assembly strength degradation. At the end of the test, the residual buckling magnitude of the beam top and bottom flanges was of 2.5 mm and 32 mm respectively as shown in Figure 5.36.

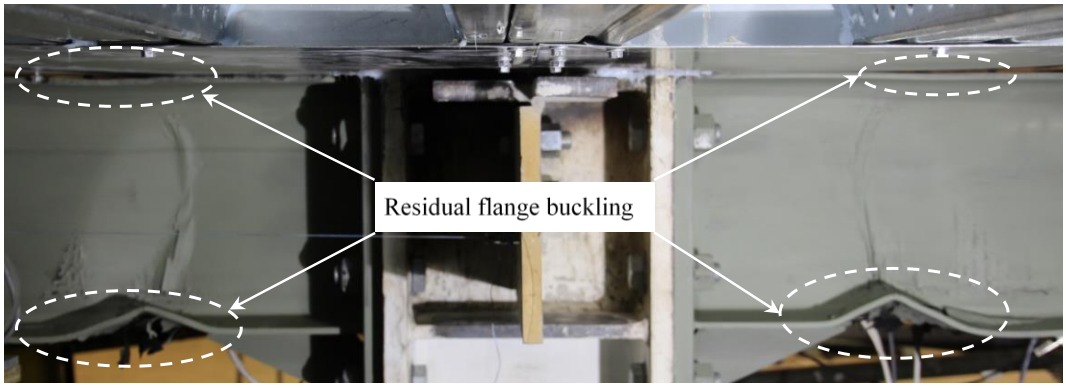

Figure 5.36 – Residual Beam bucking after 5.0% drift : FD-SU Sub-assembly

5.6.2 Cyclic Behaviour of the Panel Zone and End-plate Connection

The beam, column and the end-plate connections of the FD-SU frame sub-assembly were same as that of the BSF frame sub-assembly. As it was already found in the previous sections, the panel zone and the end-plate connection behaviour was linear and elastic, the same is expected in the FD-SU frame sub-assembly test. The cyclic panel zone shear force versus distortion

obtained from the test data is shown in Figure 5.37. The panel zone shear deformation at 2.0% lateral drift (i.e. drift corresponding to peak strength) was 0.00054 rad, which is less than the yield panel zone shear deformation of 0.0022 rad (as explained in Section 5.2). The cyclic moment versus rotation of the end-plate connection under quasi-static cyclic loading is shown in Figure 5.38. The maximum end-plate connection rotation for the south and north beam was 0.0001 rad and 0.0004 rad respectively at 2.5% lateral drift. It is clear that the maximum rotation that the connection experienced is considerably less than the yield rotation of the beam. Based on the results plotted in Figure 5.37 and Figure 5.38, it is further verified that the panel zone and the end-plate connection behaviour is linear and elastic. The average maximum lift-off for the south and north beam was 0.25 mm and the plots for connection lift-off as a function of the time step is provided in Appendix D.

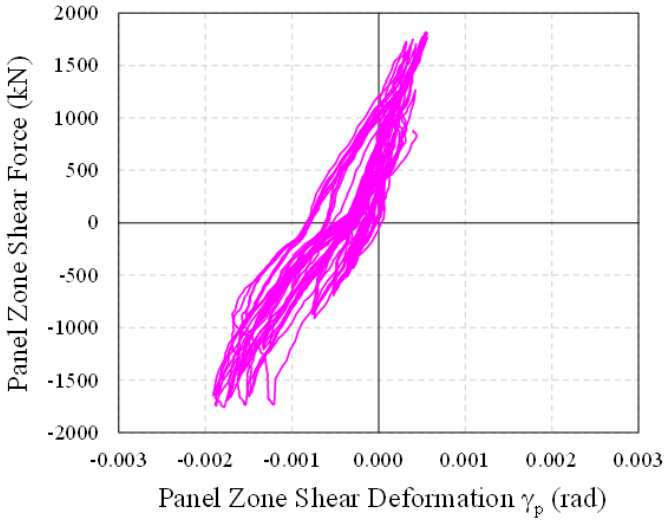

Figure 5.37 – Panel Zone Shear Deformation: FD-SU Sub-assembly

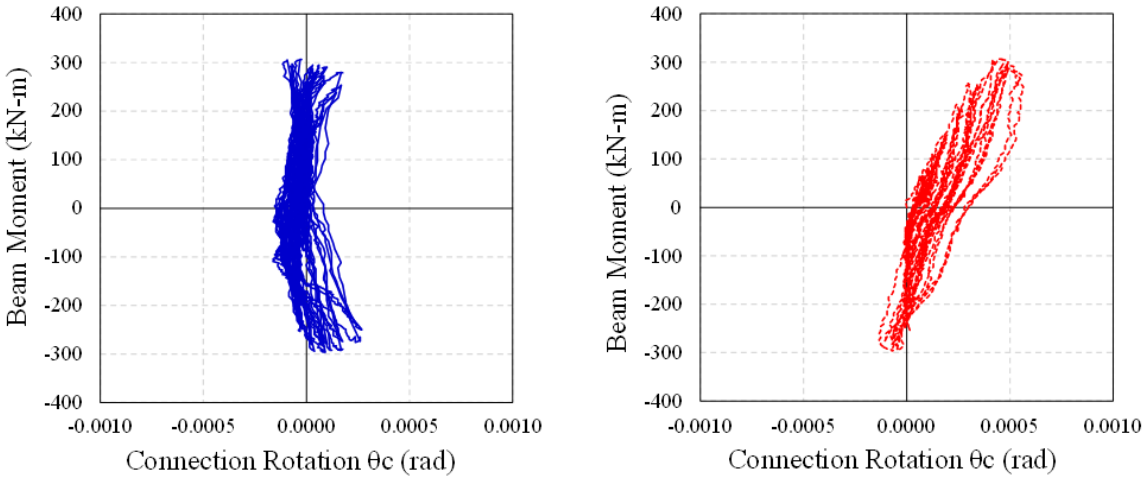

a) South Beam **b) North Beam**

Figure 5.38 – Connection Rotation: FD-SU Sub-assembly

5.6.3 Decomposition of the FD-SU Frame Sub-assembly Overall Lateral Displacement

The overall lateral displacement of the frame sub-assembly with the full depth slab is due to the deformation of its frame components such as; panel zone shear distortion (Δ_{pz}), end-plate connection rotational deformation (Δ_{conn}), column elastic flexural deformation ($\Delta_{col(el)}$), and beam elastic ($\Delta_{b(el)}$) and inelastic ($\Delta_{b(ph)}$) deformation. The plots of the individual frame components deformation to the overall lateral column displacement/drift is shown in Figure 5.39. At 1.0% lateral drift, the cumulative contribution of the panel zone shear deformation, end-plate connection rotational deformation, and the column elastic flexural deformation was 28%, and the beam's elastic flexural deformation contribution was 64% to the overall lateral displacement of the frame sub-assembly with the full depth slab. At 3.5% lateral drift, the contribution of the panel zone, endplate connection, and the column deformation remains more or less same, and the beam's overall deformation can be further divided in to elastic and plastic deformation, which was 19% and 55% respectively to the overall lateral displacement of the frame sub-assembly. It is clear from the Figure 5.39 that the frame sub-assembly displacement is predominantly due to the elastic and inelastic deformation of the beams. This is expected because the beams were designed to be much weaker than the column.

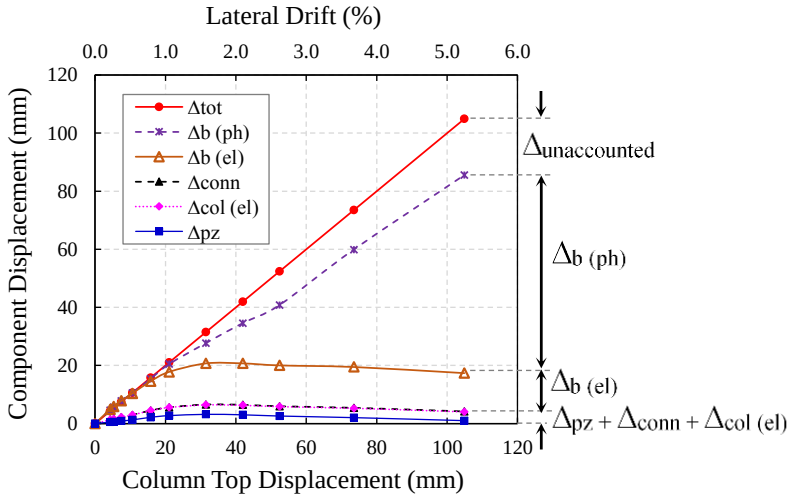

Figure 5.39 – Contribution of Frame Components Deformation to the Overall Lateral Displacement : FD-SU Sub-assembly

5.6.4 Beam Axial Deformation

The cyclic variation of the axial deformation of the beams within the plastic hinge region is depicted in Figure 5.40. Also, in the same figure, the residual axial deformation (i.e. beam elongation) is noted. Based on the cyclic beam axial deformation plots shown in Figure 5.40,

the average maximum beam axial deformation, and the average residual deformation (i.e. beam elongation) for both the beams (north and south) was 2.25 mm and 0.8 mm respectively in 2.0% lateral drift (i.e. the drift corresponding to the initiation of beam flange buckling). As expected, the residual beam axial deformation/elongation is negligible and can be ignored for practical purpose.

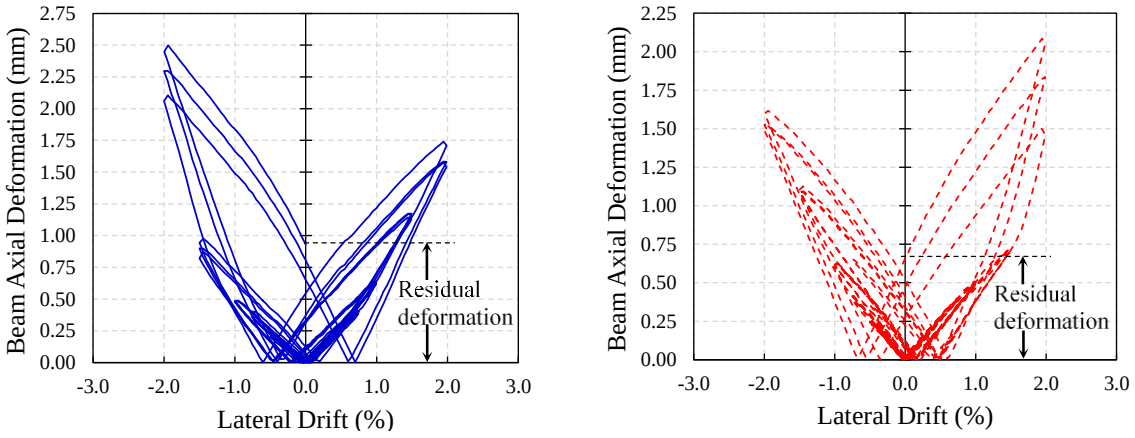

a) South Beam Axial Deformation **b) North Beam Axial Deformation**

Figure 5.40 – Beam Axial Deformation: FD-SU Sub-assembly

5.6.5 Observed Damages in the Full Depth Slab Unit

The FD-SU frame sub-assembly's deck was oriented in the transverse direction (perpendicular to the beam). As the frame sub-assembly subjected to the lateral load, the transverse cracks (tension side) were observed along the slab width at 0.25% lateral drift, shown by red dotted lines in Figure 5.41a. These cracks were observed at the third deck rib from the column centre line (i.e. in the plastic hinge region of the beam). Additional transverse cracks (shown by blue lines) were appeared approximately at the second and third shear studs from the column face in the subsequent lateral drift cycles. These transverse cracks form over the ridges of the profiled decking, which can be identified from sectional elevation view of the slab shown in Figure 5.41a. The actual cracks observed during the test in south and north side of the slab are shown in Figure 5.41b and Figure 5.41c respectively.

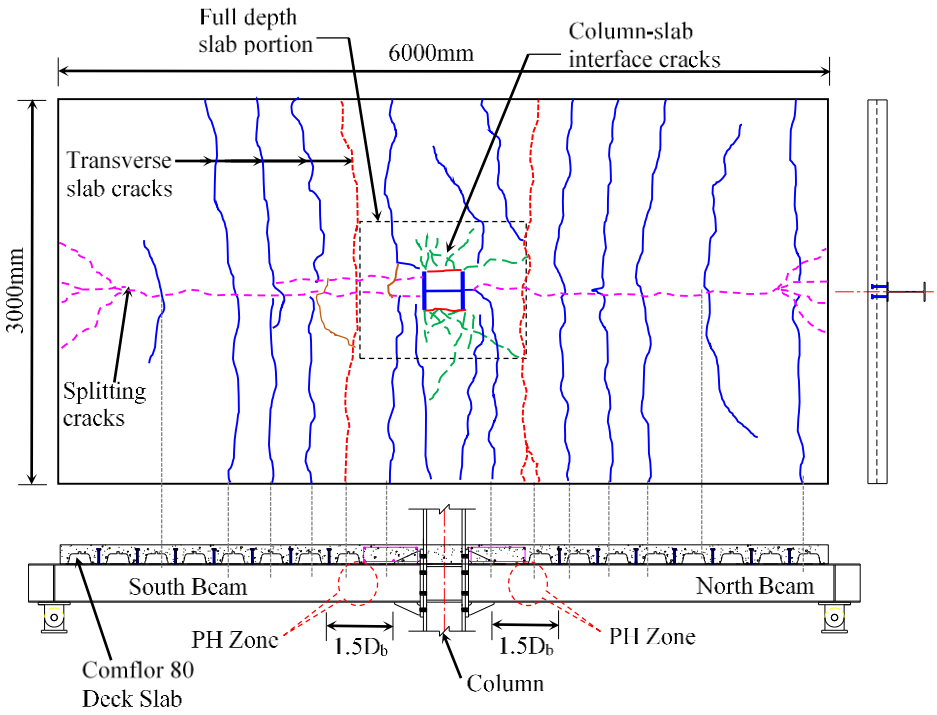

a) Schematic Representation of Observed Cracks in FD-SU Frame Sub-assembly

b) Observed Cracks in South Side of the Slab

c) Observed Cracks in North Side of the Slab

Figure 5.41 – Observed Crack Pattern in Full Depth Slab Unit

In the first cycle of 0.5% lateral drift, diagonal cracks (column-slab interface cracks) were observed at the column flange tips. These cracks are shown in Figure 5.42a. These cracks were further extended along the slab width in the subsequent drift cycles. Splitting cracks initiated in the first cycle of 1.5% lateral drift as shown in Figure 5.42b, and extended along the main beam (shown as dashed lines in magenta colour in Figure 5.41). In the first cycle of 2.0% lateral drift, additional diagonal cracks appeared and the existing diagonal cracks continued to extend along the slab width. No concrete spalling was observed in front of the column flanges up to 3.5% lateral drift, the actual damage state of the slab is shown in Figure 5.42c. It confirms that the full depth slab with confinement reinforcement increases concrete bearing resistance. The crack width of the very first transverse crack (red dotted line) increased to 1.5 mm, in 3.5% lateral drift. The transverse crack width was between 2.0 mm and 2.2 mm in 5% drift lateral cycles.

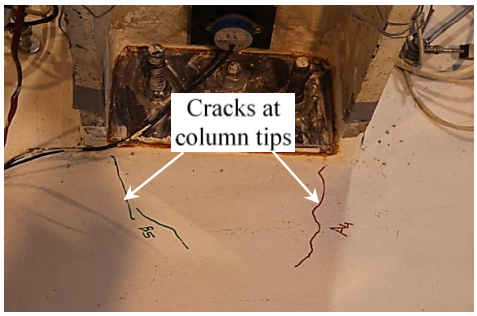

a) **Cracks Column Tips at 0.5% Drift**

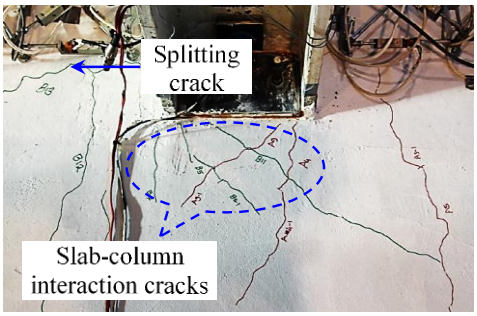

b) **Spliting Crack at 1.5% Drift**

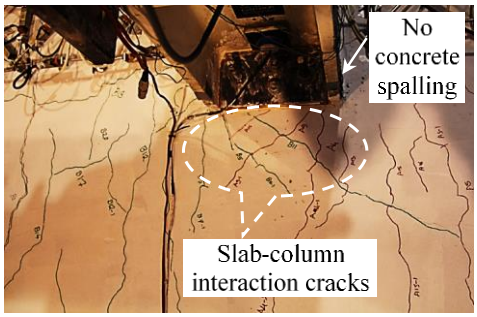

c) **No Concrete Spalling at 3.5% Drift**

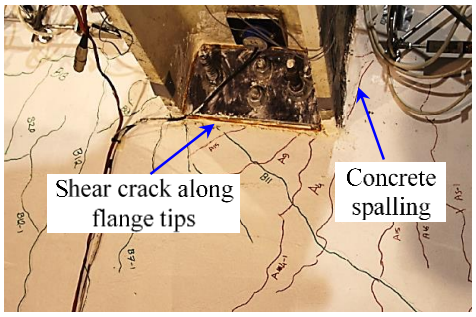

d) **Shear Crack and Concrete Spalling at 5.0% Drift**

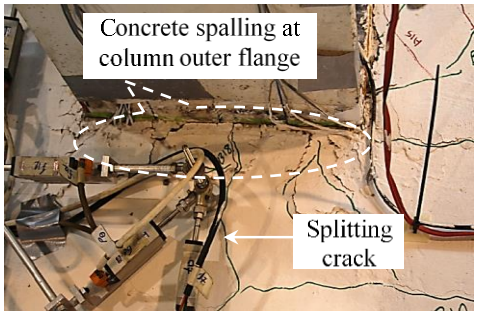

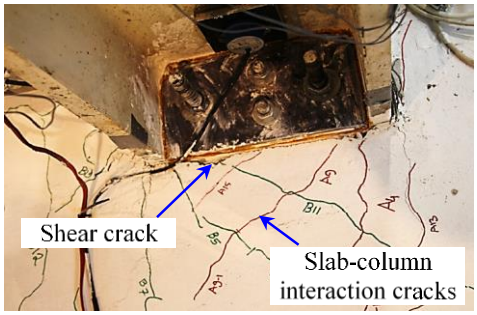

e) **Slab Damage around Column**

Figure 5.42 – Slab Damage at Column Interaction: FD-SU Test Sub-assembly.

A shear crack in front of the confinement plate and next to the column flange tips along with spalling/crushing of the concrete was initiated in the first cycle of 5.0% lateral drift (shown in Figure 5.42d. To summarize, the frame sub-assembly with full depth slab consisted of transverse cracks, diagonal cracks (slab-column interaction cracks), and the splitting cracks. Because of the increased bearing area along with the concrete confinement around the column, the frame sub-assembly was able to sustain its lateral strength and minimal damage was observed around the column at the end of 5% lateral drift as shown in Figure 5.42e.

After completion of the test, the slab was saw cut and removed; it was observed that the concrete in the full depth slab exhibited minimal damage as shown in Figure 5.43a and Figure 5.43d. Upon closer inspection, cracks were noticed along the deck flutes as shown in Figure 5.43b. The concrete in between the column flanges does not show any crushing/spalling due o

the confinement plates as shown in Figure 5.33c. After dismantling of the slab, the concrete around the shear studs was chipped off examine the shear studs, and it was observed that all the shear studs were intact at its original position as shown in Figure 5.43e.

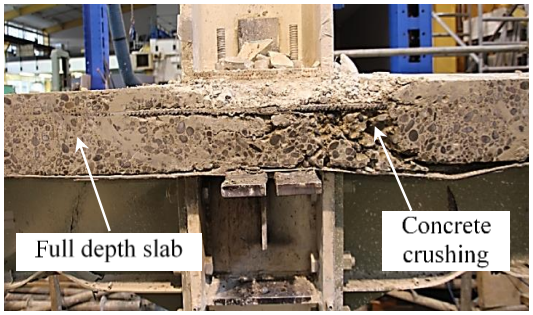

a) Slab interaction with column

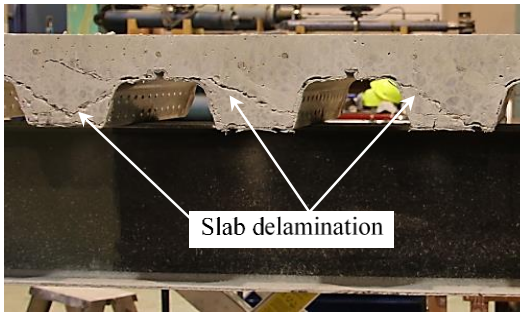

b) Slab delamination along deck flutes

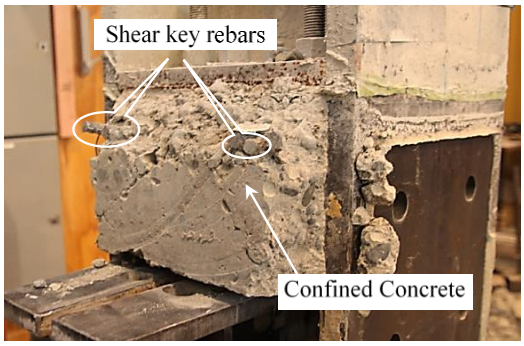

c) Confined concrete in shear key

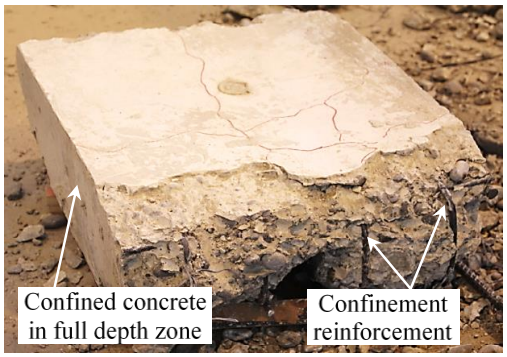

d) Confined concrete in full depth

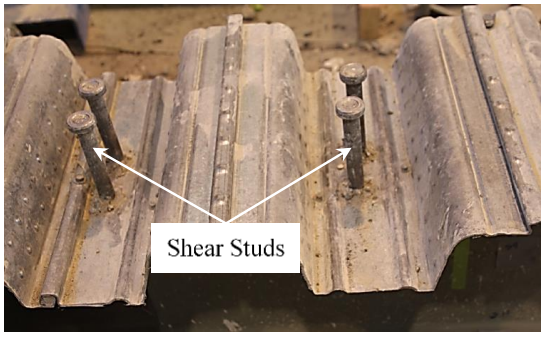

e) Shear studs position after testing

Figure 5.43 – Details of Slab Interaction and Shear Stud: FD-SU Sub-assembly

Spatial Variation of Slab Surface Deformation

The spatial variation of full depth slab surface deformation is computed using the readings from linear potentiometers mounted on the slab in a rectangular grid pattern. The absolute maximum spatial surface deformation (i.e. compression/stretch of a particular point on the surface) at the end of 5% lateral drift is shown in Figure 5.44. This plot can be used to identify maximum stress zones in the slab under a given lateral deformation. It is clear from the figure that the maximum stress zone in the slab was located between 750 mm to 1000 mm from the column

centre line (i.e. the location of the first shear stud). The absolute maximum obtained surface deformation at the end of 5% drift was approximately 6.0 mm, which is higher than the absolute maximum obtained surface deformation in fully isolated slab unit. The surface deformation plots at 1.0%, 1.5%, 3.5% and 5.0% lateral drifts are reported in Appendix D.

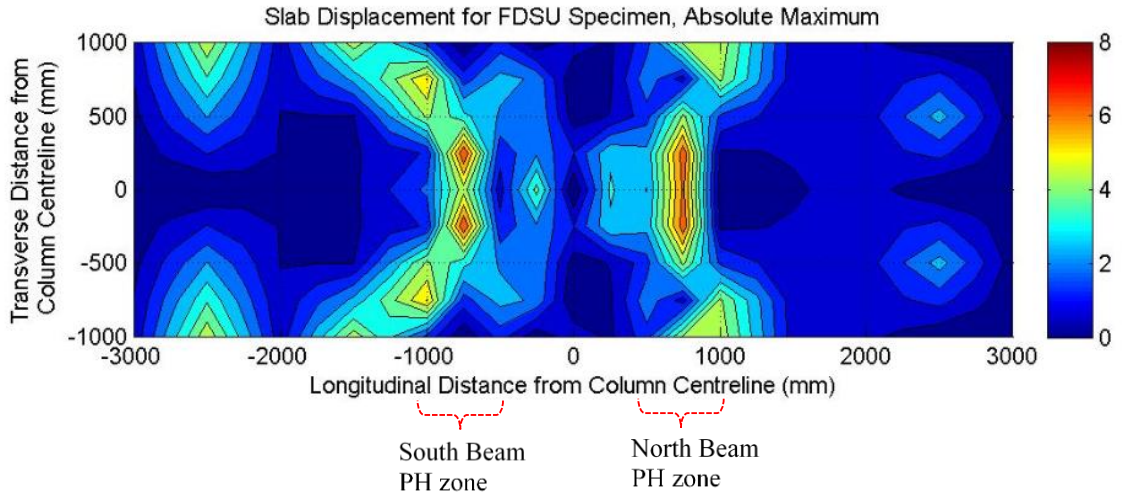

Figure 5.44 – Absolute Maximum Slab Surface Displacements: FD-SU Test Sub-assembly

5.7 Comparison of Structural Performance of Tested Sub-assemblies with different Slab Configurations

5.7.1 Load-Displacement Backbone Envelope

The load-displacement backbone envelope of the tested frame sub-assemblies is obtained by connecting the peak lateral force values at each drift level. Such generated load-displacement backbone envelope of the frame sub-assembly; without slab (BSF), fully isolated slab (FI-SU), shear key slab (SK-SU), modified shear key slab (MSK-SU), and full depth slab (FD-SU) is shown in Figure 5.45a. Also, the performance of the full depth slab (FD-SU) was compared with the conventional transverse deck slab (TD-SU) frame sub-assembly (tested by Hobbs [3]) and shown Figure 5.45b. It can be seen that, the provision of the full depth slab around the column along with confinement reinforcement enhanced the sub-assembly post-peak behaviour. In the full depth slab (FD-SU), the rate of the strength degradation was reduced by 75% (approximately) as compared to the slab with conventional detailing (TD-SU) as shown in Figure 5.45b.

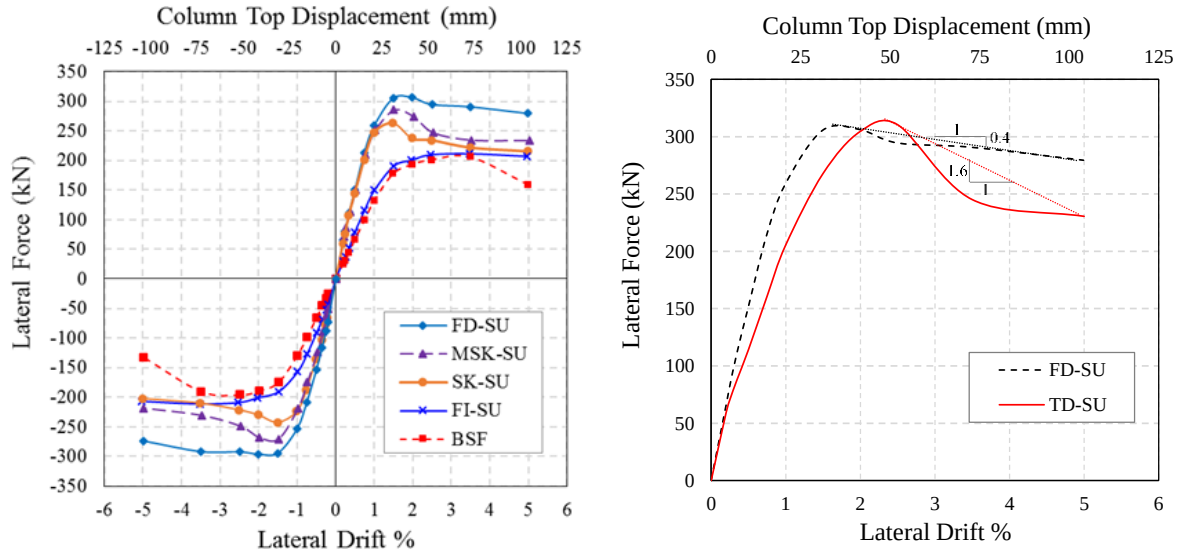

a) Backbone Curves for Different Test Sub-assembly

b) Tested Full Depth vs Conventional Transverse Deck Sub-assembly [3]

Figure 5.45 – Comparison of Backbone Curves for Different Test Sub-assembly.

The summary of initial lateral stiffness and peak strength of the frame sub-assembly with different slab configuration is reported in Table 5.1. Also, the percentage values of strength and stiffness enhancement of the frame sub-assemblies with different slab configuration compared to BSF frame sub-assembly's strength and stiffness is reported in Table 5.1.

Table 5.1: Sub-assembly Initial Stiffness and Peak Strength

Test Specimen	Initial Stiffness (kN/m)	Stiffness Increment (%)	Peak Strength (kN)	Strength Increment (%)
Bare Steel Frame **(BSF)**	6156	Base value	206	Base value
Fully Isolated Slab Unit **(FI-SU)**	8747	43	211.4	3
Shear Key Slab Unit **(SK-SU)**	15031	144	263	28
Modified Shear Key Slab Unit **(MSK-SU)**	14506	136	285.2	38
Full Depth Slab Unit **(FD-SU)**	16402	166	306.3	49

Based on the comparison of the load-displacement plots and values reported in Table 5.1, the following important conclusions with respect to the structural performance of frame sub-assemblies with different slab configurations are arrived:

i) The load-displacement curve of FI-SU frame sub-assembly is similar to that of BSF frame sub-assembly up to 3.5% lateral drift. This is because in FI-SU frame sub-assembly the contribution of the slab to the overall strength and stiffness is negligible. At 5% lateral drift, the reduction in lateral strength of the BSF frame sub-assembly is due to significant buckling of the beam. This was limited in the FI-SU frame sub-assembly because of the slab restraint.

ii) By comparing load-displacement curve of SK-SU and MSK-SU frame sub-assemblies, it is clear that the MSK-SU frame sub-assembly have higher strength and less rate of strength degradation. Also, the final strength of the MSK-SU and SK-SU frame sub-assemblies are about the same as that of FI-SU frame sub-assembly. This is because the resistance offered by the composite slab at higher drift levels is negligible due to the severe slab damage.

iii) When the load-displacement curve of FD-SU frame sub-assembly is compared against the BSF frame sub-assembly's load-displacement curve, it is clear that by appropriately designing/detailing the slab around the column, a significant increase in lateral strength and stiffness can be achieved. More importantly, a similar level of ductility associated with bare steel frame sub-assembly can be attained.

5.7.2 Energy Dissipation and Lateral Stiffness Degradation

In this section, energy dissipation and lateral stiffness degradation characteristics of the tested frame sub-assemblies are presented. The energy dissipated in each cycle was calculated from the hysteresis plot and is further converted to equivalent viscous damping. The lateral secant

stiffness degradation was calculated as the ratio of the average of the peak positive and negative forces to the peak positive and negative displacement of the intended drift cycle. The plots of the energy dissipation, equivalent viscous damping, and the secant stiffness degradation of the tested frame sub-assemblies are shown in Figure 5.46.

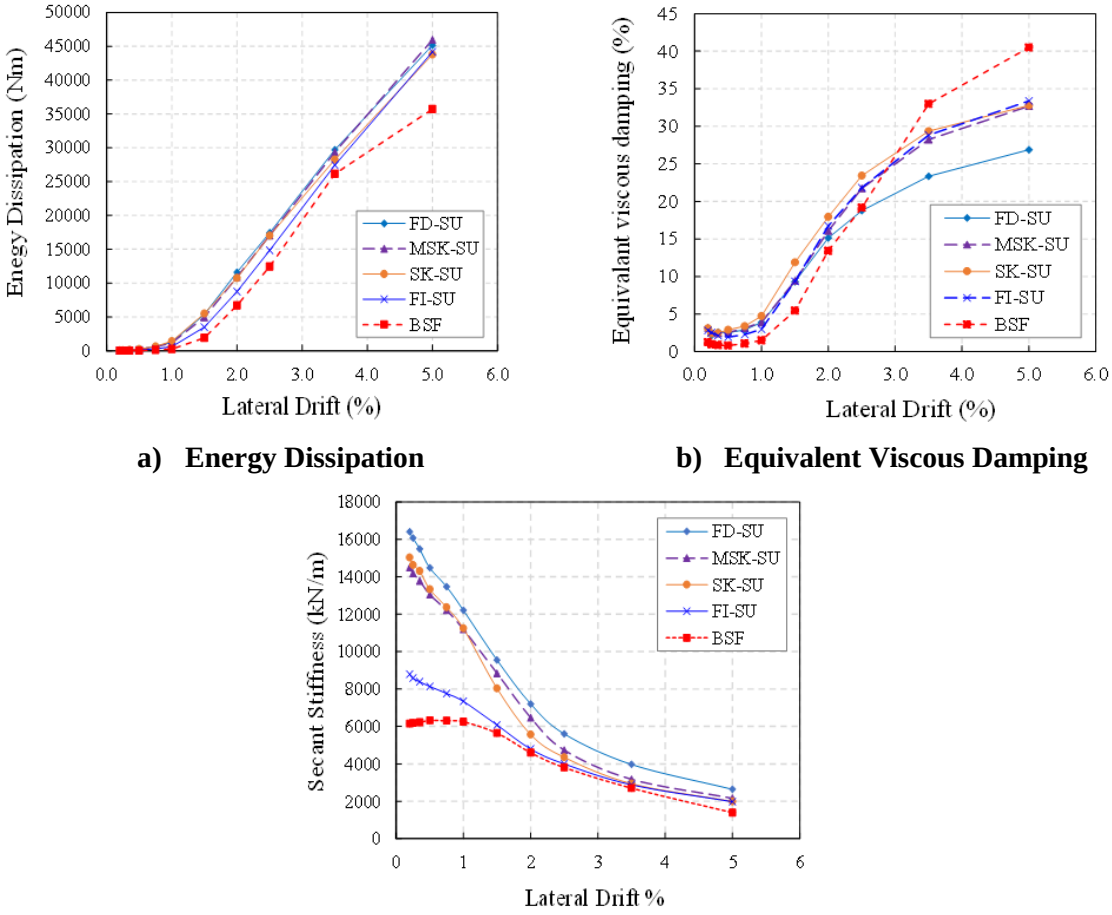

a) Energy Dissipation **b) Equivalent Viscous Damping**

c) Lateral Secant Stiffness

Figure 5.46 – Energy Dissipation, Equivalent Viscous Damping, and Lateral Secant Stiffness Degradation.

The energy dissipation of the tested specimens as a function of lateral drift is shown in Figure 5.46a, and it is clear that all the specimens (except BSF) dissipated the similar amount of energy. However, the bare steel specimen (BSF) dissipated less energy after 3.5% lateral drift cycle. This is because of rapid strength degradation (as shown in Figure 5.1). The primary mode of the energy dissipation was the yielding of the beam in the plastic hinge zones. In case of the frame sub-assemblies with composite deck slab, the energy was dissipated through the opening and closing of the crack in the slab along with the yielding of the beam. The presence of the slab increases the energy dissipation by approximately 24% at 5.0% lateral drift. As shown in Figure 5.46b equivalent viscous damping of the frame sub-assemblies is off similar trend up to 2.5% lateral drift.

In case of bare steel frame (BSF) sub-assembly, the significant increase in damping has been noted after 2.5% lateral drift, due to substantial yielding of the beam and decrease in the strain energy. The full depth slab frame sub-assembly (FD-SU) shows a reduction in damping at larger drift cycles (3.5% and 5.0%), primarily because of high strain energy. The equivalent viscous damping variation of FI-SU, SK-SU, and MSK-SU frame sub-assemblies fall in between the BSF and FD-SU frame sub-assemblies, this because their strain energy lies in between the strain energy of bare steel frame and full depth slab frame sub-assemblies.

The presence of the composite deck slab influences the stiffness degradation of the frame sub-assemblies. The variation of stiffness degradation of frame sub-assemblies is shown in Figure 5.46c. The initial stiffness of the FD-SU is highest (16402 kN/m) due to activation of both force transfer mechanisms-1 and 2, and confinement of the concrete in the slab-column zone. The SK-SU and MSK-SU sub-assemblies initial lateral stiffness was 15031 kN/m and 14506 kN/m respectively, which is slightly less than FD-SU frame sub-assembly's stiffness, this is because of the partial interaction with the column (only force transfer Mechanism-2 was active). The initial stiffness of the fully isolated slab unit (FI-SU) was 40-46% lower as compared to other sub-assemblies stiffness; this is primarily due to the absence of the slab-column interaction. The high rate of stiffness degradation in frame sub-assemblies with composite slab (with active force transfer mechanisms) is due to failure of the slab at low drift levels. Thereafter the rate of the stiffness degradation is of similar magnitude of FI-SU and BSF frame sub-assemblies stiffness degradation.

5.7.3 Observed Damage States of the Tested Sub-assemblies

The summary of observed damage milestone in the beam and the composite slab of the tested frame sub-assemblies is reported in Table 5.2. As the end-plate connection, panel zone and column are designed to remain elastic, no damage was observed in all tests.

Table 5.2: Specimen Description and Damage Mode

Test Specimen	Deck Orientation	Detailing around the Column	Active Force Transfer Mechanism	Observed Damage Mode
Bare Steel Frame **(BSF)**	-	-	-	- Yielding of the beam at 1.5% drift - Beam buckling at 2.5% drift. - Peak strength at 3.5% drift.
Fully Isolated Slab Unit **(FI-SU)**	Transverse Deck	All around isolation from the column	none	- Yielding of the beam at 1.5% drift - Beam buckling at 2.5% drift. - Peak strength at 3.5% drift. - Less buckling in beam top flanges. - Transverse cracks in the slab at deck ribs. - No spalling of concrete around the column.
Shear Key Slab Unit **(SK-SU)**	Longitudinal Deck	Slab isolated on the column outer flange	Mechanism-2	- Shear cracks next to flange tips and spalling of concrete within the column web at 1.5% drift. - Peak strength at 1.5% drift. - Yielding of the beam at 1.5% drift - Beam buckling at 2.0% drift. - Less buckling in beam top flanges. - Splitting and diagonal shear cracks in the slab. - Delamination of the topping slab at the deck ribs level along the main beams.
Modified Shear Key Slab Unit **(MSK-SU)**	Longitudinal Deck	Slab isolated on the column outer flange	Mechanism-2	- Shear cracks in the slab in between the column flanges at 1.5% drift. - Peak strength at 1.5% drift. - Yielding of the beam at 1.5% drift - Beam buckling at 2.0% drift. - Less buckling in beam top flanges. - Spalling of concrete in front of the confinement plate at 3.5% drift. - Splitting and diagonal shear cracks in the slab. - Delamination of the topping slab at the deck rib level along the main beam.
Full Depth Slab Unit **(FD-SU)**	Transverse Deck	Slab casted touching to the column on full depth	Mechanism-1 and Mechanism-2	- Transverse cracks along the deck flutes at 0.5% drift. - Yielding of the beam at 1.0% drift - Beam buckling and splitting cracks in the slab at 1.5% drift - Peak strength at 2.0% drift. - Negligible buckling in beam top flanges. - No spalling of concrete in front of the confinement plate up to 3.5% drift. - Shear cracks in front of the confinement plate and concrete spalling at 5.0% drift. - Delamination of the topping slab at the deck ribs level along the main beams.

5.8 Conclusions

In this chapter, the hysteretic behaviour of the frame sub-assemblies with different composite slab configurations, namely: (i) fully isolated slab unit (FI-SU), (ii) shear key slab unit (SK-SU), (iii) modified shear key unit (MSK-SU), and (iv) full depth slab unit (FD-SU) under quasi-static cyclic loading is reported. Based on the test results and observations, the following conclusions are arrived:

i) All tested frame sub-assemblies exhibited stable hysteresis behaviour primarily due to beam yielding. The lateral secant stiffness, nominal lateral strength, energy dissipation, initiation and rate of strength degradation, and ductility varied from one test to another primarily due to a different level of interaction of the composite slab with the steel beam and column.

ii) The nominal lateral strength of the frame sub-assembly with the isolated slab (i.e. FI-SU) is similar to that of the bare frame sub-assembly (BSF). This is because there is no interaction between the column and the composite slab. The lateral secant stiffness of the FI-SU sub-assembly is slightly more than the BSF sub-assembly due to the composite action of the slab with the beam. Because of the lateral restraint offered by the slab to the beam flanges, the FI-SU sub-assembly exhibited no strength degradation, whereas BSF frame sub-assembly exhibited strength degradation at 3.5% lateral drift due to beam web and flange buckling.

iii) The lateral secant stiffness of the frame sub-assemblies with the shear key slab unit (SK-SU) and modified shear key unit (MSK-SU) are about the same because of the same initial load resisting mechanism. The MSK-SU frame sub-assembly achieved higher lateral strength than SK-SU frame sub-assembly due to the concrete confinement within the column web and anchorage of the V-shaped rebars. When compared to BSF and FI-SU frame sub-assemblies, both SK-SU and MSK-SU frame sub-assemblies exhibited higher lateral strength and stiffness because of the slab interaction with the column.

iv) In both SK-SU and MSK-SU frame sub-assemblies, initiation of the strength degradation is at 1.5% lateral drift. The strength degradation is associated with shearing failure next to the column flange tips and bearing failure of the concrete between the column flanges. Also, because of different level of confinement, the rate of strength degradation is varied in SK-SU and MSK-SU frame sub-assemblies.

In MSK-SU frame sub-assembly the spalling of the concrete around the column is less compared to SK-SU frame sub-assembly, this is because of additional confinement.

v) In case of frame sub-assembly with the full depth slab unit (FD-SU), the initial lateral stiffness and nominal lateral strength are higher compared to the SK-SU and MSK-SU frame sub-assemblies. This is because of activation of two force transfer mechanisms in the frame sub-assembly with the full depth slab unit. Also, the rate of the strength degradation is less compared to SK-SU and MSK-SU frame sub-assemblies strength degradation because of full confinement around the column perimeter. Also, spalling of the cover concrete around the column was delayed up-to 3.5% lateral drift.

vi) As mentioned before, the tested frame sub-assemblies exhibited different levels of energy dissipation because of activation/suppression of different force transfer mechanisms between the slab and the column. The frame sub-assembly with the full depth slab unit exhibited slightly high energy dissipation when compared to other tested frame sub-assemblies.

vii) Beam peak axial deformation and the residual axial deformation (i.e. beam elongation) in the tested frame sub-assemblies with different composite slab configuration was between 1.67 mm and 2.56 mm, and 0.4 mm and 0.9 mm respectively, which is negligible for the practical design consideration.

viii) The crack patterns in the composite slab primarily depends on the deck orientation and number of active force transfer mechanisms between the slab and the column (i.e. whether there is an interaction between the slab and the column or not).

ix) In case of the transverse deck orientation (i.e. deck flutes perpendicular to the main beam), the tensile transverse cracks are observed parallel to the deck flutes, whereas with the longitudinal deck orientation; the splitting cracks parallel to the main beam are observed along with the delamination of the concrete on the deck ribs above the beam.

x) Finally, it can be concluded that hysteretic behaviour of frame sub-assembly with the composite slab depends on the following important design and detailing parameters: (a) level of concrete confinement around the column, (b) level of isolation (i.e. fully isolated around the column, only outer column flanges isolated, and only inner

column flanges)/active force transfer mechanisms (Mechanism-1 and 2), (c) deck tray direction, (d) depth of the confined concrete slab, and (e) percentage of composite action (i.e. number of shear studs per unit length of the beam).

Chapter 6: Numerical and Analytical Investigation of the Tested Frame Sub-assemblies with the Different Slab Configuration

6.1 Introduction

This chapter describes the numerical and analytical models developed for the nonlinear cyclic simulation of the tested frame sub-assemblies with the different slab configurations, i.e. (i) Fully Isolated Slab Unit (FI-SU), (ii) Shear Key Slab Unit (SK-SU), (iii) Modified Shear Key Unit (MSK-SU), and (iv) Full Depth Slab Unit (FD-SU). The numerical simulation of the tested frame sub-assemblies was carried out using two different modelling approaches, i.e. (i) micro modelling, and (ii) macro modelling. A micro-model of the tested frame sub-assemblies was developed using ABAQUS [74] software and validated against the experimental hysteresis plots. The developed micro-model was capable of capturing both local and global responses of the composite slab with the reasonable accuracy. However, it is computationally demanding in terms of modelling and simulation time. Therefore, a simple macro-model (based on the strut-and-tie approach) was developed to simulate the overall structural response using the structural analysis program SAP2000 [75]. In the macro-model, the frame sub-assemblies were modelled as an assembly of elastic line elements connected with the non-linear/linear spring elements. Further, an analytical method to predict the lateral strength and stiffness of the frame sub-assemblies with the different slab configurations was proposed. The developed analytical method considers overall equilibrium of the internal forces at the slab-column interface. Based on the possible modes of failure and strength hierarchy, a methodology to predict the lateral strength of the frame sub-assembly with the tested slab configuration is proposed.

The efficacy of the developed numerical and analytical models is evaluated by comparing the simulated results against the experimental tests results. Also, the reliability of the analytical frame-work is asserted by blind prediction of the lateral strength of two frame sub-assemblies available in the literature [3].

6.2 Finite Element Micro-Modelling

6.2.1 Model Geometry

The 3-D finite element model geometry of the tested frame sub-assemblies was developed using ABAQUS (version 6.11.2) [74] to simulate the behaviour of tested specimens. The geometrical and cross-sectional details of the frame sub-assemblies reported in Chapter 3 were

used to develop the finite element model, and the model was built in the SI units (N and mm). The beam, column, stiffener plates, gusset plates, metal deck, and column continuity plates of the frame sub-assemblies were modelled using four noded shell elements (S4R) [32] as depicted in Figure 6.1. The sectional geometry of the 310UB32 beam and 310UC198 column was modelled at the mid-surface level. Based on the experimental test results of the connection reported in the Section 5.2.2 a rigid connection was modelled between the beam and column. In order to simplify the modelling, the end-plate and bolts were not explicitly modelled. Instead, the column and beam were merged together to resemble the rigid connection.

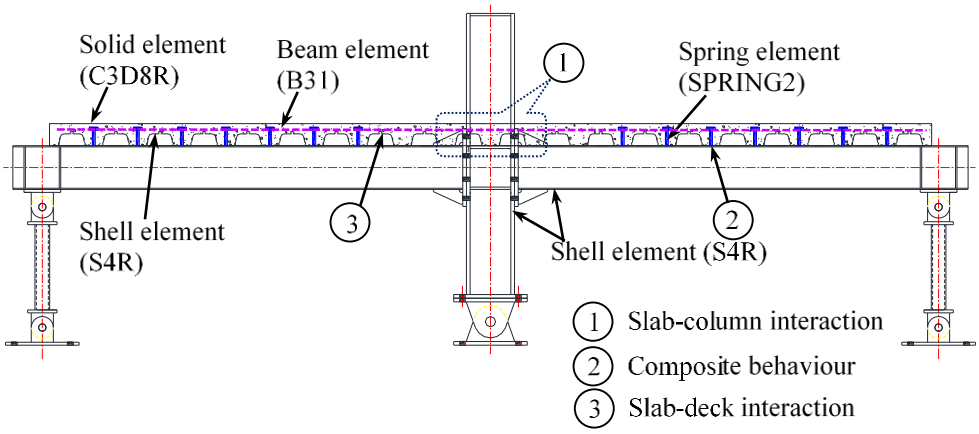

Figure 6.1 - Numerical Model Idealization of Tested Frame Sub-assembly.

The concrete slab was modelled using eight noded solid elements (C3D8R), and the rebars were modelled using the two noded beam elements (B31) as shown in Figure 6.1. The structural behaviour of the tested frame sub-assembly with increasing lateral drift is captured by incorporating three types of the nonlinearities: (i) material nonlinearity, (ii) geometric nonlinearity, and (iii) interface nonlinearity. The material nonlinearity was incorporated by utilising the nonlinear constitutive law at the stress-strain level. The geometric nonlinearities were assigned using 'Nlgom' feature available in ABAQUS software. The interface nonlinearity associated with the contact opening and closing between of the column and the slab was simulated using 'Contact pair' feature. The displacement control loading protocol is applied at the column top to investigate the behaviour of the frame sub-assembly with the increasing lateral drift.

6.2.2 Material Models

Steel

The mechanical properties of the structural steel such as nominal tensile stress (σ_{nom}) and

nominal tensile strain (ε_{nom}) obtained from the tension coupon tests and the details of this tests were reported in the Appendix C. Thus the obtained nominal stress and strain properties were converted into true stress (σ_{true}) and strain (ε^{p}_{true}) using the following equations:

$$\sigma_{true} = \sigma_{nom}\,(1 + \varepsilon_{nom}) \tag{6.1}$$

$$\varepsilon^{p}_{true} = \ln(1 + \varepsilon_{nom}) - \left(\frac{\sigma_{true}}{E}\right) \tag{6.2}$$

The true stress-strain curve developed using the coupon test results and above equations (i.e. Equation 6.1 and 6.2), which was used in the ABAQUS modelling.

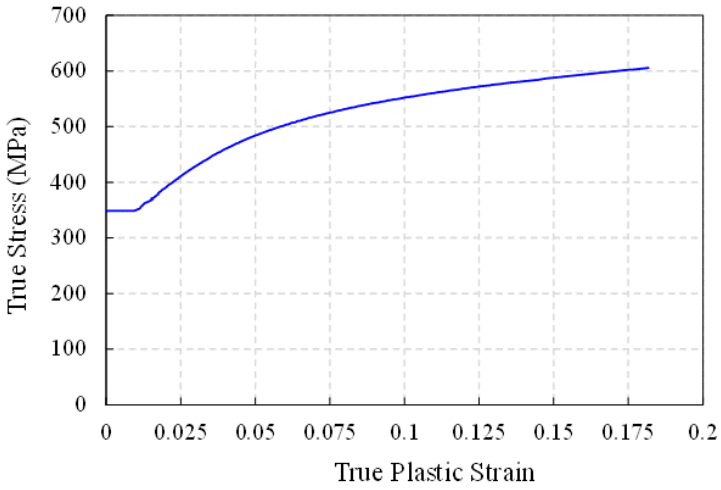

Figure 6.2 - Ture Stress-Strain curve of the Structural Steel.

The hardening of the structural steel under the cyclic loading was due to two distant behaviours; isotropic and kinematic hardening. The isotropic hardening defines the change in yield surface volume in the space, whereas the kinematic hardening postulates that the yield surface translates in space without changing its volume [76, 77]. In ABAQUS software the kinematic hardening component can be specified in three different ways; (i) by utilising 'C' and 'γ' material parameters directly, (ii) by utilising half-cycle test data, (iii) by using the test data from a stabilised cycle. In this study, the kinematic hardening parameters are specified using the half-cycle test data. Whereas, the isotropic hardening parameters are provided using the exponential law available in Simulia [74]. The material parameters required to define the isotropic hardening are; (i) stress at zero plastic strain ('$\sigma|_0$'), (ii) the maximum change in the size of yield surface ('Q_∞'), and (iii) the rate of change of the yield surface with varying plastic strain ('b'). In the absence of the coupon test data under cyclic loading, the material parameter 'Q_∞' and 'b' can be calibrated by using a trial and error method to match the experimental behaviour and these values were taken out to be as 10 σ_y (σ_y = material yield stress obtained

from the monotonic tension coupon test) and 0.26 respectively. The stress at zero plastic strain is considered to be equal to the material yield stress ($\sigma|_0 = \sigma_y$) [78].

The metal deck sheet and the rebars were modelled using an elasto-plastic material with strain hardening. A bilinear stress-strain relationship was assumed to simulate the deck sheet and rebars as shown in Figure 6.3 [79, 80].

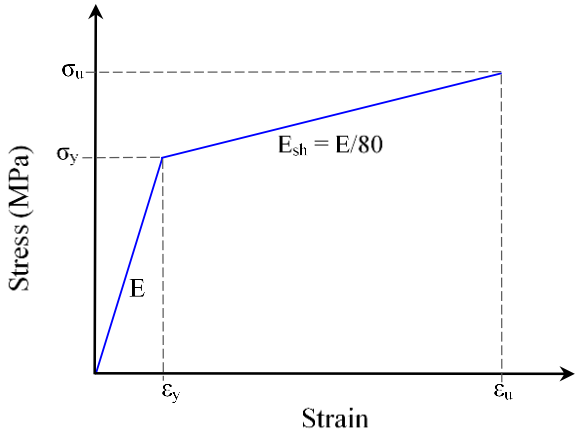

Figure 6.3 - Bilinear Stress-Strain Curve for Rebar and Metal Deck

For the rebar material, the yield stress was based on the minimum values specified in AS/NZS:4671 [81], whereas the yield stress of the metal deck sheet was obtained from the ComFlor80 [4] catalogue. The ultimate strength and strain hardening modulus for the metal deck and rebar was considered equal to 1.28 times yield stress (i.e. $\sigma_u = 1.28\sigma_y$) and 0.0125 times the modulus of elasticity (i.e. $E_{sh} = E/80$) respectively [35, 82]. The summary of the rebars and the metal deck sheet material properties is reported in Table 6.1.

Table 6.1: Material Properties of Rebar and Metal Deck

Description		**Yield Stress** (MPa)	**Ultimate Strength** (MPa)	**Modulus of Elasticity** (MPa)	**Poisson's Ratio**
Rebar	**Grade 300E**	320	409.6	200000 [47]	0.3
	Grade 500E	515	659.2		
Metal Deck Sheet		500	640	205000 [5]	0.3

Concrete

In this study, the concrete was modelled using the concrete damage plasticity (CDP) model, which is capable of simulating the monotonic and the cyclic behaviour of the concrete (along with tension stiffening) [74]. The CDP model was developed based on the two failure mechanisms in concrete which are; (i) crushing of the concrete and (ii) tensile cracking of the

concrete. The CDP model requires the input of uniaxial compression and tension response of the concrete material. It also requires additional parameters required such as; dilation angle (ψ), flow potential eccentricity (ϵ), the ratio of initial biaxial compressive yield stress to initial uniaxial compressive yield stress (f_{b0}/f_{c0}), and the ratio of the second stress invariant on the tensile meridian to the compressive meridian at initial yield (k_c). The above input parameters are obtained from laboratory tests such as; uniaxial compression test, uniaxial tension test, biaxial test, and triaxial test on concrete and these parameters can be determined through the procedure proposed by Jankowiak and Lodygowski [83]. In the absence of the relevant tests to identify these parameters, the values available in the literature [84] were used, and summary of the values are reported in Table 6.2.

Table 6.2: Summary of Material Parameters of CDP model

ψ	ϵ	f_{b0}/f_{c0}	k_c
13°	0.1	1.16	2/3

The uniaxial compression behaviour of the concrete was modelled using concrete material model proposed by Aslani and Jowkarmeimandi [85]. The proposed compression envelope was based on the Carreira and Chu [86] concrete model with the modified exponential values for the ascending and descending branches. The value of the compressive stress is provided as a tabular function of the plastic strain. In the current analysis, the uniaxial compressive stress-strain curve was assumed to be linear up to $0.4f'_c$, and thereafter it can be calculated.

$$f_c = \frac{f'_c\, n \left(\varepsilon_c / \varepsilon'_c\right)}{n - 1 + \left(\frac{\varepsilon_c}{\varepsilon'_c}\right)^n} \tag{6.3}$$

$$n = n_1 = [1.02 - 1.17(E_{sec}/E_c)]^{-0.74}\ if\ \varepsilon_c \leq \varepsilon'_c \tag{6.4}$$

$$n = n_2 = n_1 + (a + 28b)\ if\ \varepsilon_c \geq \varepsilon'_c \tag{6.5}$$

where:

f_c = Compressive stress of concrete
ε_c = Strain of concrete
f'_c = Cylinder compressive strength of concrete
ε'_c = $(f'_c/E_c)(r/r-1)$
a = Constant = $3.5(12.4 - 0.0166f'_c)^{-0.46}$
b = Constant = $0.85\ exp(-911/f'_c)$
r = Constant = $(f'_c/17) + 0.8$

The stress-strain relationship of concrete under tension was assumed to be linear up to the maximum tensile strength of concrete (i.e. $f_{tu} = 0.36\sqrt{f'_c}$) [47], where f_{tu} and f'_c are in MPa. Thereafter the tensile strength decreases (as the concrete soften) as shown in Figure 6.4b. The stress-strain model of concrete under can be constructed by using following equations [85].

$$f_t = E_c\,\varepsilon_t \qquad if\ \varepsilon_t < \varepsilon_{tu} \tag{6.6}$$

$$f_t = f_{tu}\left(\varepsilon_{tu}/\varepsilon_t\right)^{0.85} \qquad if\ \varepsilon_t > \varepsilon_{tu} \tag{6.7}$$

where:

f_t = Tensile stress of concrete
ε_t = Strain of concrete
f_{tu} = Maximum tensile strength of concrete
ε_{tu} = Strain corresponding to maximum tensile strength of concrete

The overall compression and tensile stress-strain envelope curve for the concrete are shown Figure 6.4 below.

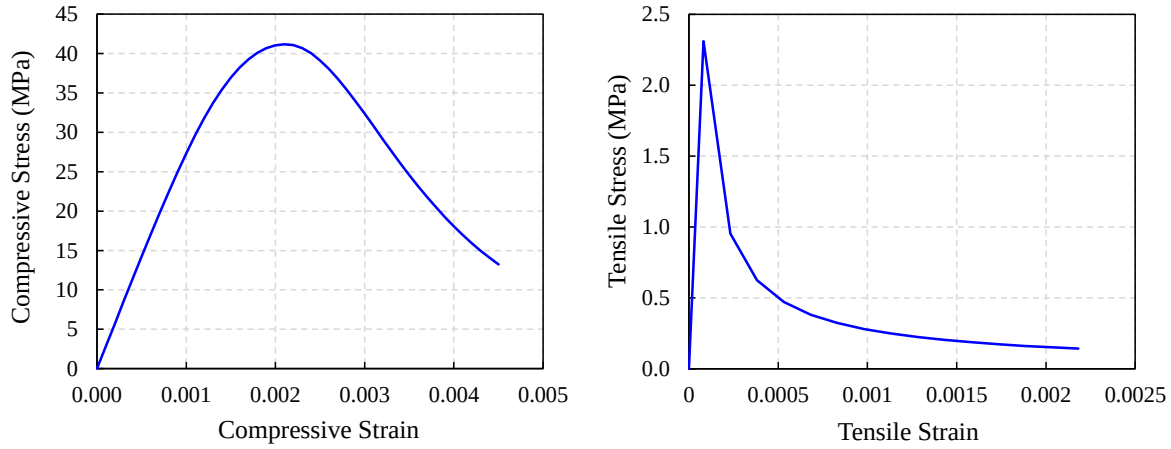

a) Compression Envelope Curve **b) Tension Envelope Curve**

Figure 6.4 - Uniaxial Stress-Strain Curve of Concrete under Compression and Tension Loading.

6.2.3 Load Pattern

The behaviour of the frame sub-assemblies with different slab configurations was thoroughly investigated under the quasi-static cyclic loading in experimental tests. To reduce the modelling and computational efforts in the micro modelling, a monotonic loading was applied instead of the quasi-static cyclic loading (with the loading steps enveloping the cyclic loading). By doing so, it is possible to capture most of the structural performance parameters such as initial lateral stiffness, peak strength, ductility, and the strength degradation.

6.2.4 Boundary Condition

The frame sub-assembly's global coordinate system is shown in Figure 6.5. The X-axis represents the out-of-plane direction of the frame sub-assembly. The Y and Z-axes coincide with the longitudinal axes of column and beam respectively. The actual boundary conditions of the tested frame sub-assembly, the column base was defined as a pin support by restraining

the translation along the X, Y and Z directions (i.e. $U_x = U_y = U_z = 0$) and allowing rotation about the X-axis (i.e. $UR_y = UR_z = 0$). Similarly, to replicate the beam ends support condition to that of the actual test, the translations along the X and Y directions were restrained (i.e. $U_x = U_y = 0$) along with the rotations about the Y and Z-axes (i.e. $UR_y = UR_z = 0$). The translation along the longitudinal direction of the main beam (i.e. Z-axis) and rotation about the X-axis was allowed to resemble the actual movement of the roller supports. The out-of-plane lateral movement at the column top in the X-direction was restrained (i.e. $U_x = 0$). The individual boundary condition was applied to the master nodes, which are located at the centre point of column and beam ends, and each master node was connected using tie constraints to the slave nodes, which are located at the periphery of the sub-assembly ends as shown in Figure 6.5.

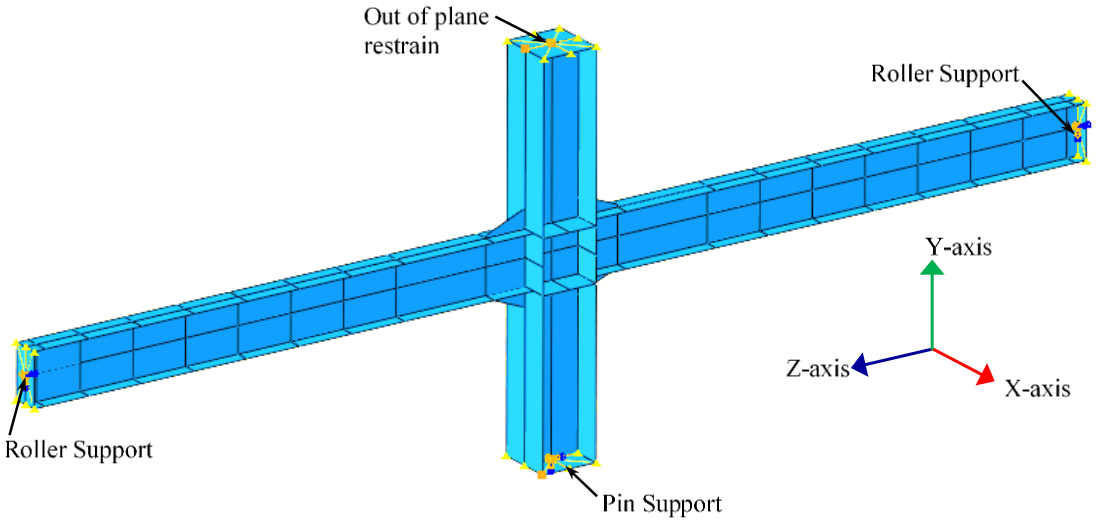

Figure 6.5 - Boundary Condition.

6.2.5 Contact Elements

Slab-Column Interaction

As discussed in the section 4.8 that the strength and stiffness of the composite frame sub-assembly depends not only on the degree of composite action between the studs and the beams but also depends on the interaction of the force transfer mechanisms like Mechanism-1 (i.e. bearing on the column outer flanges) and Mechanism-2 (i.e. bearing on the column inner flanges). To simulate this interaction between the column and the slab, contact surfaces were assigned to the column flanges, web, end-plate, gusset plates, and relevant surfaces of the slab. A surface-to-surface contact feature available in the ABAQUS was used to define the contact interaction between the column and the concrete slab. The desired interaction was achieved by providing a 'Hard' contact in the normal direction (to avoid the penetration into each other)

and ‘Friction with penalty behaviour’ in the tangential direction (with a coefficient of friction of 0.2) [15, 87]. Note that the separation between the hard contacts was allowed under a given load. The contact surfaces of the column and gussets were modelled as master surface, and the corresponding concrete slab surfaces were assigned as slave surfaces.

Slab-Beam Interaction

In composite deck slabs, the shear studs are provided to transfer the longitudinal shear between the steel beam and deck slab as well as to limit the deck slip. Dowel action is the primary force transfer mechanism when the shear studs are subjected to the induced slip at the interface of the steel and concrete element [2]. In the finite element modelling, the composite behaviour between the steel beam and composite slab can be simulated by (i) modelling the shear stud as a 3D solid element or beam element, and embedded into the concrete slab, or by (ii) using special elements like connectors / springs. The modelling of the shear studs as a 3D-solid element or beam element leads to increased computation time as well as difficulties in convergence [88], whereas employment of the spring elements (to simulate the composite action through the shear studs) is simple to use and computationally more effective [82, 87, 88]. The non-linear shear springs were provided at each stud location to represent the stud behaviour in both horizontal and vertical directions.

The beam and the metal deck were modelled with a small gap in between the beam top flange and the deck sheet in order to assign the shear spring. To assign the nonlinear shear spring, nodes were created on the beam flange at the actual locations of the shear studs and connected to the corresponding nodes on the deck sheet as shown in Figure 6.6c. As discussed in the Section 6.2.1, the beam flanges and deck sheet were modelled using shell elements with the middle surface as a reference plane. The gap between the beam top flange and the concrete slab is assumed to be equivalent to the summation of one-half of the thickness of the beam top flange and one-half of the thickness of the metal deck sheet [89] as shown in Figure 6.6b.

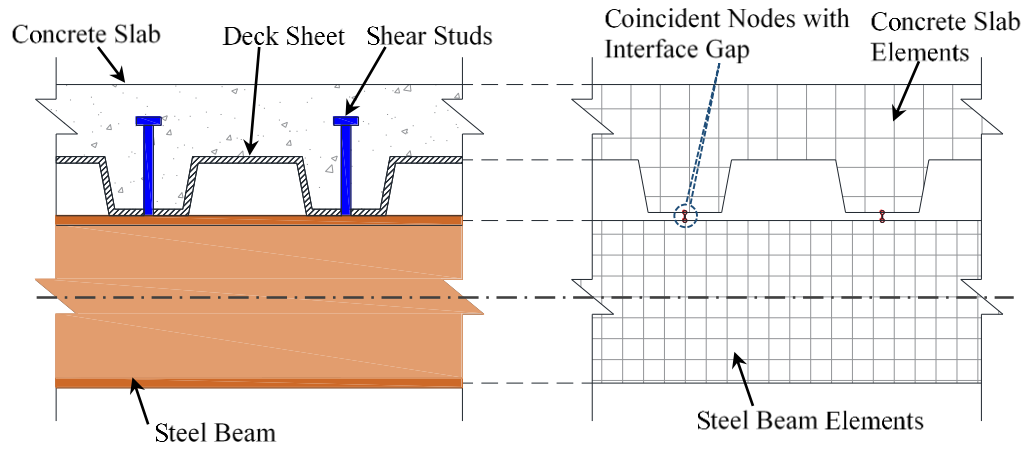

a) Shear Studs in Tested Composite Beam **b) Shear Studs in Finite Element Model**

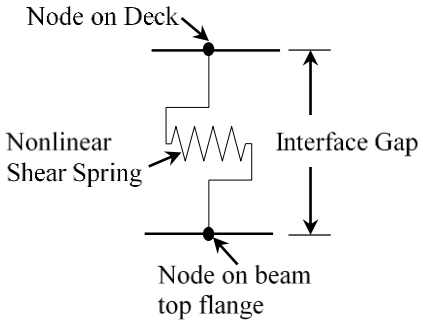

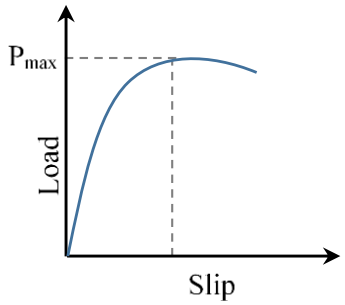

c) Stud Idealisation as Nonlinear Shear Spring **d) Load-Displacement Behaviour Shear Stud**

Figure 6.6 - Schematic Representation of Shear Stud Idealisation

The load-slip properties of the shear stud were assigned to the nonlinear shear spring. The vertical and rotational displacement of a particular node on the shell element (representing the metal deck) and its corresponding node on the beam element of the steel beam are constrained to be the same.

Similar to slab-column surface interaction, the surface-to-surface interaction was used to model the interaction between the beam top flange and the soffit of the metal deck sheet. As mentioned in the previous section hard contact behaviour in the normal direction and friction with a penalty in the tangential direction was provided. Here, the beam top flange was treated as a master surface, and the deck bottom was modelled as slave surface.

Shear Stud Spring Properties

In general, the characteristic resistance of the shear studs was experimentally evaluated, and the ultimate resistance was governed either by concrete crushing or stud shank failure [90]. However, in the absence of the test data, the force-displacement behaviour of the shear studs was derived using the methodology reported in the literature [42, 91, 92]. The parametric study conducted by Lam and El-Lobody [91] on the shear studs, reveals that the formula given in

Eurocode 4 [42] shows close agreement with the experimental test results and numerical analysis. Here, the characteristic strength of the shear studs was calculated based on the research study conducted by HERA [92], and it can be determined using the following two equations, and the minimum of these two governs the design. The calculated characteristic strength of shear studs for the frame sub-assemblies with different slab configurations is reported in Table 6.3.

$$P_{rk} = 0.8 A_{sc} f_u (k_t \; or \; k_l) \tag{6.8}$$

$$P_{rk} = 0.29 \alpha d^2 \sqrt{f_{ck} E_{cm}} (k_t \; or \; k_l) \tag{6.9}$$

where:

A_{sc} = Cross-sectional shank area of the stud
f_u = Ultimate tensile strength of the stud material
d = Diameter of the stud shank
$\alpha = 0.2\left(\frac{h_{sc}}{d} + 1\right)$ for $3 \leq {}^{h_{sc}}/_{d} \leq 4$ or $\alpha = 1$
h_{sc} = Overall nominal height of the stud
$k_t = \frac{0.7}{\sqrt{n_r}} \frac{b_o}{h_p}\left(\frac{h_{sc}}{h_p} - 1\right)$= reduction factor for the transverse deck
$k_l = 0.6 \frac{b_o}{h_p}\left(\frac{h_{sc}}{h_p} - 1\right)$ = reduction factor for the longitudinal deck
b_o = Mean width of deck haunch
h_p = Depth of deck haunch
n_r = Number of stud connectors in one rib
f'_c = Compressive strength of the concrete
f_{cm} = Tensile strength of cylinder, computed using $1.12 f'_c + 2.38$
E_{cm} = Modulus elasticity of the concrete, computed using $3320\sqrt{f_{cm}} + 6900$

Table 6.3 Characteristic strength of the Shear Stud in different Tests

Tested Slab Configuration	**Deck Direction**	**f'c** MPa	**fcm** MPa	**Ecm** MPa	**Deck Reduction Factor**			**Characteristic Strength of Shear Stud (Prk)** kN	
					Transverse		**Longitudinal**	**nr = 1**	**nr = 2**
					k_{t_nr1}	**k_{t_nr2}**	**k_l**		
Fully Isolated Slab Unit (FI-SU)	Transverse	45	53	31114	0.59	0.42	NA	56	39
Shear Key Slab Unit (SK-SU)	Longitudinal	41	49	30036	NA	NA	0.51	48	48
Modified Shear Key Unit (MSK-SU)	Longitudinal	40	47	29612	NA	NA	0.51	48	48
Full Depth Slab Unit (FD-SU)	Transverse	40	47	29612	0.59	0.42	NA	56	39

For this study, the force-displacement relationship of the shear stud was calculated using the relationship suggested by Johnson and Molenstra [1], which is reproduced in equation 6.10.

$$P = P_{rk}\left(1 - e^{-\beta s}\right)^{\alpha} \tag{6.10}$$

In equation 6.10, the values for 'α' & 'β' are selected as 0.989 and 1.535mm^{-1} respectively. Figure 6.7 shows the load-slip curve used for the nonlinear shear springs between the steel beam and the composite deck slab with different deck orientation (transverse and longitudinal).

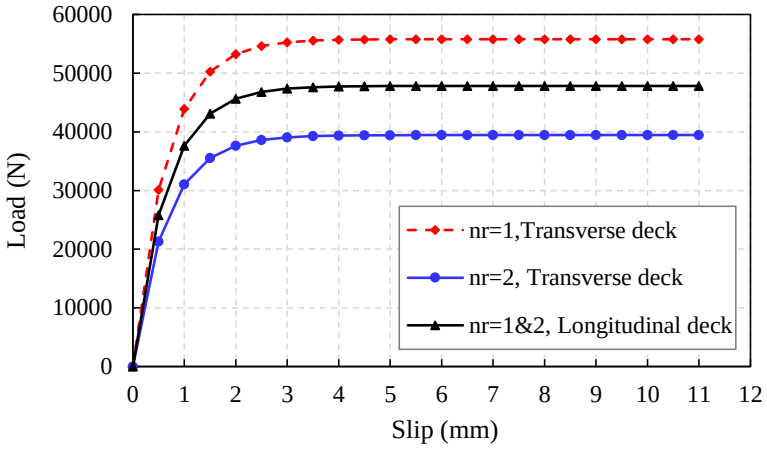

Figure 6.7 - Load-Slip Curve for Shear Stud with different Deck Orientation.

Deck – Slab and Rebar-Slab Interaction

The interaction between the concrete slab and the metal deck was assumed to have a perfect bond, and no uplift and slip were modelled to reduce the computational efforts. This assumption was realised by embedding the deck sheet into the concrete slab using the constraint option available in the ABAQUS software. The concrete slab was treated as the host region and the deck sheet as an embedded region. A similar interaction was made between the rebars and slab. The rebars were embedded into the concrete slab and rebars were treated as an embedded region and concrete as the host region [93].

6.2.6 Elements and Meshing

The finite element software ABAQUS has an extensive inbuilt library of a different element, and these elements are classified based on their degrees of freedom, a number of nodes, formulation, and number of integration points [74]. The most commonly elements used in structural analysis are; four noded shell elements (S4R), eight noded solid elements (C3D8), twenty noded brick elements (C3D20), truss elements (T3D2), beam elements (B31), and connector elements (i.e. springs or dashpots) as shown in Figure 6.8.

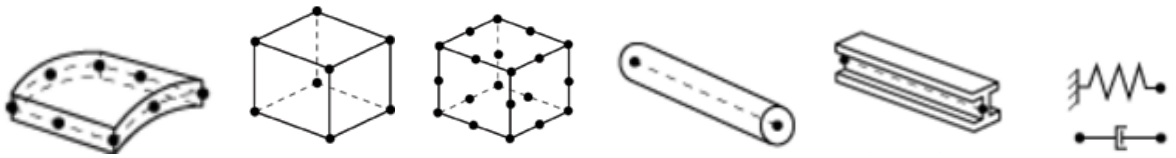

Shell Element (S4R)	4 Noded Solid Element (C3D8)	8 Noded Solid Element (C3D20)	Truss Element (T3D2)	Beam Element (B31)	Connector Elements (Springs or Dashpots)

Figure 6.8 - Different Types of Elements [74]

As mentioned in Section 6.2.1, the eight noded solid elements (C3D8R) with the reduced integration points were adopted to model the concrete slab which can capture the local failure in concrete [15, 35, 80, 87]. The frame sub-assembly structural elements such as beams, column, gusset plates, column continuity plates and metal deck were modelled using the 4 noded (S4R) shell elements with the reduced integration points [82, 93, 94]. In case of the shell elements, the reference surface of the shell was defined by the nodes and the surface normal was defined by the right-hand thumb rule. In most of the cases, the reference surface was coincident with the mid-surface of the shell. In this study, the element thickness was provided to the elements mid surface (i.e. reference surface of the shell element). The shell elements were suitable for the members with the slender geometry and easier to create the auto-meshing with good quality elements. It also requires less processing time compared to the finite element model with the solid elements. Because of this, the shell elements were selected for the modelling frame sub-assembly's [95, 96]. The various components of the frame sub-assembly were meshed using part by part assignment. The meshing of the shell elements (i.e. beam, column, gusset plates, continuity plate and metal deck) was assigned through the global seeding approach, whereas the meshing of the concrete slab (i.e. solid elements) was generated by using the mesh control feature. By using this technique, well defined structured mesh for the complicated geometry of the slab was obtained. Different mesh sizes were modelled to investigate the sensitivity effect on the overall global response of the frame sub-assembly with increasing lateral drift; the obtained responses are shown in Figure 6.9. Based on the mesh sensitivity studies, mesh size of 30 and 75 mm was selected for steel and concrete components respectively.

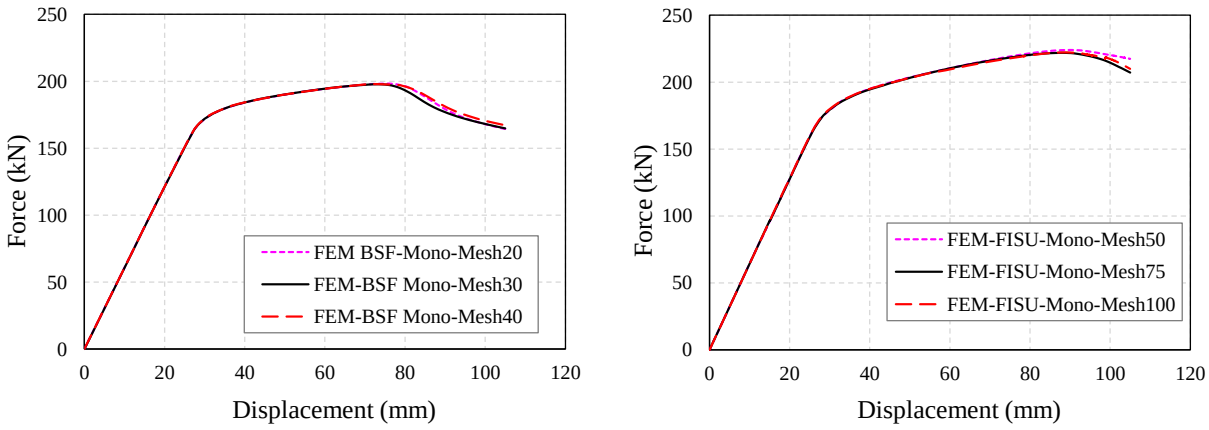

Mesh Sensitivity : Shell Element (S4R) **Mesh Sensitivity : Solid Element (C3D8)**

Figure 6.9 - Mesh Sensitivity Analysis : Load-Displacement Curves

6.2.7 Results and Discussion

The comparison of the monotonic force-displacement response obtained from the numerical analysis with the corresponding experimental test results is shown in Figure 6.10. The initial stiffness and the peak strength of numerical finite element model and experimental results are summarised in Table 6.4. It's clear from these plots that the numerical model could able to capture the initial lateral stiffness, which is in close agreement with the experimental test results (with a deviation range between of 1% and13%). This was because of assumptions made in a numerical model for simplification and to reduce the computational efforts. The behaviour of the frame sub-assembly under the monotonic regime was comparable to the experimental test results (with strength deviation range between 1% and 9%), and it follows the backbone envelope of the experimental hysteresis loops of the BSF, FI-SU, and FD-SU frame sub-assemblies as depicted in Figure 6.10a, 6.10b, and 6.10e respectively. However, in case of the SK-SU and MSK-SU frame sub-assemblies, the numerical model could not able to capture the strength degradation as observed in the experimental tests. This was because of the stiffness caused by the metal deck, which was oriented parallel to the main beam (i.e. longitudinal deck) in both the SK-SU and MSK-SU test specimens. The numerical model of the frame sub-assembly with shear key (SK-SU) slab overpredicted the peak strength by 9% as shown in Figure 6.10c and Table 6.4. This was because the numerical model could not be able to simulate the failure caused by delamination of the concrete between the column flanges, as observed during the experimental tests (refer section 4.4.5).

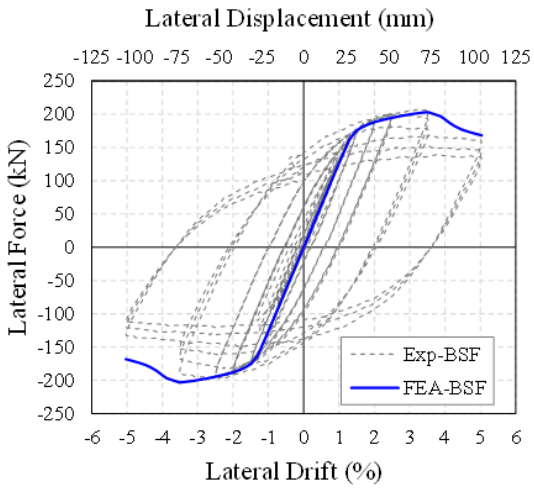

a) Bare Steel Frame (BSF: No Deck)

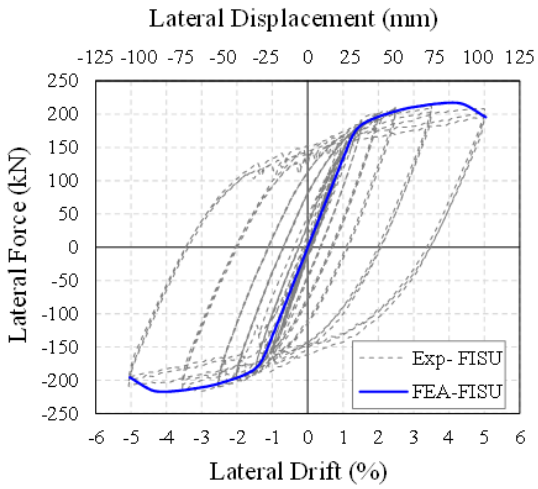

b) Fully Isolated Slab Unit (FI-SU: Transverse Deck)

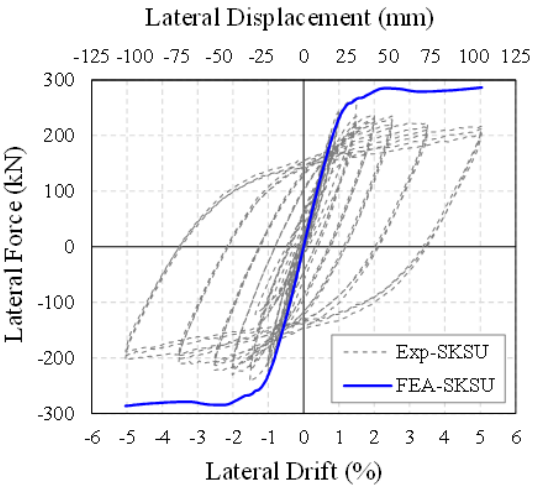

c) Shear Key Slab Unit (SK-SU: Longitudinal Deck)

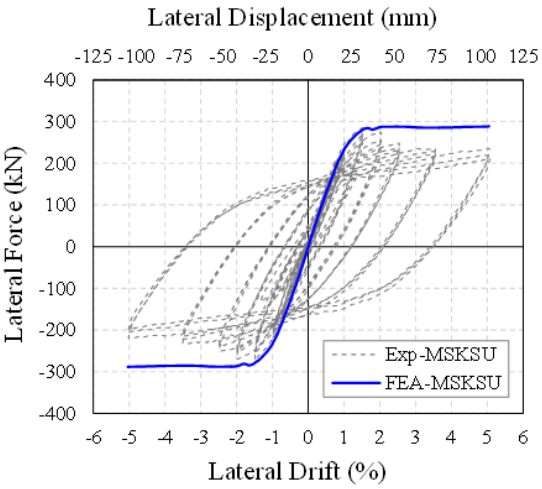

d) Modified Shear Key Slab Unit (MSK-SU: Longitudinal Deck)

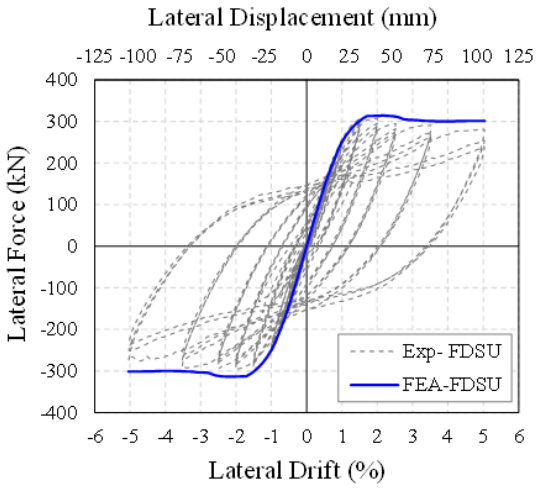

e) Full Depth Slab Unit (FD-SU : Transverse Deck)

Figure 6.10 – Comparison of Force-Displacement of Behaviour of Numerically Simulated Result with the Test Results

Table 6.4: Comparison of Sub-assemblies Initial Stiffness and Peak Strength of Numerical (FEA) Model with Experimental Results

Test Specimen	Initial Stiffness (kN/m)			Peak Strength(kN)		
	Numerical (FEA)	Experimental	Deviation (%)	Numerical (FEA)	Experimental	Deviation (%)
Bare Steel Frame **(BSF)**	6070	6156	1.0	203.13	206	1
Fully Isolated Slab Unit **(FI-SU)**	7590	8747	13	217.24	211.4	3
Shear Key Slab Unit **(SK-SU)**	12888	15031	14	286.47	263	9
Modified Shear Key Slab Unit **(MSK-SU)**	13137	14506	9	288.6	285.2	1
Full Depth Slab Unit **(FD-SU)**	14136	16402	14	313.73	306.3	2

The numerical simulation of the local behaviour of the beam flange and comparison with the experimentally observed structural damage is shown in Figure 6.11 to 6.15. The location of the flange buckling in the numerical model matches with the experimental observations. It was observed that the simulated model could able to capture the buckling of the top and bottom flanges in case of the BSF and FI-SU frame sub-assembly (i.e. no slab-column interaction). However, in case of the frame sub-assemblies (SK-SU, MSK-SU, and FD-SU) with the slab-column interaction, the numerical model could not able to capture the buckling of the beam top flange. This was due to the effective resistance offered by the deck to the beam top flanges.

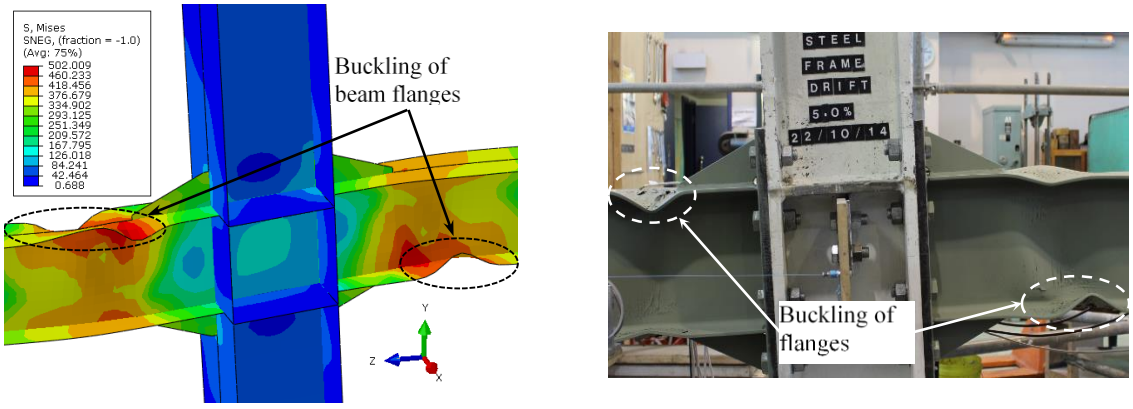

a) Numerical Model(Stress Contour at 5.0% drift)

b) Experimental Test

Figure 6.11 – Local Buckling of Beam Flanges : BSF Sub-assembly

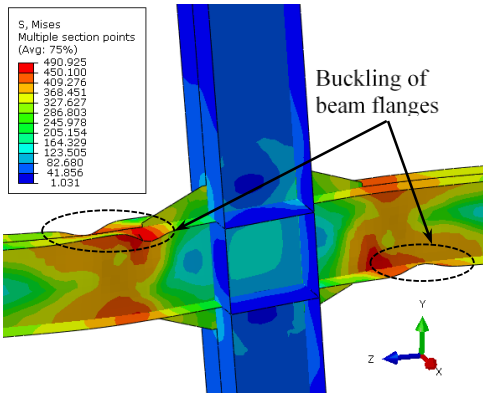

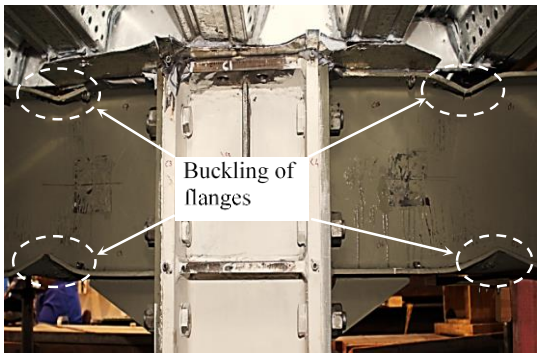

a) Numerical Model (Stress Contour at 5.0% drift)

b) Experimental Test

Figure 6.12 – Local Buckling of Beam Flanges : FI-SU Sub-assembly

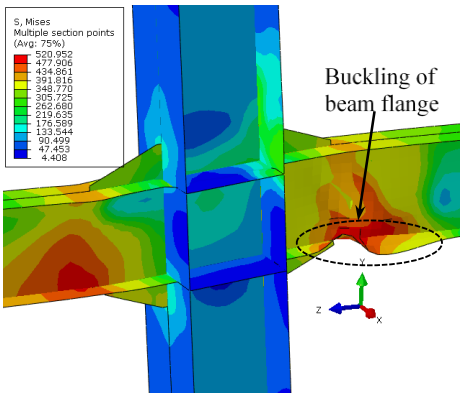

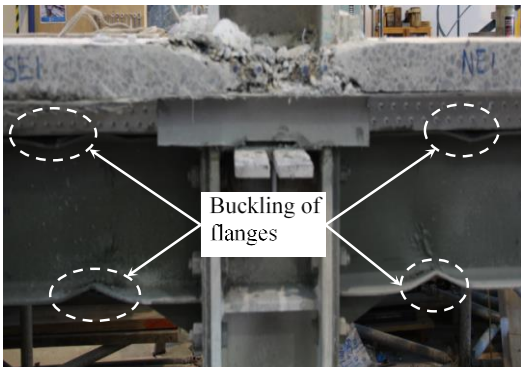

a) Numerical Model (Stress Contour at 5.0% drift)

b) Experimental Test

Figure 6.13 – Local Buckling of Beam Flanges : SK-SU Sub-assembly

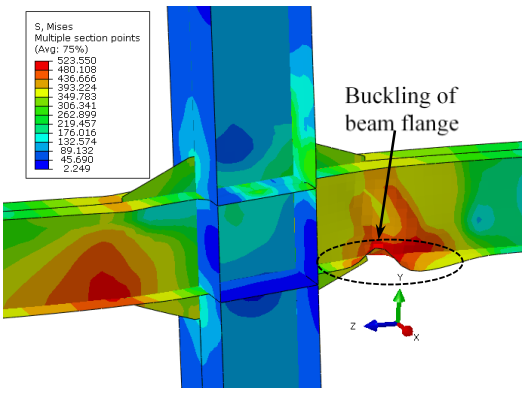

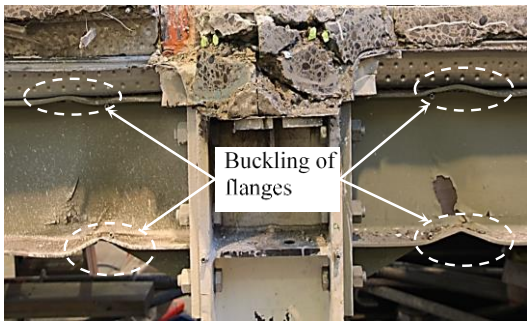

a) Numerical Model (Stress Contour at 5.0% drift)

b) Experimental Test

Figure 6.14 – Local Buckling of Beam Flanges : MSK-SU Sub-assembly

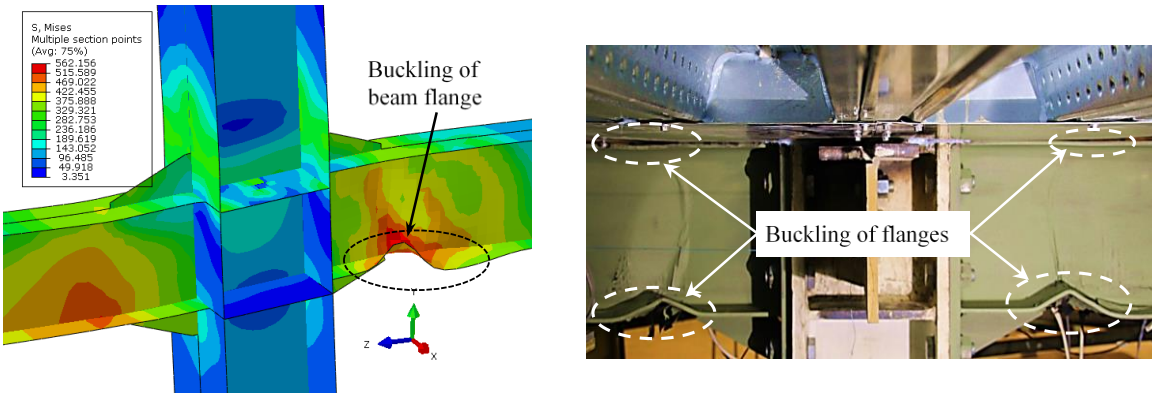

a) Numerical Model (Stress Contour at 5.0% drift) **b) Experimental Test**

Figure 6.15 – Local Buckling of Beam Flanges : FD-SU Sub-assembly

The equivalent plastic strain distribution at 5.0% sub-assembly lateral drift is shown in Figure 6.16, and it can be concluded that the column and the panel zone was in the elastic state, which was in line with the behaviour observed during the experimental tests. The equivalent plastic strains as a function of the lateral drift showing the formulation of the beam plastic hinges are depicted in Appendix E.

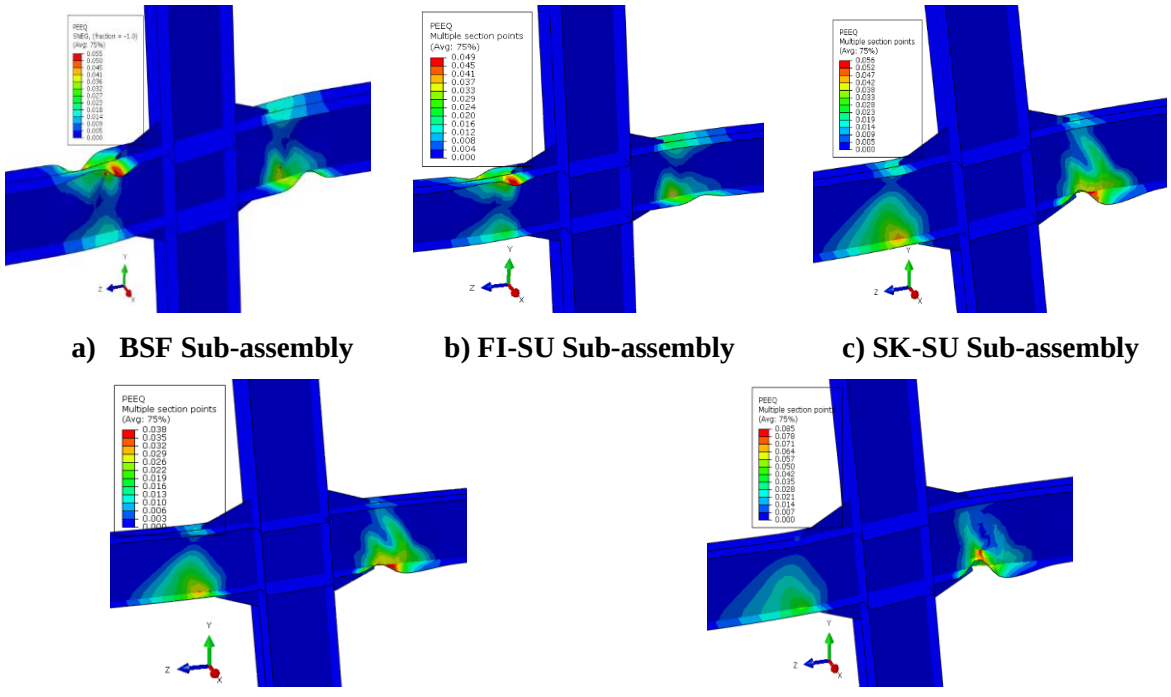

a) BSF Sub-assembly **b) FI-SU Sub-assembly** **c) SK-SU Sub-assembly**

d) MSK-SU Sub-assembly **e) FD-SU Sub-assembly**

Figure 6.16 – Equivalent Plastic Strain at 5.0% Lateral Drift

The minimum principal stress contour plots representing the compression behaviour of the slab are depicted in Figures 6.17 to 6.20. Each contour plot represents the lateral drift corresponding to the peak strength of the simulated test frame sub-assemblies. As expected, the simulated

isolated frame sub-assembly displays negligible compression stresses in the slab, which is shown in Figure 6.17. This was because of the isolation of the slab around the column, which deactivates the force transfer mechanism (resulted from the slab-column interaction). The slab behaviour observed in the numerical model matches with the experimental results discussed in section 4.3.5 and it can be concluded that the degree of slab-column interaction influences the overall behaviour of the frame sub-assembly.

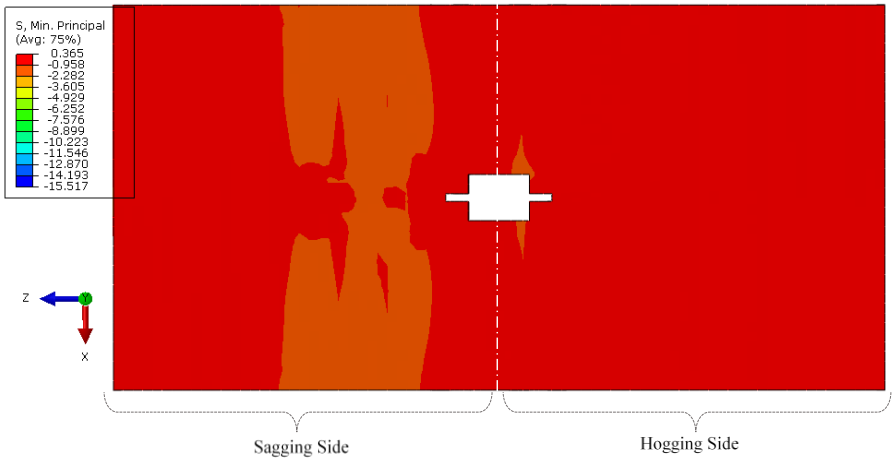

Figure 6.17 – Minimum Principal Stress Contour at 3.5% Drift : FI-SU Sub-assembly

As explained section 3.3, both the shear key and modified shear key frame sub-assemblies were isolated at the column outer flanges. This was done to activate only the force transfer Mechanism-2, and the numerical models were modelled with the similar boundary conditions by using the relevant contact interaction feature. The micro modelling of the SK-SU and MSK-SU frame sub-assemblies could able to capture the spread of compression strut associated with the force transfer Mechanism-2 which is shown in Figure 6.18 and 6.19. It is clear that the angle of compression strut was approximately 45°, and this is in agreement with the EC8 [14]. The noted maximum compressive stress in the SK-SU and MSK-SU frame sub-assemblies was 22 MPa and 34MPa respectively, which lies between $0.6f_c'$ to $0.85f_c'$ (where f_c'= 40MPa). Since the ABAQUS model could not actually model shear key failure, this is an upper bound on the actual stress expected. This peak stress was locally concentred at the tip of the column flanges, indicating the stress concentration on the sagging side of the beam. The average stress range in compression strut was around 15 MPa (i.e. $0.4f_c'$). The difference in the maximum compressive stress between the SK-SU and MSK-SU frame sub-assemblies was due to the different detailing (i.e. shear key rebars and the anchorage).

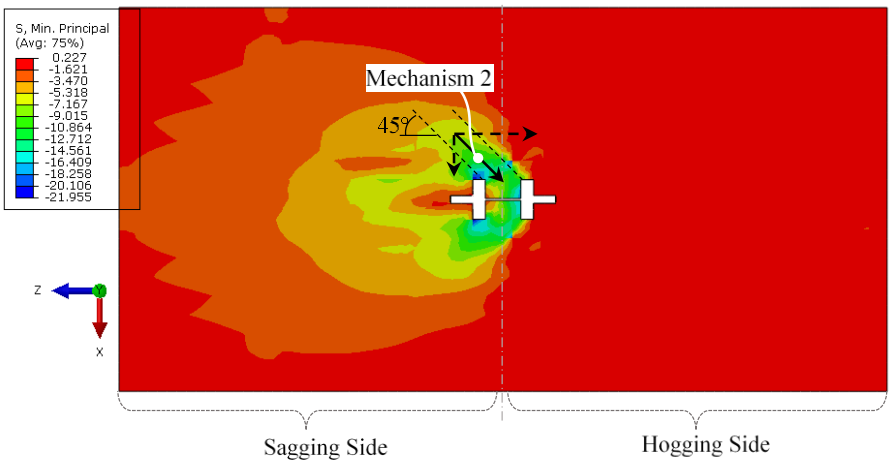

Figure 6.18 – Minimum Principal Stress Contour at 1.5% Drift : SK-SU Sub-assembly

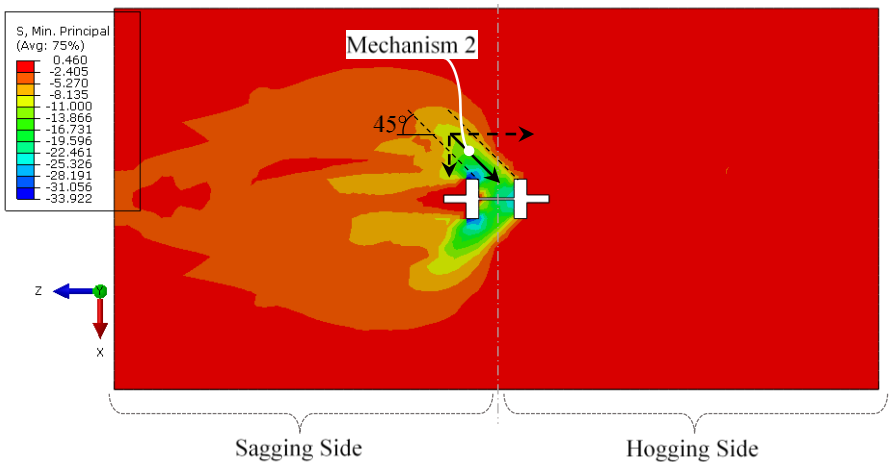

Figure 6.19 – Minimum Principal Stress Contour at 1.5% Drift : MSK-SU Sub-assembly

The compression stress field of the full depth frame sub-assembly is shown in Figure 6.20; it is clear that the stress field was different to that of the other frame sub-assemblies. This was due to the interaction of both force transfer mechanisms (i.e. Mechanism-1 and Mechanism-2) with the column. Similar to the observations made by Salvatore et al. [15], the numerical model shows high-stress levels in front of the column outer flanges (associated with the compression strut of Mechanism-1) and low-stress levels in between the column flanges (associated with compression strut of Mechanism-2). The noted maximum compression stress in the Mechanism-1 and Mechanism-2 regions was 28 MPa and 18 MPa respectively, which lies between $0.45f_c'$ to $0.7f_c'$ (where f_c'= 40MPa). It can be concluded that the contribution of the composite slab's compressive strength associated with Mechanism-1 is higher as compared to that of Mechanism-2 [32].

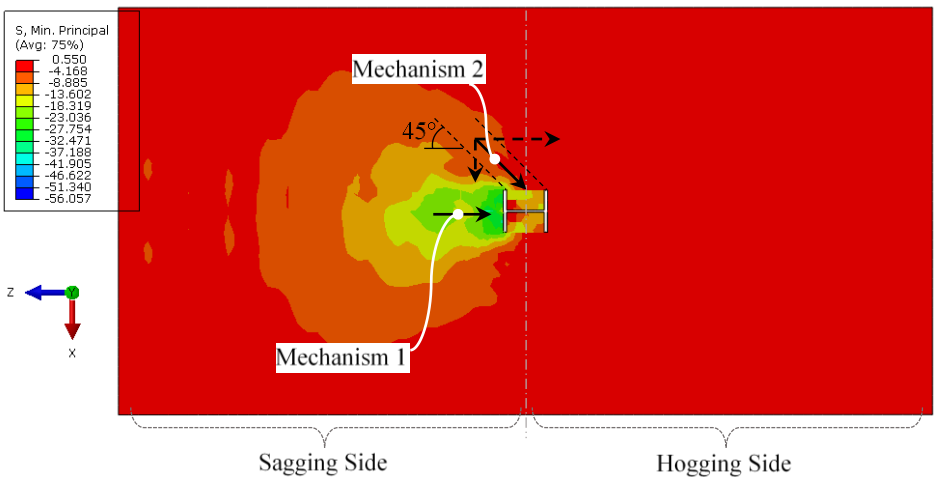

Figure 6.20 – Minimum Principal Stress Contour at 2.0% Drift : FD-SU Sub-assembly

As mentioned before, the slab-column interaction was modelled using the surface-to-surface contact interface feature in ABAQUS. The contact pressure distributions on the concrete and column flanges in different tests are shown in Figures 6.21 to 6.23.

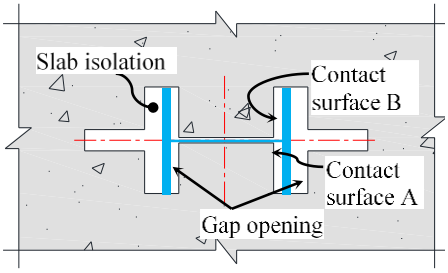

a) Designation of Contact Surface

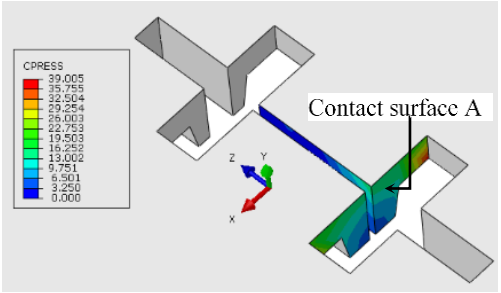

b) Contact Pressure in Concrete Slab

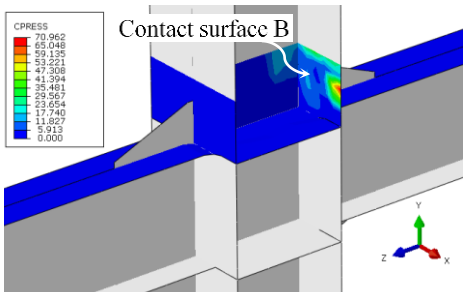

c) Contact Pressure in Column Flange

Figure 6.21 – Contact Pressure at 1.5% Drift : SK-SU Sub-assembly

It can be seen from the Figures 6.21 and 6.22 that the average contact pressure was in the range of 19-22 MPa for the SK-SU and MSK-SU frame sub-assemblies which were lower than the compressive strength of the concrete (i.e. $f_c' = 40$MPa). It can also be observed that the stress concentration has resulted in localised peak contact pressure at the tip of the column flanges.

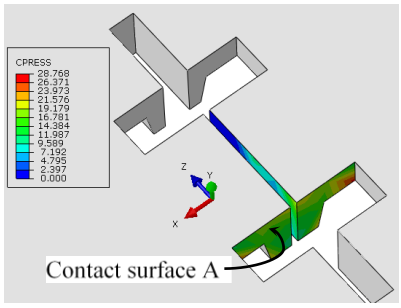

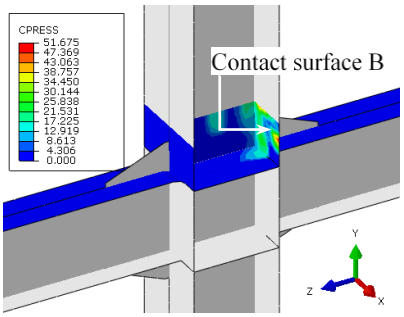

a) Contact Pressure in Concrete Slab **b) Contact Pressure in Column Flange**

Figure 6.22 – Contact Pressure at 1.5% Drift : MSK-SU Sub-assembly

The contact pressure distribution of FD-SU frame sub-assembly is shown in Figure 6.23. It's clear that the contact pressure at outer column flanges due to the force transfer Mechanism-1 was approximately 39 MPa and at the inner column flanges due to Mechanism-2 was approximately 17 MPa. As discussed earlier, the Mechanism-1 contributes more to overall lateral strength as compared to the Mechanism-2.

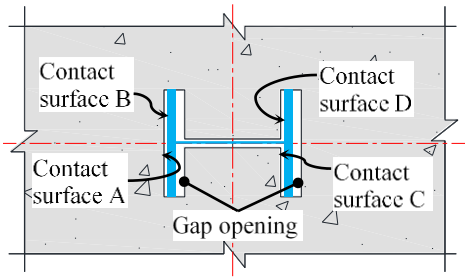

a) Designation of Contact Surface

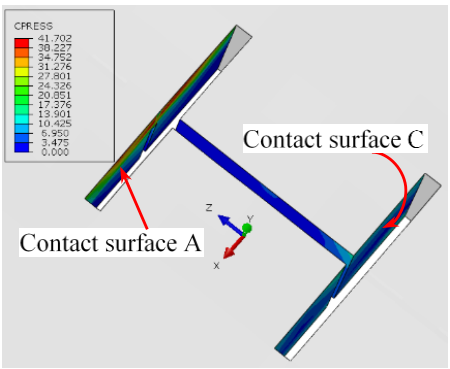

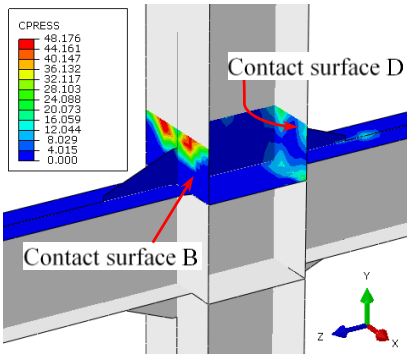

b) Contact Pressure in Concrete Slab **c) Contact Pressure in Column Flange**

Figure 6.23 – Contact Pressure at 2.0% Drift : FD-SU Sub-assembly

6.3 Macro Modelling

In this section, a simple macro modelling technique was developed using the strut-and-tie approach, which can reliably predict the cyclic behaviour of frame sub-assembly with different slab configurations. The numerical model was developed using structural analysis program SAP2000 Version 17.2.0 [75]. The composite slab was modelled as an assemblage of the line elements and the nonlinear springs.

6.3.1 Geometry Idealisation

A simple component-based numerical macro model was developed which represents an internal moment resisting frame sub-assembly, which is shown in Figure 6.24a. The developed numerical model was an assemblage of the nonlinear springs, elastic beam-column elements, and axial elements representing Mechanism-1 and 2 in the composite slab. The frame sub-assembly elements like 310UC158 column, 310UB32 beam, and composite deck slab were modelled as a line element as shown in Figure 6.24b and 6.24c.

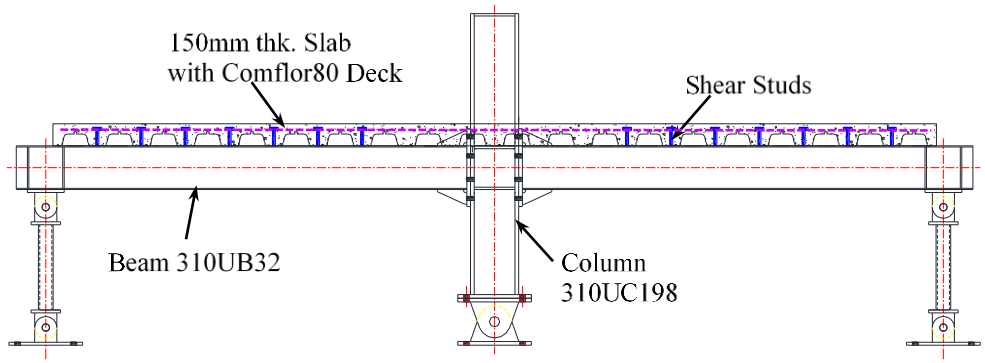

a) Experimental Test Setup

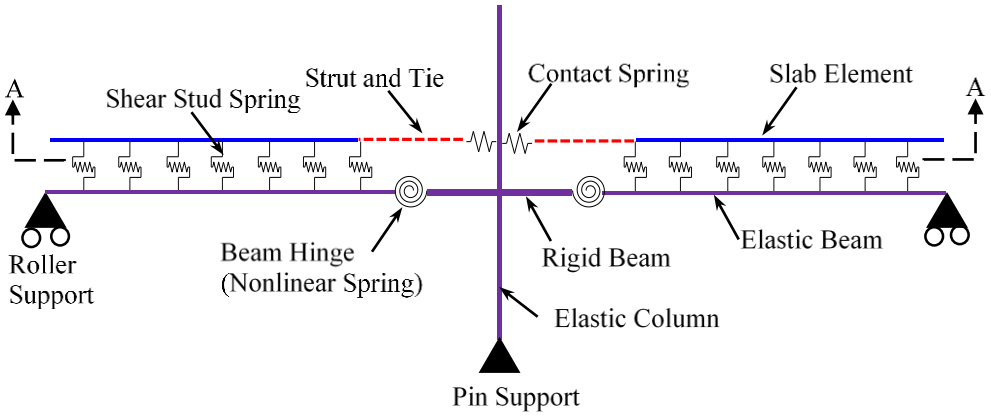

b) Schematic Representation of Numerical Model (Elevation)

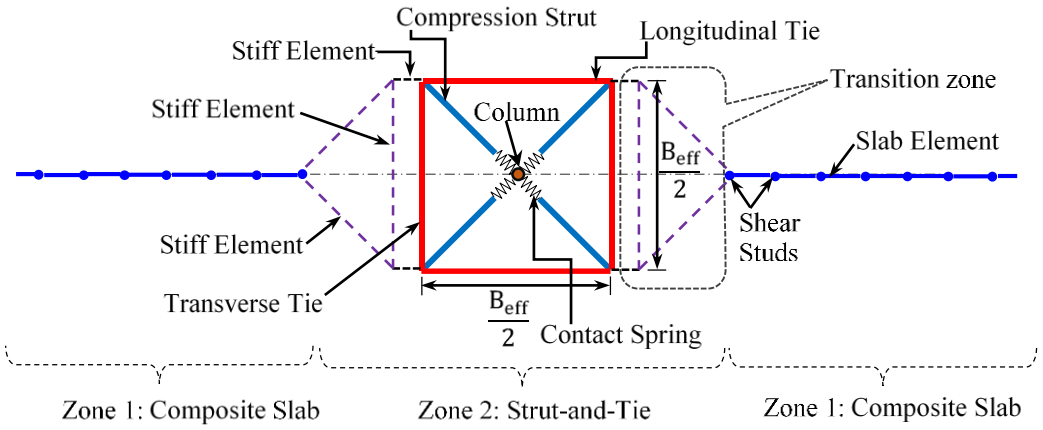

c) Schematic Representation of Numerical Model (Plan: Section A-A)

Figure 6.24 Schematic Representation of Numerical Model.

The line elements representing the beam and column were modelled along the centreline of the frame sub-assemblies components. As the tested frame sub-assembly was designed based on the capacity design principles (i.e. strong column/connection–weak beam), the column was modelled as an elastic line element, whereas beam was divided into three parts; (i) rigid beam element (representing connection), (ii) nonlinear rotational spring (representing the beam plastification), and (iii) elastic beam element (representing elastic component). As discussed in Chapter 5, the nonlinear behaviour frame sub-assembly was dominated by plastification of the beam flanges (at the tip of the gusset plate), this was captured using the nonlinear rotational spring. To simulate this nonlinear behaviour of the beam in the numerical model, a nonlinear rotational spring was introduced in the beam plastic hinge region. The beam gusset plates and the endplate connection was simulated as a rigid beam as shown in Figure 6.24b. The remaining portion of the beam was modelled as an elastic line element. The shear studs were modelled as nonlinear springs (using a multilinear plastic link element in SAP2000), which can capture the nonlinear deformation of the shear studs. These shear springs were provided at the actual locations of the shear studs as shown Figure 6.24b.

The decking slab was divided into two zones; the first zone represents the slab stretched over the shear studs, which was modelled as a line element connected to the beam element through the shear stud springs as shown in Figure 6.24c. The second zone covers the slab from the column centreline to the first shear stud (from the column), which was modelled as an assemblage of axial elements (forming a strut-and-tie arrangement) as shown in Figure 6.24c. In this zone, the stiff members were used to connect the composite slab section (i.e. slab element) to the strut-and-tie as shown by ‘transition zone’ in Figure 6.24c. These stiff members were used to avoid the numerical instability in the proposed macro model, and they act as a

dummy members. The compression struts are shown in the Figure 6.24c were connected to the contact springs to capture the slab interaction with the column flanges. The required input properties for the nonlinear rotational spring, shear stud spring, strut-and-tie elements are reported in the subsequent sections. Note that the panel zone was modelled as a rigid element, this conclusion was assumed based on the observations made in the experimental study and previous numerical studies in section 6.2.

6.3.2 Coordinate System

The global and local coordinate system used for modelling the internal frame sub-assembly is shown in the Figure 6.25. The global X-axis represents the longitudinal direction of beams, and the global Y-axis is orthogonal to the beam in the horizontal plane (representing the transverse direction). The global Z-axis defines the vertical direction of the frame sub-assembly which coincides with the longitudinal axis of the column. The sectional and force-deformation properties for the various elements were provided in their local coordinate system [75]. The local coordinate system is denoted using 1, 2 and 3 as shown in Figure 6.25. The axis 1-1 is oriented along the element length which represents the axial force (P) or translation (U1) as well as the twist (T) or torsional deformation (R1). The axes 2-2 and 3-3 represent the shear forces (V2 and V3 respectively) or transverse deformation (U2 and U3 respectively) as well as the moment (M2 and M3 respectively) and rotations (R2 and R3 respectively).

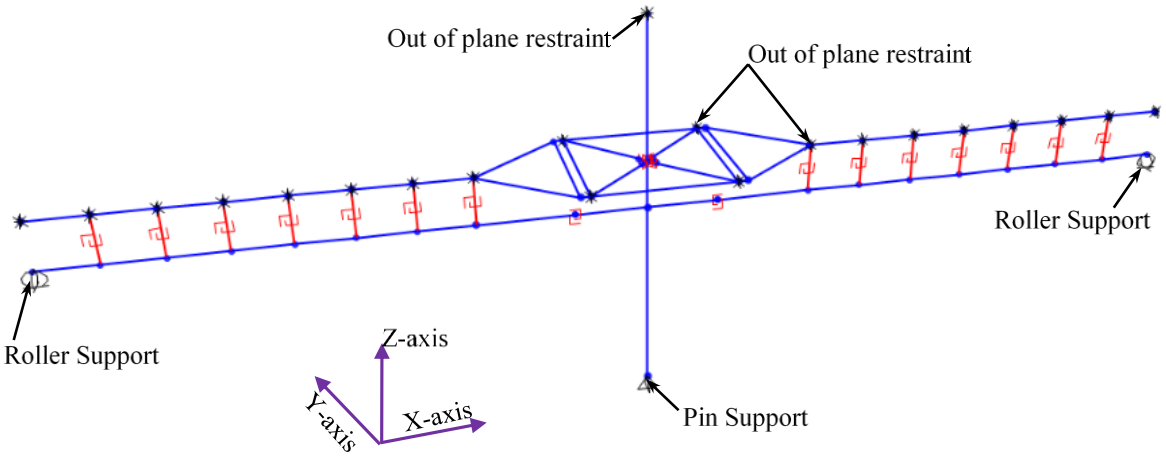

a) Sub-assembly Global Co-ordinate System and Boundary Conditions

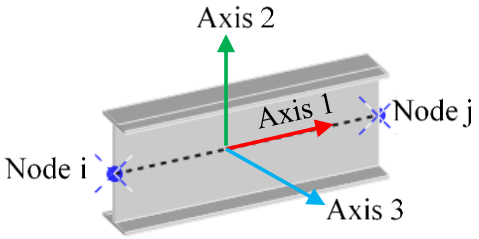

b) Member Local Co-ordinate System

Figure 6.25 Numerical Model Co-ordinate System.

6.3.3 Element Formulation

Beam Element with Rotational Spring

The idealised numerical model of the frame sub-assembly's beam is shown in Figure 6.26, which was discretized in three parts (as mentioned before); rigid zone, plastic hinge zone, and the elastic beam. The beam-to-column connection was considered as a rigid zone (based on the experimental observations). Also, to simplify the model, the end-plate connection along with gusset plates was treated as a rigid element. The moment of inertia for the rigid beam element was calculated as the sum of the moment of inertias of the bare beam and the gusset plates (i.e. $I_{rigid} = I_{beam} + I_{gusset}$).

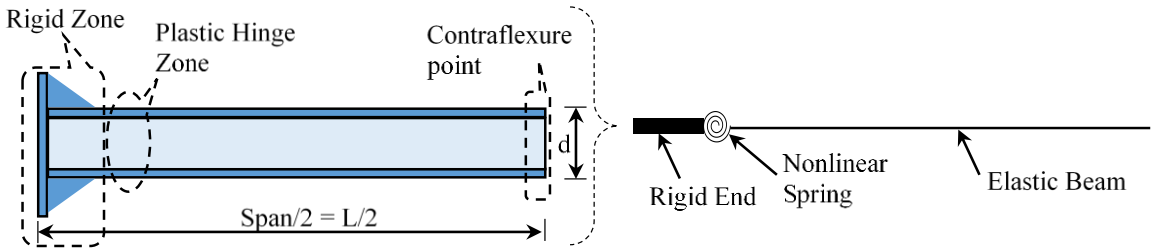

a) Actual Beam Profile **b) Numerical Model of Beam with CPH Spring**

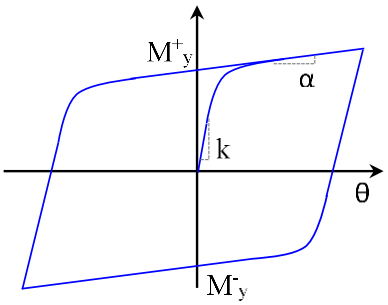

c) CPH Spring (Hysteresis behaviour of the nonlinear spring)

Figure 6.26 Beam Element Details

As mentioned before, the nonlinearity of the beam was simulated using the concentrated plastic hinge (CPH) approach. A zero length nonlinear link element was used, and the nonlinear cyclic behaviour was simulated through the Wen plasticity model available in SAP2000 [75]. A link element has six deformation degrees-of-freedom (i.e. U1, U2, U3, R1, R2 and R3). All internal deformations were independent, and the yielding in one degree of freedom does not affect the behaviour of the other deformation [75]. As explained before, the force-deformation properties of the link elements were provided in its local coordinates. The degrees-of-freedom that were utilised for the nonlinear spring is as follows:

i) Axial deformation in translational direction-1 (i.e. U1) with the linear properties
ii) Shear deformation in translational direction-2 and direction-3 (i.e. U2 and U3 respectively) with linear properties
iii) Rotation in direction-3 (i.e. R3) with nonlinear properties
iv) Rigid rotational deformation in direction-1and 2 (i.e. R1 and R2)

The axial stiffness ($K_{axial,1}$) for 'U1' and shear stiffness ($K_{shear,2}$ and $K_{shear,3}$) for 'U2' and 'U3' was calculated using the following equations:

$$K_{axial,1} = \frac{A.E}{L_1} \tag{6.11}$$

$$K_{shear,2} = \frac{A_{s2}.G}{L_1}, \text{ and } K_{shear,3} = \frac{A_{s3}.G}{L_1} \tag{6.12}$$

where:

A = Cross-sectional area of the steel beam
A_{s2} = Effective shear area of the steel beam in translational direction-2 = $d.t_w$
A_{s3} = Effective shear area of the steel beam in translational direction-3 = $5/6(2.b_f.t_f)$
E = Modulus of elasticity of steel
G = Shear modulus of steel
L_1 = Beam span between the plastic hinges

The input properties required for the Wen plasticity spring are; (i) initial flexural stiffness, (ii) post-yield stiffness ratio, (iii) yield moment, and (iv) exponent coefficient. The initial flexural stiffness of the rotational spring (K_{spring}) was calculated using equation 6.13 and 6.14:

$$K_{spring} = n.\frac{6.E.I_{mod}}{L_1} \tag{6.13}$$

$$I_{mod} = I_{beam}.\frac{n+1}{n} \tag{6.14}$$

where:

I_{mod} = Modified moment of inertia of the beam
I_{beam} = Moment of inertia beam about the major axis
n = Multiplication factor, here it is 10

The initial flexural stiffness of the rotational spring was modified by a constant 'n' to account for the combined effect of the nonlinear springs and the elastic beam-column element. The rotational spring at the beam end was modelled as a rigid-plastic (by multiplying initial stiffness with 'n') so that the numerical model does not pose any numerical instability issues [97].

As reported by Ibarra and Krawinkler [98], the overall hysteretic response of the beam was a combination of the individual moment-rotation of the rotational spring and the elastic beam-column element. In the nonlinear time history analysis, the rotational spring dominates the overall moment-rotation behaviour of the beam, and the response of the beam-column element remains elastic. Since the rotational spring and the elastic beam-column element are connected in series, the post-yielding to elastic stiffness ratio (i.e. the strain hardening coefficient) was adjusted to obtain the strain hardening coefficient of the rotational spring. The methodology suggested by Ribeiro et al. [97] was adopted here to obtain the strain hardening coefficient of the rotational spring. The post-yield stiffness ratio of the rotational spring was calculated as:

$$\alpha_{spring} = \frac{\alpha}{1+[n.(1-\alpha)]} \tag{6.15}$$

Where 'α' is the nominal strain hardening ratio, which was considered to be equal to 3% (this value was assumed based on the literature and the section analysis of the beam 310UB32). The post-yield stiffness ratio of the rotational spring α_{spring} was equal to 0.0028 (for n = 10), and this value was used in the current numerical simulation. The effect of the isotropic hardening was captured in the model by increasing the predicted plastic moment (M_p), which was obtained by multiplying plastic section modulus (Z_p) with the measured yield stress (σ_y). The predicted plastic moment was multiplied by a multiplication factor (ϕ_m) to account for isotropic hardening; this factor was obtained using the methodology suggested by Kawashima et al. [99]. Lignos and Krawinkler [100] has proposed a multiplication factor of 1.17 for the beam section other than RBS (i.e. reduced beam section) sections. The yield moment ($M_{y\ eff}$) is calculated as:

$$\phi_m = \frac{(\sigma_u/\sigma_y)+1}{2} \tag{6.16}$$

$$M_{y\ eff} = \phi_{m.} M_p \tag{6.17}$$

where:

σ_y	=	Yield stress obtained from tension coupon test
σ_u	=	Ultimate stress obtained from tension coupon test
ϕ_m	=	Multiplication factor
M_p	=	Plastic moment
$M_{y\ eff}$	=	Effective moment which accounts for isotropic hardening

In the Wen plasticity model, the sharpness of the hysteresis was influenced by the yielding exponent coefficient. Here, it assumed to be equal to one.

Shear Stud Idealisation

In the numerical model, the shear stud was modelled using a non-linear link element available in SAP 2000. A nonlinear load-slip behaviour shown in Figure 6.27 of the shear stud was used to simulate the interaction between the steel and concrete. The use of spring element simplifies the numerical model and results in better convergence [101]. The shear spring was provided from the beam mid-height to the mid-thickness of the topping concrete as shown in Figure 6.27 (b). A single shear spring was modelled to represent the two shear studs at a single point in the numerical model. Accordingly, the properties of load-slip envelope were modified. Rigid constraints were assigned in the respective axes of the link element to capture the shear stud rotation and embedment.

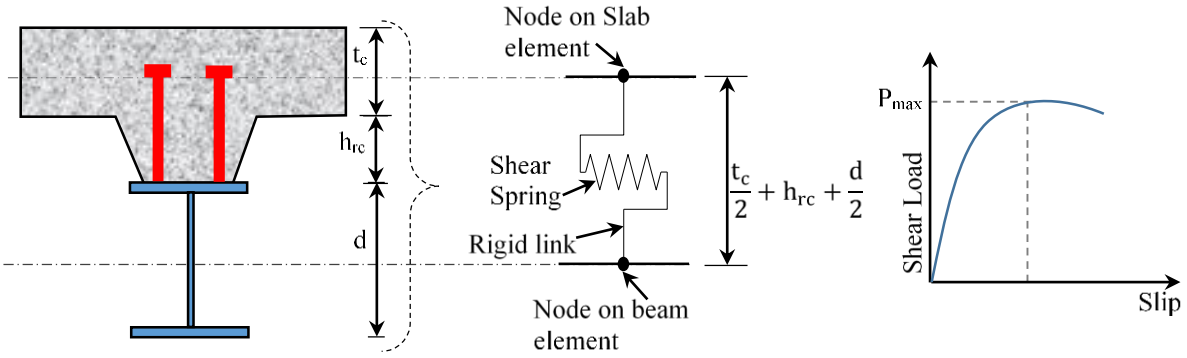

a) Shear Stud **b) Analytical model** **c) Load-Slip Envelope**

Figure 6.27 Nonlinear Shear Spring to Model the Behaviour of Shear Stud.

6.3.4 Slab-Column Interaction Idealisation (Strut-and-Tie Mechanism)

The slab-column interaction of the frame sub-assembly was numerically simulated using a simple strut-and-tie formulation. This strut-and-tie formulation was developed based on the force transfer mechanisms reported in the Eurocode 8 [14]. In the current model, the force transfer Mechanism-1 (i.e. direct bearing onto column outer flanges) and Mechanism-2 (i.e. compression strut developed on column sides) were considered. The third force transfer mechanism (Mechanism-3) which arises from the torsional effect of the secondary beam (i.e. transverse beam) framing into the column panel zone is activated only if there is a composite action between the secondary beam and the deck slab through the shear studs. In the current experimental study the secondary beam (transverse beam) was not connected to the slab

through the shear studs, therefore, the force transfer Mechanism-3 was absent. So, in the current macro model, force transfer Mechanism-3 was not modelled.

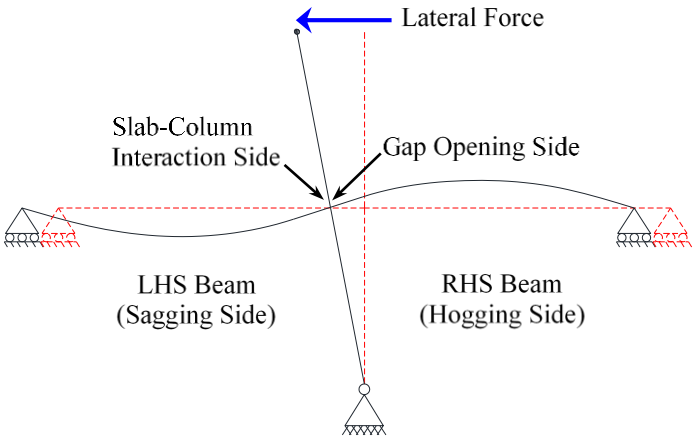

Figure 6.28 Frame Sub-assembly subjected to Lateral Load.

The response of the internal frame sub-assembly under a given lateral load is shown in Figure 6.28. The slab around the column would interact with the column faces (i.e. column flange and web surface) if the slab was without gap aligned with the column. If the gap was provided around the column, no interaction between the column and slab occurs, resulting in the deactivation of the force transfer mechanisms. In the conventional construction practice, the slab was casted without the gap with the column, thereby resulting in the development of the force transfer Mechanism-1 (i.e. direct compression on the column outer flange) and Mechanism-2 (i.e. compression on column sides) as shown in Figure 6.29.

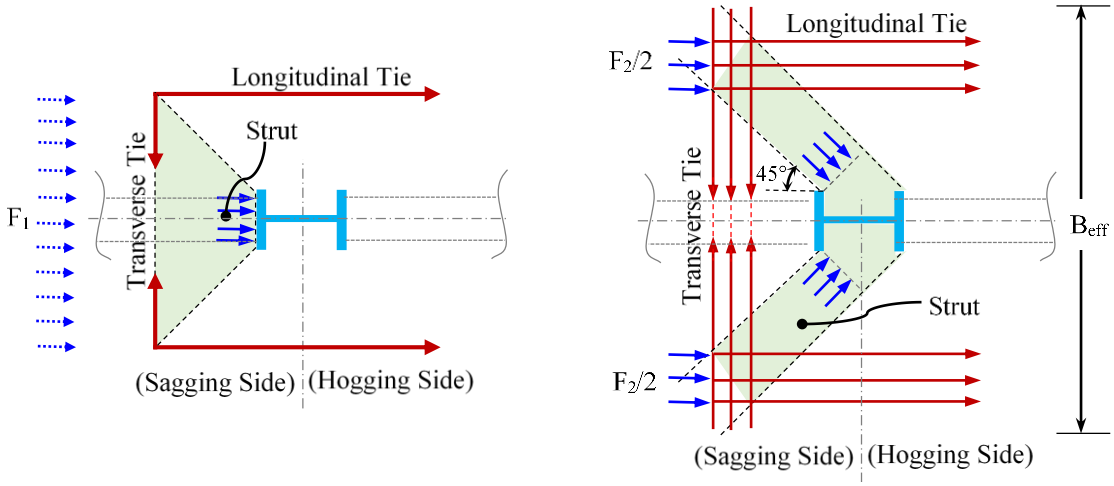

a) Mechanism-1: Direct Bearing onto Column Outer Flange

b) Mechanism-2: Compression on Column Sides

Figure 6.29 Force Transfer Mechanisms between Slab and Column [14]

In the current macro model, the formulation of the strut-and-tie at the slab-column interaction zone was based on the assumption that both the force transfer Mechanism-1 and Mechanism-2 act in parallel, therefore they were represented by a single compression strut with an equivalent strut area (i.e. sum of strut areas of the Mechanism-1 and Mechanism-2) and the detail calculation of an equivalent strut area are reported in Appendix E. This equivalent compression strut was assumed to act at the inclination of 45°. This equivalent compression strut was connected to the column centre line with a nonlinear contact spring as shown in Figure 6.30. A nonlinear link element has been used to incorporate the behaviour of the slab in the contact zone, which is also shown in Figure 6.30.

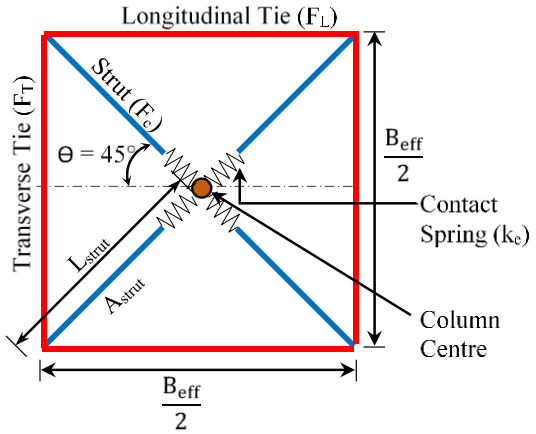

Figure 6.30 Idealised Strut-and-Tie model.

The force-displacement properties of the nonlinear contact spring were calculated using the concrete compression stress-strain envelope shown in Figure 6.4a. The compression force was obtained by multiplying stress with the area of the strut ($F_c = f'_c \times A_{strut}$), whereas the corresponding displacement was obtained by multiplying the corresponding concrete strain with the length of the strut (i.e. $\Delta_{strut} = \varepsilon_c \times L_{strut}$). The force-displacement constitutive law of the contact spring used in the numerical model is shown in Figure 6.31.

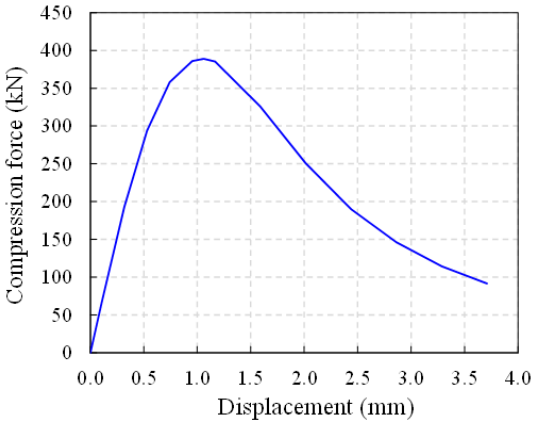

Figure 6.31 Contact Spring: Force-Displacement Envelope.

The internal force (equal to F_1+F_2, shown in Figure 6.29) developed in the effective width (B_{eff}) in the composite slab section was transferred to the different force transfer mechanisms at the slab-column interaction zone, and that depends on the slab construction detail around the column. It was assumed that the combined concrete compressive struts (i.e. equivalent strut) from Mechanism-1 and Mechanism-2 as shown in Figure 6.24 and 6.30 starts from the centre of the column and spread up to the points located at $B_{eff}/4$ from the beam centerline at an angle of 45°. The transition zone in between the composite slab section (zone-1) and the strut-and-tie (zone-2) was connected through the series of rigid elements which facilitates the transfer of the axial forces as shown in Figure 6.24. The cross-sectional area for these rigid elements was assigned as, $A_{stiff} = B_{eff}/2 \times t_c$. The slab in the composite section region was assigned as a linear elastic flexural member with the upper limit on tensile strength (F_{ten}). It was also assumed that the slab in tension losses its strength immediately after cracking, however, the steel rebar effect in this region were ignored for modelling simplicity, but this could have been considered using parallel elements. The slab elements tension force was calculated as, $F_{ten} = f'_{ct} \times A_s$ where f'_{ct} is maximum tensile stress (i.e.$0.36\sqrt{f'_c}$, here f'_c is in Mpa) and 'A_s' is the effective slab area ($B_{eff} \times t_c$). The struts in the slab-column interaction zone were assigned with the compression-only properties, whereas the tie members were assigned with tension only property. Both the transverse and longitudinal tie members were modelled as linear elastic members with the material properties of the rebars.

6.3.5 Material properties

The material properties used in the macro model were similar to the material properties used in the micro model which are reported in the Section 6.2.2.

6.3.6 Boundary Conditions and Loading Protocol

To replicate the boundary conditions of the tested frame subassembly, the beam ends were provided with the roller supports and the column bottom with a pin support. The shear studs and the corners of strut-and-tie elements were provided with the out-of-plane restraints to avoid numerical instability as depicted in Figure 6.25a. Displacement control loading protocol as specified in ACI T1.1-01 [57] was applied to the column top, and the numerically applied loading protocol was same as that of the loading protocol used in the experimental tests.

6.3.7 Results and Discussion

The comparison of the overall hysteresis behaviour of the frame sub-assemblies with different slab configurations obtained using the numerical performed using SAP2000 (macro model) with the corresponding experimental test results are shown in Figure 6.32. It can be observed that the numerical model was able to simulate the cyclic behaviour of the frame sub-assembly with the different slab configurations with a reasonable accuracy. Also, it can be seen from the load-displacement plots that the numerical model was able to capture the initial lateral stiffness,

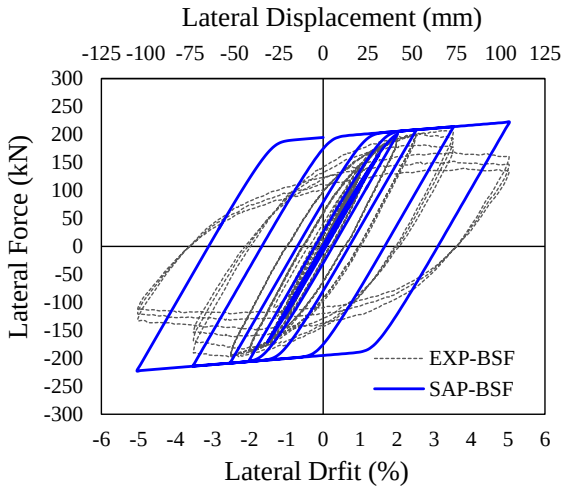

a) Bare Steel Frame

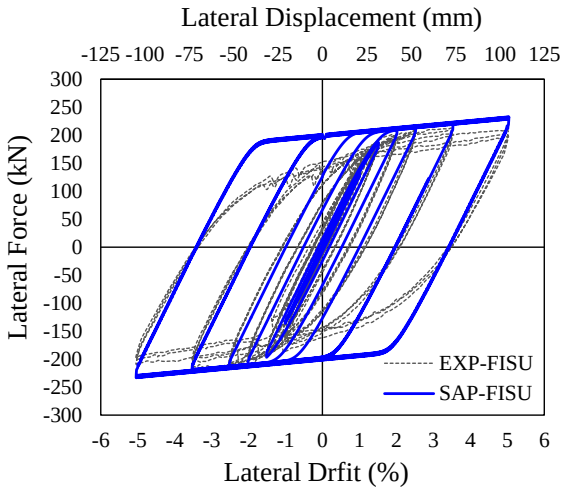

b) Fully Isolated Slab Unit

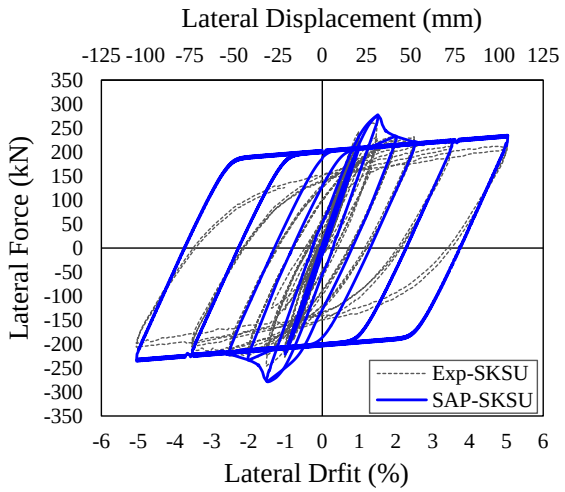

c) Shear Key Slab Unit

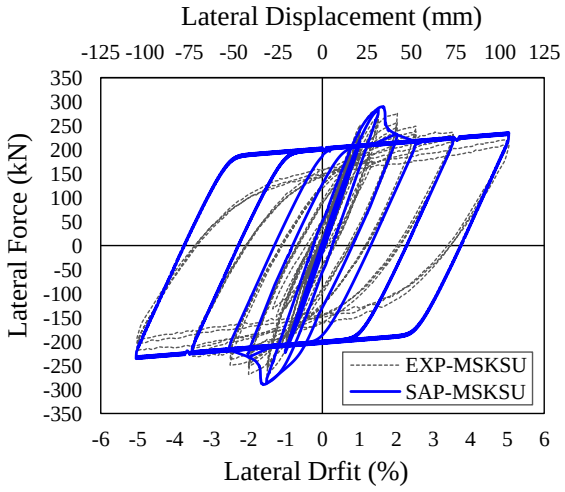

d) Modified Shear Key Slab Unit

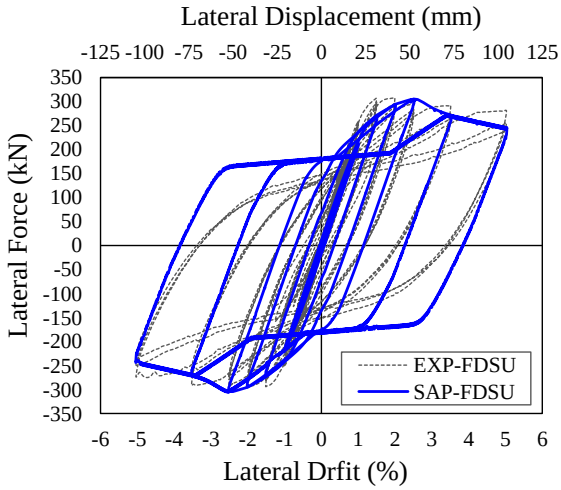

e) Full Depth Slab Unit

Figure 6.32 Comparison of Numerically Simulated Hysteresis Plots with Test Results

which is in close agreement with the experimental test results and is summarised in Table 6.5. The deviation in hysteresis loop of the BSF frame sub-assembly shown in Figure 6.32a was due to the limitation of the nonlinear spring, which cannot capture the degradation associated with the buckling of beam flanges (as observed in the experimental test). It is clear that the developed numerical model was able to accurately simulate the hysteresis behaviour of the FI-SU, SK-SU, MSK-SU, and FD-SU frame assemblies as shown in Figure 6.32b-e.

Table 6.5: Comparison of Sub-assemblies Initial Stiffness and Peak Strength of Numerical Macro Model with Experimental Results

Test Specimen	**Initial Stiffness (kN/m)**			**Peak Strength(kN)**		
	Numerical (Macro Model)	**Experimental**	**Deviation (%)**	**Numerical (Macro Model)**	**Experimental**	**Deviation (%)**
Bare Steel Frame **(BSF)**	6212	6156	1.0	214.11	206	4
Fully Isolated Slab Unit **(FI-SU)**	7879	8747	10	219	211.4	4
Shear Key Slab Unit **(SK-SU)**	13183	15031	12	277.62	263	6
Modified Shear Key Slab Unit **(MSK-SU)**	13283	14506	8	271.94	285.2	5
Full Depth Slab Unit **(FD-SU)**	13298	16402	19	326.68	306.3	7

In the current model, the properties of contact spring (used at slab-column interaction) were considered the concrete bearing/crushing failure, however the effect of other failure modes (shown in Figure 6.33) such as; (i) shear failure along column flange tips, (ii) strength of the

compression strut along length, (iii) yielding of transverse and longitudinal rebars, and (iv) column flange bending is not considered in the current macro-model for the modelling simplicity. As seen above, even considering the concrete bearing/crushing failure mode, the macro-model could reliably predict the frame sub-assembly lateral strength, a further refinement can be done in the proposed macro-model to consider the effect of failure modes listed above.

6.4 Analytical Prediction of Lateral Strength & Stiffness and Comparison with the test Results

In this section analytical equations to predict the lateral strength and stiffness of the frame subassemblies with different composite slab configurations was developed. As mentioned before, the composite slab resists the lateral load by developing force transfer Mechanism-1 and Mechanism-2. Figure 6.33 explains the force transfer mechanisms in the slab and possible modes of failure within the slab-column interaction zone. In cases where the Mechanism-1 was active, the lateral strength of the frame sub-assembly depends on the strength of the shear stud (i.e. mode-1), or crushing of the concrete at the column outer flanges (i.e. mode-2), or bending of the column flanges (i.e. mode-6), or yielding of tie reinforcement (i.e. mode-7 or mode-8). For the cases where Mechanism-2 was active, the strength hierarchy depends either on strength of the shear stud (i.e. mode-1), or the crushing of the concrete at the column internal flanges (i.e. mode-3), or shear failure along the column flange tips (i.e. mode-4), or strength of the compression strut (i.e. mode-5), or bending of the column flanges (i.e. mode-6), or yielding of tie reinforcement (i.e. mode-7 or mode-8). In the cases where both force transfer mechanisms (Mechanism-1 and Mechanism-2) are active, the frame sub-assemblies lateral strength depends on the strength hierarchy of the different modes of failure shown in Figure 6.33. As no bending in the column flanges was observed in the experimental test, this mode of failure was ignored in the analytical computations. As mentioned before, the lateral strength of the frame sub-assembly at the column centre was computed using the horizontal and rotational equilibrium of the internal forces shown in Figure 6.34.

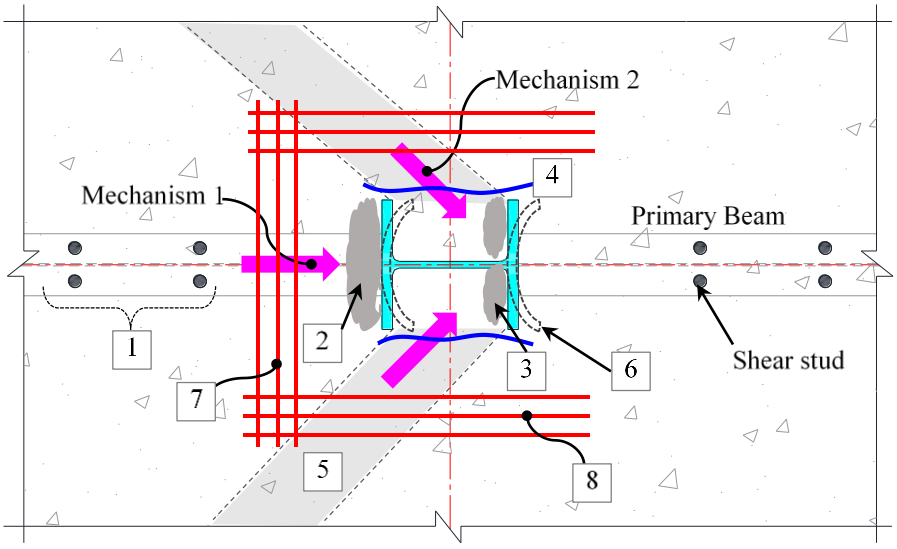

1	: Failure of shear studs	5	: Strength of the compression strut
2	: Concrete crushing on column outer flanges	6	: Strength of the compression strut
3	: Concrete crushing on column internal flanges	7	: Transverse tie (rebar) yielding
4	: Shear failure along column flange tips	8	: Longitudinal tie (rebar) yielding

Figure 6.33 – Possible Modes of Failure in the Slab-Column Interaction Zone

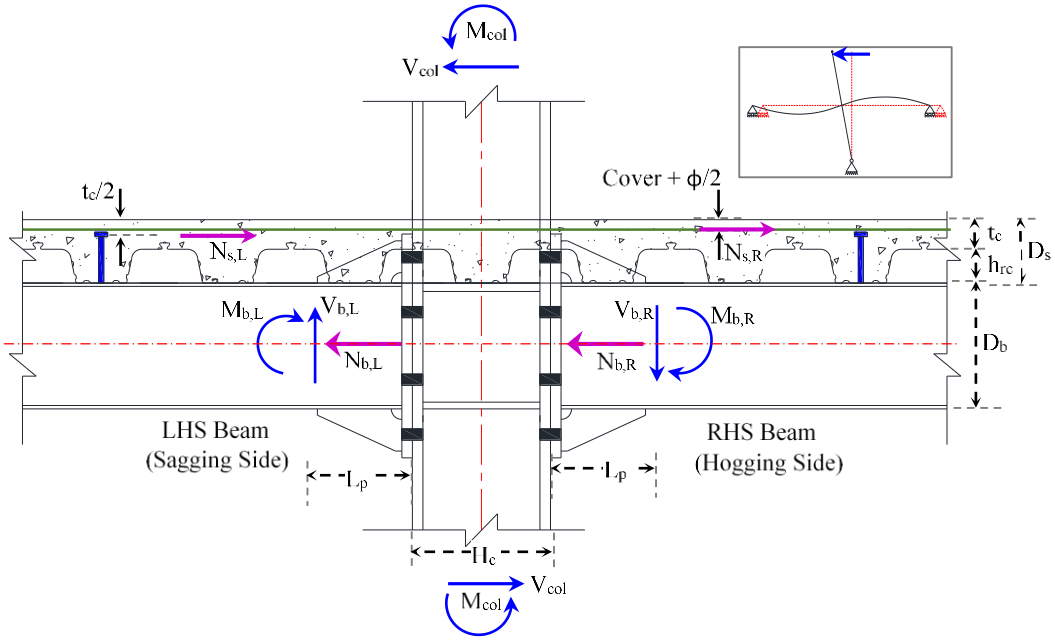

a) Forces on the Joint

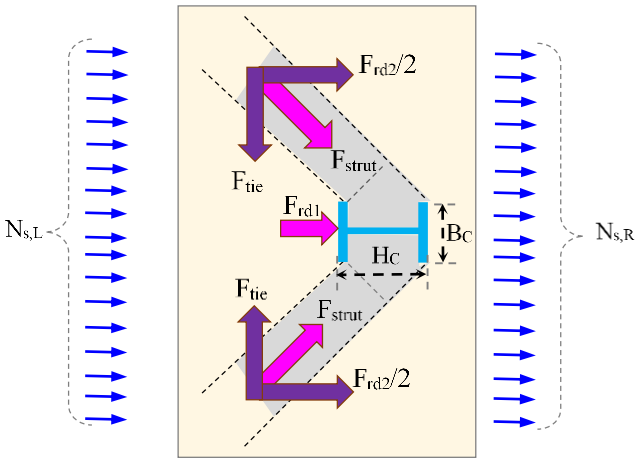

b) Forces in the Slab-Column Interaction Zone

Figure 6.34 Forces in the Beam-Column Sub-assembly

The internal slab force ($N_{s,L}$) on the sagging side of the slab was assumed to act at the mid-depth of the topping concrete (i.e. $t_c/2$), whereas on the hogging side the internal slab force ($N_{s,R}$) was assumed to act the centre of the rebar mesh (Cover + $\phi/2$), which is schematically shown in Figure 6.34a. This assumption arrived because, as the concrete cracks in tension, and the forces are transferred through the rebars. The slab forces on the sagging (left) and hogging

(right) sides of the frame sub-assembly are evaluated using the following equations:

$$N_{s,L} = min\begin{cases} Shear\ Stud\ Strength\ (F_{stud} = n_s \times P_{rk}) \\ Concrete\ Compresive\ Strength\ (F_{conc} = 0.85f_c' \times b_{eff} \times t_c) \\ Steel\ Beam\ Strength\ \left(F_{steel} = A_g \times f_y\right) \end{cases} \quad (6.18)$$

$$N_{s,R} = min\begin{cases} Shear\ Stud\ Strength\ (F_{stud} = n_s \times P_{rk}) \\ Rebar\ Strength\ \left(F_{rebar} = n_{\emptyset} \times A_{\emptyset} \times f_{y\emptyset}\right) \\ Steel\ Beam\ Strength\ (F_{steel} = A_g \times f_y) \end{cases} \quad (6.19)$$

where:

P_{rk}	=	Characteristic strength of the shear stud
n_s	=	Number of the shear studs
f'_c	=	Concrete compression strength
B_{eff}	=	Effective width of the composite slab
t_c	=	Effective thickness of the composite slab (topping slab thickness)
A_g	=	Area of steel beam framing into the column
f_y	=	Yield strength of the steel beam flange
n_ϕ	=	Number of rebars within effective width of the concrete slab
A_ϕ	=	Area of individual rebar
$f_{y\phi}$	=	Yield strength of the rebar

As mentioned before, at the slab-column interaction zone, the two force transfer mechanisms are developed as shown in Figure 6.34b. The first one is Mechanism-1 (i.e. the direct compression on the column outer flanges, F_{rd1}) and the second one is Mechanism-2 (i.e. compressed concrete struts inclined to the column sides, F_{rd2}). As mentioned before in Section 3.3.3, the force transfer Mechanism-3 (i.e. the force transferred through the secondary/transverse beam framing into the column web) was not considered in the experimental investigation. However, in the conventional slab construction where the slabs with the shear studs were connected to the transverse beam, the force transfer Mechanism-3 exists. One of the tests conducted by Hobbs [3] has the frame sub-assembly configuration similar to that of the conventional construction practice with the longitudinal deck orientation (i.e. deck ribs oriented parallel to the main beam), wherein all the three force transfer mechanisms are active and this configuration is considered to predict the strength associated with Mechanism-3. The resistance offered by Mechanism-1 can be related to the crushing strength of the concrete as suggested by Braconi et al. [27]. The internal force developed in the Mechanism-1 was calculated using the following equation (reproduced from EC8 [14]):

$$F_{rd1} = 0.85f_c' \times B_c \times t_c \quad (6.20)$$

The strength associated with the force transfer Mechanism-2 was developed through formation two compressive struts on the column sides which is shown in Figure 6.34b. The angle of inclination of the compression strut in the Mechanism-2 was around 45°[14]. The schematic

representation of the force transfer Mechanism-2 is shown in Figure 6.35.

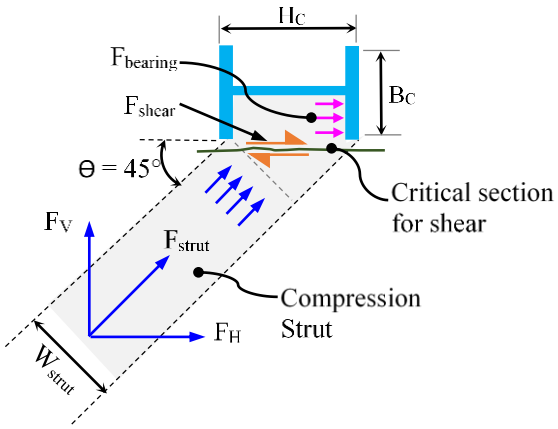

Figure 6.35 Schematic Representation of Force Transfer Mechanism-2

The compressive struts in the Mechanism-2 are analogous to the inclined struts formed into the reinforced concrete deep beam. The amount of interaction force at the column sides depends on the (i) bearing force developed on the internal column flanges, (ii) shear capacity along the column flange tips, and (iii) capacity of the compression strut. The width of the compression strut (W_{strut}) was calculated using the following equation:

$$W_{strut} = H_c \cos\theta \tag{6.21}$$

The force in the compression strut was calculated using Equation 6.22.

$$F_{strut} = \upsilon \times 0.85 f_c' \times W_{strut} \times t_c \tag{6.22}$$

The horizontal and vertical force component (F_H and F_V) of the compression strut are given by equation 6.23 and 6.24 respectively.

$$F_H = F_{strut} \cos\theta = (\upsilon \times 0.85 f_c' \times W_{strut} \times t_c) \cos\theta \tag{6.23}$$

$$F_V = F_{strut} \sin\theta = (\upsilon \times 0.85 f_c' \times W_{strut} \times t_c) \sin\theta \tag{6.24}$$

where:

υ	=	Reduction factor [14, 30]
W_{strut}	=	Width of the compressive strut
f'_c	=	Concrete compression strength
t_c	=	Effective thickness of the composite slab (topping slab thickness)

The shear resistance (F_{shear}) at the critical section (located at the tip of the column flange as shown in Figure 6.35) was calculated using the shear friction method. The shear resistance provided by the rebar mesh was not considered here since the rebar mesh in this zone may be cut for construction. However, the shear resistance/capacity of the section (next to the column flange tip) can be enhanced by providing the shear key rebars (as discussed in Chapter 5). The shear resistance (F_{shear}) at the critical section in front of the column tip was calculated using

Equation 6.25 [47].

$$F_{shear} = A_v f_{y\phi}(\mu \sin\alpha + \cos\alpha) + N^*\mu \quad (6.25)$$

where:

A_v	=	Area of the shear key rebars
$f_{y\phi}$	=	Yield strength of the shear key rebar
μ	=	Coefficient of friction = 1.4λ, for concrete placed monolithically
λ	=	Reduction factor for shear-friction strength = 1.0 for normal density concrete
N^*	=	Load acting perpendicular to the shear plane = F_V
α	=	Angle between shear-friction reinforcement and shear plane

The slab interaction with the internal column flange results in bearing force ($F_{bearing}$), and this can be calculated as:

$$F_{bearing} = 0.85 f_c' \times \left(\frac{B_c - t_{wc}}{2}\right) \times t_c \quad (6.26)$$

where:

B_c	=	Column flange width
t_{wc}	=	Thickness of the column web

As discussed earlier, the internal force associated with the Mechanism-2 (F_{rd2}) depends on the strength hierarchy; (i) horizontal component of the compressive strut, (ii) shear resistance at the critical section, (iii) bearing resistance at the internal column flange. The internal force was calculated using Equation 6.27.

$$F_{rd2} = min\begin{cases} 2.F_H \\ 2.F_{shear} \\ 2.F_{bearing} \end{cases} \quad (6.27)$$

In the conventional slab construction, in addition to the above-mentioned force transfer mechanisms (i.e. Mechanism-1 and Mechanism-2), force transfer Mechanism-3 was developed through the interaction of the shear studs (installed on the secondary beam) and the concrete. The compression force developed on the shear studs was transferred to the column through shear, and twisting of the transverse beam [30]. Figure 6.36 explains pictorially, the slab force transfer Mechanism-3 from transverse beam to the column.

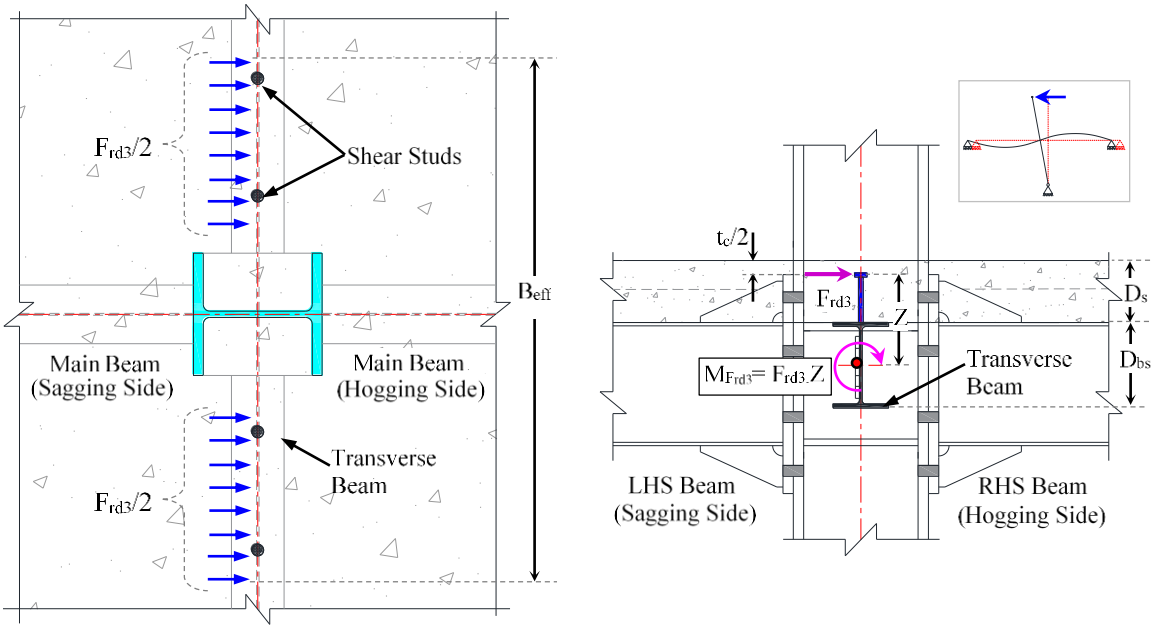

a) Plan View **b) Sectional Elevation View**

Figure 6.36 Slab Force Transfer on the Transverse Beam (Mechanism-3)

The internal force associated the Mechanism-3 was calculated based on the recommendations specified by EC8 [14], which is given by Equation 6.28.

$$F_{rd3} = n_{s\_tr} \times P_{rk} \tag{6.28}$$

where:

P_{rk} = Characteristic strength of the shear stud
n_{s_tr} = Number of the shear studs on the transverse beam installed within the effective width
B_{eff} = Effective width of the composite slab

The additional in-plane moment demand on the column panel zone due to the force transfer Mechanism-3 is calculated as:

$$M_{rd3} = F_{rd3}\left(\frac{D_{bs}}{2} + D_s - \frac{t_c}{2}\right) \tag{6.29}$$

At the slab-column interaction, the total interaction force (F_{int}) developed due to Mechanism-1 (F_{rd1}), Mechanism-2 (F_{rd2}), and Mechanism-3 (F_{rd3}) was calculated as the summation of the individual forces, which is given by Equation 6.30.

$$F_{int} = F_{rd1} + F_{rd2} + F_{rd3} \tag{6.30}$$

The governing slab force is a minimum of the internal force developed in the composite section and the force developed due to the mechanisms-1, 2 and 3, which is given by the following equation:

$$N_{slab} = minimum\ of \begin{cases} F_{int} \\ N_{sL} + N_{sR} \end{cases} \tag{6.31}$$

The total moment acting at the column centre ($M_{col,\,CL}$) accounting for the beam and slab effect was calculated as:

$$M_{col,CL} = M_{pb,L} + M_{pb,R} + N_{slab}\left(\frac{D_b}{2} + D_s - \frac{t_c}{2}\right) + V_{b,R}\left(\frac{D_c}{2} + L_p\right) + V_{b,L}\left(\frac{D_c}{2} + L_p\right) + F_{rd3}\left(\frac{D_{bs}}{2} + D_s - \frac{t_c}{2}\right) \tag{6.32}$$

In the above equations, the beam moments ($M_{pb,L}$ & $M_{pb,R}$) are modified to consider the axial-moment interaction as per NZS3404:1 [5], the modified beam moments for the sagging and hogging sides are calculated as:

$$M_{pb,L} = min \begin{cases} 1.18\left(1 - {\left(N_{slab}/2\right)}/{A_{b,L}f_{y,L}}\right)M_{b,L} \\ M_{b,L} \end{cases} \tag{6.33}$$

$$M_{pb,R} = min \begin{cases} 1.18\left(1 - {\left(N_{slab}/2\right)}/{A_{b,R}f_{y,R}}\right)M_{b,R} \\ M_{b,R} \end{cases} \tag{6.34}$$

where:

$M_{pb,L}$ & $M_{pb,R}$	=	Modified moment in left (sagging) and right (hogging) beam respectively
$N_{b,L}$ & $N_{b,R}$	=	Axial force in the left and right beam respectively, $N_{b,L} = N_{s,L}$ and $N_{b,R} = N_{s,R}$
$A_{b,L}$ & $A_{b,R}$	=	Area of the left and right beam respectively
$f_{y,L}$ & $f_{y,R}$	=	Yield strength of steel beam flange of the left and right beam respectively
$M_{b,L}$ & $M_{b,R}$	=	Beam maximum section moment capacity at the plastic hinge location in left and right beam respectively [76, 99, 102]
	=	$(f_y + f_u)/2.\ Z_e$

The shear demand in the beam corresponding to the nominal yield strength of the beam is given by:

$$V_{b,L} = \frac{M_{b,L}}{L_{b,L}}\ \&\ V_{b,R} = \frac{M_{b,R}}{L_{b,R}} \tag{6.35}$$

where:

$L_{b,L}$ & $L_{b,R}$	=	Beam length between plastic hinge (i.e. tip of the gusset plate) and point of contraflexure for the left and right beam respectively

The predicated lateral strength at the column top ($V_{col,prd}$) is evaluated the story height (H) as:

$$V_{col,prd} = \frac{M_{col,CL}}{H} \tag{6.36}$$

The lateral strength of the tested frame sub-assemblies was calculated using the above mentioned analytical equations. The lateral strength of the frame sub-assembly corresponding to the yield strength (f_y), average strength ((f_y+f_u)/2), and the ultimate strength (f_u) of the beam was calculated. Table 6.6 summaries the predicted lateral strength of the tested frame sub-assemblies and compared with the test results. The lateral strength corresponding to the yield and ultimate strength of the beam provides the lower and upper bound values. It can be seen from the Table 6.6 that the lateral strength calculated based on the average strength of the beam was in close agreement with the experimental test results. Based on the results summarised in Table 6.6, it can be concluded that the proposed analytical methodology can reliably predict the lateral strength of the frame sub-assembly with different slab configuration. Also, the proposed methodology considers the strength hierarchy of all possible failure modes depicted in Figure 6.33 and accounts for the effect of different force transfer mechanisms (i.e. Mechanism-1, 2 and 3).

Table 6.6 Comparison of Predicted Lateral Strength of Frame Sub-assemblies with Test Results

Specimen Description	**Predicted Lateral Strength (kN)**			**Experimental Lateral Strength (kN)**
	Lower Bound based on yield strength (f_y)	**Upper Bound** based on ultimate strength (f_u)	**Average** based on strength (f_y + f_u)/2	
Bare Steel Frame **(BSF)**	174.54	255.88	215.21	206
Fully Isolated Slab Unit **(FI-SU)**	174.54	255.88	215.21	211.4
Shear Key Slab Unit **(SK-SU)**	246.37	318.8	282.6	263
Modified Shear Key Slab Unit **(MSK-SU)**	252.77	322.08	287.43	285.2
Full Depth Slab Unit **(FD-SU)**	250.17	320.75	285.46	306.3
Transverse Deck Slab Unit **(TD-SU)** [3]	278.52	349.79	314.15	305
Longitudinal Deck Slab Unit **(LD-SU)** [3]	313.62	379.22	346.42	361

The frame sub-assemblies considered in the present study represent the interior joint of a typical steel frame building. When the internal frame sub-assembly is subjected to lateral

loads, it results in the development of positive bending (i.e. sagging) in one beam and negative bending (i.e. hogging) in another beam, which leads to a different moment of inertia for the sagging and hogging sides. Therefore, the initial lateral stiffness of the frame sub-assemblies with a composite slab was calculated using an equivalent moment of inertia (I_{eq}), which takes into account for the effective moment of inertia on the sagging and hogging sides, which is given by Equation 6.37 [14, 103]:

$$I_{eq} = 0.6I_{eff\_sag} + 0.4I_{eff\_hogg} \tag{6.37}$$

The effective moment of inertia of the composite beam (I_{eff}) considering the effect of partial composite action was calculated using Equation 6.38 [5]:

$$I_{eff} = I_{st} + 0.85p^{0.25}(I_{tr} - I_{st}) \tag{6.38}$$

where:

I_{eff_sag} & I_{eff_hogg}	=	Effective moment of inertia of composite beam in positive (sagging) bending and negative (hogging) bending respectively
I_{st}	=	Moment of inertia of steel beam alone
I_{tr}	=	Moment of inertia of composite beam transformed into an equivalent steel section (refer Appendix E)
p	=	Percentage of partial of composite action

Detailed calculations for the evaluation of initial lateral stiffness and lateral strength of the frame sub-assembly are reported in Appendix E. The comparison of analytically predicted strength and stiffness of the frame sub-assemblies with the different slab configurations with the test results are shown in Figure 6.37. As observed in the experimental tests, FI-SU frame sub-assembly possesses higher stiffness as compared to that of a bare steel frame, but the peak lateral strength was same for both the cases. Ignoring the slab contribution in the calculation of initial stiffness of FI-SU frame sub-assembly will result in an underprediction of the initial lateral stiffness. Therefore, the initial stiffness of the isolated slab unit (FI-SU) was calculated assuming the effective width of the slab equal to the width of the beam flange. It can be seen from the Figure 6.37 that the experimentally obtained peak lateral strength falls within the predicted lower and upper bound values. Based on the compression study, it can be concluded that the proposed methodology can reliably predict the strength and stiffness of the frame sub-assemblies with the different slab configurations.

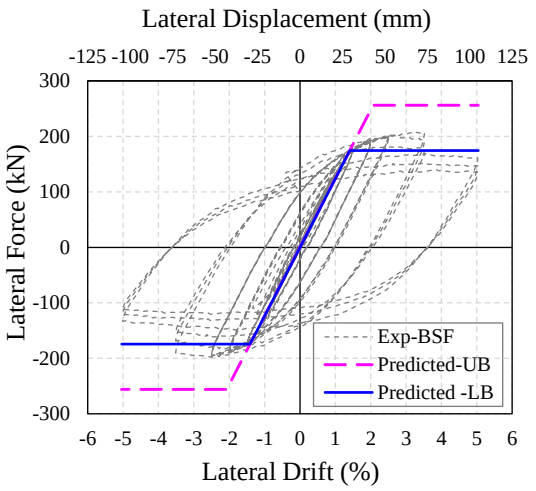

a) Bare Steel Frame

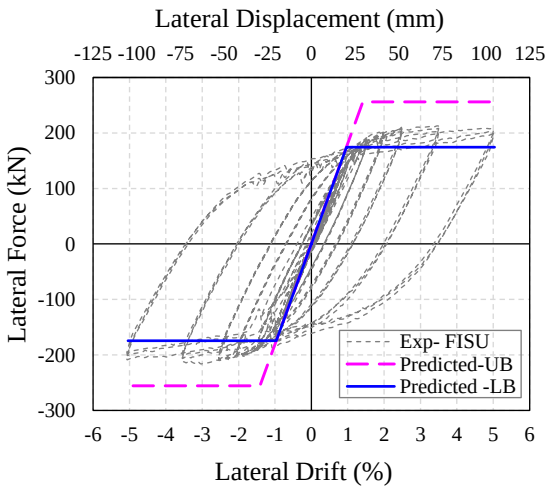

b) Fully Isolated Slab Unit

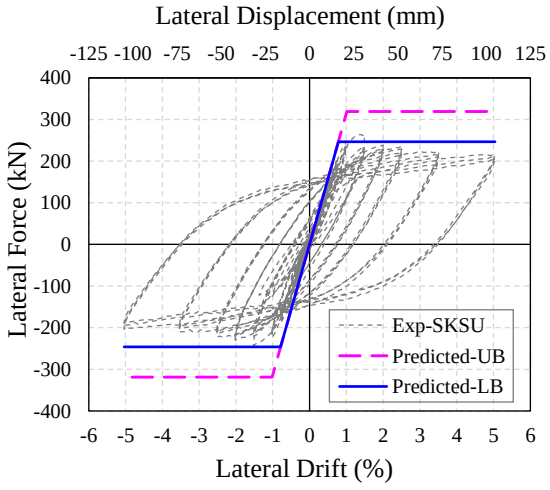

c) Shear Key Slab Unit

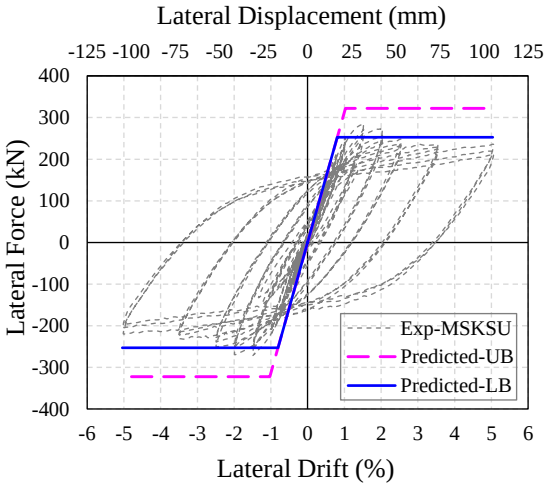

d) Modified Shear Key Slab Unit

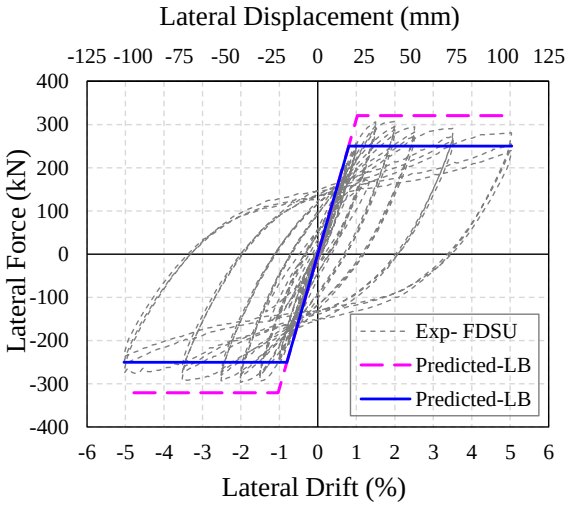

e) Full Depth Slab Unit

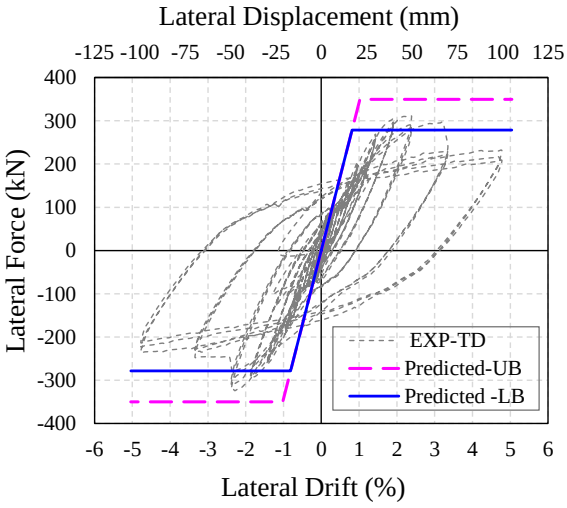

f) Transverse Deck Slab Unit [3]

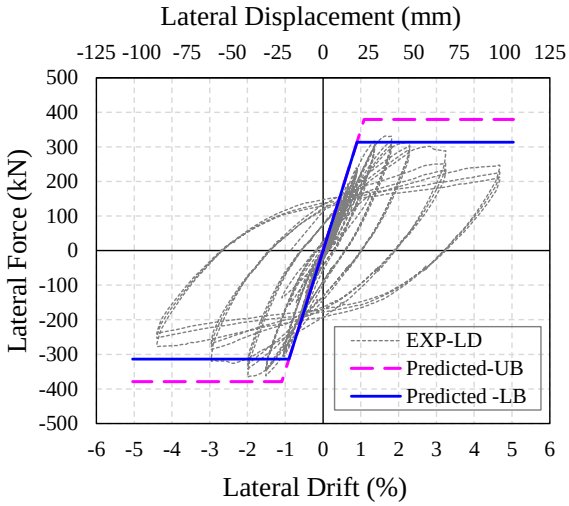

g) Longitudinal Deck Slab Unit [3]

Figure 6.37 - Comparison of Lateral Strength & Stiffness : Predicted and Experimental

The moment demand contribution on the column due to beam and slab deformations is shown in Figure 6.38. It's clear that the slab interaction with the column contributed around 30 to 40% of the total moment demand on the column. The moment demand on the column due to the composite action of the slab primarily depends on the degree of the interaction and the number of active force transfer mechanisms. As it can be seen in case of the isolated frame sub-assembly (FI-SU), the moment demand due to slab deformation onto column demand is negligible; this was due to the absence of the active force transfer mechanisms. In case of the longitudinal deck frame sub-assembly (LD-SU) with all three active force transfer mechanisms, the moment demand due to slab deformation was maximum (i.e. around 44%) when compared to slab contribution in other frame sub-assemblies. Note that the steel beam contribution includes the axial (P)-moment (M) interaction, so the strength associated with the beam on specimens with a slab is not the same as that without the slab.

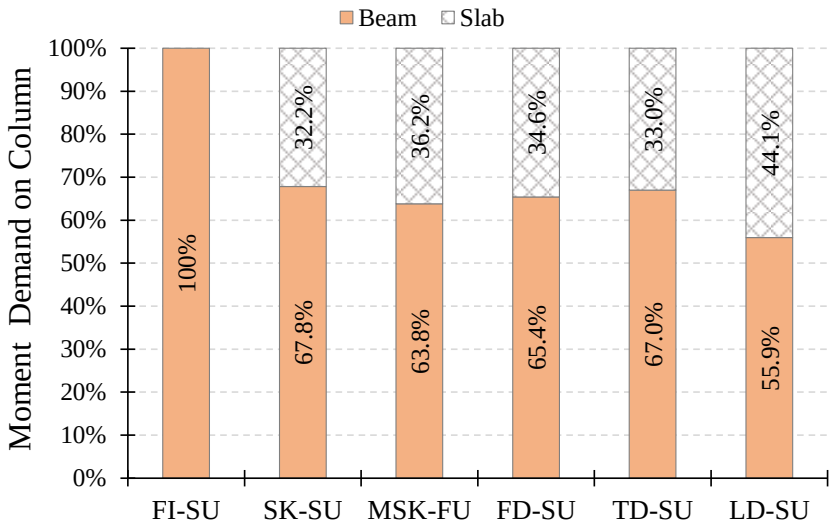

Figure 6.38 – Moment Demand onto Column due to Beam and Slab Deformation

The lateral strength of the frame sub-assembly with the composite deck slab was dictated by a number of active force transfer mechanisms and the strength of each individual mechanism. Based on the analytical studies, the two major parameters that affect the lateral strength of the frame sub-assembly are; (i) the degree of composite action, and (ii) the effectiveness factor (υ). Also, a parametric study was carried out to evaluate the influence of these parameters on the lateral strength of the frame sub-assembly with different slab configurations.

The effect of the degree of the composite action (i.e. the number of shear studs) on the frame sub-assembly's lateral strength was studied, and the summary of the results are reported in Table 6.7. In case of the full depth frame sub-assembly (FD-SU), the lateral strength was increased by 10% for the full composite action. The frame sub-assembly's lateral strength was limited by the studs shear strength and the governing force transfer mode (i.e. shear stud strength) remains same irrespective of the percentage of the composite action. This was because the provision of full depth slab around the column enhances the strength of the other modes. In case of the transverse deck and longitudinal deck frame sub-assemblies (TD-SU and LD-SU), the governing force transfer mode changes from strength of the shear stud (46% composite action) to the concrete crushing onto the column flange (i.e. mode 2 and mode 3 shown in Figure 6.33) with increase in the percentage of composite action.

Table 6.7 Effect of Composite Action (P_{comp}) on Lateral Strength of Frame Sub-assemblies

Specimen Description	**Percentage of composite action (P_{comp})**	**Predicted Lateral Strength (kN)**	**Governing Force Transfer Mode** (refer Figure 6.33)
Fully Isolated Slab Unit **(FI-SU)**	46%	215.21	Beam Yielding
	75%		
	100%		
Shear Key Slab Unit **(SK-SU)**	46%	282.59	Mode 3: Concrete crushing on internal column flanges
	75%		
	100%		
Modified Shear Key Slab Unit **(MSK-SU)**	46%	287.43	Mode 3: Concrete crushing on internal column flanges
	75%		
	100%		
Full Depth Slab Unit **(FD-SU)**	46%	285.46	Mode 1: Failure of shear stud
	75%	301.02	
	100%	314.76	
Transverse Deck Slab Unit **(TD-SU)** [3]	46%	314.15	Mode 1: Failure of shear stud
	75%	323.73	Mode 2 and Mode 3: Concrete crushing on column outer and internal column flanges
	100%		
Longitudinal Deck Slab Unit **(LD-SU)** [3]	46%	346.42	Mode 1: Failure of shear stud
	75%	362.27	Mode 2 and Mode 3: Concrete crushing on column outer and internal column flanges
	100%		

The influence of percentage of composite action on the frame sub-assembly lateral strength was seen only in the FD-SU, TD-SU, and LD-SU frame sub-assemblies, wherein both the force transfer Mechanism-1 and 2 were active, which is shown in Figure 6.39. In case of FI-SU frame sub-assembly where no active force transfer mechanisms, frame sub-assembly's lateral strength remains constant irrespective of the increase in the percentage of the composite action. Similar observations were made for the SK-SU and MSK-SU frame sub-assemblies, where only force transfer Mechanism-2 was active. It can be concluded that the lateral strength of the frame sub-assembly depends on the number of active force transfer mechanisms, and the strength associated with each individual components.

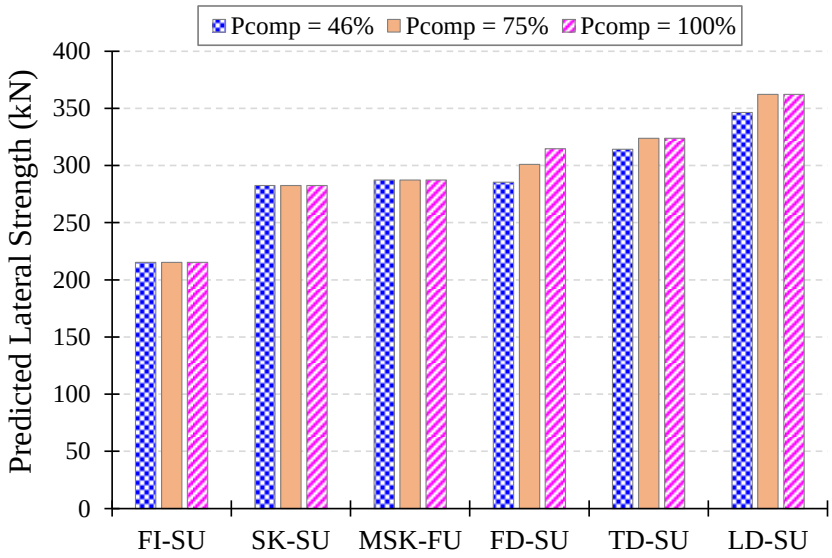

Figure 6.39 – Effect of Number of Shear Studs

As discussed earlier, the force transfer Mechanism-2 was developed due to the formation of the compression struts in the slab as shown in Figure 6.35. The compressive strength of these struts depends on the effectiveness factor (υ). The value of the compression strut effectiveness factor varies from 0.6 to 1.0 [30, 47, 104]. The effect of this factor (υ) on the frame sub-assembly's lateral strength was evaluated, and the results are reported in Table 6.8.

Table 6.8 Effect of the Factor (υ) on Lateral Strength of Frame Sub-assemblies

Specimen Description	**Compression strut effectiveness factor (ν)**	**Predicted Lateral Strength (kN)**	**Governing Force Transfer Mode** (refer Figure 6.33)
Fully Isolated Slab Unit **(FI-SU)**	0.6	215.21	Beam Yielding
	0.7		
	1.0		
Shear Key Slab Unit **(SK-SU)**	0.6	271.32	Mode 5: Strength of compression strut
	0.7	275.04	Mode 5: Strength of compression strut
	1.0	282.58	Mode 3: Concrete crushing on internal column flanges
Modified Shear Key Slab Unit **(MSK-SU)**	0.6	274.54	Mode 5: Strength of compression strut
	0.7	278.79	Mode 5: Strength of compression strut
	1.0	287.43	Mode 3: Concrete crushing on internal column flanges
Full Depth Slab Unit **(FD-SU)**	0.6	285.46	Mode 1: Failure of shear stud
	0.7		
	1.0		
Transverse Deck Slab Unit **(TD-SU)** [3]	0.6	314.15	Mode 1: Failure of shear stud
	0.7		
	1.0		
Longitudinal Deck Slab Unit **(LD-SU)** [3]	0.6	346.42	Mode 1: Failure of shear stud
	0.7		
	1.0		

The influence of the effectiveness factor on the sub-assembly's lateral strength was seen only in the SK-SU and MSK-SU frame sub-assemblies, where only Mechanism-2 was active which is shown in Figure 6.40, and the strength increment was around 5.0% by changing effectiveness factor (υ) from 0.6 to 1.0. However, in case of the frame sub-assemblies with the active Mechanism-1 and 2, the effect of the factor (υ) on the sub-assembly's strength is negligible. It can be concluded that the effect of effectiveness factor (υ) can be ignored for the practical purposes.

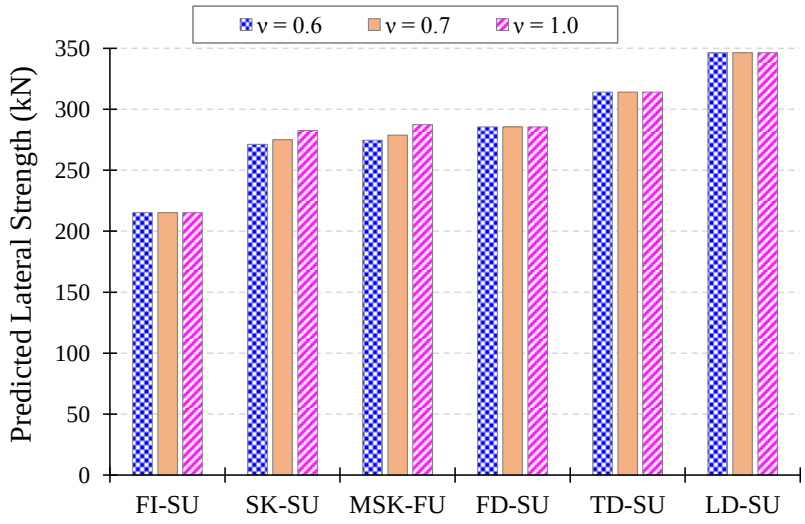

Figure 6.40 – Effect of Effectiveness Factor on the Lateral Strength of the Frame Sub-assembly

6.5 Conclusions

In this chapter, the hysteretic behaviour of the frame sub-assemblies with the different slab configuration was numerically investigated by using two modelling approaches, (i) micro-modelling, and (ii) macro-modelling. Also, a simple analytical framework was proposed to predict the lateral strength of the frame sub-assembly with different slab configuration. Based on the numerical and analytical investigations, the following conclusions are drawn;

xi) The developed 3D finite element model was able to predict the lateral strength and stiffness of the frame sub-assemblies with the different slab configurations. Also, it captured the location of the buckling in the beam flanges. The concrete damage plasticity (CDP) model was able to simulate the frame sub-assemblies nonlinear behaviour under monotonic loading. Modelling features such as contact elements and interaction elements were able to simulate the realistic behaviour of the frame sub-assembly with the composite slab.

xii) The micro modelling of the SK-SU and MSK-SU frame sub-assemblies were able to capture the spread of the compression strut associated with the force transfer Mechanism-2, and it matches with the specification of Eurocode 8 [14].

xiii) The simulated finite element model shows the high-stress levels in front of the column outer flanges associated with the Mechanism-1 and low-stress levels associated with Mechanism-2, which indicated that the resistance offered by Mechanism-1 is achieved first and based on the deformation compatibility, the force is distributed in Mechanism-2.

xiv) The average contact pressure resulted due to slab-column interaction was found to be lower than the compressive strength of the concrete (f'_c), and the localised contact pressure was higher than the average contact pressure, this was due to stress concentration.

xv) Based on the numerical investigation, the most likely strength hierarchy in a frame sub-assembly with all three active force transfer mechanisms would be as follows-

a) Yielding of the beam
b) Crushing of the concrete in front of the column flanges
c) Concrete shear failure next to the column flange tips
d) Buckling of the beam flanges in case of the non-compact section

xvi) The proposed macro model developed using the strut-and-tie approach was able to simulate the cyclic behaviour of the frame sub-assembly with the different slab configurations. It can capture key modes of deformation, and it is simple and easy to implement in practice.

xvii) The macro modelling of SK-SU, MSK-SU, and FD-SU frame sub-assemblies was similar to the macro modelling of the FI-SU frame sub-assembly; the compression and tension forces associated with the mechanisms-1 and 2 were modelled using strut-and-tie elements.

xviii) The strength contributed by the Mechanism-1 and 2 in the composite slab to the frame sub-assemblies strength can be computed using the developed strut-and-tie model, which was developed by utilising and modifying the equation available in the Eurocode 8 [14]. By comparing the analytical predicted lateral strength with the numerical analysis and test results, it can be concluded that the developed analytical approach considers all significant modes of failure and the strength hierarchy associated with force transfer Mechanism-1 and 2.

xix) An analytical equation developed using shear friction theory can be reliably used to estimate the shear capacity of the concrete and rebars (provided within the column web).

xx) The slab interaction with the column influences the moment demand onto the column, and it contributes around 30 to 40% of the total moment demand.

xxi) Based on the parametric study results, it can be concluded that the number of shear studs has negligible effect in case of FI-SU, and SK-SU and MSK-SU (with only one active mechanism) frame sub-assembly's strength, whereas in other frame sub-

assemblies (i.e. FD-SU, TD-SU, and LD-SU), the effect of composite action varies, and it cannot be ignored.

xxii) The proposed analytical method was found reasonable to estimate the moment demand on the column due to the slab-column interaction and different force transfer mechanisms. The developed analytical model was simple and easy to implement in practice. Engineers can choose the suitable construction detailing, and the proposed method can reliably estimate the column moment.

Chapter 7: Conclusions and Scope for Future Research Work

7.1 Introduction

In this research, the non-linear cyclic behaviour of the beam column sub-assemblies with different slab configurations were investigated. To assess the effect of different slab configurations on the seismic behaviour of frame sub-assemblies, this research study was divided into four different stages as set out earlier in Section 1.3; (i) identification of different composite slab configurations, (ii) experimental test program, (iii) numerical analysis, and (iv) analytical methodology. The associated research objectives related to each stage were investigated, and the key findings of the research in relation to the questions presented in Section 1.3 are reported.

7.2 Key Findings/Conclusions

i) ***Is it possible to minimise the damage to the composite slab (around the column) in a seismic shaking by isolating the column from the slab?***

Structural damage to the composite slab in the seismic event was limited by isolating the slab around the column. However, an appropriate isolation material is required. This material should be stiff enough to resist the pressure of wet concrete, but not so stiff that it transfers bearing forces to the column, and it should be fire resistant. In this research different infill material such as Polystyrene, Spiralite 400, and Actifoam were tested, and the test results are reported. Based on the experimental results, actifoam material was found suitable to be used as an infill material. It was experimentally shown that the damage to the composite slab could be almost eliminated in the tested isolated frame sub-assembly (FI-SU) by isolating the slab around the column. Also, the effect of isolating the slab on the strength and stiffness of the moment frame system was evaluated. It can be concluded that because of the isolation, the demand onto the column is only due to the steel beam overstrength capacity. The lateral strength and stiffness of the FI-SU frame sub-assembly were very much similar to that of the bare steel frame (BSF) sub-assembly, with beam top and bottom flange buckling as the predominant failure mode. Because of the lateral restraint offered by the slab to the beam flanges, the FI-SU sub-assembly exhibited negligible strength degradation, whereas BSF sub-assembly exhibited significant strength degradation at higher lateral drifts due to beam web and flange buckling. An additional requirement for isolation is that not only the column, but also the gusset plate, end-plate, and bolt heads, upon which the slab may bear, need to be isolated.

ii) ***Is it practicable to modify the detailing in the composite slab (within the column web region) so that the rapid strength degradation associated with the shear failure in the slab next to the column flange tips can be delayed and minimized?***

The load-displacement behaviour of the composite slab frame sub-assembly was improved by providing the shear key rebars within the column web in the SK-SU frame sub-assembly. Based on the comparative analysis between a frame sub-assembly with and without shear key rebars within a column web, it can be concluded that the peak strength was slightly increased, and the rate of the strength degradation was slightly decreased. The shear key rebar arrangement was modified and improved in the MSK-SU frame sub-assembly. Because of these modifications, the slab damage next to the column flange tips was minimised, and significant improvement in the post capping behaviour was observed. The provision of an additional confinement plates limited the spalling around the column. The load-displacement characteristics of Mechanism-2 can be significantly improved by the proposed detailing; it can be concluded that the overall hysteretic behaviour of the frame system with the proposed shear detailing can result in improved conventional frame system performance.

iii) ***Can the slab around the column be detailed such that strength degradation is minimised while composite strength is maintained?***

The provision of the full depth slab around the column with confinement reinforcement significantly improved the strength and stiffness of the frame sub-assembly and has been shown by tests on frame sub-assemblies with full depth slab configurations. This is due to activation of two force transfer mechanisms (Mechanism-1 and 2) in the frame sub-assembly with the full depth slab unit. Because of the confinement reinforcement, the overall ductility has been increased, and rate of the lateral strength degradation was decreased (by 75%). Also, due to the effective confinement around the perimeter of the column, the minimal concrete crushing in slab-column interaction zone was observed at the higher lateral drift levels, and the rate of the strength degradation was less than that of the shear key (SK-SU and MSK-SU) frame sub-assemblies. The sequence of failure for the full depth slab sub-assembly was; (a) yielding of the beam, (b) minor cover concrete spalling in front of the column flanges, (c) shear cracks next to the column flange tips (at 5.0% lateral drift), (d) beam buckling, and (e) transverse cracks in the slab.

iv) ***Does the sub-assembly's force-displacement hysteresis relationship change with different slab detailing?***

Experimental investigations were carried out under lateral quasi-static cyclic loading, to assess the effect of different composite slab configurations on the frame sub-assemblies performance. In general, all the tested frame sub-assemblies exhibited stable hysteresis behaviour primarily due to beam yielding in plastic hinge regions. However, the lateral secant stiffness, nominal lateral strength, energy dissipation, initiation and rate of strength degradation varied from one test to another primarily due to a different level of interaction of the composite slab with the steel beam and the column. Less damage has been observed in the specimen with the confined concrete in the slab-column interaction zone. The deck orientation affects both the strength and stiffness of the sub-assembly and specimen with longitudinal deck exhibiting a higher stiffness than the specimen with transverse deck. Provision of the gap between the slab and column minimises the slab damage at the slab-column interaction zone, whereas the isolated sub-assembly strength remains similar to the bare steel frame. The crack pattern in the composite slab primarily depends on the deck orientation and a number of active force transfer mechanisms between the slab and the column (i.e. Mechanisms-1, 2 and 3). Based on the experimental and numerical findings, it can be concluded that the overstrength factor for the design of the connection, column, and panel zone is in the range of 1.25 to 1.5, this is in agreement with the values specified in New Zealand steel structures standard (NZS3404:1 [5]). The force-displacement hysteretic behaviour of frame sub-assembly with the composite slab depends on the following important design and detailing parameters; (a) level of concrete confinement around the column, (b) level of isolation (i.e. fully isolated around the column, only outer column flanges isolated, and only inner column flanges isolated) and active force transfer mechanisms (Mechanism-1, 2 and 3), (c) deck tray direction, (d) depth of the confined concrete slab, and (e) percentage of composite action.

v) ***Can the experimental behaviour be reliably predicted by numerical modelling?***

The developed numerical models (3D monotonic finite element micro-model and cyclic macro-model) were able to reliably capture the nonlinear hysteretic behaviour of the tested frame sub-assemblies, and it was found that the predicted values were in close agreement with the test results (with deviation of 7% to 9%). The load resistance within the slab associated with force transfer mechanism can be reliably simulated/modelled using the developed macro modelling technique. In the proposed macro-model this has been captured using the strut-and-tie approach

(based on the recommendations of Eurocode 8 [14]), which is easy to implement in practice. The numerical macro modelling of SK-SU, MSK-SU, and FD-SU frame sub-assembly was very much similar to the numerical macro modelling of the FI-SU frame sub-assembly; the compression and tension forces associated with Mechanism-1 and 2 were modelled using strut-and-tie elements.

vi) ***Can simple hand methods be used to estimate composite beam-column slab sub-assembly parameters for design?***

An analytical methodology to evaluate the lateral strength of the frame sub-assembly with composite slab was proposed. The analytical equation is an improvement of the existing analytical equation (available in NZS3404 [5]) and considers the strength hierarchy of different active force transfer mechanisms for evaluation of the slab forces. The analytical equations can be used to evaluate the lateral strength of the frame sub-assemblies by simply using the beam plastic moment capacity (considering axial-moment interaction) and the slab forces based on the strut-and-tie mechanism. The lateral strength contributed by Mechanisms-1 , 2 and 3 in the composite slab to the frame sub-assembly can be estimated/computed using the strut-and-tie model which was developed utilising and modifying the equation available in Eurocode 8 [14]. By comparing the analytical predicted strengths with the numerical analysis and test results, it can be concluded that the developed analytical approach considers the significant modes of failure and strength hierarchy associated with force transfer Mechanisms-1, 2 and 3. The column demand due to the slab-column interaction can be reliably estimated using the proposed analytical equation and used for the design of the connection, panel zone, and column. Upper and lower bound strength was also estimated.

7.3 Scope for Future Research Work

This research study focuses on the experimental behaviour of the frame sub-assemblies with different slab configurations followed by the numerical simulation using 3D micro-model and macro-model using non-linear springs with frame elements. A simple analytical methodology has been proposed to estimate the demand on the column considering the effect of the composite slab on the beam-column subassembly of the moment resisting frame. The study covers a number of research aspects on slab effects. Still a number of areas in which future research work is needed to improve our understanding of the slab interaction with the column. The possible areas for future research are identified in order to complement the objectives accomplished in this study.

a) Study on Column Instability due to Slab Isolation

In a conventional steel moment resisting frame, the composite slab is casted aligned to the column thereby offering lateral support to the column. As concluded, the isolation of slab around the column, minimises the slab damage, but results in reduction of the effective lateral restraint offered to the column thereby making the column susceptible to local instability [19], particularly in minor axis of the moment resisting frame wherein the transverse beam is generally connected with shear tab/fin plate (pinned connections). Also in case of the gravity column, where all the beam framing into are connected with the pinned connection is susceptible to the local instability. There is a need to conduct both the experimental as well as numerical investigations to quantify the effect of the column axial load along with the lateral load on the beam-column sub-assembly with the isolated slab.

b) Possible Improvements to the Numerical Models

In the current research study, the tested frame sub-assemblies were numerically simulated using 3D finite element analysis under the monotonic loading to reduce the computational efforts. The finite element model was able to simulate both the strength and stiffness of the tested frame sub-assemblies with reasonable accuracy. However, it failed to capture the strength degradation associated with the brittle failure of concrete (especially in specimens with longitudinal deck). The proposed finite element model needs to be extended to simulate the behaviour of frame sub-assembly under the cyclic loading along with capturing the strength degradation. Further, the model can be extended to simulate the behaviour of frame sub-assemblies with bolted connections.

In case of the simplified macro-model, the nonlinear properties of the contact spring (representing the slab-column interaction in the macro-model) was calculated considering only the failure associated with the concrete bearing on the column flange. However, as discussed in Section 5.4, there are additional modes of failure namely; (i) shear failure along column flange tips, (ii) strength of compression strut, (iii) yielding of strut-and-tie rebars, and (iv) strength associated with column flange bending. There is a need to evaluate the contact spring properties based on the strength hierarchy of the above-listed failure modes. Also, the current model is based on the assumption of rigid panel zone and rigid connection. The macro-model needs to be extended to take into account the effect of panel zone deformation and connection rigidity. In addition to above, the effect of the force transfer Mechanism-3 needs to be considered in the contact spring calibration.

c) Experimental Investigation with Isolation on Column Sides

The primary objective of the frame sub-assemblies with shear key rebars (SK-SU and MSK-SU) was to improve the failure associated with the shear fracture at the column flange tips as well as to evaluate the effect of the force transfer Mechanism-2 on the sub-assemblies strength and stiffness. However, the tested sub-assemblies failed to address the sudden strength degradation associated with shear fracture at the larger drift cycles. This kind of failure can be avoided if the slab is isolated on the column sides (i.e. deactivation of the force transfer Mechanism-2), thereby relying on the force transfer through the bearing of the slab on the column outer flanges (i.e. Mechanism-1). There is need to investigate the effect of force transfer Mechanism-1 on the strength and stiffness of the frame sub-assembly. This will also help to understand the failure modes associated with the force transfer Mechanism-1.

d) Performance of Low Damage Connection with the Isolated Slab

Even though the slab was isolated and slab damage was eliminated, the damage to the beam is unavoidable due to the formation of the plastic hinges in the conventional steel frame system. However, in the existing low damage system (i.e. sliding hinge connections) where the damage to the frame components (beam and column) is minimal, with the addition of the proposed slab isolation technique (using actifoam or similar material), the damage to the composite slabs can be eliminated (as shown in this research), thereby minimising the damage to the structural components in an earthquake shaking. There is need to experimentally investigate the feasibility and seismic performance of low damage beam-column sub-assemblies with the isolated slab unit.

e) Investigation on Slab Performance in the Weak Axis Bending

The current study focuses on the effects of slab on the moment resisting frame (i.e. primary beam framing into the major axis of the column). However, the interaction of the slab on the column weak axis needs to be evaluated. Generally, the transverse beam (framing into the column weak axis) is connected using the shear tab/fin plate connection, and these plates are welded onto the column web. Under the bidirectional loading, the slab interaction with the weak axis of the column leads to development of the partially restraint connection. As observed by Green et al. [24], the panel zone yielding was due to out plane distortion of the column web caused by loading in the column weak axis, and resulted in a punch-through failure of the column web due to force transfer from the shear tab connection (provided in weak axis of the column). Although the authors suggested providing a full depth slab around the column will

improve its performance, no further information is available on the effect of the full depth slab on the weak axis of the column. Also, the height of the shear tab is generally provided equal to the depth of the transverse beam. If the height of shear tab is modified (i.e. increased) to fit into the column continuity plates (which are provided for the moment connection on column major axis), then the out of plane distortion of the column web panel can be minimised and there is need to investigate the performance of the proposed modified shear tab configuration considering the slab effect. Also, there is need to investigate the mode of the force transfer mechanisms acting on the column weak axis under the bidirectional loading and its effects on the strength and stiffness of the frame sub-assembly.

References

[1]. Johnson, R.P. and N. Molenstra (1991). "Partial shear connection composite beams for buildings." Proceedings of Institute of Civil Engineers, Part 2, 679-704.

[2]. Oehlers, D.J. and M.A. Bradford (1995). "Composite steel and concrete structural members : fundamental behaviour." Elsevier, Kidlington, Oxford, UK.

[3]. Hobbs, M. (2014). "Effects of Slab-Column Interaction in Steel Moment Resisting Frames with Steel-Concrete Composite Floor Slabs." Master Thesis, University of Canterbury, Christchurch, New Zealand.

[4]. ComFlor80 (2014). "Product guide ComFlor80, available at "http://www.comflor.co.nz/wp-content/uploads/ComFlor/Brochures/ComFlor80Brochure.pdf"."

[5]. NZS3404:1 (1997). "Steel structures standard part 1-Incorporating amendment no 1 and no 2", Standards New Zealand, Wellington.

[6]. MacRae, G.A., et al. (2007)."Overstrength effects of slabs on demands on steel moment frames." Pacific Structural Steel Conference 2007.

[7]. Mehanny, S.S. and G.G. Deierlein (2001). "Seismic damage and collapse assessment of composite moment frames." Journal of Structural engineering, 127(9), 1045-1053.

[8]. Lee, S.-J. and L.-W. Lu (1989). "Cyclic tests of full-scale composite joint subassemblages." Journal of Structural Engineering, 115(8), 1977-1998.

[9]. Hajjar, J.F., et al. (1998). "Seismic response of composite moment-resisting connections. II: Behavior." Journal of Structural Engineering, 124(8), 877-885.

[10]. Doneux, C. and H. Parung (1998)."A study on composite beam-column subassemblages." Proceedings of the 11th ECEE Conference, Paris.

[11]. Civjan, S.A., et al. (2001). "Slab effects in SMRF retrofit connection tests." Journal of Structural Engineering, 127(3), 230-237.

[12]. Braconi, A., et al. (2008). "Seismic performance of a 3D full-scale high-ductile steel–concrete composite moment-resisting frame — part II: test results and analytical validation." Earthquake Engineering & Structural Dynamics, 37(14), 1635-1655.

[13]. Leon, R.T., et al. (1998). "Seismic response of composite moment-resisting connections. I: Performance." Journal of Structural Engineering, 124(8), 868-876.

[14]. EC8 (2004). "Eurocode 8: Design of structures for earthquake resistance - Part 1: General rules, seismic actions and rules for buildings", European Committee for Standardization, B-1050 Brussels.

[15]. Salvatore, W., et al. (2005). "Design, testing and analysis of high ductile partial-strength steel–concrete composite beam-to-column joints." Computers & structures, 83(28), 2334-2352.

[16]. Moehle, J.P., et al. (2010). "Seismic Design of cast-in-place concrete diaphragms, chords, and collectors." Seismic design technical brief, US Department of Commerce, Building and Fire Research Laboratory, National Institute of Standards and Technology.

[17]. Cowie, K., et al. "Seismic design of composite metal deck and concrete-filled diaphragms–A discussion paper." Proc., NZSEE Conference.

[18]. Uang, C.-M. and C.-C. Fan (2001). "Cyclic stability criteria for steel moment connections with reduced beam section." Journal of Structural Engineering, 127(9), 1021-1027.

[19]. Zhang, X. and J.M. Ricles (2006). "Seismic behavior of reduced beam section moment connections to deep columns." Journal of structural engineering, 132(3), 358-367.

[20]. DuPlessis, D.P. and J.H. Daniels (1972). "Experiments on composite beams under positive end moment." Report No 374.2, Fritz Engineering Laboratory ,Lehigh University, Bethlehem, Pennsylvania.

[21]. Liu, J. and A. Astaneh-Asl (2000). "Cyclic testing of simple connections including effects of slab." Journal of Structural Engineering, 126(1), 32-39.

[22]. Leon R. T. (1994). "Composite semi-rigid construction." Engineering Journal, 31, 57-66.

[23]. Liu, J. and A. Astaneh-Asl (2004). "Moment–rotation parameters for composite shear tab connections." Journal of Structural Engineering, 130(9), 1371-1380.

[24]. Green, T.P., et al. (2004). "Bidirectional tests on partially restrained, composite beam-to-column connections." Journal of Structural Engineering, 130(2), 320-327.

[25]. Gil, B. and E. Bayo (2008). "An alternative design for internal and external semi-rigid composite joints. Part I : Experimental research." Engineering Structures, 30(1), 218-231.

[26]. Braconi, A., et al. (2008). "Seismic performance of a 3D full-scale high-ductility steel–concrete composite moment-resisting structure—Part I: Design and testing procedure." Earthquake engineering & structural dynamics, 37(14), 1609-1634.

[27]. Braconi, A., et al. (2010). "Seismic behaviour of beam-to-column partial-strength joints for steel–concrete composite frames." Journal of Constructional Steel Research, 66(12), 1431-1444.

[28]. Hobbs, M., et al. (2013)."Slab column interaction - significant or not?" Steel Innovations, SCNZ.

[29]. MacRae, G., et al. (2013). "Slab Effects on Beam-Column Subassemblies—Beam Strength and Elongation Issues." Composite Construction in Steel and Concrete VII, ed.^eds., 77-92

[30]. Plumier, A. and C. Doneux (2001). "Seismic behaviour and design of composite steel concrete structures." ECOEST2 and ICONS, LNEC Lisboa, Portugal.

[31]. El-Lobody, E. and D. Lam (2003). "Finite element analysis of steel-concrete composite girders." Advances in Structural Engineering, 6(4), 267-281.

[32]. Mago, N. and C.G. Clifton (2008). "Investigation of the slab participation in moment resisting steel frames (HERA report R 4-140)." New Zealand Heavy Engineering Research Association, Manukau City, New Zealand.

[33]. Zhou, F., et al. (2007). "Finite-element analysis of a composite frame under large lateral cyclic loading." Journal of Structural Engineering, 133(7), 1018-1026.

[34]. Nakashima, M., et al. (2007). "Full-scale test of composite frame under large cyclic loading." Journal of Structural Engineering, 133(2), 297-304.

[35]. Mirza, O. and B. Uy (2011). "Behaviour of composite beam-column flush end-plate connection subjected to low-probability, high-consequence loading." Engineering Structures, 33, 647-662.

[36]. Kattner, M. and M. Crisinel (2000). "Finite element modelling of semi-rigid composite joints." Computers & Structures, 78(1), 341-353.

[37]. Rassati, G.A., et al. (2004). "Component modeling of partially restrained composite joints under cyclic and dynamic loading." Journal of Structural Engineering-ASCE, 130(2), 343-351.

[38]. EC3 (2005). "Eurocode 3: Design of steel structures - Part 1-1: General rules and rules for buildings", European Committee for Standardization, B-1050 Brussels.

[39]. MacRae, G.A. and U. Gunasekaran "A concept for consideration of slab effects on building seismic performance." Proc., Proc. NZSEE New Zealand Society for Earthquake Engineering Conference.

[40]. Kim, J., et al. "Approximate methods of accounting for beam growth effects." Proc., 13th World Conference on Earthquake Engineering.

[41]. Elghazouli, A., et al. (2008). "Seismic performance of composite moment-resisting frames." Engineering structures, 30(7), 1802-1819.

[42]. EC4 (2004). "Eurocode 4: Design of composite steel and concrete structures - Part 1-1: General rules and rules for buildings", European Committee for Standardization, B-1050 Brussels.

[43]. ANSI/AISC:341-10 (2010). "Seismic provisions of structural steel buildings", American Institute of Steel Construction, Chicago, Illinois, USA.

[44]. SteelandTube (2016). "SE82 Seismic Mesh, available at "http://steelandtube.co.nz/product/rei/hrc-mesh/seismic-mesh/se82"."

[45]. Chaudhari, T.D. and G.A. MacRae (2016). "Selection of gap infill material for structural seismic applications." Journal of the Structural Engineering Society of New Zealand Inc (SESOC), 29(01).

[46]. MacRae, G., et al. (2016). "Slab effects on beam-column subassemblies-beam strength and elongation issues." Composite Construction in Steel and Concrete VII, ed.^eds., 77-92

[47]. NZS3101:1 (2006). "Concrete structures standard: Part 1 - The design of concrete structures", Standards New Zealand, Wellington.

[48]. OneSteel (2016). "http://www.onesteelmetalcentre.com/products/structural-steel." (07/09/2016, 2016).

[49]. AS/NZS:3679.1 (2010). " Structural steel part 1: hot-rolled bars and sections", Standards New Zealand, Wellington.

[50]. AS:1391 (2007). "Metallic materials - tension testing at ambient temperature", Standards Australia Limited, Sydney.

[51]. NZS:3112.2 (1986). "Methods of test for concrete Part 2", Standards New Zealand, Wellington.

[52]. AS/NZS:1252 (1996). "High-strength steel bolts with associated nuts and washers for structural engineering", Standards New Zealand, Wellington.

[53]. BlacksFasteners (2016). "http://www.blacksfasteners.co.nz/assets/Metric-8_12466_1.pdf."

[54]. AS/NZS:1554.2 (2003). "Structural steel welding part 2: stud welding (steel studs to steel)", Standards New Zealand, Wellington.

[55]. AS/NZS:1554.1 (2014). "Structural steel welding part 1: welding of steel structures", Standards New Zealand, Wellington.

[56]. SikaNZ (2016). "Concrete curing compounds available at "http://nzl.sika.com/en/solutions_products/construction-markets/diy-trade/02a024/02a024sa002/02a024sa002ssa03.html"." (18/12/2016).

[57]. ACI (2001). "ACI T1.1-01: Acceptance criteria for moment frames based on structural testing", American Concrete Institute.

[58]. Krawinkler, H., et al. (1971). "Inelastic behavior of steel beam-to-column subassemblages." Report No. EERC-71/7, Earthquake Engineering Research Center, University of California, Berkeley, California.

[59]. Civjan, S.A. (1998). "Investigation of retrofit techniques for seismic resistant steel moment connections." Doctor of Philosophy, The University of Texas, Austin.

[60]. Blodgett, O.W. (1966). "Design of welded structures." James F. Lincoln Arc Welding Foundation, Cleveland.

[61]. MacRae, G.A. (1989). "The seismic response of steel frames." Ph.D. Thesis, University of Canterbury, Christchurch, New Zealand.

[62]. MacRae, G.A., et al. (2009). "Axial shortening of steel columns in buildings subjected to earthquakes." Bulletin of the New Zealand Society for Earthquake Engineering, 42(4), 275-287.

[63]. Dhakal, R.P. (2010). "Damage to non-structural components and contents in 2010 Darfield earthquake." Bulletin of the New Zealand Society for Earthquake Engineering, 43(4), 404-411.

[64]. MacRae, G.A., et al. (2012). "Review of design and installation practices for non-structural components." Prepared for the Engineering Advisory Group by New Zealand Consultants, Industry and Related Experts, University of Canterbury, Christchurch.

[65]. PlasticsNZ (2016). "EPS technical information available at "http://www.plastics.org.nz/about-us/sector-groups-main/eps-sector-group/eps-technical-information#properties"." (12 DEC 2016).

[66]. Firepro (2016). "Spiralite technical information available at "http://www.firepro.co.nz/datasheets/b400acoustic.pdf "." (12 Dec 2016).

[67]. BEELE_ENGG. (2016). "Actifoam technical information available at "http://www.beele.co.nz/images/PDF/handbook_actifoam.pdf"." (13 DEC 2016).

[68]. MacRae, G.A., et al. (2014)."Which structural system is best?" Australasian Structural Engineering Conference Structural Engineering Society New Zealand.

[69]. Tasligedik, S. (2014). "Damage mitigation strategies for non-structural infill walls." Ph.D. Thesis, University of Canterbury, Christchurch, New Zealand.

[70]. USG (2017). "USG drywall steel stud and track system available at "http://www.greenusg.co.nz/products/pdfs/USG%20Steel%20Stud.pdf"." (24 March 2017).

[71]. Rondo (2017). "Rondo key-lock concealed suspended ceiling system available at "http://www.rondo.co.nz/images/PDFs/designManual/Secured/keylock_web.pdf"." (24 March 2017).

[72]. ANSI/AISC:360-10 (2010). "Specification for structural steel buildings", American Institute of Steel Construction, Chicago, Illinois, USA.

[73]. FEMA451 (2006). "NEHRP recommended provisions: design example." National Institute of Building Sciences, Washington, D.C.

[74]. Simulia (2011). "ABAQUS version 6.11. User's manual." Dassault Systemes.

[75]. CSI Berkeley, U. (2015). "Analysis reference manual." SAP2000 V17.2.0.

[76]. Bruneau, M., et al. (2011). "Ductile design of steel structures." McGraw Hill Professional.

[77]. Roufegarinejad, A. and R. Tremblay (2012). "Finite element modeling of the inelastic cyclic response and fracture life of square tubular steel bracing members subjected to seismic inelastic loading." Behaviour of Steel Structures in Seismic Areas, 97-103.

[78]. Mago, N. (2003). "Finite element analysis of moment end plate connections (HERA report R4-117)." New Zealand Heavy Engineering Research Association, Manukau City, Auckland, New Zealand.

[79]. Liang, Q.Q., et al. (2005). "Strength analysis of steel–concrete composite beams in combined bending and shear." Journal of Structural Engineering, 131(10), 1593-1600.

[80]. Prakash, A., et al. (2011). "Three dimensional FE model of stud connected steel-concrete composite girders subjected to monotonic loading." International Journal of Mechanics and Applications, 1(1), 1-11.

[81]. AS/NZS:4671 (2001). "Steel reinforcing materials", Standards New Zealand, Wellington.

[82]. Smitha, M.S. and S.R.S. Kumar (2013). "Steel-concrete composite flange plate connections - finite element modeling and parametric studies." Journal of Constructional Steel Research, 82, 164-176.

[83]. Jankowiak, T. and T. Lodygowski (2005). "Identification of parameters of concrete damage plasticity constitutive model." Foundations of civil and environmental engineering, 6(1), 53-69.

[84]. Alfarah, B., et al. (2017). "New methodology for calculating damage variables evolution in Plastic Damage Model for RC structures." Engineering Structures, 132, 70-86.

[85]. Aslani, F. and R. Jowkarmeimandi (2012). "Stress-strain model for concrete under cyclic loading." Magazine of Concrete Research, 64(8), 673-685.

[86]. Carreira, D.J. and K.H. Chu (1985). "Stress-strain relationship for plain concrete in compression." Journal of the American Concrete Institute, 82(6), 797-804.

[87]. Gil, B. and E. Bayo (2008). "An alternative design for internal and external semi-rigid composite joints. Part II : Finite element modelling and analytical study." Engineering Structures, 30(1), 232-246.

[88]. Henriques, J., et al. (2013). "Numerical modeling of composite beam to reinforced concrete wall joints Part I : Calibration of joint components." Engineering Structures, 52, 747-761.

[89]. Baskar, K., et al. (2002). "Finite-element analysis of steel-concrete composite plate girder." Journal of Structural Engineering-ASCE, 128(9), 1158-1168.

[90]. Hicks, S. and A. Smith (2014). "Stud shear connectors in composite beams that support slabs with profiled steel sheeting." Structural Engineering International, 24(2), 246-253.

[91]. Lam, D. and E. El-Lobody (2005). "Behavior of headed stud shear connectors in composite beam." Journal of Structural Engineering-ASCE, 131(1), 96-107.

[92]. Hicks, S. (2011). "Design resistances of 19 mm diameter headed stud connectors through-deck welded within the ribs of Comflor 60 and Comflor 80 profiled steel decking." HERA, Manukau City, New Zealand, (Received through private communication from Steve Stickland).

[93]. Alashker, Y., et al. (2010). "Progressive collapse resistance of steel-concrete composite floors." Journal of Structural Engineering, 136(10), 1187-1196.

[94]. Sadek, F., et al. (2008). "Robustness of composite floor systems with shear connections: modeling, simulation, and evaluation." Journal of Structural Engineering, 134(11), 1717-1725.

[95]. Kim, T. (2003). "Experimental and analytical performance evaluation of welded steel moment connections to box or deep w-shape columns." Ph.D. Thesis, University of

California, Berkeley.

[96]. Broekaart, D. (2016). "Simuleon FEA Blog - 5 reasons why you should use a mid-surface shell mesh for thin-walled parts available at "http://info.simuleon.com/blog/5-reasons-why-your-fea-simulations-should-be-setup-with-a-mid-surface-shell-mesh-for-thin-walled-parts"." (7 June 2017).

[97]. Ribeiro, F.L.A., et al. (2015). "Deterioration modeling of steel moment resisting frames using finite-length plastic hinge force-based beam-column elements." Journal of Structural Engineering, 141(2).

[98]. Ibarra, L. and H. Krawinkler (2005). "Global collapse of frame structures under seismic excitations." John A. Blume Earthquake Engineering Center Technical Report 152, Stanford University

[99]. Kawashima, K., et al. (1992). "The strength and ductility of steel bridge piers based on loading tests." Journal of Research, Japan, 29.

[100]. Lignos, D.G. and H. Krawinkler (2011). "Deterioration modeling of steel components in support of collapse prediction of steel moment frames under earthquake loading." Journal of Structural Engineering, 137(11), 1291-1302.

[101]. Wang, Z. and W. Tizani (2010). "Modelling techniques of composite joints under cyclic loading." In Computing in Civil and Building Engineering, Proceedings of the International Conference, (Nottingham University Press, Nottingham, UK), Paper 254, p. 507.

[102]. FEMA350 (2000). "Recommended Design Criteria for New Steel Moment Frame Buildings." Federal Emergency Management Agency, Washington DC.

[103]. Cowie, K. (2015)."Australian/New Zealand Standard for Composite Structures, AS/NZS 2327, Seismic Provisions Development." Steel Innovations Conference 2015, Steel Construction New Zealand.

[104]. Yun, Y.M. and J.A. Ramirez (1996). "Strength of struts and nodes in strut-tie model." Journal of Structural Engineering, 122(1), 20-29.

Appendix A: Sub-assembly Design Calculation and Drawings

The structural design calculations for the test specimen subassembly are presented in this appendix. The test specimen considered herein is the internal beam-column joint of a fictitious building with a moment resisting frame comprising a composite deck slab. As this is a follow up study on research work carried out by Hobbs, some of the design calculations are reproduced in this appendix. The structure was designed for the following design assumptions:

a) A moment resisting frame is based on the strong column - weak beam philosophy and designed as per the NZ3404

b) The column was design to maintain its strength and not to damage under reasonable testing circumstances.

c) All connections were designed as per HERA Report R4-100.1:2003 "Structural Steel Connections Guide"

Primary Beam Section Properties (From OneSteel Tables)

Primary Beam size 310UB32, Specimen Length = 6000mm, weight =0.314kN/m

$d = 298mm$	$b_f = 149mm$	$t_f = 8mm$
$t_w = 5.5mm$	$d_1 = 282mm$	$A_g = 4080mm2$
$I_x = 63.2\times106mm4$	$Z_x = 424\times103mm3$	$S_x = 475\times103mm3$
$I_y = 4.42\times106mm4$	$Z_y = 59.3\times103mm3$	$S_y = 91.8\times103mm3$
$Z_{ex} = 467\times103mm3$	$Z_{ey} = 86.9\times103mm3$	$J = 86.5\times103mm4$
$I_w = 92.9\times109mm4$	$r_x = 124mm$	$r_y = 32.9mm$
$f_{yf} = 440MPa$	$f_{yw} = 440MPa$	$k_f = 0.915$
$E = 200000MPa$	$G = 70000MPa$	$r_1 = 13mm$

N.B.: yield stress values (f_{yf} & f_{yw}) for the beams are deliberately set at the maximum plausible limit for stock grade 300 steel. This ensures that the columns will be able to withstand the beam overstrengths without damage.

Un-factored Beam Moment Capacity (NZS3404)

Section Capacity

$M_{sx} = f_{yf} \times Z_{ex} = 440MPa \times 467\times10^3mm^3 = 205.5\times10^6Nmm$

$M_{sy} = f_{yf} \times Z_{ey} = 440MPa \times 86.9\times10^3mm^3 = 38.2\times10^6Nmm$

Member Capacity

Bending about x axis

k_t = 1.0 (restraint provided by floor slab)

k_l = 1.4 (beam loaded at top flange)

k_r = 1.0

$L_e = k_t\, k_l\, k_r\, L$

$= 1.0 \times 1.4 \times 1.0 \times 6000mm = 8400mm$

$$M_o = \sqrt{\left[\frac{\pi^2 EI_y}{L_e^2}\right]\left[GJ + \left(\frac{\pi^2 EI_w}{L_e^2}\right)\right]}$$

$$M_o = \sqrt{\left[\frac{\pi^2 \times 200000MPa \times 4.42 \times 10^6 mm^4}{8400^2_{mm}}\right]\left[70000MPa \times 86.5 \times 10^3 mm^4 + \left(\frac{\pi^2 \times 200000MPa \times 92.9 \times 10^9 mm^4}{8400^2_{mm}}\right)\right]}$$

$$M_o = 32.7 \times 10^6 Nmm$$

$$\alpha_s = 0.6 \times \left(\sqrt{\left(\frac{M_s}{M_o}\right)^2 + 3} - \frac{M_s}{M_o}\right)$$

$$\alpha_s = 0.6 \times \left(\sqrt{\left(\frac{205.5 \times 10^6 Nmm}{32.7 \times 10^6 Nmm}\right)^2 + 3} - \frac{205.5 \times 10^6 Nmm}{37.2 \times 10^6 Nmm}\right) = 0.141$$

Unsure of BMD details for beam so assume (conservatively) α_m = 1.0

$$M_{bx} = min\{\alpha_s \alpha_m M_{sx}, M_{sx}\}$$

$$M_{bx} = min\{0.141 \times 1.0 \times 205.5 \times 10^6 Nmm, 205.5 \times 10^6 Nmm\}$$

$$M_{bx} = 28.9 \times 10^6 Nmm$$

$= 28.9kNm$

Bending about y axis

k_t = 1.0 (restraint provided by floor slab), k_l = 1.0, k_r = 1.0

$L_e = k_t\, k_l\, k_r\, L = 1.0 \times 1.0 \times 1.0 \times 6000mm = 6000mm$

$$M_o = \sqrt{\left[\frac{\pi^2 EI_x}{L_e^2}\right]\left[GJ + \left(\frac{\pi^2 EI_w}{L_e^2}\right)\right]}$$

$$M_o = \sqrt{\left[\frac{\pi^2 \times 200000MPa \times 63.2 \times 10^6 mm^4}{6000^2_{mm}}\right]\left[70000MPa \times 86.5 \times 10^3 mm^4 + \left(\frac{\pi^2 \times 200000MPa \times 92.9 \times 10^9 mm^4}{6000^2_{mm}}\right)\right]}$$

$$M_o = 197 \times 10^6 Nmm$$

$$\alpha_s = 0.6 \times \left(\sqrt{\left(\frac{M_s}{M_o}\right)^2 + 3} - \frac{M_s}{M_o}\right)$$

$$\alpha_s = 0.6 \times \left(\sqrt{\left(\frac{38.2 \times 10^6 Nmm}{197 \times 10^6 Nmm}\right)^2 + 3} - \frac{38.2 \times 10^6 Nmm}{197 \times 10^6 Nmm}\right) = 0.929$$

Unsure of BMD details for beam so assume (conservatively) α_m = 1.0

$$M_{by} = min\{\alpha_s \alpha_m M_{sy}, M_{sy}\}$$

$$M_{by} = min\{0.929 \times 1.0 \times 38.2 \times 10^6 Nmm, 38.2 \times 10^6 Nmm\}$$

$$M_{by} = 35.5 \times 10^6 Nmm$$

$= 35.5kNm$

Overstrengths

M^*_x = 28.9kNm

M^*_y = 35.5kNm

Overstrength factor ϕ_o = 1.25

M_{ox} = 36.1kNm

M_{oy} = 44.4kNm

Deck Details (From Corus Tables)

COMFLOR80
t = 0.9mm
Rib width = 180mm
Trough width =
Rib height = 80mm (+15mm dovetail)
Sheet width = 600mm
Self-weight = 0.11kN/m
M_n = 15.4kNm/m

Slab Details

Slab thickness (t_o) = 150mm
Thickness above ribs = 70mm
f_c' = 30MPa
f_{cos}' = 10MPa
Average slab depth (t_{avg})= 106mm

Floor Capacity Check

Span = 3.0m
Gravity UDL = (w_c×1m× t_{avg}) + Self-Weight = (24kN/m^3×1m× 0.106m) + 0.11kN/m
= 2.65kN/m
w_g = 1.2×2.65kN/m
= 3.18kN/m

M* = $w_gL^2/8$ = 3.18kN/m × 3^2m/8 = 3.6kNm

ϕM_n = 15.4kNm
> 3.6Nm/0.85
> 4.23kNm (OK)

Un-factored Composite Beam Moment Capacity (NZS3404)

- Must consider ribs oriented both perpendicular and parallel to beam

<u>Ribs Perpendicular to Beam</u>

$$M_o = \sum M_{oi} + N_{slab}\left({}^{d_b}/_{2} + t_o - {}^{t_{ef}}/_{2}\right)$$

$$\sum M_{oi} = min\left\{1.18 \times \left(1 - N_{slab}/\sum\left(A_g f_y\right)_i\right) \times \sum M_{bi}^{o}\,;\sum M_{bi}^{o}\right\}$$

$$N_{slab} = min\left\{1.3 t_{ef} b_{sef}(f'_c + f'_{cos});\sum\left(A_g f_y\right)_i\right\}$$

A_g = 4080mm^2
f_y = 440MPa

For ribs perpendicular to beam:

$b_{sef} = b_{fc}$ (column flange width)

= 311mm

$t_{ef} = t$

$= t_o - h_{rc}$ (from NZS3404(1997) 13.1.2.5.2)

= 150mm – 80mm = 70mm

$N_{slab} = min\{1.3 \times 70mm \times 311mm \times (30MPa + 10MPa); 2 \times 4080mm^2 \times 440MPa\}$

$= 1132 \times 10^3$N

$M_{oxi} = 36.1$kNm $= M^o_{bi}$

$\sum M_{oi} = min\left\{1.18 \times \left(1 - \frac{1132040N}{2 \times 4080mm^2 \times 440MPa}\right) \times (2 \times 36.1 \times 10^6 Nmm); (2 \times 36.1 \times 10^6 Nmm)\right\}$

$= 58.4 \times 10^6$Nmm

$M_o = 58.4 \times 10^6 Nmm + 1132040N \times \left({}^{356mm}/_{2} + 150mm - {}^{70mm}/_{2}\right)$

$= 357.2 \times 10^6$Nmm

= 357.2kNm

<u>Ribs Parallel to Beam</u>

$M_o = \sum M_{oi} + N_{slab}\left({}^{d_b}/_{2} + t_o - {}^{t_{ef}}/_{2}\right)$

$\sum M_{oi} = min\left\{1.18 \times \left(1 - N_{slab}/\sum(A_g f_y)_i\right) \times \sum M^o_{bi}; \sum M^o_{bi}\right\}$

$N_{slab} = min\left\{1.3 t_{ef} b_{sef} (f'_c + f'_{cos}); \sum(A_g f_y)_i\right\}$

$A_g = 4080$mm^2

$f_y = 440$MPa

For ribs parallel to beam:

$b_{sef} = b_{fc}$ (column flange width)

= 311mm

$t_{ef} = t_o$ (from NZS3404(1997) 12.10.2.4)

= 150mm

$N_{slab} = min\{1.3 \times 150mm \times 311mm \times (30MPa + 10MPa); 2 \times 4080mm^2 \times 440MPa\}$

$= 2426 \times 10^3$N

$M_{oxi} = 36.1$kNm $= M^o_{bi}$

$\sum M_{oi} = min\left\{1.18 \times \left(1 - \frac{2425800N}{2 \times 4080mm^2 \times 440MPa}\right) \times (2 \times 36.1 \times 10^6 Nmm); (2 \times 36.1 \times 10^6 Nmm)\right\}$

$= 27.7 \times 10^6$Nmm

$M_o = 27.7 \times 10^6 Nmm + 2425800N \times \left({}^{356mm}/_{2} + 150mm - {}^{150mm}/_{2}\right)$

$= 571.0 \times 10^6$Nmm

= 571kNm

Comparing the two results, it is clear that ribs parallel to the beam gives the greatest overstrength moment hence this will be used for all further calculations.

The overstrength moment for the composite beams, **M_o = 571kNm**

Axial Load from Floor Slab & Beams

Width = 3000mm, Length = 6000mm

Volume of Concrete = 3m×6m×0.106m = $1.91m^3$

Weight of concrete = $w_c \times V_c = 24kN/m^3 \times 1.91m^3 = 45.8kN$

Weight of Deck Tray = $0.11kN/m^2 \times 3m \times 6m = 1.98kN$

Weight of Beams = 0.497kN/m×6m = 1.88kN

Total Dead Weight = 45.8kN+1.98kN+1.88kN= 49.7kN

Assumed live load = 3kPa×3m×6m = 54kN

Total Unfactored Weight = **103.7kN**

Column Section Properties (From OneSteel Tables)

Column size 310UC158, Specimen Length = 2100mm, weight = 1.55kN/m

d = 327mm	b_f = 311mm	t_f = 25mm
t_w = 15.7mm	d_1 = 277mm	A_g = 20100mm2
$I_x = 388\times10^6$mm4	$Z_x = 2370\times10^3$mm3	$S_x = 2680\times10^3$mm3
$I_y = 125\times10^6$mm4	$Z_y = 807\times10^3$mm3	$S_y = 1230\times10^3$mm3
$Z_{ex} = 2680\times10^3$mm3	$Z_{ey} = 1210\times10^3$mm3	$J = 3810x10^3$mm4
$I_w = 2860\times10^9$mm4	r_x = 139mm	r_y = 78.9mm
f_{yf} = 280MPa	f_{yw} = 300MPa	k_f = 1.0
E = 200000MPa	G = 70000MPa	r_1= 16.5mm

N.B.: yield stress values (f_{yf} & f_{yw}) for the columns are deliberately set at the minimum plausible limit for stock grade 300 steel. This ensures that the columns will be able to withstand the beam overstrengths without damage.

Un-factored Column Moment Capacity (NZS3404)

<u>Section Capacity</u>

$M_{sx} = f_{yf} \times Z_{ex} = 280MPa \times 2370\times10^3mm^3 = 750.4\times10^6Nmm$

$M_{sy} = f_{yf} \times Z_{ey} = 280MPa \times 1210\times10^3mm^3 = 338.8\times10^6Nmm$

<u>Member Capacity</u>

Bending about x axis

$k_t = 1.0$

$k_l = 1.0$

$k_r = 1.0$

$L_e = k_t\, k_l\, k_r\, L = 1.0\times1.0\times1.0\times2000mm = 2000mm$

$$M_o = \sqrt{\left[\frac{\pi^2 E I_y}{L_e^2}\right]\left[GJ + \left(\frac{\pi^2 E I_w}{L_e^2}\right)\right]}$$

$$M_o = \sqrt{\left[\frac{\pi^2\times200000MPa\times125\times10^6mm^4}{2000^2_{mm}}\right]\left[70000MPa \times 3810 \times 10^3mm^4 + \left(\frac{\pi^2\times200000MPa\times2860\times10^9mm^4}{2000^2_{mm}}\right)\right]}$$

$$M_o = 10.2 \times 10^9 Nmm$$

$$\alpha_s = 0.6 \times \left(\sqrt{\left(\frac{M_s}{M_o}\right)^2 + 3} - \frac{M_s}{M_o}\right)$$

$$\alpha_s = 0.6 \times \left(\sqrt{\left(\frac{750.4\times10^6 Nmm}{10.2\times10^9 Nmm}\right)^2 + 3} - \frac{750.4\times10^6 Nmm}{10.2\times10^9 Nmm} \right) = 0.996$$

Unsure of BMD details for beam so assume (conservatively) $\alpha_m = 1.0$

$M_{bx} = min\{\alpha_s \alpha_m M_{sx}, M_{sx}\}$

$M_{bx} = min\{0.996 \times 1.0 \times 750.4 \times 10^6 Nmm, 750.4 \times 10^6 Nmm\}$

$M_{bx} = 747.3 \times 10^6 Nmm$

= 747.3kNm

Bending about y axis

$k_t = 1.0$ (restraint provided by floor slab)

$k_l = 1.0$

$k_r = 1.0$

$L_e = k_t\, k_l\, k_r\, L = 1.0\times1.0\times1.0\times2000mm = 2000mm$

$$M_o = \sqrt{\left[\frac{\pi^2 E I_x}{L_e^2}\right]\left[GJ + \left(\frac{\pi^2 E I_w}{L_e^2}\right)\right]}$$

$$M_o = \sqrt{\left[\frac{\pi^2\times200000MPa\times388\times10^6 mm^4}{2000_{mm}^2}\right]\left[70000MPa \times 3810 \times 10^3 mm^4 + \left(\frac{\pi^2\times200000MPa\times2860\times10^9 mm^4}{2000_{mm}^2}\right)\right]}$$

$M_o = 17.9 \times 10^9 Nmm$

$$\alpha_s = 0.6 \times \left(\sqrt{\left(\frac{M_s}{M_o}\right)^2 + 3} - \frac{M_s}{M_o} \right)$$

$$\alpha_s = 0.6 \times \left(\sqrt{\left(\frac{338.8\times10^6 Nmm}{17.9\times10^9 Nmm}\right)^2 + 3} - \frac{338.8\times10^6 Nmm}{17.9\times10^9 Nmm} \right) = 1.03$$

Unsure of BMD details for beam so assume (conservatively) $\alpha_m = 1.0$

$M_{by} = min\{\alpha_s \alpha_m M_{sy}, M_{sy}\}$

$M_{by} = min\{1.03 \times 1.0 \times 338.8 \times 10^6 Nmm, 338.8 \times 10^6 Nmm\}$

$M_{by} = 338.8 \times 10^6 Nmm$

= 338.8kNm

M^*_x = 747.3kNm

M^*_y = 338.8kNm

Factored Column Axial Capacity (NZS3404)

Section Capacity

$N_s = k_f \times A_g \times f_{yf}$ = 1.0 × 20100mm^2 × 280MPa = 5628×10^{3}N

Member Capacity

$N_c = \alpha_c \times N_s$

$L_e = k_e\, L$

= 1.2×2000mm (k_e = 1.2 (NZS3404, 4.8.3.2 case 4))

= 2400mm

About x axis

$\lambda_n = \frac{L_e}{r}\sqrt{k_f}\sqrt{\frac{f_y}{250}}$

$\lambda_n = \frac{2400mm}{139mm}\sqrt{1.0}\sqrt{\frac{280MPa}{250}}$

$\lambda_n = 18.3$

$\alpha_a = \frac{2100(\lambda_n - 13.5)}{\lambda_n^2 - 15.3\lambda_n + 2050}$

$\alpha_a = 4.76$

$\alpha_b = 0$ (UC member with $k_f = 1$)

$\lambda = \lambda_n$

$\eta = \max(0.00326(\lambda\text{-}13.5); 0)$

$= 0.00326\times(18.3\text{-}13.5)$

$= 0.0156$

$\xi = \frac{\left(\frac{\lambda}{90}\right)^2 + 1 + \eta}{2\left(\frac{\lambda}{90}\right)^2}$

$\xi = \frac{\left(\frac{18.5}{90}\right)^2 + 1 + 0.0156}{2\left(\frac{18.5}{90}\right)^2}$

$\xi = 12.82$

$\alpha_c = \xi\left(1 - \sqrt{\left[1 - \left(\frac{90}{\xi\lambda}\right)^2\right]}\right)$

$\alpha_c = 12.82\left(1 - \sqrt{\left[1 - \left(\frac{90}{12.82\times 18.5}\right)^2\right]}\right)$

$\alpha_c = 0.984$

$N_{cx} = \alpha_c \times N_s$

$= 0.984 \times 5628\times 10^3 N$

$= 5538\times 10^3 N = 5538kN$

$\phi N_{cx} = 0.8\times 5538kN = 4431kN$

About y axis

$\lambda_n = \frac{L_e}{r}\sqrt{k_f}\sqrt{\frac{f_y}{250}}$

$\lambda_n = \frac{2400mm}{78.9mm}\sqrt{1.0}\sqrt{\frac{280MPa}{250}}$

$\lambda_n = 32.2$

$\alpha_a = \frac{2100(\lambda_n - 13.5)}{\lambda_n^2 - 15.3\lambda_n + 2050}$

$\alpha_a = 15.1$

$\alpha_b = 0$ (UC member with $kf = 1$)

$\lambda = \lambda_n$

$\eta = \max(0.00326(\lambda\text{-}13.5); 0)$

$= 0.00326\times(32.2\text{-}13.5)$

$= 0.0609$

$\xi = \frac{\left(\frac{\lambda}{90}\right)^2 + 1 + \eta}{2\left(\frac{\lambda}{90}\right)^2}$

$\xi = \frac{\left(\frac{32.2}{90}\right)^2 + 1 + 0.0609}{2\left(\frac{32.2}{90}\right)^2}$

$\xi = 4.64$

$\alpha_c = \xi\left(1 - \sqrt{\left[1 - \left(\frac{90}{\xi\lambda}\right)^2\right]}\right)$

$\alpha_c = 4.64\left(1 - \sqrt{\left[1 - \left(\frac{90}{4.64\times 32.2}\right)^2\right]}\right)$

$\alpha_c = 0.935$

$N_{cy} = \alpha_c \times N_s$

$= 0.935 \times 5628\times 10^3 N$

$= 5264\times 10^3 N = 55264kN$

$\phi N_{cy} = 0.8 \times 5264kN = 4211kN$

Column Moment Capacity Check

Section Capacity

$\frac{N^*}{\phi N_s} + \frac{M_x^*}{\phi M_{sx}} \leq 1$

$M_x^* \leq \phi M_{sx}\left(1 - \frac{N^*}{\phi N_s}\right)$

$\phi = 0.8$

N* = 1.2×(49.7kN + Column Weight) + 1.5×54kN (Refer page 5)

= 1.2×(49.7kN + (1.55kN/m×2m)) + 1.5×54kN = 144.3kN

$M_x^* \leq 0.8 \times 747kNm \times \left(1 - \frac{144.3kN}{0.8\times 5628kN}\right)$

$M_x^* \leq 581kNm$

Member Capacity

$\left(\frac{M_x^*}{\phi M_{cx}}\right)^{1.4} \leq 1$

$M_x^* \leq \phi M_{cx}\sqrt[1.4]{1}$

$M_{cx} = min\{M_{ix},\ M_{ox}\}$

$M_{ox} = M_{bx}\left(1 - \frac{N^*}{\phi N_{cy}}\right)$

$M_{ox} = 747kNm \times \left(1 - \frac{144.3kN}{0.8 \times 5264kN}\right)$

$M_{ox} = 719.9kNm$

$M_{ix} = M_{sx}\left(1 - \frac{N^*}{\phi N_{cx}}\right)$

$M_{ix} = 750kNm \times \left(1 - \frac{144.3kN}{0.8 \times 5538kN}\right)$

$M_{ix} = 726.0kNm$

$M_{cx} = 719.9kN.m$

$M_x^* \leq 0.8 \times 719.9kNm \times \sqrt[1.4]{1}$

$M_x^* \leq 576kNm$

Therefore Member Capacity governs for bending about the columns strong axis:

$M_x^* \leq 576kNm$

This is greater than the composite beam overstrength moment

$M^*_x = 576kNm > 571kNm$

FOS = 576kNm/571kNm = 1.01
(Although this is not a high FOS it will be sufficient given the extra overstrength of the beams)

Column Panel Zone Checks (NZS3404)

Must ensure the panel zone of the column is not damaged so as to allow for repeated use of the columns. Thus, the panel zone strength is designed to exceed the overstrength moment capacity of the composite beams.

<u>Panel Zone Demand</u>

$V_{pb} = H\left(\frac{L_c}{L_b}\frac{(L_b - d_c)}{(d_b - t_{fb})} - 1\right)$ (Simplified from NZS3404 12.9.5.2 (as per ENCI425 course reader)

H = Column shear at Beam-Column Joint

As the loading point of the column is 1m above the centreline of the beam-column joint:

$H \approx M_o \times 1m = 571kNm \times 1m = 571kN$

$L_c = 2000mm$

$L_b = 6000mm$

$d_c = 327mm$

$d_b = 298mm$

$t_{fb} = 8mm$

$V_{pb} = 571kN \times \left(\frac{2000mm}{6000mm}\frac{(6000mm-327mm)}{(298mm-8mm)} - 1\right)$

$V_{pb} = 571kN \times (6.52 - 1)$

$V_{pb} = 3153kN$

Panel Zone Capacity

$V_c = 0.60 f_{yp}^* d_c (t_{wc} + t_p)\eta \left[1 + \frac{3b_c t_{fc}^2}{d_b d_c (t_{wc}+t_p)}\right]$

b_c = 311mm

t_{fc} = 25mm

t_{wc} = 15.7mm

t_p is only used if web stiffener plates are used, set this equal to zero for now.

$f_{yp}^* = \frac{t_{wc} f_{yc} + t_p f_{yp}}{t_{wc}+t_p}$

$= f_{yc}$ = 300MPa

$\eta = \sqrt{1.15 - \left(\frac{N^*}{\phi N_s}\right)^2} \leq 1.0$

$\eta = \sqrt{1.15 - \left(\frac{192kN}{0.8 \times 5628kN}\right)^2} = 1.0$

$V_c = 0.60 \times 300MPa \times 327mm \times 15.7mm \times 1.0 \times \left[1 + \frac{3 \times 311mm \times 25_{mm}^2}{298mm \times 327mm \times 15.7mm}\right] = 1276kN$

So without web stiffeners, the panel zone is not strong enough to carry the applied load. As such stiffener panels must be added to the web.

Use 2×16mm plates, one on either side of the web:

t_p = 32mm

f_{yp} = 300MPa

$f_{yp}^* = \frac{t_{wc} f_{yc} + t_p f_{yp}}{t_{wc}+t_p} = \frac{15.7mm \times 300MPa + 36mm \times 300MPa}{15.7mm + 36mm}$ = 300MPa

$\eta = 1.0$

Web Contribution

$V_c = 0.60 \times 300MPa \times 327mm \times (15.7mm + 20mm) \times 1.0 \times 1$

$V_c = 2807kN$

< 3152kN

Flange Contribution

$V_c = 0.60 \times 300MPa \times 327mm \times (15.7mm + 20mm) \times 1.0 \times \left[\frac{3 \times 311mm \times 25_{mm}^2}{298mm \times 327mm \times (15.7mm + 20mm)}\right]$

$V_c = 352kN$

The total shear capacity of the section is therefore:

$V_c = 2807kN + 352kN$

$V_c = 3160kN$

FOS = 3160kN/3152kN = 1.0

So with 2×16mm plates, there is sufficient strength to withstand the panel zone shear.

Continuity Plate Checks

For the tension flange:

$A_s f_y > (A_{fb} - t_{wc} t_{fb}) f_{yb}$

$A_{fb} = t_{fb} \times b_f = 8mm \times 149mm = 1192mm^2$

$t_{wc} = 15.7mm$

$t_{fb} = 8mm$

$f_{yb} = 300MPa$

$A_s f_y > (1967mm^2 - 15.7mm \times 11.5mm) \times 300MPa$

$> 319.9 \times 10^3 N$

For the compression flange:

$A_s f_y > \phi_{oms} A_{fb} f_{yb} - t_{wc} (t_{fb} + 5t_{fc} + 2t_{ep} + 2t_{wf}) f_{yc}$

$\phi_{oms} = 1.25$

$t_{fc} = 25 mm$

$t_{ep} = 25mm$

$t_{wf} = 8mm$

$f_{yb} = 310MPa$

$A_s f_y > 1192mm^2 \times 300MPa - 15.7mm \times (8mm + 5(25mm) + 2(25mm) + 2(8mm)) \times 310MPa$

$> -490.3 \times 10^3 N$

Therefore compression flange governs:

$A_s f_y > 490.3 \times 10^3 N$

Assume $f_y = 300MPa$

$A_s > 490.3 \times 10^3 N / 300MPa > 1634mm^2$

$b_{cp} = (b_f - t_{wc} - t_{ep})/2 = 132mm$

$t_{cp} > 1634mm^2 / 132mm$

$> 12.4mm$

Therefore use 16mm plate for continuity plates (choice of f_y was OK)

$A_s f_y = (16mm \times 132mm) \times 300MPa = 631.9 \times 10^3 N$

$FOS = 631.9 \times 10^3 N / 490.3 \times 10^3 N = 1.29$

Beam-Column Joint Design (HERA Report R4-100)

The beam-column joint is a simple (non-gusseted) bolted moment end plate design based on HERA standard designs. The joint strength is designed to exceed the overstrength moment capacity of the beam.

M_o = 571kNm/2 = 286kN (two beams)

HERA moment end plate connection tables specify:

- 8×Grade 8.8 M24 bolts (4 rows of 2)
- 570mm×200mm×25mm end plate
- 12mm fillet welds on flange
- 8mm fillet welds on web

ϕM_n = 271kNm

ϕV = 298kN

The moment capacity is slightly lower than that required. Want to reduce the depth of the end plate (and hence the lever arm) to better match beam section and to increase the width to allow for M30 bolts if required. Try a 530mm×250mm×25mm end plate, 8×Grade 8.8 M24 bolts, full penetration butt welds in the beam flanges and web weld details as per HERA tables:

M* = 286kNm

V* = 192kN/2 = 96kN

As per the design process given in the HERA Structural Steelwork Connections Guide Part 1 for moment end plates assuming:

- 530mm×250mm×25mm, grade 350 end plate
- 8×Grade 8.8 M24 bolts
- Full penetration butt welds on flange
- 8mm fillet welds on web

a_{e1} = 55mm (top bolt end edge distance)

$1.75d_f < a_{e1} < 2.5\ d_f$

d_f = 24mm

$1.75d_f$ = 42mm (53mm for M30 bolt)

b_i = 250mm

s_g = 150mm (bolt hole pitch)

$b_i - s_g/2 = e = 50mm > 1.75d_f$

as shown above, $1.75d_f$ = 52.5mm for M30 bolt hence increase b_i to 260mm

e = 55mm

<u>Moment Capacity</u>

$\phi M_{con} = \phi N_{r1} d_{r1} + \phi N_{r2} d_{r2} + \psi_{r3} \phi N_{r3} d_{r3} \geq M^*$

$\phi N_{rx} = \min(\phi N_1, \phi N_2, \phi N_3, \phi N_v)$

$\phi N_1 = \frac{\phi_s f_{yi} I_{erx} t_i^2}{m}$

$\phi N_2 = \frac{0.5\phi_s f_{yi} I_{erx} t_i^2 + n2\phi_b N_{tf}}{m+n}$

$\phi N_3 = 2\phi_b N_{tf}$

$\phi N_v = 0.6\phi_s f_{yi} 2 I_{erx} t_i$

where:

$\phi_s = 0.9$

$\phi_b = 0.8$

$f_{yi} = 340MPa$

$t_i = 25mm$

$\phi_b N_{tf} = 234kN$ (bolt tensile capacity)

I_{erx}, m and n are different for each bolt row and, for the top row, are dependent on whether gusset plates are included.

For the top row of bolts (without gusset plates):

$m = a_f - 0.8t_{wf}$

$a_f = ((d_{plate} - d_{beam})/2) - a_{e1} = 61mm$

$t_{wf} = 8mm$ (assumed 8mm fillet welds on flange (will be full penetration butt welds))

$m = 54.6mm$

$n = \min(1.25m, a_{e1}) = 55mm$

$I_{er1} = \min(I_7, I_8, I_9, I_{10}, I_{11})$

$I_7 = 0.5b_f = 130mm$

$I_8 = 2m + 0.625a_{e1} + 0.5s_g = 219mm$

$I_9 = 2m + 0.625a_{e1} + e = 171mm$

$I_{10} = 4m + 1.25a_{e1} = 287mm$

$I_{11} = 2\pi m = 343mm$

$I_{er1} = 130mm$

With gusset plates:

$m_3 = a_f - 0.8t_{wf} = 54.6mm$

$m_4 = \frac{s_g}{2} - \frac{t_{ig}}{2} - 0.8t_{wg}$

$t_{ig} = 12mm$

$t_{wg} = 10mm$ (10mm fillet welds on both sides of gusset plate)

$m_4 = 61mm$

$m = m_4 = 61mm$

$n = \min(1.25m, a_{e1}) = 55mm$

$\lambda_1 = \frac{m_4}{m_4+e} = 0.53$

$\lambda_2 = \frac{m_3}{m_4+e} = 0.47$

$\alpha = \min(8.13 + 4.49\lambda_1 - 3.44\lambda_2 - 16.7\lambda_1^2 + 4.66\lambda_2^2 - 6.8\lambda_1\lambda_2 + 8.75\lambda_1^3 - 1.2\lambda_2^3 - 1.23\lambda_1\lambda_2^2 + 8.32\lambda_1^2\lambda_2, 2\pi) = 5.69$

$I_{er1} = \min(I_1, (I_2, I_3)_{max}, (I_5, I_6)_{max})$

$I_1 = 2\pi m_4 = 383mm$

$I_2 = 4m_4 + 1.25\ a_{e1} = 313mm$

$I_3 = \alpha m_4 = 347mm$

$I_5 = 2m_4 + 0.625e + a_{e1} = 211mm$

$I_6 = \alpha m_4 - (2m_4 + 0.625e) + a_{e1} = 246mm$

$I_{er1} = 246mm$

For the second row of bolts:

$m_1 = \frac{s_g}{2} - \frac{t_w}{2} - 0.8t_{ww}$

$t_w = 5.5mm$

$t_{ww} = 8mm$ (8mm fillet welds assumed on both sides web)

$m_1 = 65.85mm$

$m_2 = p_f - t_f - 0.8t_{wf}$

$p_f = 69mm$

$t_f = 8mm$

$m_2 = 54.6mm$

$m = m_1 = 64.95mm$

$n = \min(1.25m, e) = 55mm$

$\lambda_1 = \frac{m_1}{m_1+e} = 0.54$, $\lambda_2 = \frac{m_2}{m_1+e} = 0.45$

$\alpha = \min(8.13 + 4.49\lambda_1 - 3.44\lambda_2 - 16.7\lambda_1^2 + 4.66\lambda_2^2 - 6.8\ \lambda_1\lambda_2 + 8.75\lambda_1^3 - 1.2\lambda_2^3 - 1.23\lambda_1\lambda_2^2 + 8.32\lambda_1^2\ \lambda_2, 2\pi) \quad = 5.58$

$I_{er2} = \min(I_1, (I_2, I_3)_{max})$ (2 rows of bolts)

$I_1 = 2\pi m_1 = 414mm$

$I_2 = 4m_1 + 1.25e = 332mm$

$I_3 = \alpha m_1 = 370mm$

$s_p = 80mm$

$I_{er2} = 370mm$ (2 rows of bolts)

Try first without gusset plates:

For row 1	For row 2
$\phi N_1 = 455kN$	$\phi N_1 = 1076kN$
$\phi N_2 = 348kN$	$\phi N_2 = 506kN$
$\phi N_3 = 468kN$	$\phi N_3 = 468kN$
$\phi N_v = 597kN$	$\phi N_v = 1700kN$
$\phi N_{r1} = 348kN$	$\phi N_{r2} = 468kN$
$d_{r1} = d - 0.5t_f + a_f = 355mm$	$d_{r2} = d_{r1} - a_f - p_f = 225mm$

Therefore:

$\phi M_{con} = \phi N_{r1} d_{r1} + \phi N_{r2} d_{r2}$

$= 348kN \times 0.355m + 468kN \times 0.225m$

$= 272kNm$

$\leq M^* = 286kNm$, No Good

Other options

2 rows with gussets:

For row 1	For row 2
$\phi N_1 = 770kN$	$\phi N_1 = 1075kN$
$\phi N_2 = 424kN$	$\phi N_2 = 506kN$
$\phi N_3 = 468kN$	$\phi N_3 = 468kN$
$\phi N_v = 1128kN$	$\phi N_v = 1700kN$
$\phi N_{r1} = 424kN$	$\phi N_{r2} = 468kN$
$\phi M_{con} = \phi N_{r1} d_{r1} + \phi N_{r2} d_{r2} = 300kNm$	$\geq M^* = 286kNm$

FOS = 1.04, This design is OK, so use the option with gusset plates.

From the above results, it can be seen that 2 bolt rows with gusset plates gives a sufficient factor of safety. Use this layout to consider the shear capacity of the joint.

$\phi V_{con} = \min(\phi V_b, \phi V_i, \phi V_{sup}, \phi V_{gsb}, \phi V_{ww})$

$\phi V_b = n_{bb} \phi_b V_{fn}$ (bottom bolt group shear)

$n_{bb} = 4$

$\phi_b V_{fn} = 133kN$

$\phi V_b = 532kN$

$\phi V_i = \min(\phi V_{bi}, \phi V_{tti}, \phi V_{gsi})$

$\phi V_{bi} = n_{bb} \phi_s 3.2 f_{ui} d_f t_i$ (Bolt hole bearing)

$f_{ui} = 430MPa$; $d_f = 24mm$; $t_i = 25mm$

$= 2972kN$

$\phi V_{tti} = n_{bb} \phi_s a_{e1} f_{ui} t_i$ = (Plate transverse yielding)

$= 2129kN$

$\phi V_{gsi} = 2\phi_s f_{yi} d_f t_i$ (Gross transverse shear yield)

$f_{yi} = 340MPa$

$= 4055kN$

$\phi V_i = 2129kN$

$\phi V_{sup} = \min(\phi V_{bsup}, \phi V_{tsup})$

$\phi V_{bsup} = n_{bb} \phi_s 3.2 f_{us} d_f t_s$ (Support Bearing)

$f_{us} = 440MPa$

$t_s = 8mm$

$= 973kN$

$\phi V_{tsup} = n_{bb} \phi_s a_{e1} f_{us} t_s$ (Support Tearing)

$= 849kN$

$\phi V_{sup} = 849kN$

$\phi V_{gsb} = 0.6\phi_s 0.6 d t_w f_{yw}$ (Web shear)

$= 159kN$

$\phi V_{ww} = \phi N_{ww}$ (Weld shear)

$= 2\phi_w 0.6 f_{uw}(d - 2t_f)t_{ww}/\sqrt{2}$

$\phi_w = 0.8$

$f_{uw} = 480MPa$

$t_{ww} = 8mm$

$\phi V_{ww} = 735kN$

$\phi V_{con} = 159kN > V^* = 96kN$

FOS = 1.67

Check for the weld capacity against the Web and Flange tension capacity.

Flange overstrength capacity:

$N^*_{ft} = \phi_{oms} b_f t_f f_{yf}$

$= 1.25 \times 149mm \times 8mm \times 300MPa$

$= 402kN$

$\phi N_{wf} = 2\phi_w 0.6 f_{uw} b_f t_{wf}/\sqrt{2}$

$= 2 \times 0.8 \times 0.6 \times 480MPa \times 149mm \times 8mm/\sqrt{2}$

$= 388kN < N^*_{ft}$

Given that 8mm fillet welds are insufficient full penetration Butt welds will be specified.

Web capacity:

$N^*_{ww} = 0.9(d - 2t_f)\, t_w\, f_{yw}$

$= 0.9 \times 282mm \times 5.5mm \times 300MPa$

$= 419kN$

$< \phi N_{ww} = 735kN$ (FOS = 1.76) Web welds are Ok.

Slab Design

The composite slab with ComFlor 80 deck sheet were design using ComFlor software version 9, analysis software and the design details as follow:

SCI Tata Steel v9.0.22.0

Job Reference:		Date:	14/4/2014
Deck Reference:	CF80/0.9_550	Time:	19:10:24
Company Name:		Job No:	
Client Name:		Calcs By:	
Checked By:		File Name:	Composite Slab Design 1 - Thru Comflor software.pmd

Full Output

Note: Section Designed to Eurocodes, UK National Annex

Construction Stage:	PASS	**Max Unity Factor:**	0.42
Normal Stage:	PASS	**Max Unity Factor:**	0.28
Fire Condition:	PASS	**Max Unity Factor:**	0.17
Serviceability:	SATISFACTORY	**Max Unity Factor:**	0.65

***** Section Adequate *****

Floor Plan Data (unpropped composite construction with ComFlor 80/0.9/G550 decking)

Beam centres - equal	3.00 m	Profile span type	Double
Beam or wall width	149 mm	Propping	None
		Concrete span type	Internal

Profile Data (ComFlor 80/0.9/G550 decking. Grade C30/37)

Depth	80 mm	Pitch of deck ribs	300 mm
Trough width	120 mm	Crest width	150.0 mm
Nominal sheet thickness	0.90 mm	Design sheet thickness	0.86 mm
Deck weight	0.11 kN/m²	Yield strength	450 N/mm²

Concrete Slab (Normal Weight Concrete ; Mesh : 662/265)

Overall slab depth	150 mm		
Concrete characteristic strength	30 N/mm²	Concrete wet density	2550 kg/m³
Modular ratio	10	Concrete dry density	2450 kg/m³
Bar reinforcement :			
Diameter	10 mm	Yield strength	500 N/mm²
Distance from slab soffit	70 mm		
Mesh reinforcement :			
Mesh	662/265	Yield strength	500 N/mm²
Cover to Mesh	35 mm	Mesh Layers	Single
Account for End Anchorage	Yes	Shear connectors per rib	1
Diameter of Shear Connectors	19 mm		
Screeds	N/A		

Section Properties

*** Note - 1: All values of inertia are expressed in steel units
*** Note - 2: Average inertia is used for deflection calculations for the composite stage
*** Note - 3: Cracked dynamic inertia is used for natural frequency calculations

Deck Profile

Sagging Inertia, Iy	157.100 cm4/m	Area of profile (Net), Ap	1382 mm²/m
Hogging Inertia, Iy	136.480 cm4/m	Effective area of profile	1273.00 mm²/m

Composite

Inertia, Iy - Uncracked	2273 cm4/m	Inertia, Iy - Cracked	1139 cm4/m
Average inertia	1706 cm4/m	Cracked inertia (dynamic)	1276 cm4/m
Shear bond coefficients - Mr	89.31	Kr	0.240700
Concrete volume	0.106 m³/m/m		

Loads Acting on Slab (Actions)

*** Note: Slab subjected to uniformly distributed loads (UDL) ONLY

Imposed (occupancy)	3.00 kN/m²	Partitions	0.00 kN/m²
Ceilings and services	0.00 kN/m²	Finishes	0.00 kN/m²
Self weight of concrete slab (wet)	2.65 kN/m²	Self weight of decking	0.11 kN/m²
Self weight of concrete slab (dry)	2.55 kN/m²	Screeds	None
Construction load	1.50 kN/m²		

Line Loads Perpendicular to Deck Span (Actions)

None

Line Loads Parallel to Deck Span (Actions)

None

Fire Data

Design method	Bar Method	Fire resistance period	60 mins
Non-permanent imposed loads	N/A		

Partial Safety Factors

Actions		**Materials**	
Permanent, gamma G	1.35	Structural steel - elastic, gamma M0	1.00
Permanent - accidental, gamma GA	N/A	Structural steel - buckling, gamma M1	1.00
Variable, gamma Q	1.50	Concrete, gamma C	1.50
Combination factor - Fire, psi 1	0.50	Reinforcement, gamma S	1.15
Combination factor, psi 0	0.70	Combination factor, psi 2	0.30

Construction Stage

Loadings	**@ SLS (kN/m²)**	**@ ULS (kN/m²)**
Self weight of decking	0.11	0.15
Self weight of concrete slab (wet)	2.65	3.98
Reinforcement	0.07	0.09
Total weight of slab	2.83	4.22
Construction live load	0.75	1.13
Construction live load patch	0.75	1.13

Effective Span of Deck

Effective span Le, is the smaller of

1) c/c of supports	= 3.00 m
2) clear span + deck depth	= 2.85 + 80.0 / 1000
	= 2.93 m
Therefore Le	= 2.93 m

Shear Resistance Check (BS EN 1993-1-3 Clause 6.1.5 and 6.1.7.3)

Applied shear	11.51 kN/m			
Web shear resistance, Pv	61.87 kN/m	Unity Factor	0.19	PASS
Applied reaction	18.14 kN/m			
Web crushing resistance, Pw	43.85 kN/m	Unity Factor	0.41	PASS

Bending Resistance Check (BS EN 1993-1-3 Clause 6.1.4.1)

*** Note: A 100% redistribution of hogging moment is taken based on equilibrium of the continuous decking as the sagging moment does not exceed the design resistance

Sagging

Max applied moment	5.38 kNm/m			
Moment resistance	12.70 kNm/m	Unity Factor	0.42	PASS

Hogging

Applied moment	0.00 kNm/m			
Moment resistance	10.64 kNm/m	Unity Factor	0.00	PASS

Combined Effects

Bending and Web Crushing (BS EN 1993-1-3 Clause 6.1.11)

*** Note: A 100% redistribution of hogging moment is taken based on equilibrium of the continuous decking as the sagging moment does not exceed the design resistance

Design unity factor is the worst case of

1. Maximum hogging:

(9.80 / 43.85 + 0.00 / 10.64) / 1.25 = 0.18

2. Maximum reaction:

(18.14 / 43.85 + 0.00 / 10.64) / 1.25 = 0.33

Design unity factor 0.33 PASS

Bending and Shear (BS EN 1993-1-3 Clause 6.1.10)

*** Note: Low shear - This check is not required

Support Interaction Check at Serviceability Limit State (BS EN 1993-1-3 Clause 7.2)

Design unity factor is the worst case of

1. Maximum hogging:

(14.96 / 43.85 + 4.13 / 10.64) / (0.9 * 1.25) = 0.65

2. Maximum reaction:

(14.96 / 43.85 + 4.13 / 10.64) / (0.9 * 1.25) = 0.65

Design unity factor 0.65 PASS

Deflection

Allowable deflection is the lesser of

1) Effective span / deflection limit without ponding	16.28 mm
2) Deflection limit without ponding, absolute maximum value	20.00 mm
3) Slab depth / 10	15.00 mm

Max self weight deflection = 3.59mm <= 15.00mm SATISFACTORY

Normal Stage

Span

The effective composite span is 2.96 m

Loadings	@ SLS (kN/m²)	@ ULS (kN/m²)
Dead (Profile, concrete, reinforcement)	2.73	3.68
Imposed	3.00	4.50
Superimp (Ceiling, services, screed, finishes)	0.00	0.00
Total	5.73	8.18

All line and point described above in 'Loading Details' are applied at the Normal stage

Shear Resistance Check

Vertical Shear (BS EN 1992-1-1 Clause 6.2.2)

Maximum applied shear	11.72 kN/m	
Shear resistance of end diaphragm (ComFlor 225 only)	0.00 kN/m	***test value

Vertical shear resistance is the greater of:

1. (0.54 * 400.00 * 113.36) / 1000 + 0.00

2. (0.12 * 2.00 * (100 * 0.02 * 30.00)^1/3) * 400.00 * 113.36) / 1000 + 0.00

= 42.60 kN/m

Unity Factor = 11.72/42.60 = 0.28 < 1 PASS

Punching Shear (BS EN 1994-1-1 Clause 9.7.6)

N/A - no concentrated loads have been applied

Bending Resistance Check (BS EN 1994-1-1 Clause 9.7.2)

Applied bending moment	7.99 kNm/m	
Depth of concrete stress block	13.82 mm	
Lever arm	94.60 mm	
Compression in concrete	234.99 kN/m	
Moment Resistance	31.59 kNm/m	
Unity Factor = 7.99/31.59 = 0.25 < 1		PASS

Fire Resistance

Effective span in fire is the greater of		
1) c/c supports - support width	2.82 m	
2) c/c supports -150	2.81 m	
Therefore effective span in fire	2.82 m	
Fire total UDL	4.30 kN/mm²	
Fire free moment	4.37 kNm/m	
Moment resistance	10.84 kNm/m	
Total moment resistance	25.01 kNm/m	
Unity Factor	0.17	PASS

Deflection

Properties

Modular ratio	10.00	
Uncracked section inertia	22725500.00 cm4	
Cracked section inertia	11386490.00 cm4	

Deflection Checks

Imposed load deflection	0.84 mm	
Allowable deflection (20 mm max)	20.00 mm	SATISFACTORY
Total deflection	0.84 mm	
Allowable deflection	11.86 mm	PASS

Dynamic Sensitivity

Dynamic inertia (cracked section)	1275.53 cm4	
Maximum deflection	1.13 mm	
Frequency	16.95 Hz	
Unity Factor = 5.00/16.95 = 0.29 < 1		PASS

A.1 Structural assembly/fabrication drawings for the column, main beam and secondary beam

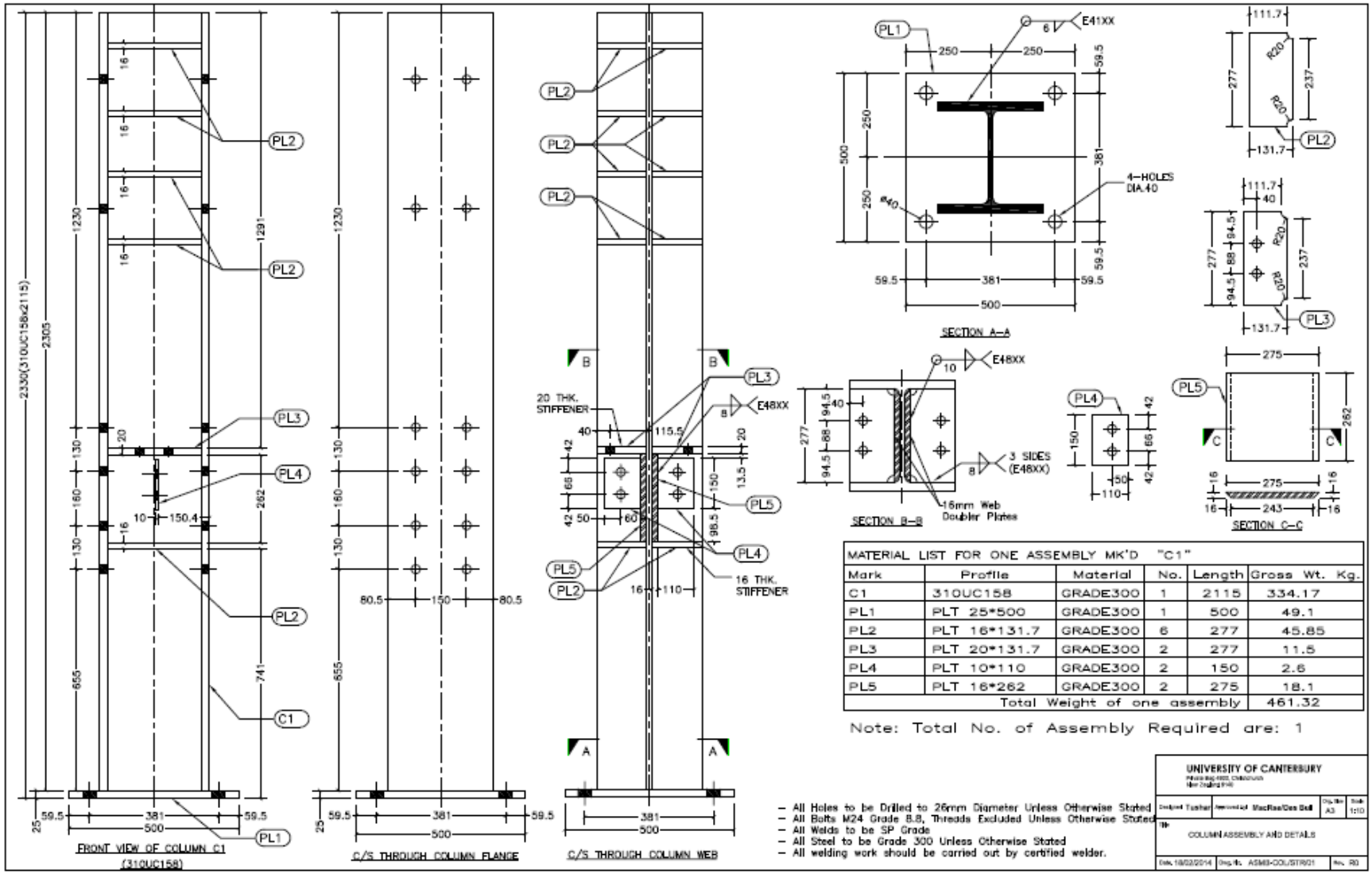

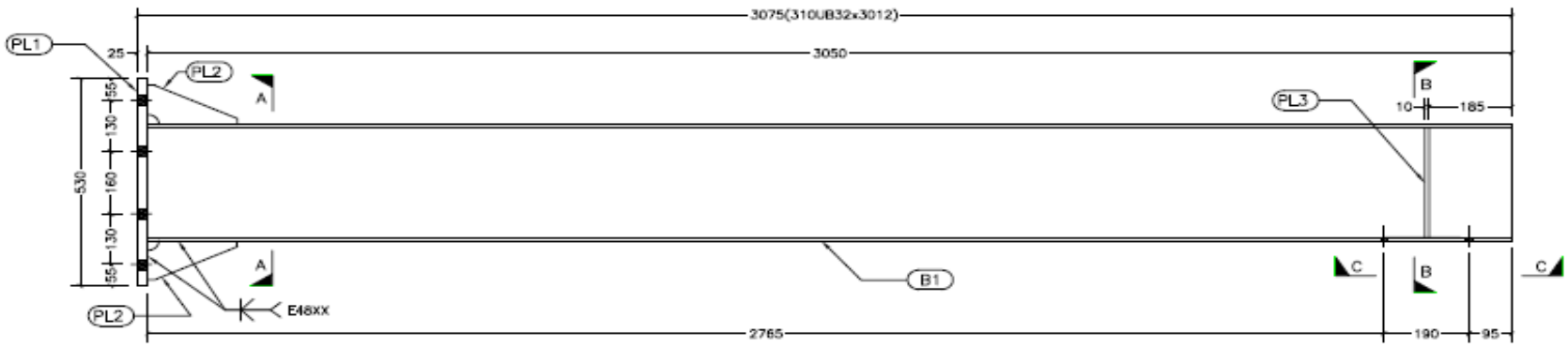

PRIMARY BEAM PB1
310UB32

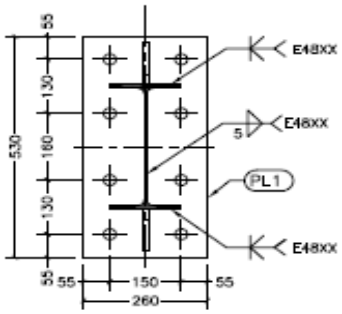

SECTION A–A

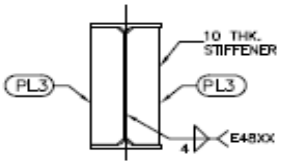

SECTION B–B

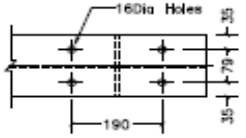

SECTION C–C

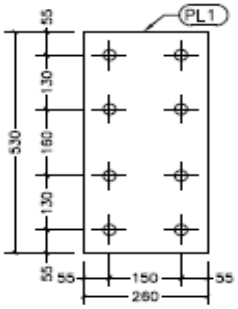

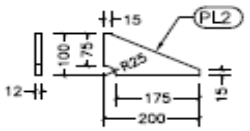

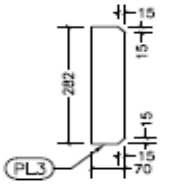

MATERIAL LIST FOR ONE ASSEMBLY MK'D "PB1"					
Mark	Profile	Material	No.	Length	Gross Wt. Kg.
B1	310UB32	GRADE300	1	3050	97.6
PL1	PLT 25*260	GRADE350	1	530	27.1
PL2	PLT 12*100	GRADE300	2	200	3.8
PL3	PLT 10*70	GRADE300	2	282	3.1
				Total Weight of one assembly	131.6

Note: Total No. of Assembly Required are: 4

- All Holes to be Drilled to 26mm Diameter Unless Otherwise Stated
- All Bolts M24 Grade 8.8, Threads Excluded Unless Otherwise Stated
- All Welds to be SP Grade
- All Steel to be Grade 300 Unless Otherwise Stated
- All welding work should be carried out by certified welder.

UNIVERSITY OF CANTERBURY

Designed Tushar | Approved | Misc/Rad/Des Bull | Drg Size A3 | Scale 1:10

Title: BEAM ASSEMBLY & DETAILS FOR TRANSVERSE DECK

Date 13/02/2014 | Drg No. ASMB-PB1/STR/02 | Rev. R0

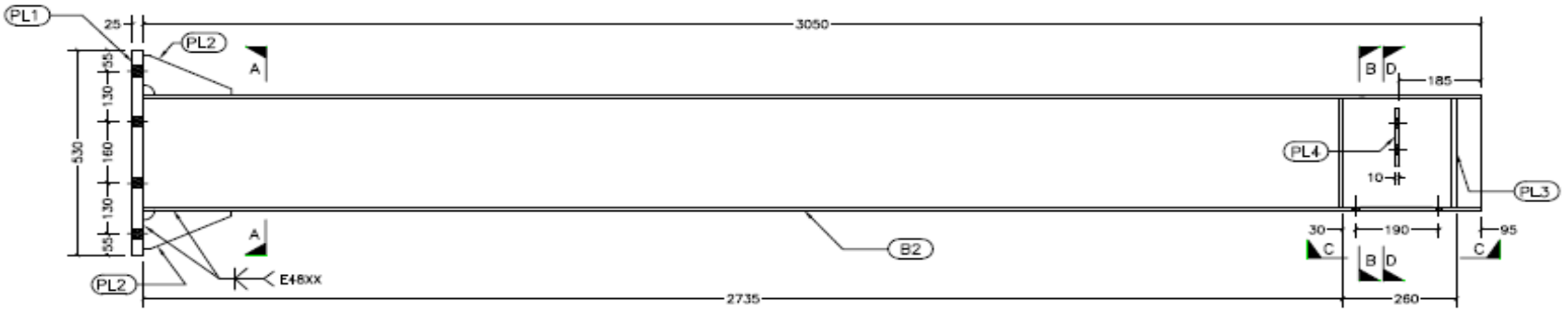

PRIMARY BEAM PB2
310UB32

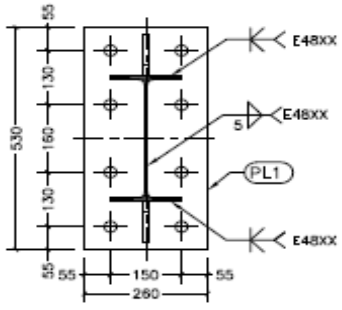

SECTION A–A

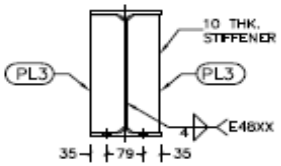

SECTION B–B

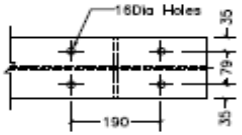

SECTION C–C

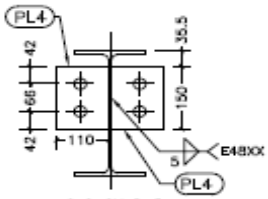

SECTION D–D

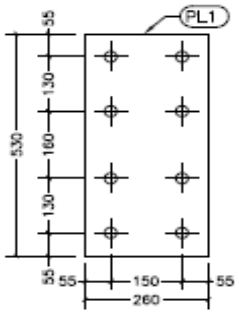

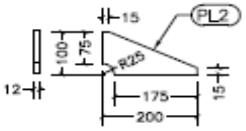

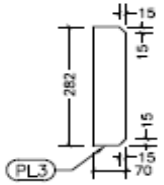

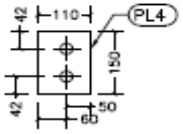

MATERIAL LIST FOR ONE ASSEMBLY MK'D "PB2"					
Mark	Profile	Material	No.	Length	Gross Wt. Kg.
B1	310UB32	GRADE300	1	3050	97.6
PL1	PLT 25*260	GRADE350	1	530	27.1
PL2	PLT 12*100	GRADE300	2	200	3.8
PL3	PLT 10*70	GRADE300	4	282	6.2
PL4	PLT 10*110	GRADE300	2	150	2.6
		Total Weight of one assembly			137.3

Note: Total No. of Assembly Required are: 4

- All Holes to be Drilled to 26mm Diameter Unless Otherwise Stated
- All Bolts M24 Grade 8.8, Threads Excluded Unless Otherwise Stated
- All Welds to be SP Grade
- All Steel to be Grade 300 Unless Otherwise Stated
- All welding work should be carried out by certified welder.

UNIVERSITY OF CANTERBURY

Drafted: Tushar | Approved: MacRae/Das Bull | Orig. Size: A3 | Scale: 1:10

Title: BEAM ASSEMBLY & DETAILS FOR LONGITUDINAL DECK

Date: 13/02/2014 | Orig. No.: ASMB-PB2/STR03 | Rev.: R0

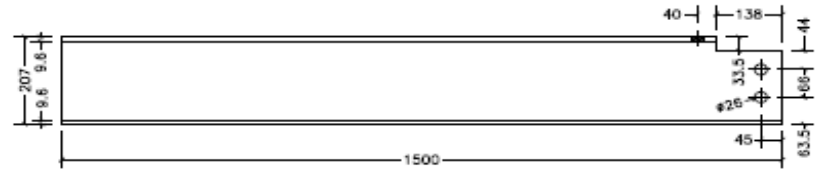

SECONDARY BEAM SB1
200UB29.8

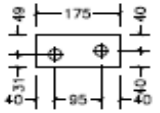

CONTINUITY PLATE PL1
(For top flange moment connection)

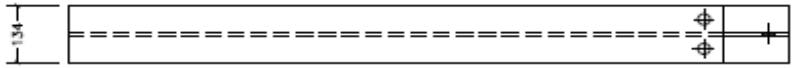

TOP VIEW

MATERIAL LIST FOR ONE ASSEMBLY MK'D "SB1"					
Mark	Profile	Material	No.	Length	Gross Wt. Kg.
SB1	200UB29.8	GRADE300	1	1500	44.7
PL1	PLT 16*80	GRADE350	2	175	3.52
			Total Weight of one assembly		48.22

Note: Total No. of Assembly Required are: 6

- All Holes to be Drilled to 26mm Diameter Unless Otherwise Stated
- All Bolts M24 Grade 8.8, Threads EXcluded
- All Steel to be Grade 300 Unless Otherwise Stated

UNIVERSITY OF CANTERBURY

Designed: Tushar | Drg.Size: A3 | Scale: 1:10

SECONDARY BEAM ASSEMBLY & DETAILS

Date: 13/02/2014 | Drg.No.: ASMBLSB1/STR/04 | Rev.: R0

A.2 Reinforcement and Shear Stud Layout for Specimens FI-SU, SK-SU, MSK-SU and FD-SU

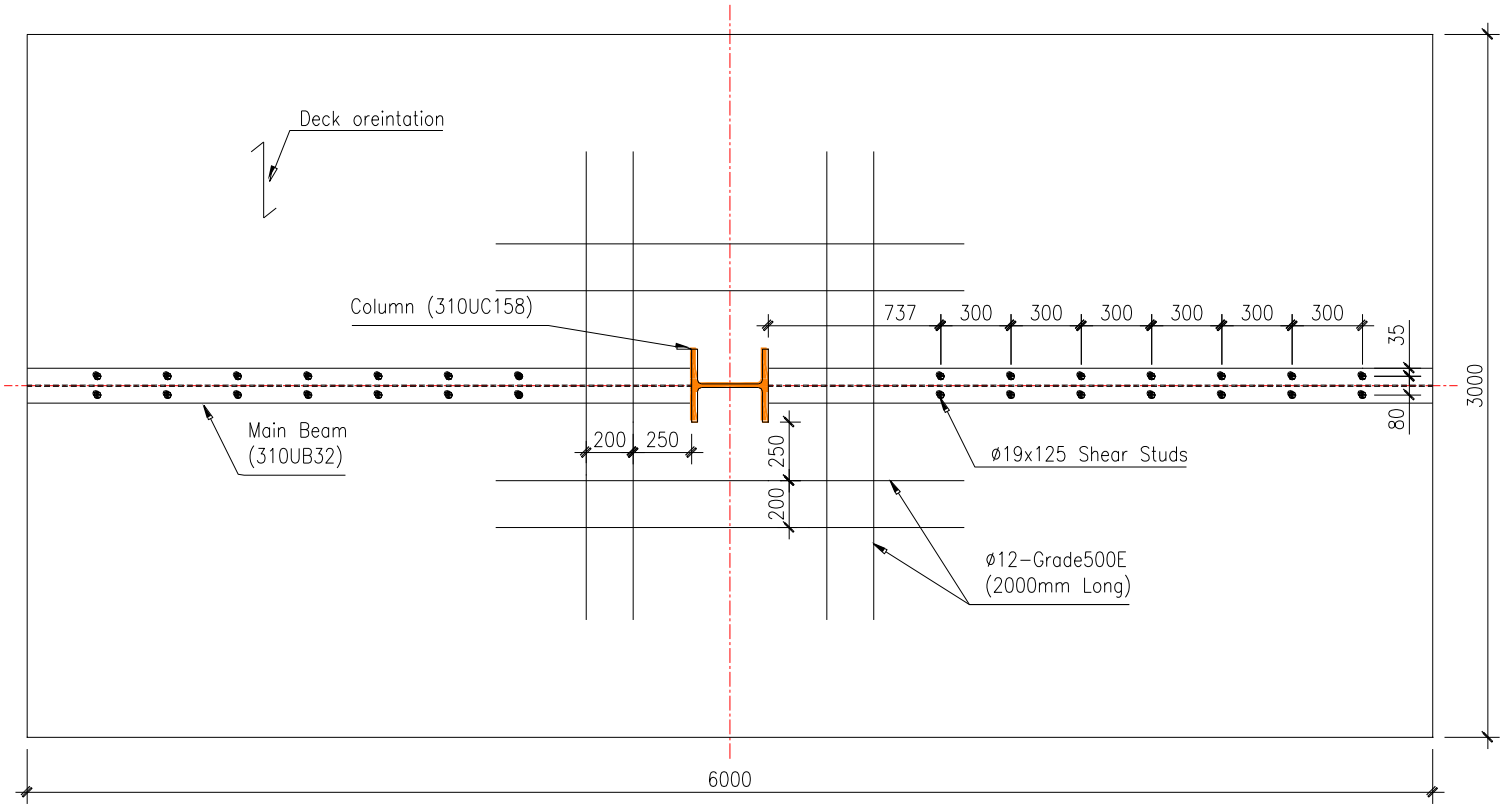

Reinforcement and Shear Stud Layout for FI-SU Subassembly

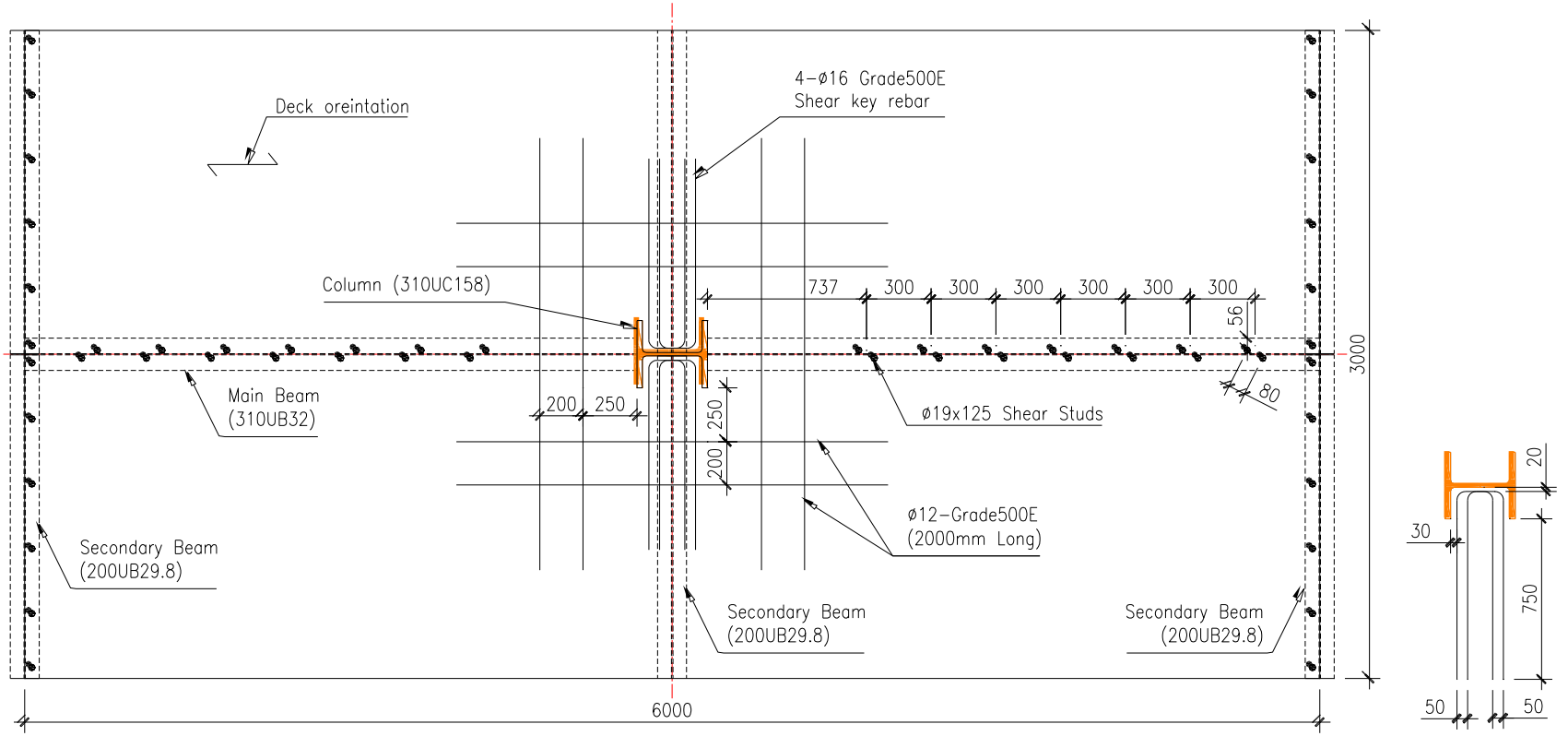

Reinforcement and Shear Stud Layout for SK-SU Subassembly

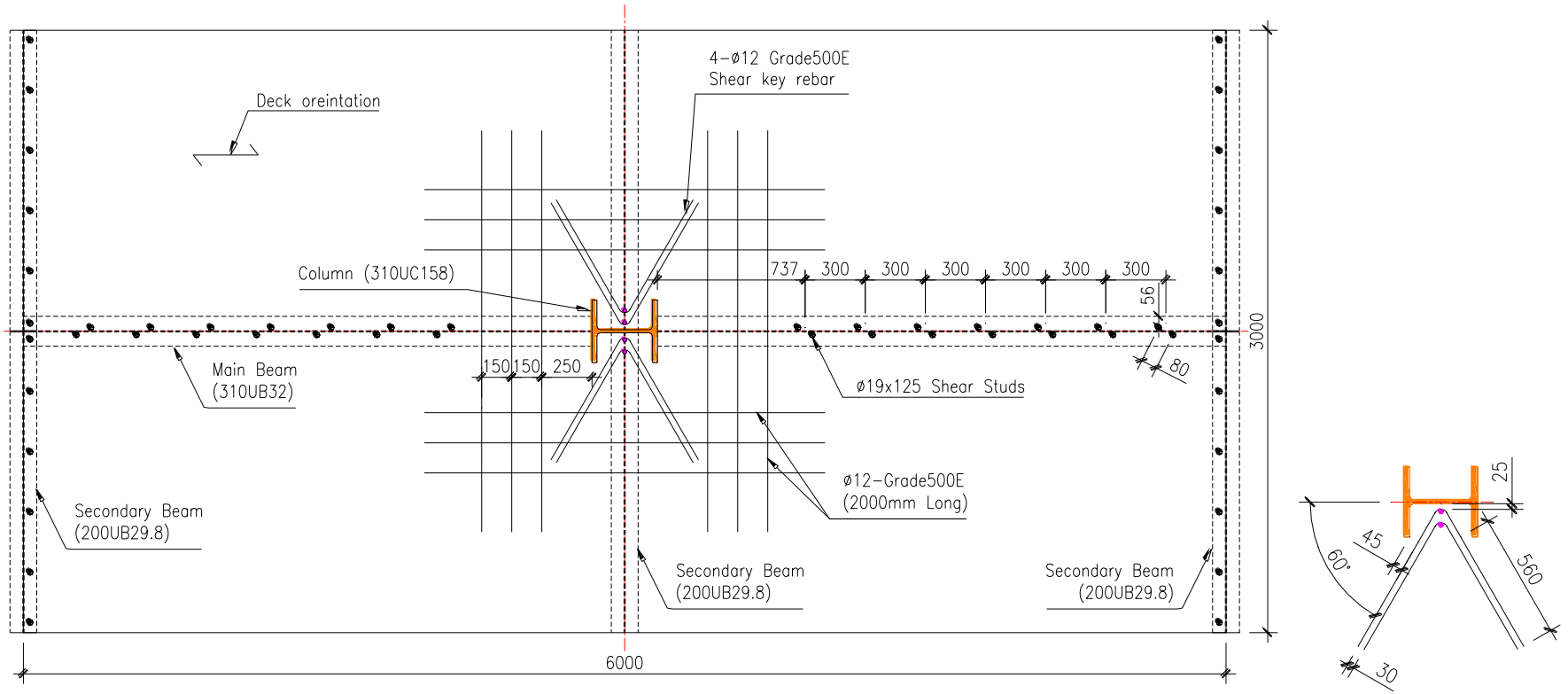

Reinforcement and Shear Stud Layout for MSK-SU Subassembly

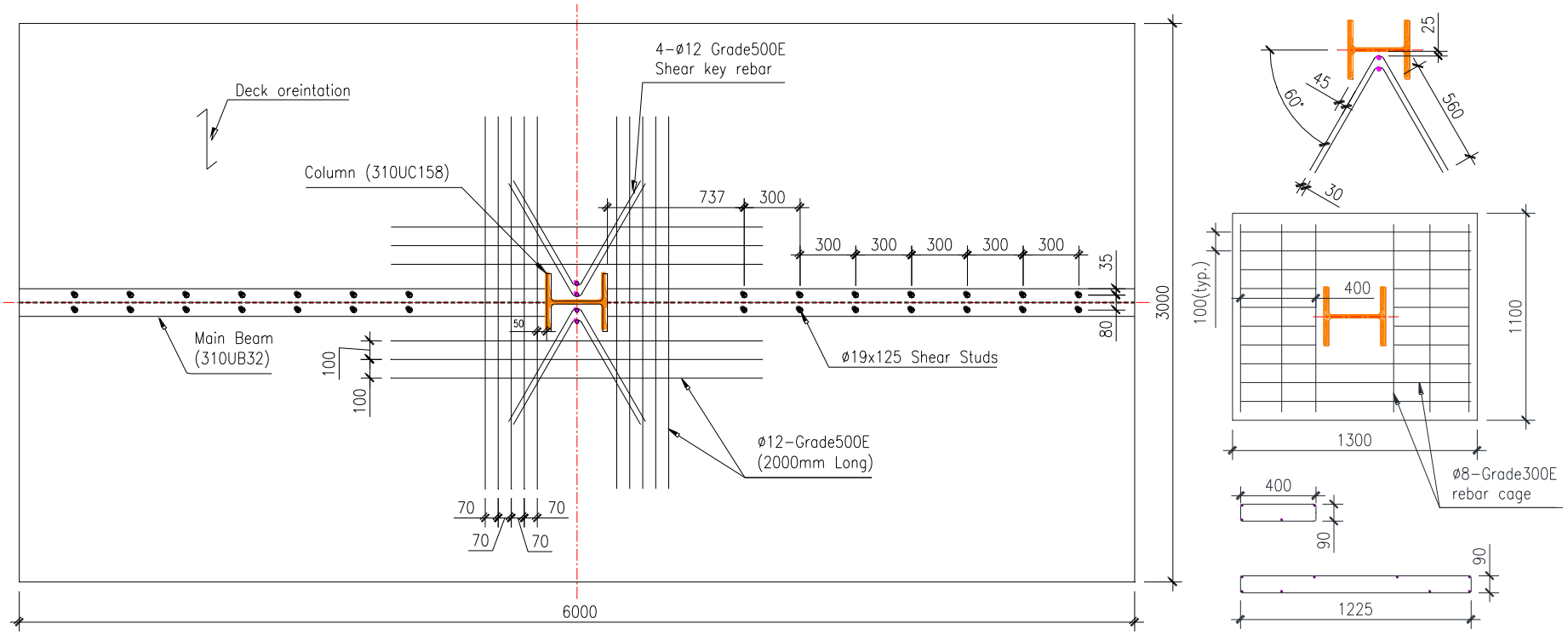

Reinforcement and Shear Stud Layout for FD-SU Subassembly

Appendix B: Conceptual Details of MSK-SU and SE82 Mesh Splicing Details

B.1 Conceptual development of Modified Shear Key Slab Unit

An experimental test carried out on the shear key slab unit (SK-SU), shows that there is a need of concrete confinement from the slab top to the concrete in-between the column flanges, as well as to the shear key rebars, which requires a sufficient anchorage. At the conceptual level, several configurations are assessed based on the ease of application, confinement, cost-effectiveness, and arresting of shear crack. The decision was made through the subjective quantitative analysis, and the relevant details of different options are as below.

Option 1: Welded Steel Plate (By Prof Des Bull)

As proposed by Prof Des Bull, a steel plate could be welded in between the column flanges parallel to the continuity plates and matching with the slab top as shown in Figure B.1

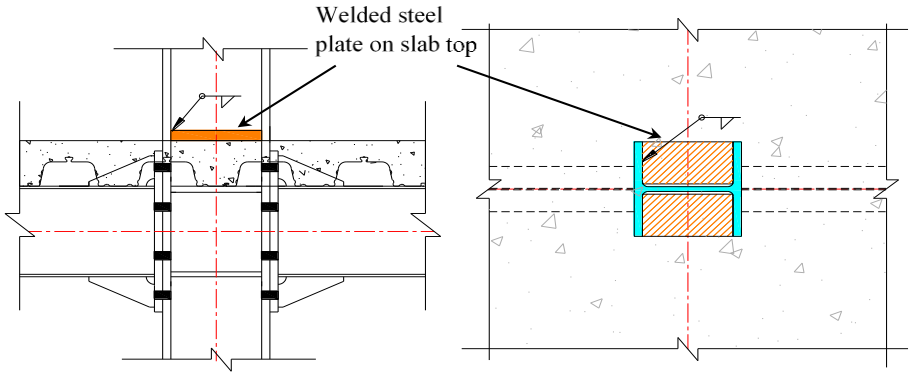

a) Elevation **b) Plan**

Figure B.1 – Welded Steel Plate

Advantages:

a) The steel plate will help to provide a passive confinement from top side to the slab portion in between the column flanges.

b) Ease of application can be welded while fabricating the column.

c) Economical as compared to option 7 and 8.

Disadvantages:

a) The degree of confinement might be less due to the passive confinement to the slab top.

b) Limited access for concreting under the pocket form due to the welded top plate, which might result in the poor quality of concrete in this zone.

c) May not help to arrest the shear cracks along the tip of column flanges.

Option 2: Steel plate with shear studs (By Assoc. Prof Gregory MacRae)

In this configuration, as proposed by Assoc. Prof Greg, a steel plate with welded shear studs could be inserted during slab casting in between the column flanges parallel to the continuity plates and matching with the slab top as shown in Figure B.2

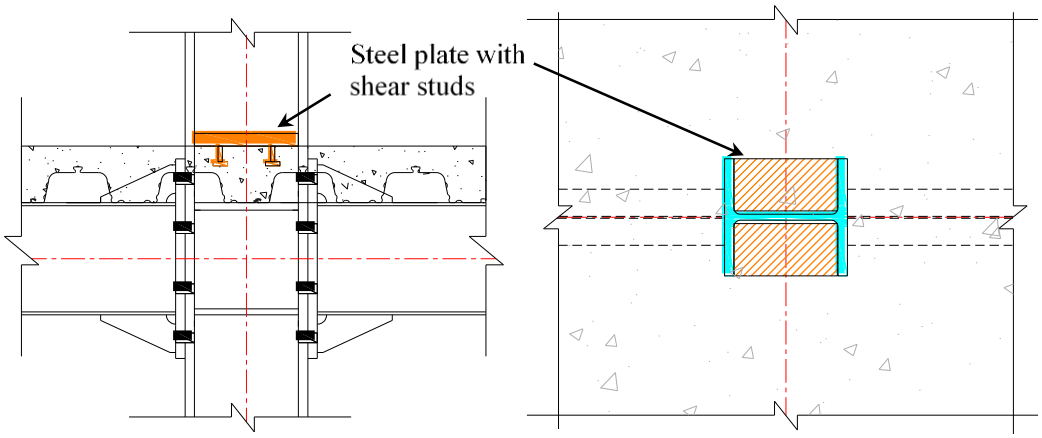

a) Elevation **b) Plan**

Figure B.2 – Steel Plate with shear studs

Advantages:

a) Will help to provide a passive confinement from top side to the slab portion in between the column flanges.

b) Ease of application and steel plate can be inserted while concreting.

c) Economical as compared to option 7 and 8.

Disadvantages:

a) Need to insert a steel plate on the freshly laid concrete; the position of the plate may be dislocated during compaction of the concrete.

b) The degree of confinement might be less due to the passive confinement to the slab top.

c) May not help to arrest the shear cracks along the tip of column flanges.

Option 3: Bolted Steel plate

This configuration comprises a bolted steel plate in between the column flanges parallel to the continuity plates and matching with the slab top as shown in Figure B.3. The bolts will be debonded from surrounding concrete using the PVC shim pipe.

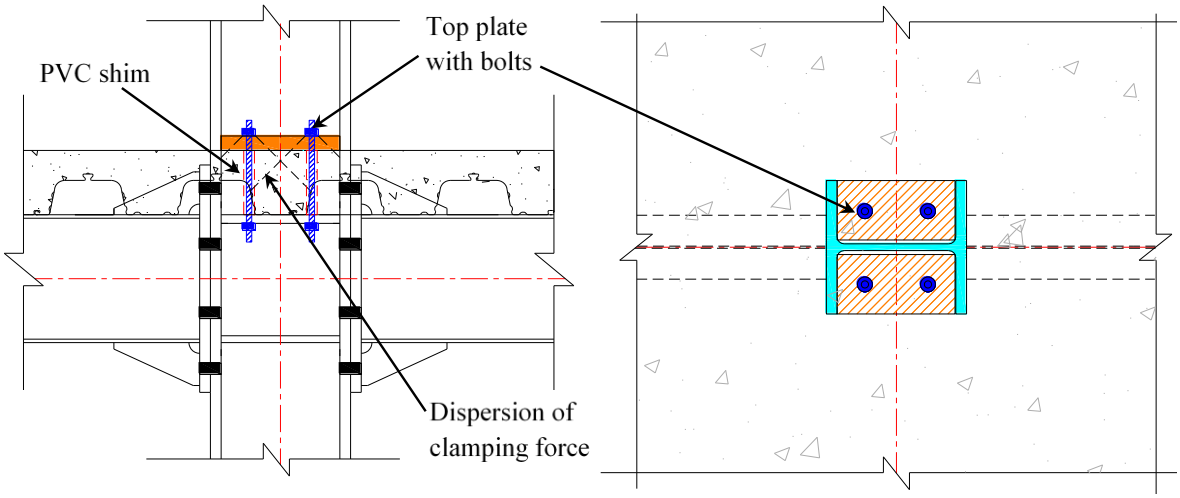

a) Elevation **b) Plan**

Figure B.3 – Steel Plate with Bolts

Advantages:

a) Provide active confinement from the slab top to the concrete in between the column flanges.

b) Compression on the slab top can be controlled by adjusting the clamping force through the bolts.

c) Economical as compared to options 7 and 8, however, costlier as compared to options 1 and 2.

d) Ease of application.

Disadvantages:

a) May not help to arrest the shear cracks along the tip of column flanges.

Option 4: Inverted Steel Channel (By Assoc. Prof Gregory MacRae)

In this proposed concept, a steel channel section will be inserted from the top in between the column flanges as shown in Figure B.4. It is hypothesized that the channel will be projected for at least a length of two times the column flanges outstand, to act as a shear key.

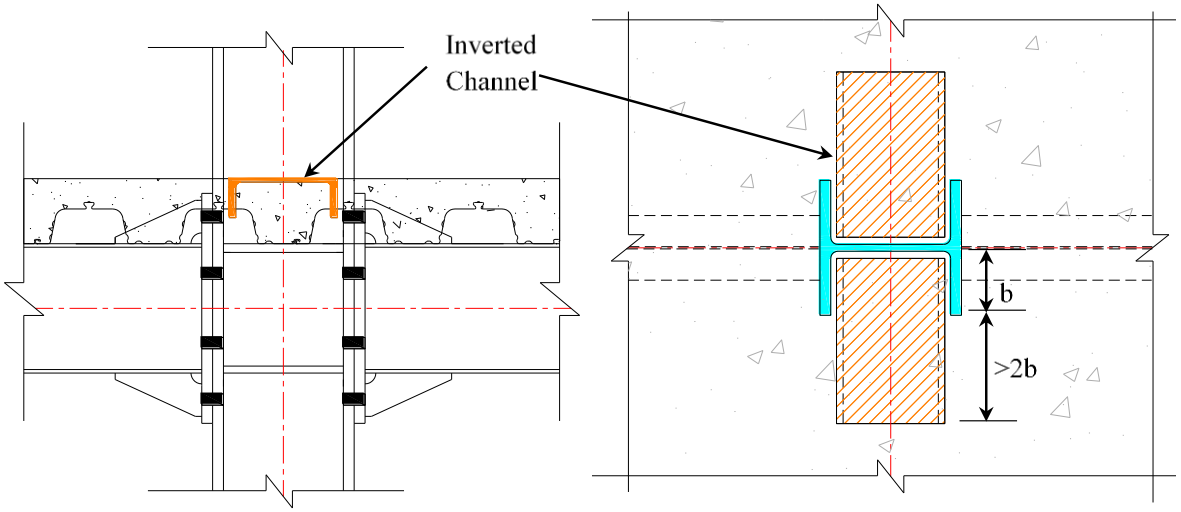

a) Elevation **b) Plan**

Figure B.4 – Inverted Steel Channel

Advantages:

a) Provides passive confinement from the top side to the slab portion in between the column flanges.

b) The flanges of the channel may help to arrest the shear cracks along the tip of column flanges.

c) Ease of application and channel can be inserted from the top while concreting.

d) Economical as compared to option 7 and 8.

Disadvantages:

a) Limited availability of suitable channel size to fit inside the column flanges and the making of a tailor-made channel might result into an increase in construction time.

b) The degree of confinement might be less due to the passive confinement to the slab top.

c) Need to insert a channel on the freshly laid concrete and the position of the channel may be dislocated during compaction of the concrete.

Option 5: Extended Steel Wings Plates (based on Salvatore work)

In this configuration, vertical steel plates in between the column flanges will be inserted adjacent to the inner column flange so that it will act like steel wings as shown in Figure B.5. A series of a welded rebars will be provided to maintain the distance between two wing plates.

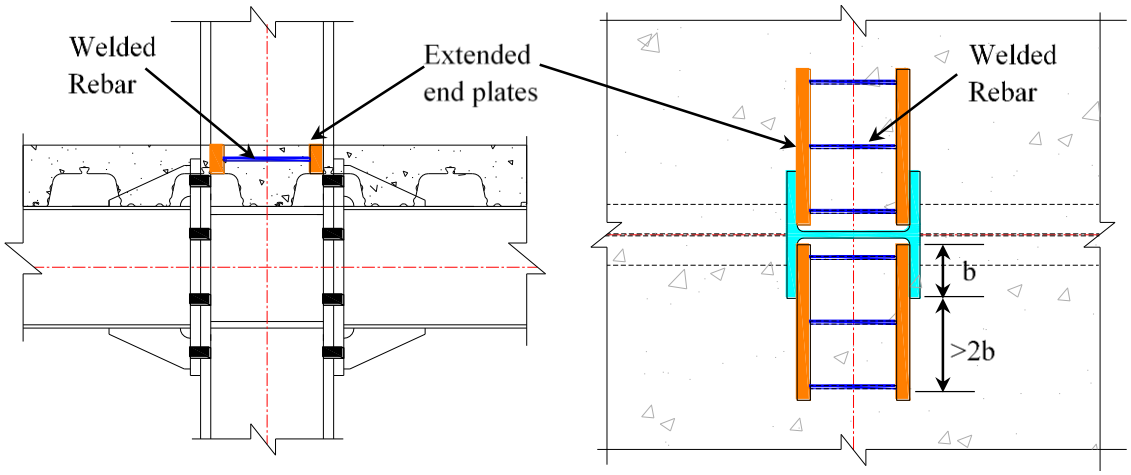

a) Elevation **b) Plan**

Figure B.5 – Extended Steel Wing Plates

Advantages:

a) The extended wing plates may help to arrest the shear cracks along the tip of column flanges.

b) Ease of application and wing plates can be inserted while concreting.

Disadvantages:

a) Lack of confinement from the slab top.

b) The wing plate position may be dislocated during compaction of the concrete.

Option 6: Inverted Steel Angle (By Assoc. Prof Gregory MacRae)

In this proposed concept, the steel angles with gusset plates (like an inverted counterfort retaining wall) will be inserted adjacent to the inner column flanges and will further extend into the slab as shown in Figure B.6. It is hypothesized that the angle will be projected at least for a length of two times the column flange outstands to act as a shear key.

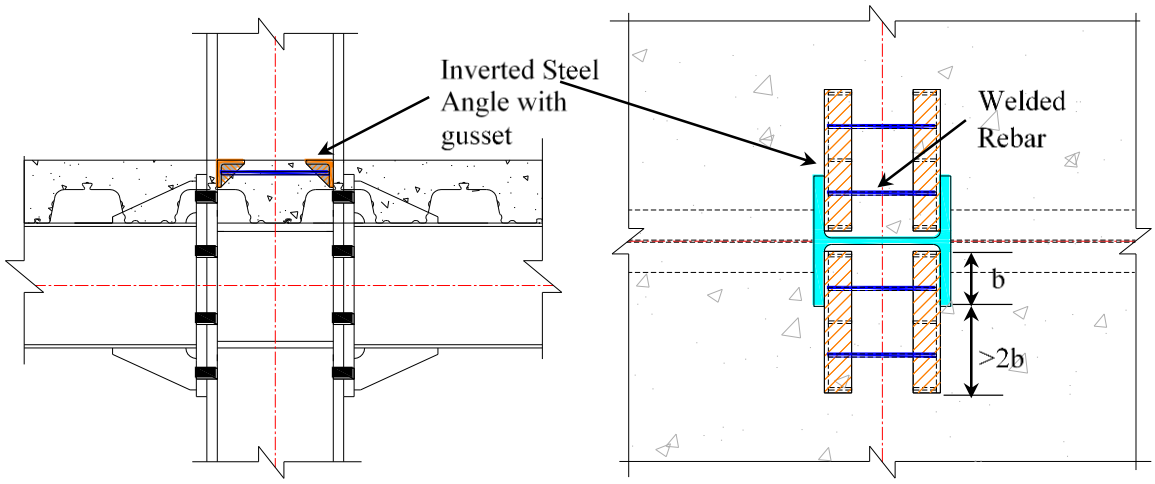

a) Elevation **b) Plan**

Figure B.6 – Inverted Steel Angle

Advantages:

a) The extended steel angles may help to arrest the shear cracks along the tip of the column flanges.

b) The flanges of angle will enhance the slab top confinement but to some extent in the form of a partial passive confinement.

c) Ease of application and steel angles can be inserted while concreting.

Disadvantages:

a) A partial confinement from the slab top.

b) The steel angles position may be dislocated during compaction of the concrete.

c) It can be costlier than the above options due to an additional fabrication work for the gusset plates.

Option 7: Concealed Concrete Beam

In this concept, the deck sheet will be cut in such way that, it will form a full depth beam with a width equal to the depth of column section. A reinforcement cage will be inserted along with steel wing plates as shown in Figure B.7. It is hypothesized that the concealed beam will be projected at least for a length of two times the column flanges outstand, to act as a shear key.

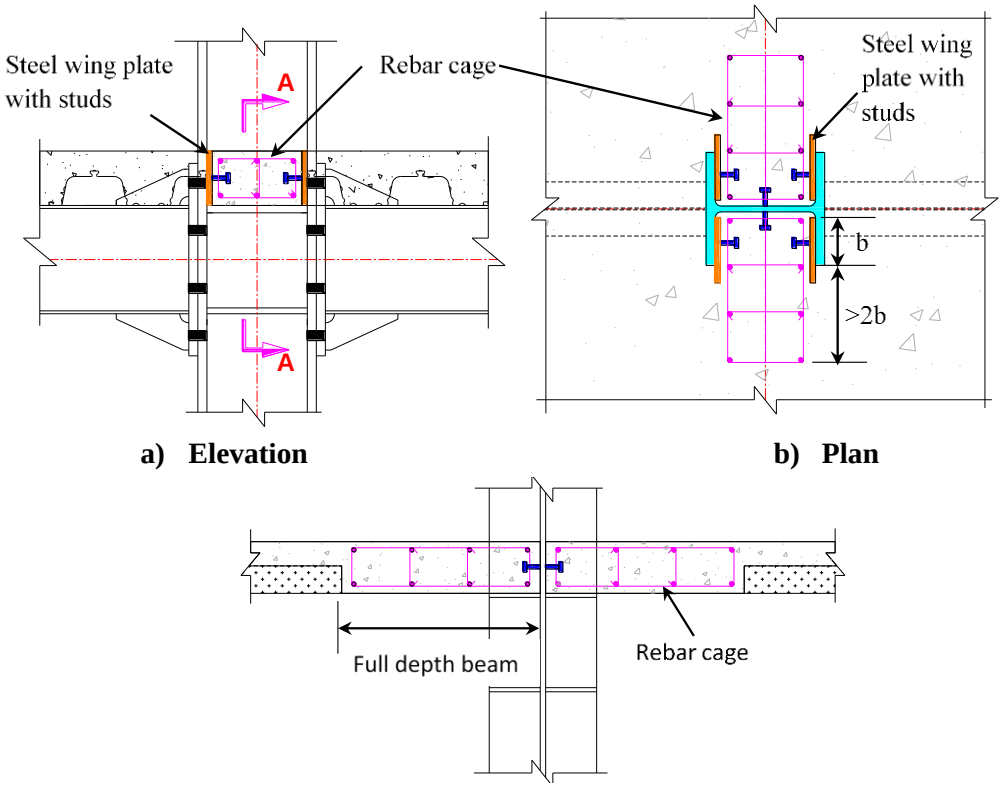

a) Elevation **b) Plan**

c) Section AA

Figure B.7 – Inverted Steel Angle

Advantages:

a) The reinforcement cage of a hidden beam will help to arrest the shear crack as well as to provide concrete confinement to some extent.

b) Less stress concentration at column flanges, since full depth with monolithic construction, will contribute to spread the force on the larger area.

Disadvantages:

a) Increase in the construction time since activates like making of reinforcement cage, formwork (from three sides) are involved.

b) It can be costlier than the above options due to an additional fabrication of the rebar cage and wing plates with studs.

Option 8: Steel Corbel

In this proposed concept, the deck sheet will be cut in such way that, it will form a full depth beam with a width equal to the depth of column section. Two steel angles will be inserted to form a steel corbel along with the top confining plate, which will be bolted to the steel angles as shown in Figure B.8. It is hypothesized that the angle will be projected at least for a length of two times the column flanges outstand, to act as a shear key.

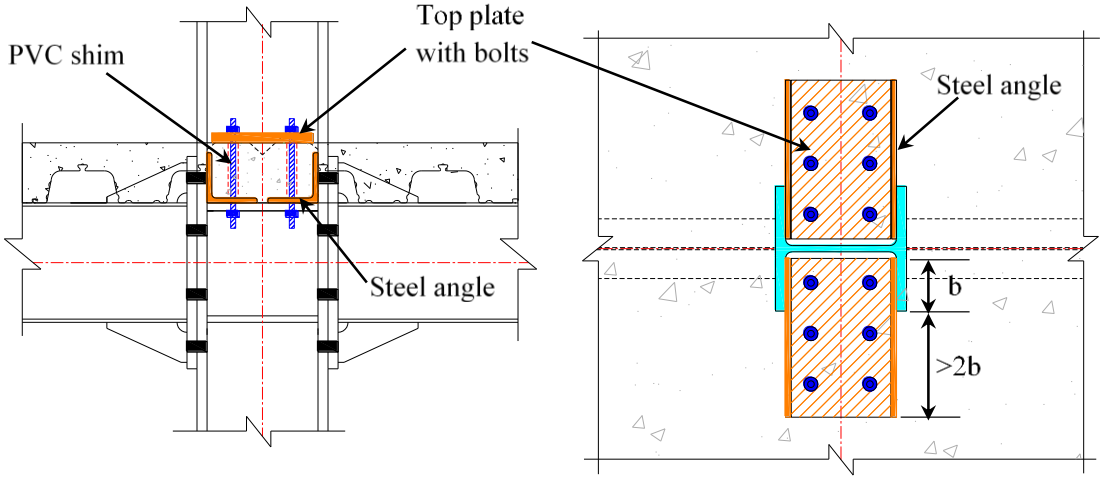

a) Elevation **b) Plan**

Figure B.8 – Steel Corbel

Advantages:

a) The steel corbel helps to arrest the shear cracks along the tip of the column flanges.

b) Provide an active confinement to the slab portion in between the column flanges.

c) Compression on the slab top can be controlled by adjusting the clamping force through the bolts.

d) Less stress concentration at column flanges, since steel corbel will help to spread the force on the larger area.

e) Ease of application. No need of additional formwork as the inserted angles will support the wet concrete.

Disadvantages:

a) Availability of suitable size of angles to fit inside the column flanges or it needs to cut to suit; this might increase the construction time.

b) Top steel plate extended beyond the column tips may hinder the floor finish.

c) It can be costlier than the above options due to an additional material cost.

Option 9: Bolted Steel Plate with Rebars (By Assoc. Prof Gregory MacRae & Tushar)

In this proposed concept, the rebars in the form of V- shape will be anchored to the two centrally located welded threaded rods. These threaded rods will be welded to the column continuity plates. A top confining plate will be bolted to additional threaded rods, located to near to the column inner flanges as shown in Figure B.9. It is hypothesized that the V-shape rebars will help to arrest a shear crack along the column flange tips.

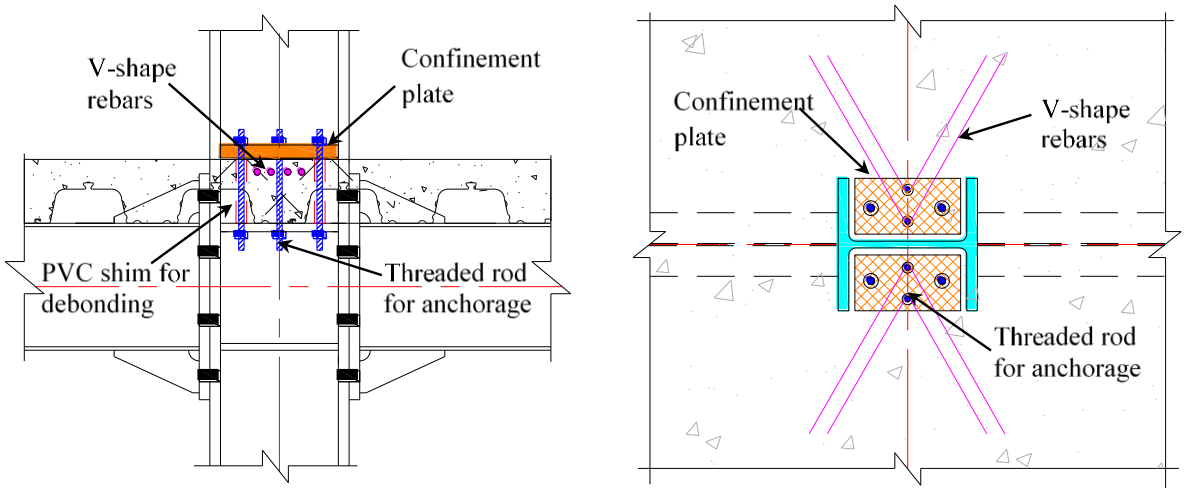

a) Elevation **b) Plan**

Figure B.9 – Bolted Steel Plate with Rebars

Advantages:

a) The V-shape rebars will help to arrest the shear cracks along the column flange tips.

b) Provide an active confinement to the slab portion in between the column flanges.

c) Compression on the slab top can be controlled by adjusting the clamping force through the bolts.

d) Ease of application and economical as compared to option 7 and 8

Disadvantages:

a) Chances of failure due to delayed delamination.

A subjective quantitative analysis (SQA) is performed to determine the most suitable option, and the subjective ranking was based on the confinement, controlling delamination, arresting of the shear crack, ease of application and low cost. The weight percentage was given on the subjective importance of each criterion. Table B.1 shows the details of the subjective quantitative analysis.

Table B.1: SQA Scores (S) on Shear Key Conceptual details

Shear Key Options	Confinement	Controlling Delamination	Arresting of Shear crack	Ease of application	Low Cost	Rank (∑S*W)	Remark
Weights (W)	**25%**	**25%**	**25%**	**15%**	**10%**		
Option 1: Welded Steel Plate	6	4	1	8	9	4.85	Partially active confinement
Option 2: Steel Plate with shear studs	4	3	1	8	8	4.0	Passive confinement
Option 3: Bolted Steel Plate	9	6	3	7	7	6.25	Active confinement
Option 4: Inverted Steel Channel	4	6	7	6	6	5.75	Passive confinement
Option 5: Extended Steel Wing Plates	1	6	8	7	7	5.5	Lack of confinement
Option 6: Inverted Steel Angle	4	6	7.5	6	5.5	5.825	Partially passive confinement
Option 7: Concealed Concrete Beam	5	6	7	5	4	5.65	Passive confinement
Option 8: Steel Corbel	9	6	8	3	4	6.6	Active confinement
Option 9: Bolted Steel Plate with Rebars	9	6	7	6	5	**6.9**	Active confinement

Scale 'S' = 1 to 10 (Poor to Good)

Based on the above SQA, with the rating and weighing scales used, the option 9 (Bolted steel plates with rebars) is found to be more promising than the other option considered herein.

B.2 Selection of SE82 mesh splice location

The available size of SE82mesh is 2440mm wide and 6100mm long. Splicing of the SE82 rebar mesh was essential since an available width of mesh was lesser than the specimen width (3000mm). Several splicing options have been a workout, to select the best splice location and their details are summarised in the Table B.2 below.

Table B.2: Different Splice Options for SE82 Rebar Mesh

Splicing Options	Description	Pros	Cons	Remark
Option 1 (Figure B.10)	The rebar mesh will be placed centrally. The slab will be without a rebar mesh for 250 mm distance from the slab edge.	1) No splicing of the mesh. 2) The Mesh is placed equally all over the slab.	1) The mesh needs to be inserted from the top. 2) The loading ram needs to be removed at every test to allow for the mesh placement. 3) Lack of reinforcement at the slab edges.	1) Ideal Case but impractical in practice. 2) The absence of secondary effects, since no splicing around the column.
Option 2 (Figure B.11)	The rebar mesh will start from the one edge of the slab, and it will be spliced at the other side to cover the balance 480mm width of the slab.	1) The rebar mesh thoroughly covers the slab.	1) The mesh needs to be inserted from the top. 2) The loading ram needs to be removed at every test. 3) Unequal distribution of the rebar mesh, since an extra reinforcement on splice band on one side of the slab.	1) Unsymmetrical reinforcement.
Option 3 (Figure B.12)	The rebar mesh will be inserted from the side, and a chunk of the rebars will be cut to clear the column opening	1) No need to remove the loading ram to place the rebar mesh. 2) The rebar mesh thoroughly covers the slab.	1) Splicing of the reinforcement will be made at two places. 2) Unequal distribution of the rebar mesh, since an extra reinforcement on splice band on one side of the slab.	1) Unsymmetrical reinforcement.
Option 4 (Figure B.13)	In this arrangement, the mesh 1 and mesh 2 will be inserted from the side and splicing of the meshes will be done along the primary beam.	1) No need to remove the loading ram. 2) The rebar mesh is placed equally all around the slab. 3) The rebar mesh thoroughly covers the slab.	1) Splice is on the primary beam. 2) Extra care needs in splicing to develop tension anchorage.	1) Proper anchorage is necessary in order to develop the strut-n-tie mechanism.
Option 5 (By Prof Des Bull) (Figure B.14)	In this arrangement, a mesh of three different sizes will be inserted from sides and splices at two places.	1) No need to remove the loading ram.	1) The rebar mesh does not cover the full slab width. 2) The extra reinforcement on one side of the slab close to primary beams.	1) Splice is located into the strut –n-tie zone of the slab. 2) Chances of the development of the secondary effects.

Option 6 (By Prof Des Bull) (Figure B.15)	In this arrangement, rebar mesh of two different sizes will be inserted from the sides and splices along the secondary beam.	1) No need to remove the loading ram.	1) The rebar mesh does not cover the full slab width. 2) The extra reinforcement on one side of the slab close to secondary beams	1) Splice is located into the strut –n-tie zone of the slab. 2) Chances of the development of the secondary effects.

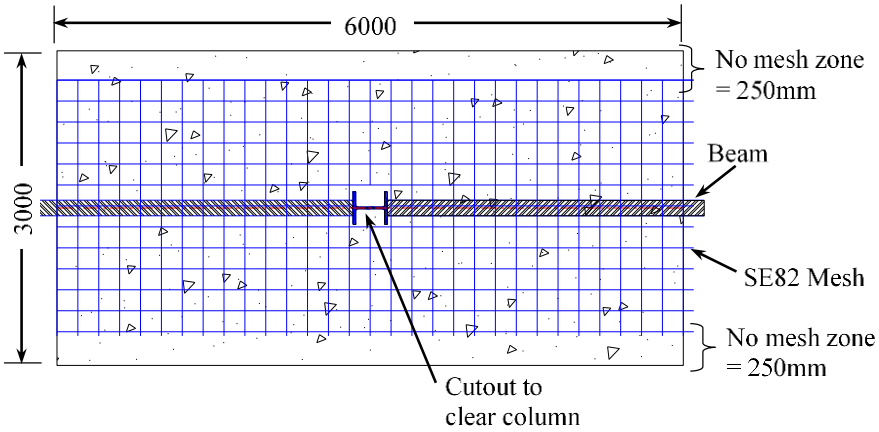

Figure B.10 – Option 1: No Rebar Mesh Splice

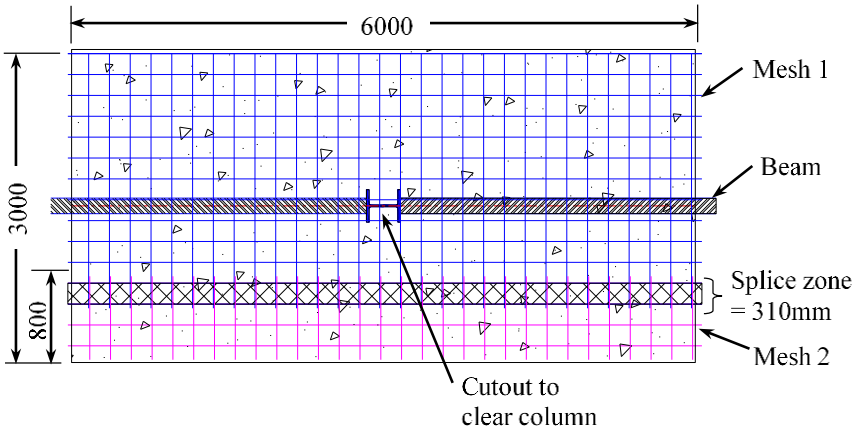

Figure B.11 – Option 2: Rebar Mesh Splice Along One Edge

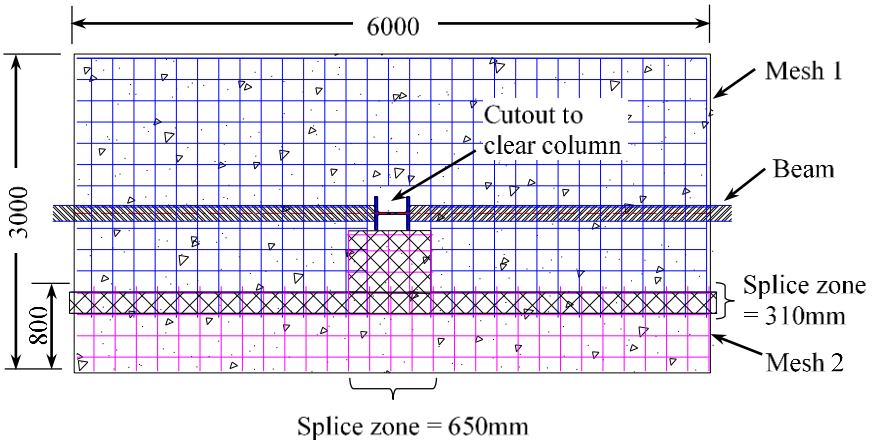

Figure B.12 – Option 3: T shape Rebar Mesh Splice

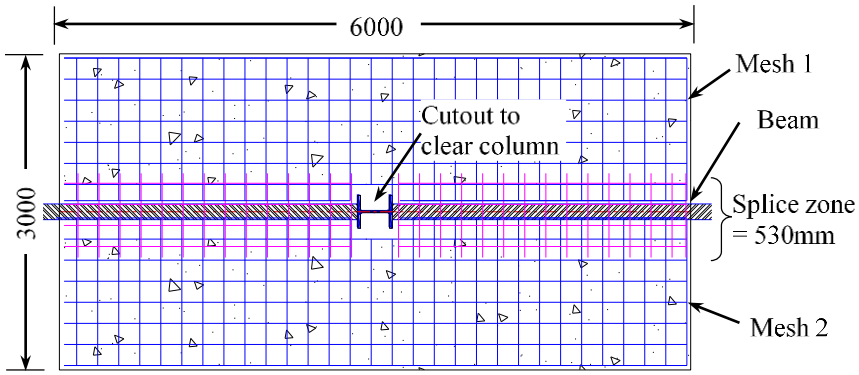

Figure B.13 – Option 4: Rebar Mesh Splice along Main Beam

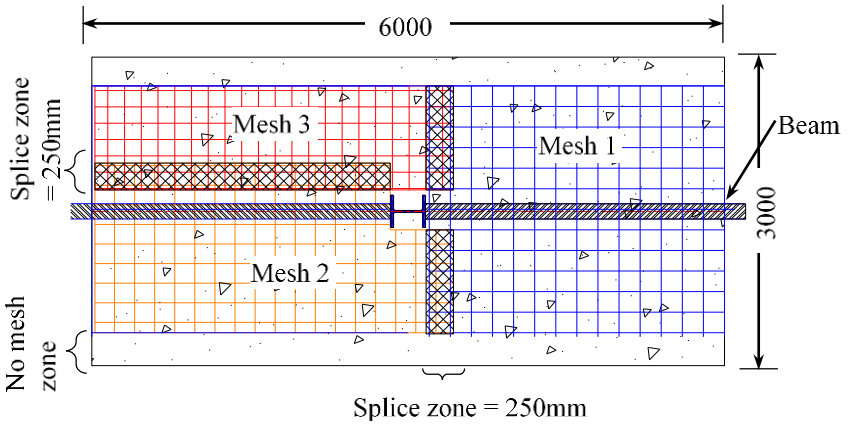

Figure B.14 – Option 5: Rebar Mesh Splice along Half Span and Width

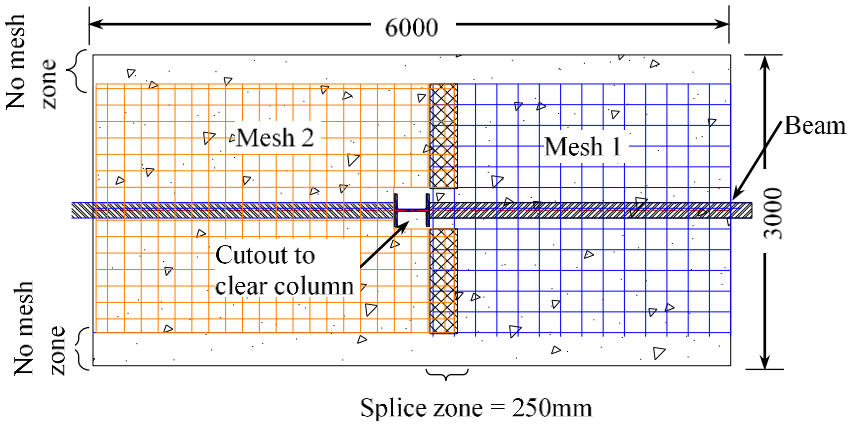

Figure B.15 – Option 6: Rebar Mesh Splice along Width

From the above after considering the ease of application and symmetry of the rebar mesh distribution, the mesh splicing option 4, as shown in Figure B.13 had been selected for the current experimental study.

Appendix C: Material Test Data and Mill Certificates

C.1 Steel Properties and Mill Certificates

The tensile test data on the steel beam (310UB32) and column (310UC158) is presented in this section. The material testing has been carried out at the structural laboratory of the University of Canterbury.

Dimension of the tensile test coupons

The test coupons were obtained from the steel sections and cut to size as suggested by AS 1391. The tensile coupon dimensions are shown in Figure C.1.

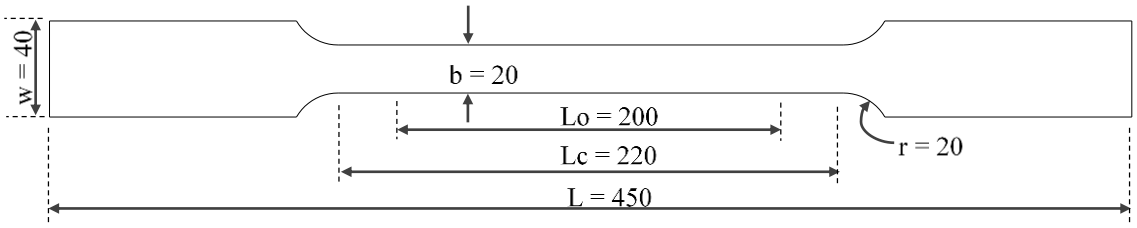

Figure C.1 – Tensile Test Coupon Details

For each specimen three test pieces were fabricated and tested; Table C.1 shows the measured dimensions at three different location and average values of these are used.

Table C.1 Dimensions of the Test Coupon

Section			Width (mm)	Avg. Width (mm)	Thickness (mm)	Avg. Thickness (mm)
Beam 310UB32	Flange	TF1	20.89	20.78	7.38	7.39
			20.78		7.38	
			20.68		7.42	
		TF2	20.33	20.22	7.94	7.92
			20.32		7.93	
			20.02		7.89	
		TF3	19.69	20.32	7.86	7.86
			19.96		7.86	
			20.17		7.65	
	Web	TW1	19.25	19.80	5.55	5.52
			19.89		5.51	
			20.25		5.49	
		TW2	20.61	20.39	5.5	5.49
			20.42		5.46	
			20.15		5.5	
		TW3	20.34	19.58	5.52	5.47
			19.84		5.48	
			18.55		5.42	

Column 310UC158	Flange	CF1	25.04	25.05	20.14	20.34
			25.12		20.44	
			24.99		20.45	
		CF2	25.12	25.08	20.30	20.41
			25.03		20.48	
			25.08		20.46	
		CF3	25.14	25.18	20.74	20.88
			25.27		20.95	
			25.12		20.96	
	Web	CW1	21.01	20.91	15.45	15.44
			20.95		15.44	
			20.76		15.44	
		CW2	20.40	20.54	15.46	15.44
			20.47		15.42	
			20.74		15.45	
		CW3	20.71	20.54	15.42	15.43
			20.52		15.45	
			20.40		15.43	

Tensile Test Data

The test data obtained for the coupon test is presented in below tables.

Table C.2 Test Data for the Beam (310UB32)

Specimen		**Yield Stress σ_y (MPa)**	**Yield Strain ε_y**	**Ultimate Stress σ_u (MPa)**	**Ultimate Strain ε_u**	**Avg. Yield Stress, $\sigma_{y\ avg}$ (MPa)**	**Avg. Ultimate Stress, $\sigma_{u\ avg}$ (MPa)**
Flange	TF1	345.77	0.00216	504.44	0.161	342.83	502.06
	TF2	345.34	0.00211	507.7	0.139		
	TF3	337.38	0.0022	494.04	0.13		
Web	TW1	368.39	0.0029	505.44	0.104	365.32	505.93
	TW2	364.5	0.0024	512.77	0.14		
	TW3	363.07	0.0021	499.57	0.9		

Table C.3 Test Data for the Column (310UC158)

Specimen		**Yield Stress σ_y (MPa)**	**Yield Strain ε_y**	**Ultimate Stress σ_u (MPa)**	**Ultimate Strain ε_u**	**Avg. Yield stress, $\sigma_{y\ avg}$ (MPa)**	**Avg. Ultimate Stress, $\sigma_{u\ avg}$ (MPa)**
Flange	CF1	288.10	0.0021	471.34	0.1554	287.01	474.54
	CF2	298.98	0.0020	479.27	0.1463		
	CF3	273.96	0.0020	473.02	0.1487		
Web	CW1	311.63	0.0024	478.76	0.16	309.05	477.37
	CW2	295.83	0.0019	476.53	0.159		
	CW3	319.7	0.0016	476.83	0.1525		

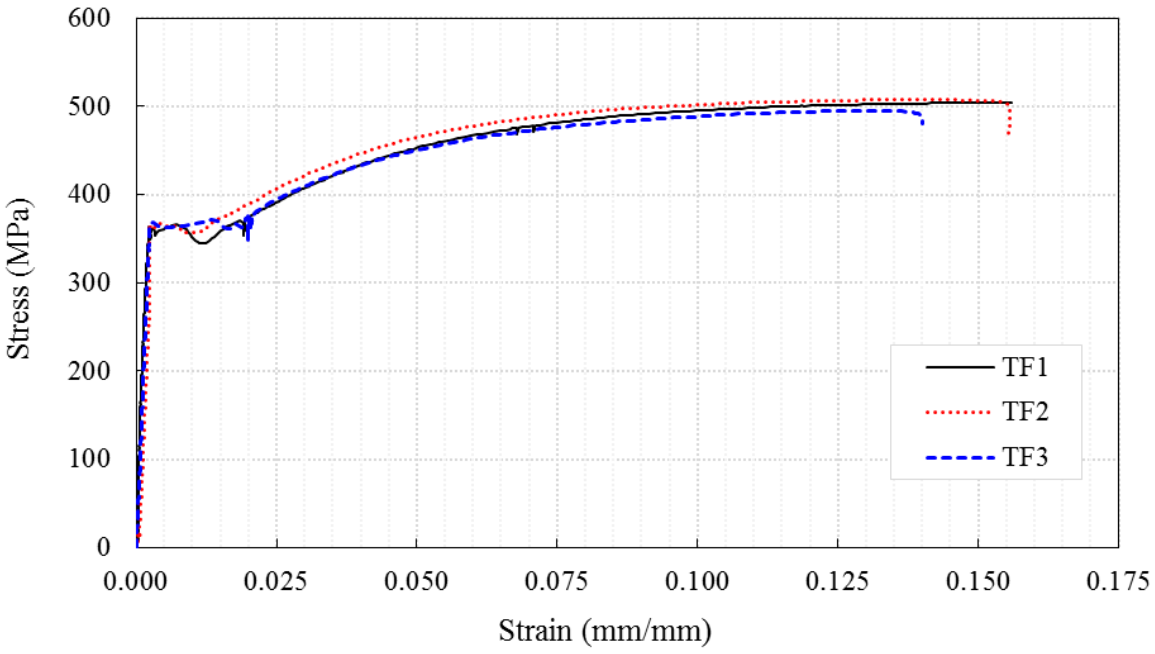

Figure C.2 – Stress-Strain Plot for Beam Flange

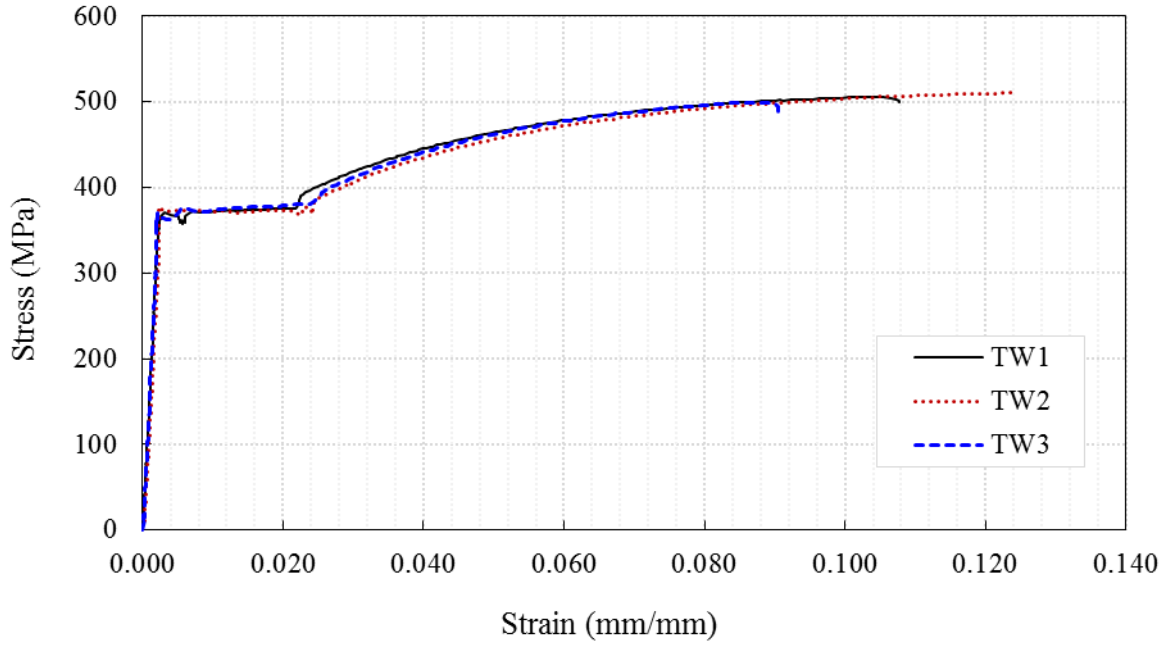

Figure C.3 – Stress-Strain Plot for Beam Web

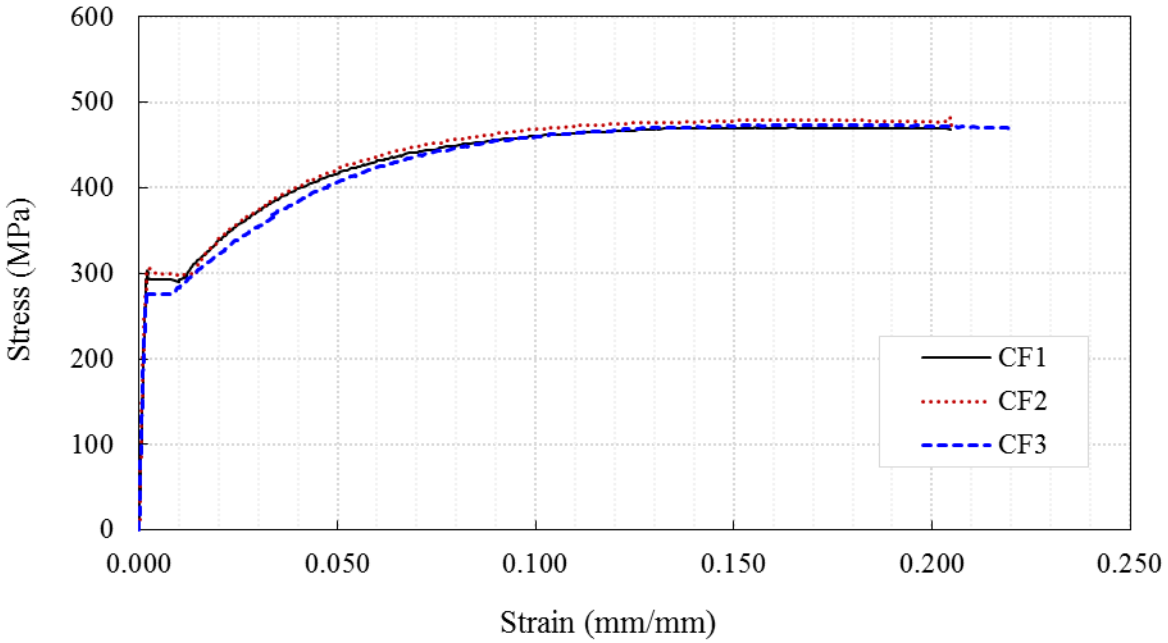

Figure C.4 – Stress-Strain Plot for Column Flange

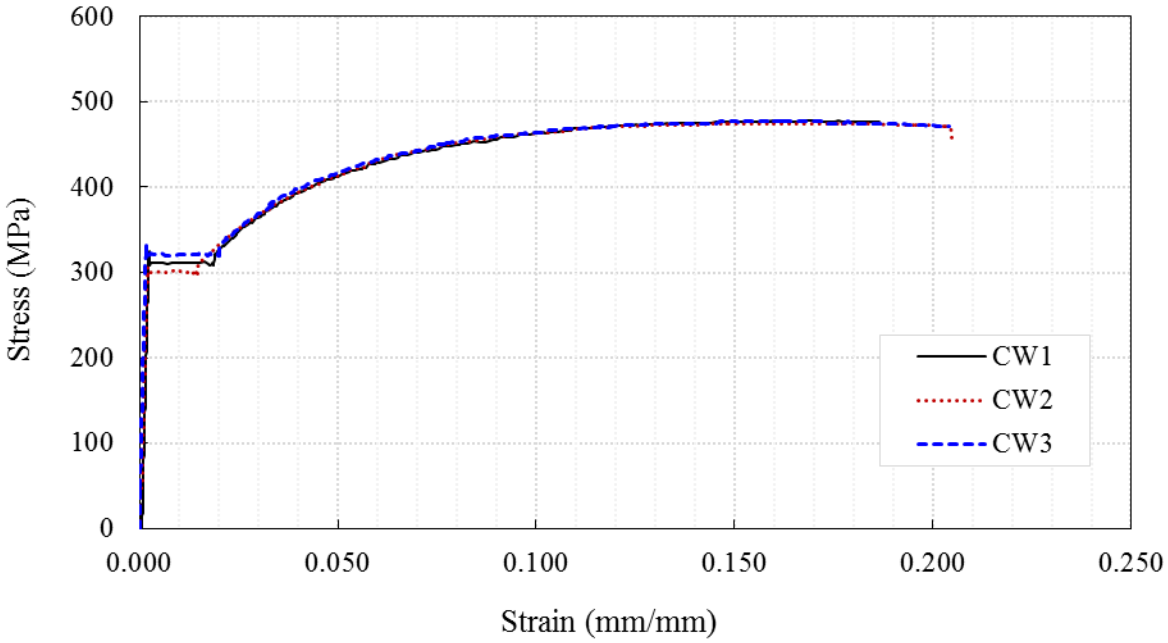

Figure C.5 – Stress-Strain Plot for Column Web

Tension Test Data provided by OneSteel Manufacturing (Mill Test Certificate)

The steel sections were manufactured, tested and certified by the OneSteel. The details of mill test certificates are reproduced below.

onesteel

TEST CERTIFICATE

Page 1 of 2
Certificate No.: W852928
Transmission Date: 31/05/13

Customer:	**VULCAN STEEL LTD** **PO BOX 58009** **GREENMOUNT** **AUCKLAND**	Supplier:	OneSteel Manufacturing Pty Limited Whyalla, SA - 5600, Australia A.B.N. 42 004 651 325
Ship To:	NEW ZEALAND	Sales Order No: Printed on:	Z3020 31/05/2013

NATA — Accredited for compliance with ISO/IEC 17025. This document shall not be reproduced except in full.

Sampling undertaken by OneSteel Whyalla 15352
Approved Signatory - M. Bubicich
Chemical results as identified are from Amdel Ltd, Whyalla 0834
Approved Signatory - K. Barsby
Mechanical results as identified are from Amdel Ltd, Whyalla 0794
Approved Signatory - I. Harrison

STEELMAKING: Basic Oxygen - Slab Cast
SPECIFICATION: ***300PLUS S0***
PRODUCT: ***310UC158***

INSPECTION: Supplier
CERTIFICATION: Supplier

ITEMS COVERED BY THIS TEST CERTIFICATE

Item No	Heat No	Customer Order	Length
0585	533795	88140	15.000
0585	533841	88140	15.000
0585	533842	88140	15.000

3m cut offend

CHEMICAL ANALYSIS

Percentage of element by mass (L=Cast, P=Product, -S=Soluble, -T=Total, CF=Chemical Formula, n=Min, x=Max)

Item No	Heat / Unit No	NATA Lab	L/P	C	P	Mn	Si	S	Ni	Cr	Mo	Cu	Sn	Al
0585	533795	0834	L	.190	.015	1.36	.140	.010	.001	.006	.001	.006	.002	.028
0585	533841	0834	L	.172	.011	1.42	.140	.009	.004	.005	.001	.014	.005	.022
0585	533842	0834	L	.168	.011	1.45	.150	.011	.005	.006	.001	.014	.006	.027

Item No	Heat / Unit No	NATA Lab	L/P	Nb	Ti	B	V	N	Ca	Zr	CF1
0585	533795	0834	L	.001	.001	.0004	.001	.0036	.0001	.001	.42
0585	533841	0834	L	.001	.001	.0003	.001	.0042	.0007	.001	.41
0585	533842	0834	L	.001	.001	.0003	.001	.0053	.0007	.001	.41

CF1=C+Mn/6 + (Cr+Mo+V)/5 + (Ni+Cu)/15

MECHANICAL TESTING

Tensile

Item No	Heat No	Tested Unit	NATA Lab	Test Report	ReH MPa	Rm MPa	ELONGN %
0585	533795	533795	0794	53455	335	500	32
0585	533795	533795	0794	53455	325	490	32
0585	533841	533841	0794	53455	315	480	32
0585	533842	533842	0794	53455	315	490	32
0585	533842	533842	0794	53457	330	490	32

Yield Strength - determined in accordance with requirements of nominated product standard

Charpy V-Notch

Item No	Heat No	Tested Unit	NATA Lab	Test Report	Wo mm	THICK mm	TEMP DEG C	ENERGY JOULES	ENERGY JOULES	ENERGY JOULES	AVG EGY JOULES
0585	533795	533795	0794	53460	10.0	10.0	0	156	141	152	149
0585	533795	533795	0794	53460	10.0	10.0	0	134	137	101	124
0585	533841	533841	0794	53460	10.0	10.0	0	176	170	163	169
0585	533842	533842	0794	53460	10.0	10.0	0	135	133	140	136

AVG EGY = Average Energy

COMMENTS

OneSteel Whyalla is quality endorsed to AS/NZS ISO9001 under SAI GLOBAL Lic. No. - QEC0351.
300PLUS S0 satisfies the requirements of AS/NZS 3679.1-300 and NZS3404 (Table 12.4) This document shall not be reproduced except in full.

onesteel

TEST CERTIFICATE

Certificate No.: W865111
Transmission Date: 09/10/13

Customer:	VULCAN STEEL LTD PO BOX 58009 GREENMOUNT AUCKLAND	Supplier:	OneSteel Manufacturing Pty Limited Whyalla, SA - 5600, Australia A.B.N. 42 004 651 325
Ship To:	NEW ZEALAND	Sales Order No: Printed on:	Z3020 09/10/2013

NATA

Accredited for compliance with ISO/IEC 17025. This document shall not be reproduced except in full.

Sampling undertaken by OneSteel Whyalla 15352
Approved Signatory - M. Bubicich
Chemical results as identified are from Amdel Ltd, Whyalla 0834
Approved Signatory - K. Barsby
Mechanical results as identified are from Amdel Ltd, Whyalla 0794
Approved Signatory - I. Harrison

STEELMAKING: Basic Oxygen - Slab Cast
SPECIFICATION: *AS/NZS3679.1-300*
PRODUCT: *310UB32.0*

INSPECTION: Supplier
CERTIFICATION: Supplier

ITEMS COVERED BY THIS TEST CERTIFICATE

Item No	Heat No	Customer Order	Length
1476	535252	89115	12.000
1476	535253	89115	12.000
1476	535543	89115	12.000
1477	535249	89115	18.000
1477	535250	89115	18.000

CHEMICAL ANALYSIS

Percentage of element by mass (L=Cast, P=Product, -S=Soluble, -T=Total, CF=Chemical Formula, n=Min, x=Max)

Item No	Heat / Unit No	NATA Lab	L/P	C	P	Mn	Si	S	Ni	Cr	Mo	Cu	Sn	Al
1476	535252	0834	L	.190	.010	1.32	.170	.010	.003	.005	.001	.009	.005	.030
1476	535253	0834	L	.184	.014	1.39	.160	.009	.001	.007	.001	.007	.001	.032
1476	535543	0834	L	.171	.010	1.42	.140	.009	.003	.004	.001	.005	.006	.014
1477	535249	0834	L	.168	.011	1.43	.150	.010	.003	.004	.001	.009	.004	.022
1477	535250	0834	L	.170	.014	1.42	.150	.014	.003	.006	.001	.008	.004	.024

Item No	Heat / Unit No	NATA Lab	L/P	Nb	Ti	B	V	N	Ca	Zr	CF1
1476	535252	0834	L	.001	.001	.0003	.001	.0054	.0007	.001	.41
1476	535253	0834	L	.001	.001	.0003	.001	.0057	.0001	.001	.42
1476	535543	0834	L	.001	.001	.0003	.001	.0049	.0009	.001	.41
1477	535249	0834	L	.001	.001	.0003	.001	.0057	.0006	.001	.41
1477	535250	0834	L	.001	.001	.0003	.001	.0060	.0006	.001	.41

CF1=C+Mn/6 + (Cr+Mo+V)/5 + (Ni+Cu)/15

MECHANICAL TESTING

Tensile

Item No	Heat No	Tested Unit	NATA Lab	Test Report	ReH MPa	Rm MPa	ELONGN %
1476	535252	535252	0794	53681	375	510	37
1476	535252	535252	0794	53681	360	510	38
1476	535252	535252	0794	53683	365	500	34
1476	535253	535253	0794	53681	345	470	35
1476	535253	535253	0794	53681	350	500	34
1476	535543	535543	0794	53681	335	480	36
1476	535543	535543	0794	53681	345	480	35
1477	535249	535249	0794	53683	360	510	35
1477	535249	535249	0794	53683	365	510	36
1477	535250	535250	0794	53683	360	490	34
1477	535250	535250	0794	53683	350	490	37

Yield Strength - determined in accordance with requirements of nominated product standard

onesteel

TEST CERTIFICATE

Certificate No.: W865111
Transmission Date: 09/10/13

COMMENTS

OneSteel Whyalla is quality endorsed to AS/NZS ISO9001 under SAI GLOBAL Lic. No. - QEC0351.

I certify the conformance of the material to the requirements and that the information on this certificate is in accordance with the records of the company.
S. Stuppos - OneSteel Whyalla

onesteel

TEST CERTIFICATE

Certificate No.: W878898
Transmission Date: 08/04/14

Customer:	VULCAN STEEL LTD PO BOX 58009 GREENMOUNT AUCKLAND	Supplier:	OneSteel Manufacturing Pty Limited Whyalla, SA - 5600, Australia A.B.N. 42 004 651 325
Ship To:	NEW ZEALAND	Sales Order No: Printed on:	Z4020 08/04/2014

NATA

Accredited for compliance with ISO/IEC 17025. This document shall not be reproduced except in full.

Sampling undertaken by OneSteel Whyalla 15352
Approved Signatory - M. Bublcich
Chemical results as identified are from Amdel Ltd, Whyalla 0834
Approved Signatory - K. Barsby
Mechanical results as identified are from Amdel Ltd, Whyalla 0794
Approved Signatory - I. Harrison

STEELMAKING: Basic Oxygen - Slab Cast
SPECIFICATION: *AS/NZS3679.1-300*
PRODUCT: *200UB29.8*

INSPECTION: Supplier
CERTIFICATION: Supplier

ITEMS COVERED BY THIS TEST CERTIFICATE

Item No	Heat No	Customer Order	Length
0423	541150	90156	12.000

CHEMICAL ANALYSIS

Percentage of element by mass (L=Cast, P=Product, -S=Soluble, -T=Total, CF=Chemical Formula, n=Min, x=Max)

Item No	Heat / Unit No	NATA Lab	L/P	C	P	Mn	Si	S	Ni	Cr	Mo	Cu	Sn	Al
0423	541150	0834	L	.168	.016	1.41	.190	.009	.003	.010	.001	.009	.010	.002

Item No	Heat / Unit No	NATA Lab	L/P	Nb	Ti	B	V	N	Ca	Zr	CF1
0423	541150	0834	L	.001	.001	.0003	.001	.0078	.0001	.001	.40

CF1=C+Mn/6 + (Cr+Mo+V)/5 + (Ni+Cu)/15

MECHANICAL TESTING

Tensile

Item No	Heat No	Tested Unit	NATA Lab	Test Report	ReH MPa	Rm MPa	ELONGN %
0423	541150	541150	0794	54422	345	500	35
0423	541150	541150	0794	54422	360	510	35
0423	541150	541150	0794	54422	350	500	35

Yield Strength - determined in accordance with requirements of nominated product standard

COMMENTS

OneSteel Whyalla is quality endorsed to AS/NZS ISO9001 under SAI GLOBAL Lic. No. - QEC0351.
This document shall not be reproduced except in full.

I certify the conformance of the material to the requirements and that the information on this certificate is in accordance with the records of the company.
S. Stuppos - OneSteel Whyalla

C.2 Concrete Properties and Batch Record

The concrete cylinders of 100mm diameter and 200mm high were casted at every slab pour. They were cured at the control temperature inside the fog room. Cylinders are tested in compression test machine as shown in Figure C.6

a) Compression Test

b) Tested Cylinders

Figure C.6 – Compression Cylinder Test

Three cylinders were tested, and the test results are tabulated in Table C.4 below.

Table C.4 Compression cylinder test data

Test Specimen		Compressive Cylinder Strength (MPa)		
		21 Days	**28 Days**	**Test Day**
Fully Isolated Slab Unit (FI-SU)	C1	43.135	43.737	45.596
	C2	37.757	40.971	42.906
	C3	38.841	45.546	47.322
	Average	**39.91**	**43.42**	**45.27**
Shear Key Slab Unit (SK-SU)	C1	31.52	36.00	41.8
	C2	36.153	40.00	40.7
	C3	34.321	40.99	41.0
	Average	**34.00**	**39.00**	**41.17**
Modified Shear Key Slab Unit (MSK-SU)	C1	30.87	38.67	*38.67
	C2	34.50	40.81	*40.81
	C3	36.63	39.34	*39.34
	Average	**34.00**	**39.61**	***39.61**
Fully Depth Slab Unit (FD-SU)	C1	35.58	40.00	*40.00
	C2	30.03	40.10	*40.10
	C3	36.07	38.71	*38.71
	Average	**33.89**	**39.61**	***39.61**

*The slab test was carried on the 28th Day

Batch Record provided by Allied Concrete

The concrete was supplied by the ready mix supplier "Allied Concrete," and the batch record furnished by the provider is shown below.

1) Batch record for Fully Isolated Slab Unit

Batch Variation Report

Start Date : 1/01/2014 **Plant :** 1 **Product :** 3019
End Date : 24/07/2014 **Customer :** **Project :**

Ticket # : 6607745 **Ticket Date :** 17/07/2014 **Batch Time :** 10:30 **Truck # :** 217 **Plant :** 1
Product : 3019 30MPa 19mm Concrete **Load Size :** 2.5 m3 **Customer :** 1021 **Project**

Material Code	Description	Supplier	Total			Per m3			Moisture	Actual Water
			Target	Actual	Error	Target	Actual	Error	%	(L/m3)
CEM-HGP	Holcim GP Cement	Holcim	663	660 kg	-3	265.20	264.00	-1.20		
PR13	13mm Pound Road	Fulton	1414	1410 kg	-4	565.60	564.00	-1.60	1.00	5.58
PR19	19mm Pound Road	Fulton	1407	1430 kg	23	562.80	572.00	9.20	0.50	2.85
PR05	5mm Sand Pound Road	Fulton	2233	2250 kg	17	893.20	900.00	6.80	5.30	45.30
WR-SP500	SikaPlast 500 - Water	Sika NZ	3313	3300 ml	-13	1325.2	1320.0	-5.20		
WT-FRESH	Fresh Water	Town	0.0	0.0 L	0.0	0.00	0.00	0.00		
WT-RECYC	Recycled Water	Recycled	219.0	220.0 L	1.0	87.60	88.00	0.40		88.00
TEMPER2	Fresh Water		17.0	17.0 L	0.0	6.80	6.80	0.00		6.80

Total Cost : Total Water 148.53

2) Batch record for Shear Key Slab Unit

Batch Variation Report

Start Date : 1/12/2014 **Plant :** 1 **Product :**
End Date : 26/05/2015 **Customer :** **Project :**

Ticket # : 6619807 **Ticket Date :** 9/12/2014 **Batch Time :** 08:59 **Truck # :** 419 **Plant :** 1
Product : 3019 30MPa 19mm Concrete **Load Size :** 2.2999999 **Customer :** 1021 **Project**

Material Code	Description	Supplier	Total			Per m3			Moisture	Actual Water
			Target	Actual	Error	Target	Actual	Error	%	(L/m3)
CEM-HGP	Holcim GP Cement	Holcim	610	602 kg	-8	265.22	261.74	-3.48		
PR13	13mm Pound Road	Fulton	1297	1310 kg	13	563.91	569.57	5.65	0.70	3.96
PR19	19mm Pound Road	Fulton	1294	1290 kg	-4	562.61	560.87	-1.74	0.50	2.79
PR05	5mm Sand Pound Road	Fulton	2058	2060 kg	2	894.78	895.65	0.87	5.50	46.69
WR-SP500	SikaPlast 500 - Water	Sika NZ	3048	3100 ml	52	1325.2	1347.8	22.61		
WT-FRESH	Fresh Water	Town	0.0	0.0 L	0.0	0.00	0.00	0.00		
WT-RECYC	Recycled Water	Recycled	218.0	220.0 L	2.0	94.78	95.65	0.87		95.65
TEMPER2	Fresh Water		0.0	0.0 L	0.0	0.00	0.00	0.00		

Total Cost : Total Water 149.09

3) Batch record for Modified Shear Key Slab Unit

Batch Variation Report

Start Date : 1/12/2014 **Plant :** 1 **Product :**
End Date : 26/05/2015 **Customer :** **Project :**

Ticket # : 6626904 **Ticket Date :** 17/03/2015 **Batch Time :** 12:29 **Truck # :** 351 **Plant :** 1
Product : 3019 30MPa 19mm Concrete **Load Size :** 2.2999999 **Customer :** 1021 **Project**

Material Code	Description	Supplier	Total			Per m3			Moisture	Actual Water
			Target	Actual	Error	Target	Actual	Error	%	(L/m3)
CEM-HGP	Holcim GP Cement	Holcim	621	616 kg	-5	270.00	267.83	-2.17		
PR13	13mm Pound Road	Fulton	1300	1290 kg	-10	565.22	560.87	-4.35		
PR19	19mm Pound Road	Fulton	1300	1300 kg	0	565.22	565.22	0.00		
PR05	5mm Sand Pound Road	Fulton	2060	2060 kg	0	895.65	895.65	0.00	6.80	57.03
WR-SP500	SikaPlast 500 - Water	Sika NZ	3726	3700 ml	-26	1620.0	1608.7	-11.30		
WT-FRESH	Fresh Water	Town	0.0	0.0 L	0.0	0.00	0.00	0.00		
WT-RECYC	Recycled Water	Recycled	189.0	190.0 L	1.0	82.17	82.61	0.43		82.61
TEMPER1	Fresh Water		0.0	0.0 L	0.0	0.00	0.00	0.00		

Total Cost : Total Water 139.64

4) Batch record for Full Depth Slab Unit

ALLIED CONCRETE
SOCKBURN, CHRISTCHURCH

Truck	Driver	User	Disp Ticket Num	Ticket ID	Time	Date
0419	419	dwayne		82371	8:45 8:49	5-26-15

Load Size	Mix Code	Returned	Qty	Mix Age	Seq	Load ID
2.50 m3	3019				L1	87272

Material	Design Qty	Required	Batched	✓	% Var	% Moisture	Actual Wat	
PR19	565 kg	1413 kg	1450 kg	✓	2.65%			2.65
PR13	565 kg	1413 kg	1410 kg	✓	-0.18%			2.65
PR05	840 kg	2208 kg	2200 kg	✓	-0.36%	5.36% A	112 kg	2.63
CEM-HGP	270 kg	675 kg	670 kg	✓	-0.74%			3.15
WR-SP500	1485 mL	3713 mL	3700 mL	✓	-0.34%			1.23
WT-FRESH	155 kg	kg	kg	✓				1
WT-RECYC	100.000 kg	# 249.595 kg	250.000 kg	✓	0.16%		245.292 kg	1.012
TEMPER 1		2 L	2 L		0.00%		2 kg	0

Actual Num Batches: 1 Manual 8:45:26
Load Total: 5986 kg Design 0.574 Water/Cement 0.578 T Design 387.5 kg Actual 359.3 kg To Add: 28.2 k
Slump: 100.00 mm Water in Truck: 0.0 kg Adjust Water:-30. kg / Load Trim Water: 0.0 kg/ m3

SLUMP WATER – 26L

FINAL WATER/CEMENT $= \frac{387,5 + 26}{670} = \frac{413,5}{670} = 0,617$

PREDICTED STRENGTH – 34 MPa [TMS – 36MPa]
@ 28days

28/5/15

Appendix D: Experimental Results-Additional Information

This appendix provided additional information about the experimental test results of the different test configurations.

D.1 End-plate Lift-off

In this section, the plot of the end-plate lift-off of the beam-column connection is shown for the different test configurations. The end-plate lift-off has been calculated from the spring potentiometer mounted in between the end-plate and the column outer flange. The detail methodology has been discussed in data processing Section 3.9.

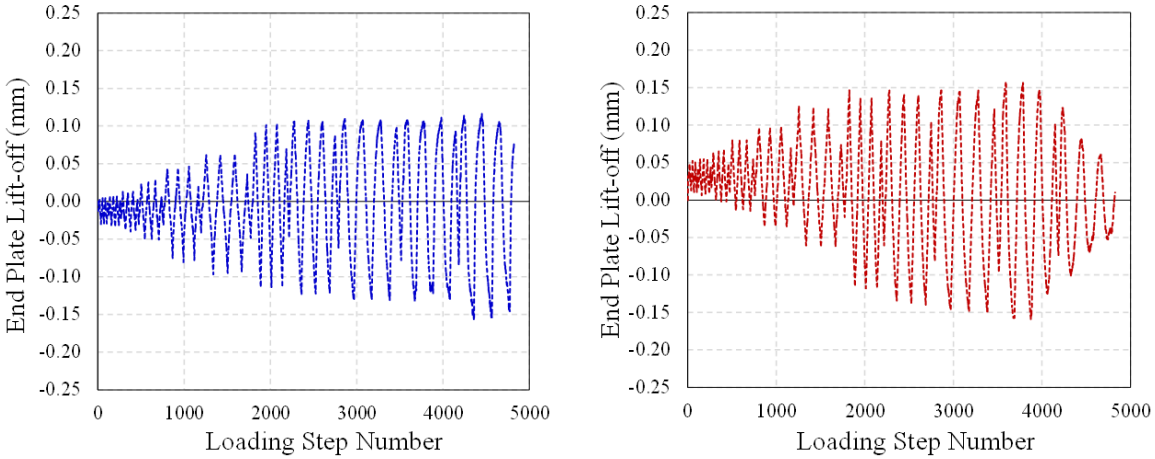

a) South Beam **b) North Beam**

Figure D.1 - End-plate Lift-off : BSF Sub-assembly

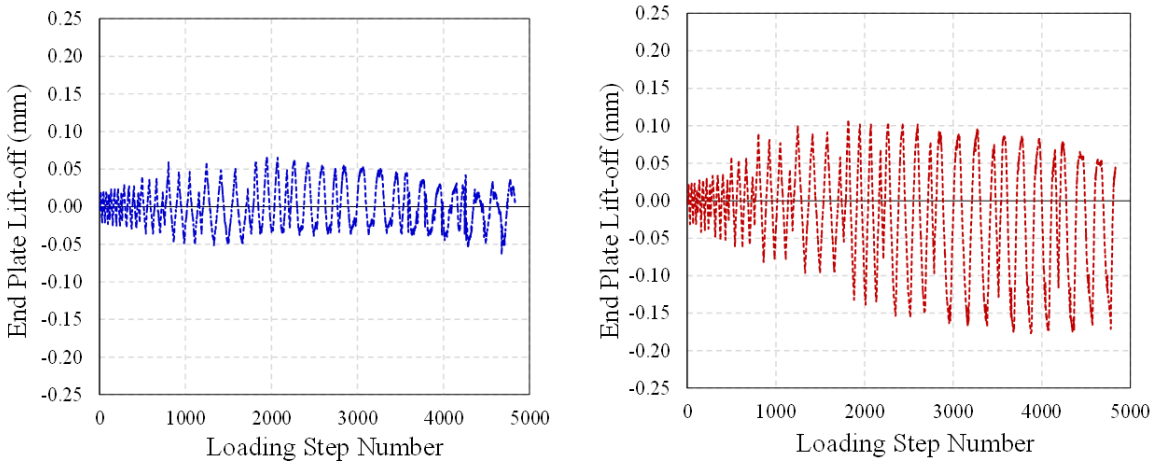

a) South Beam **b) North Beam**

Figure D.2 - End-plate Lift-off : FI-SU Sub-assembly

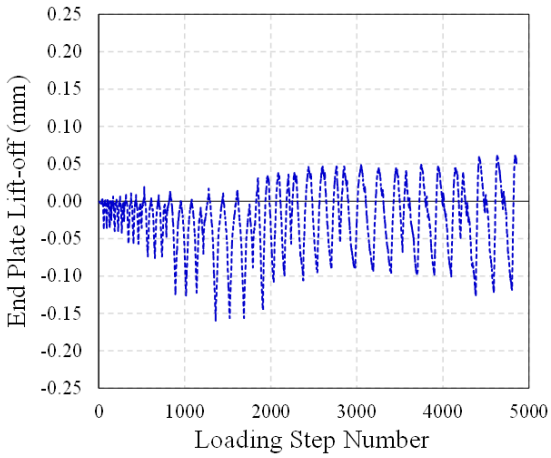

a) **South Beam**

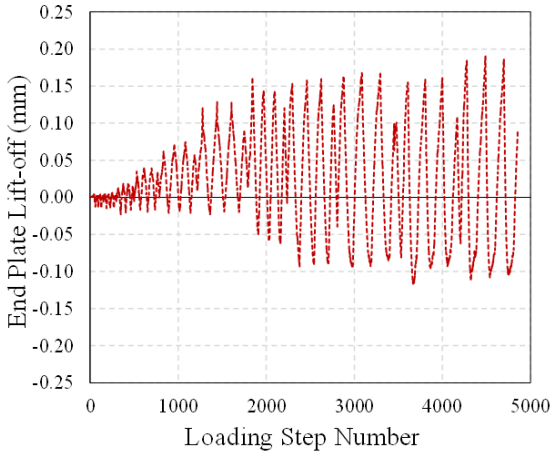

b) **North Beam**

Figure D.3 - End-plate Lift-off : SK-SU Sub-assembly

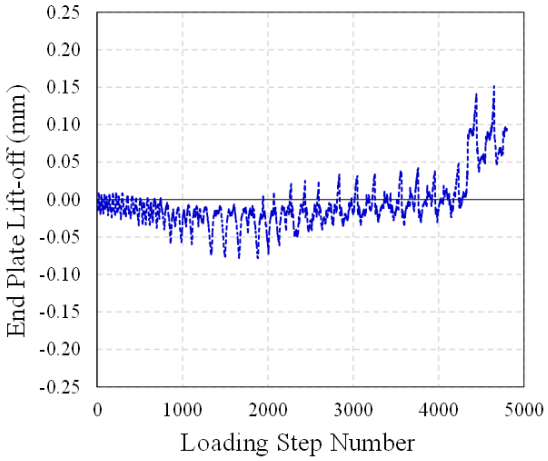

a) **South Beam**

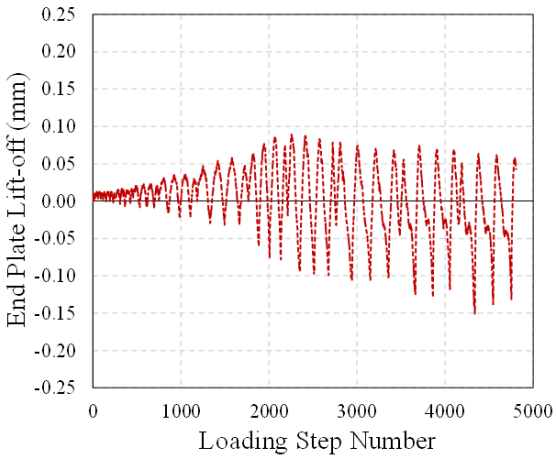

b) **North Beam**

Figure D.4 - End-plate Lift-off : MSK-SU Sub-assembly

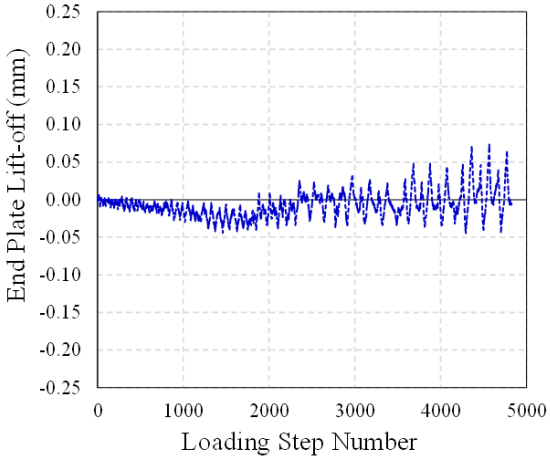

a) **South Beam**

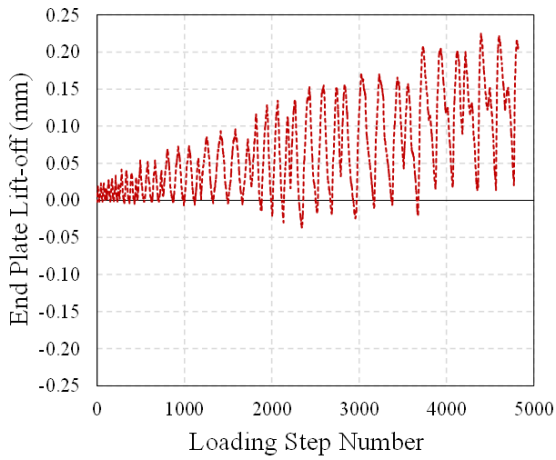

b) **North Beam**

Figure D.5 - End-plate Lift-off : FD-SU Sub-assembly

D.2 Column Base Slip

The slip at the column base has been obtained through the spring potentiometer installed in between the base plate and the strong floor in order to correct the column top displacement to the base slip if any; the base slip plots are shown in the following Figure D.6.

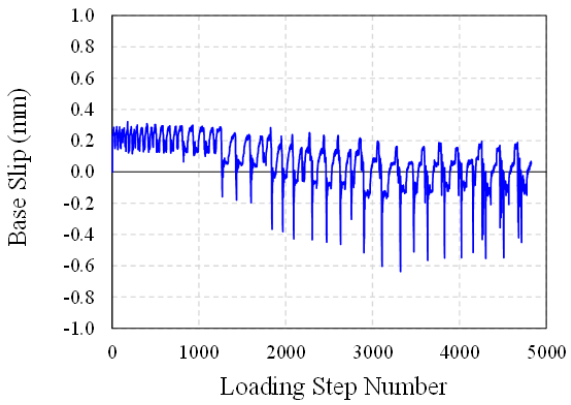

a) BSF Sub-assembly

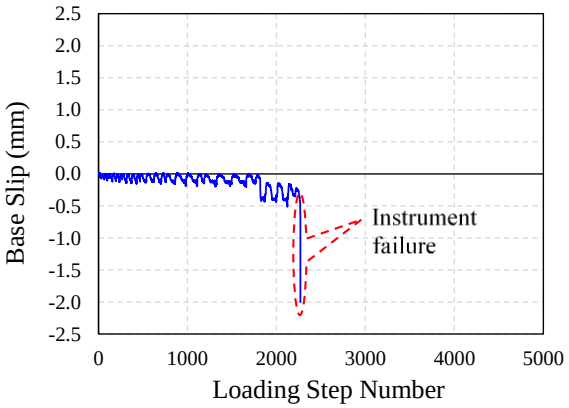

b) FI-SU Sub-assembly

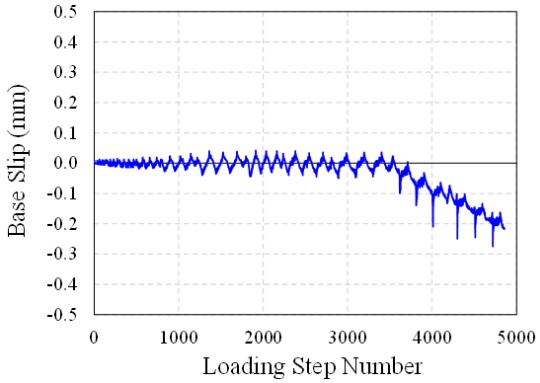

c) SK-FU Sub-assembly

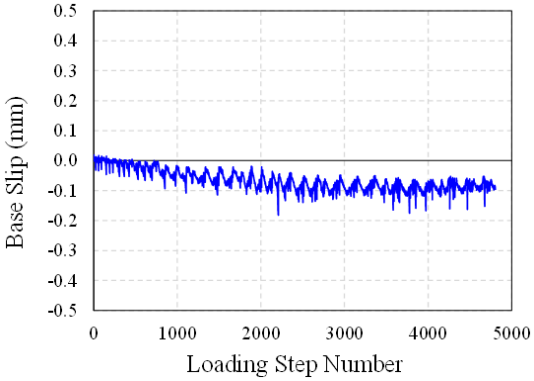

d) MSK-SU Sub-assembly

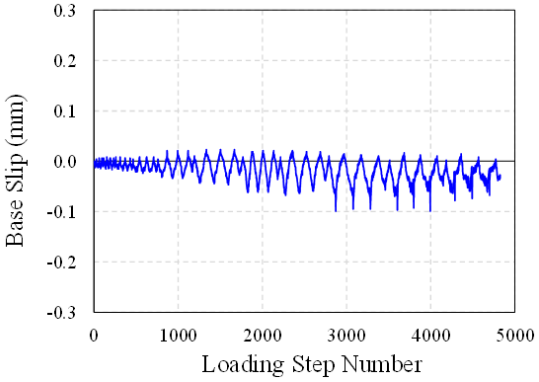

e) FD-SU Sub-assembly

Figure D.6 - Base Slip of Different Test Configuration

D.3 Deck Slip

The deck slip has been captured through the spring potentiometer installed in between the deck soffit and the Sub-assembly main beam. The deck slip was noted at the two different locations, first is located at the 2nd shear stud (Location 1) and the second location is at the 3rd shear stud (Location 2) from the column face. The deck slip plots are shown in the following Figure D.7.

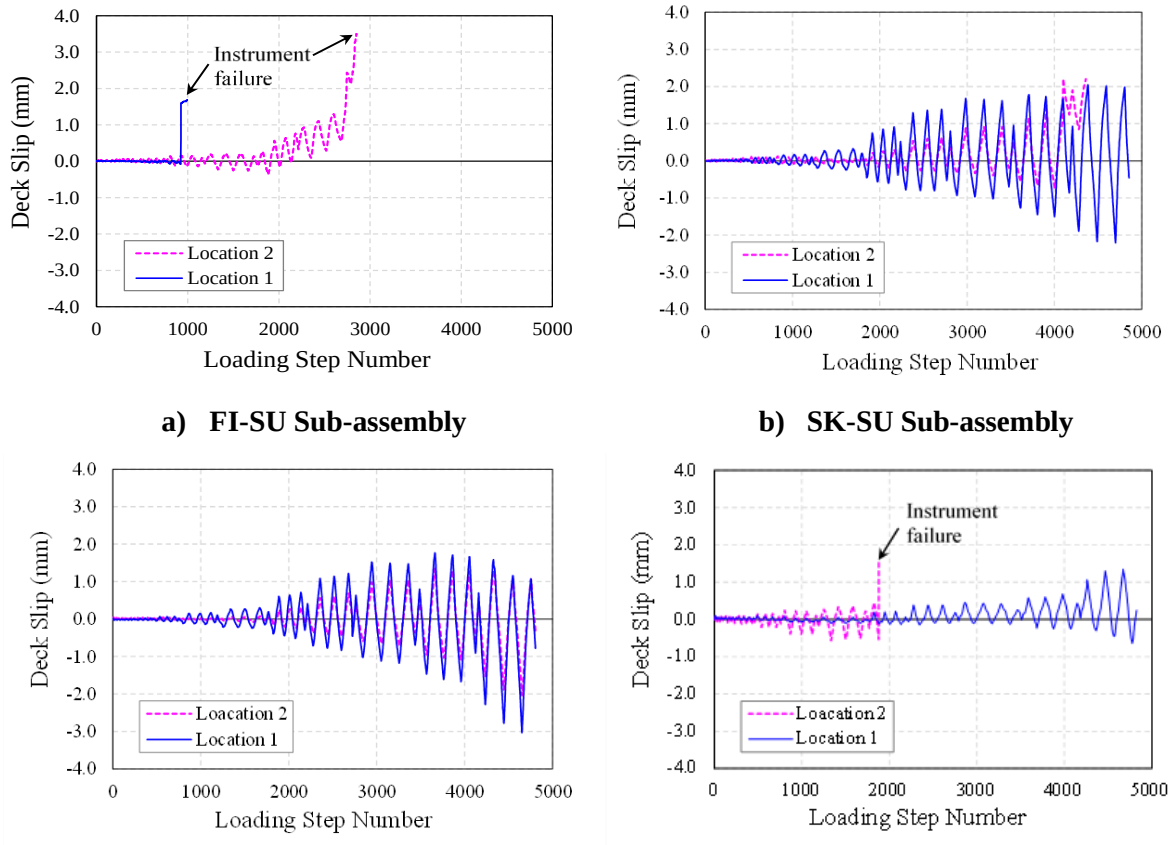

a) FI-SU Sub-assembly

b) SK-SU Sub-assembly

c) MSK-FU Sub-assembly

d) FD-SU Sub-assembly

Figure D.7 - Deck Slip of Different Test Configuration

D.4 Slab Surface Deformation

As discussed in Chapter 4, this section provides a drift wise plot of the slab surface deformation for the 1.0%, 1.5%, 3.5% and 5.0% drifts of different slab configurations are shown in Figures D.8 to D.11.

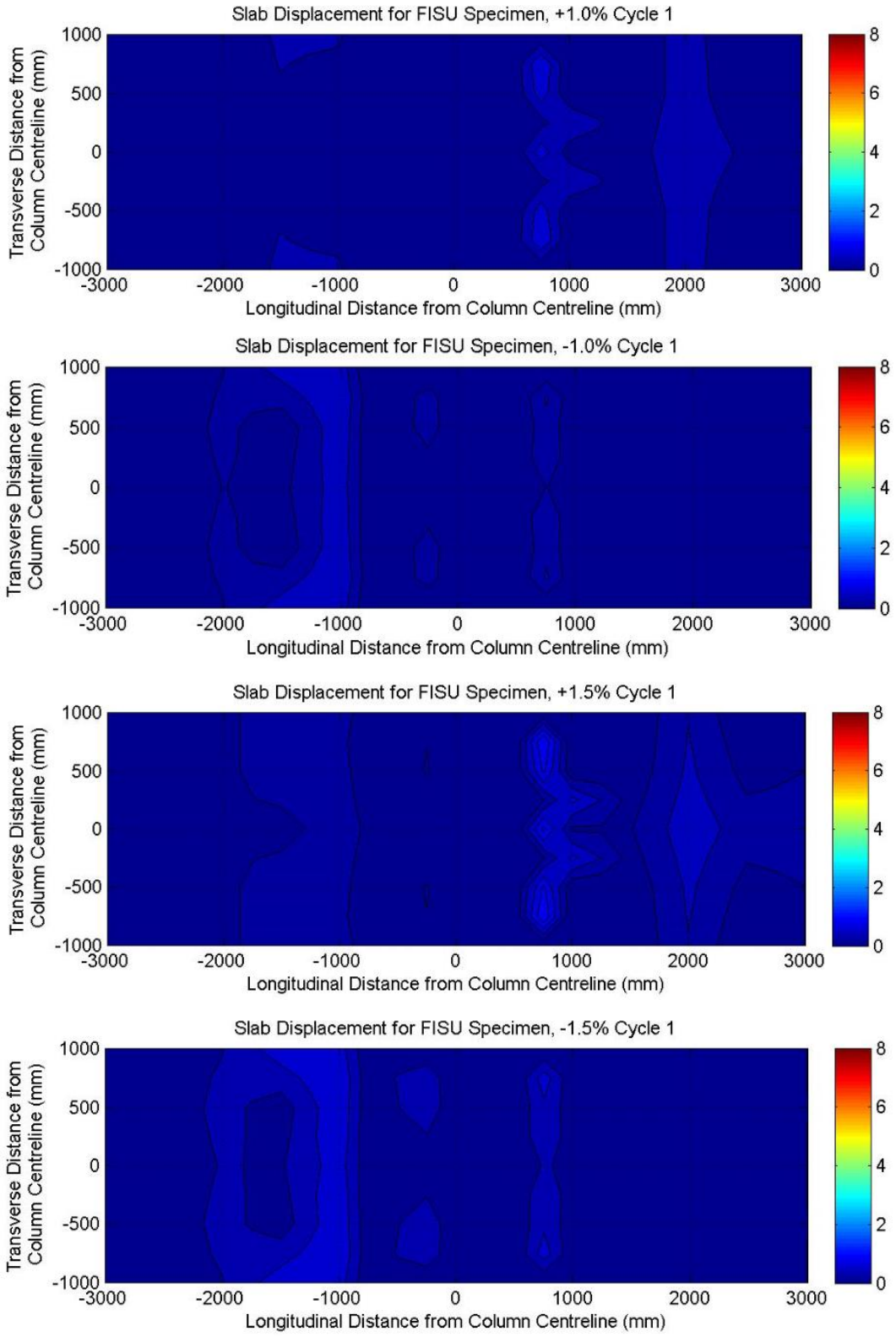

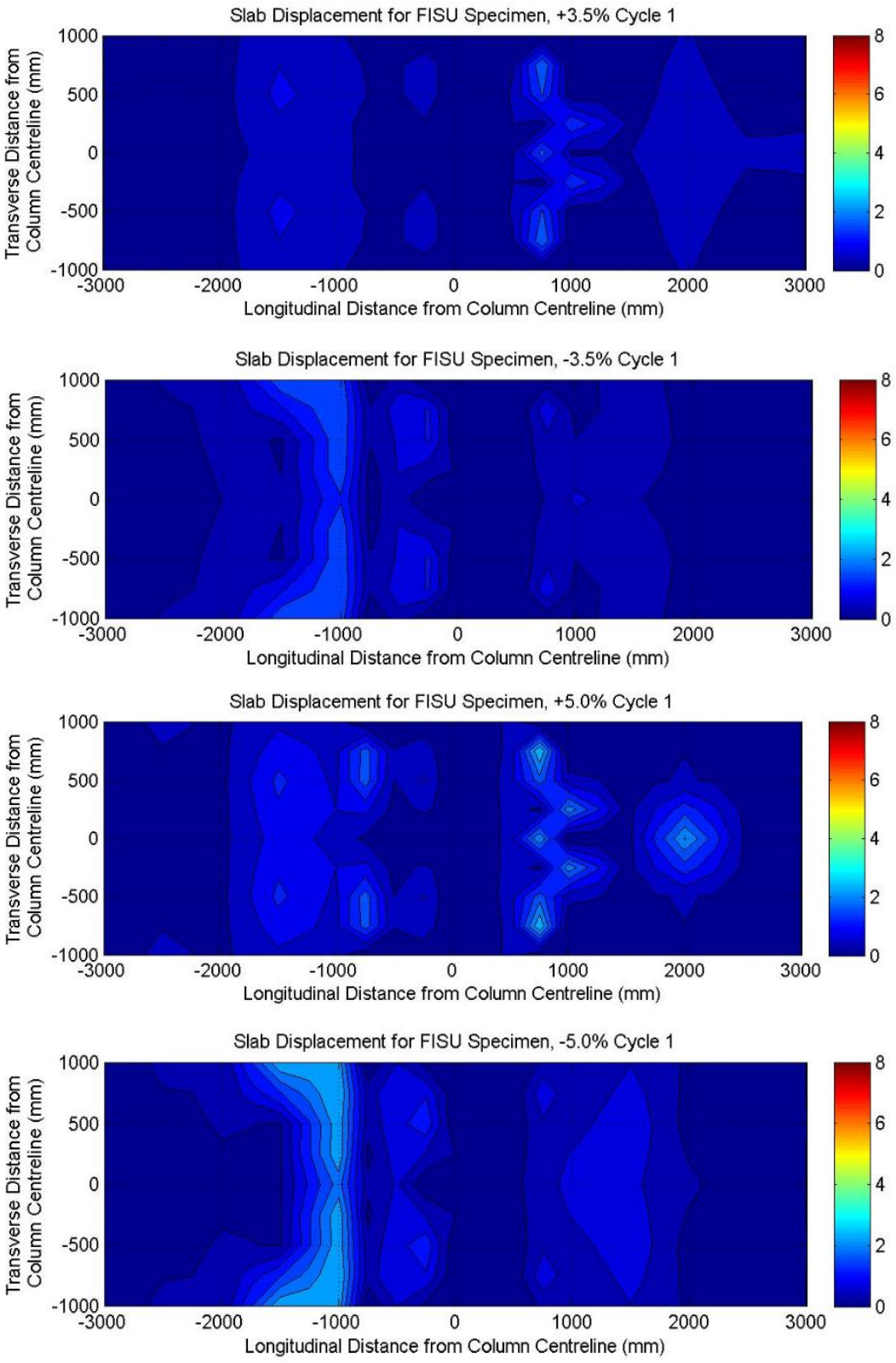

Figure D.8 - Slab Surface Deformation : FI-SU Sub-assembly

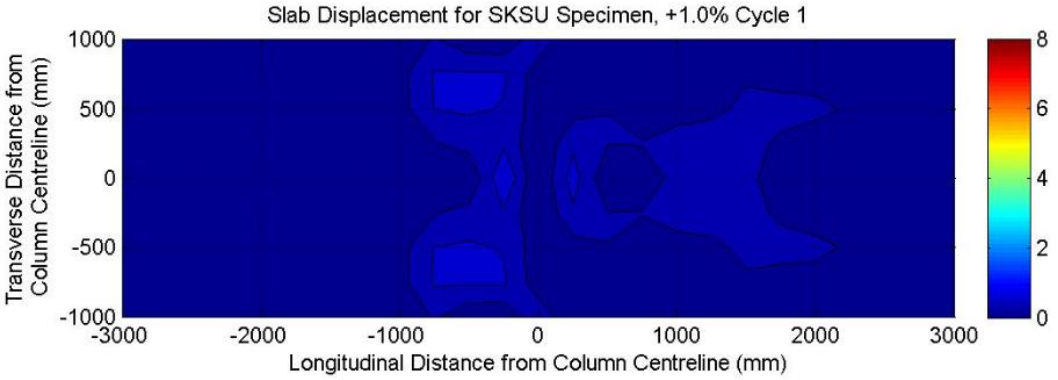
Slab Displacement for SKSU Specimen, +1.0% Cycle 1
Transverse Distance from Column Centreline (mm)
1000
500
0
-500
-1000
-3000
-2000
-1000
0
1000
2000
3000
Longitudinal Distance from Column Centreline (mm)
8
6
4
2
0

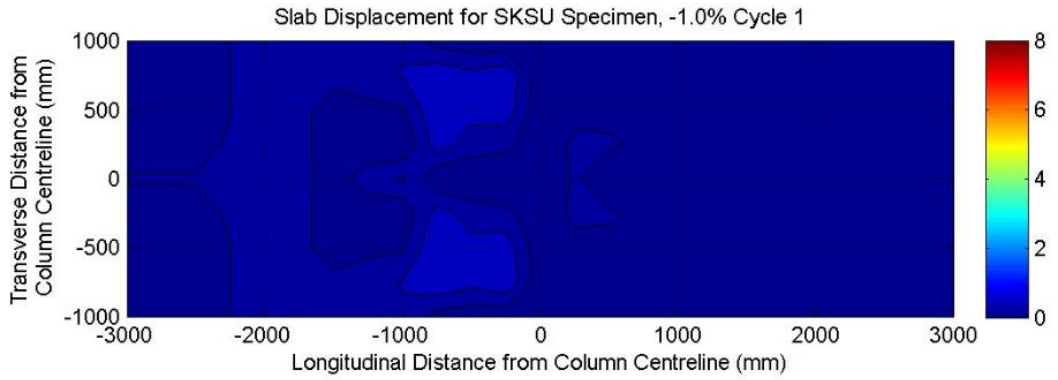
Slab Displacement for SKSU Specimen, -1.0% Cycle 1
Transverse Distance from Column Centreline (mm)
1000
500
0
-500
-1000
-3000
-2000
-1000
0
1000
2000
3000
Longitudinal Distance from Column Centreline (mm)
8
6
4
2
0

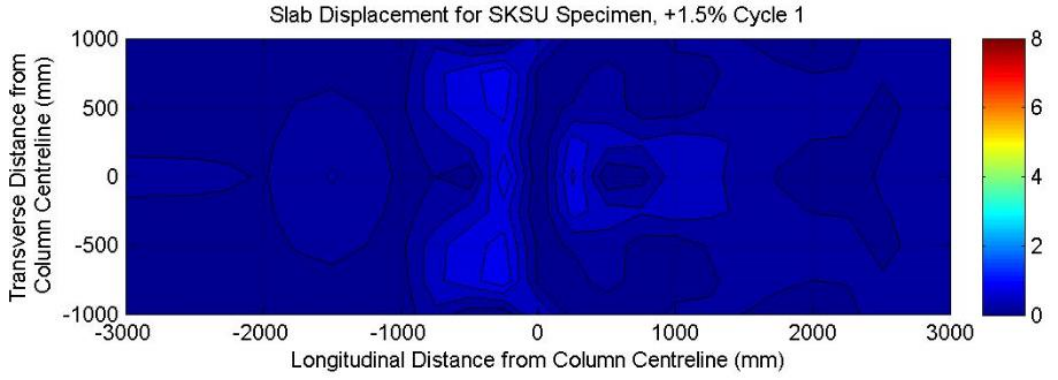
Slab Displacement for SKSU Specimen, +1.5% Cycle 1
Transverse Distance from Column Centreline (mm)
1000
500
0
-500
-1000
-3000
-2000
-1000
0
1000
2000
3000
Longitudinal Distance from Column Centreline (mm)
8
6
4
2
0

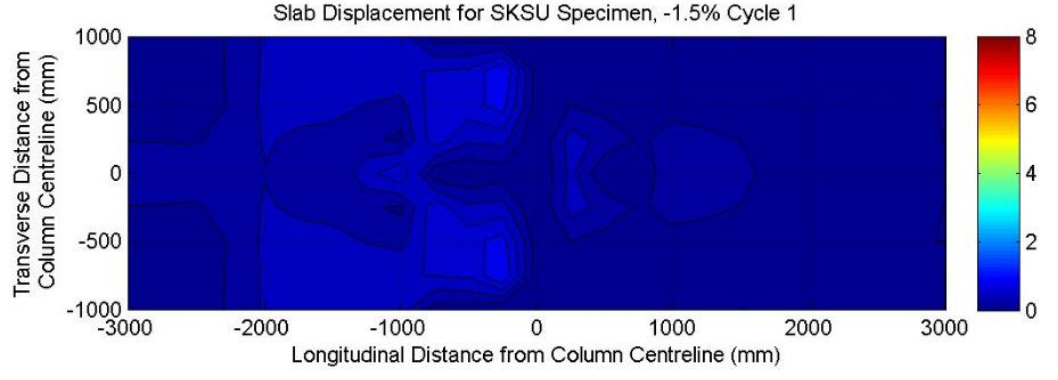
Slab Displacement for SKSU Specimen, -1.5% Cycle 1
Transverse Distance from Column Centreline (mm)
1000
500
0
-500
-1000
-3000
-2000
-1000
0
1000
2000
3000
Longitudinal Distance from Column Centreline (mm)
8
6
4
2
0

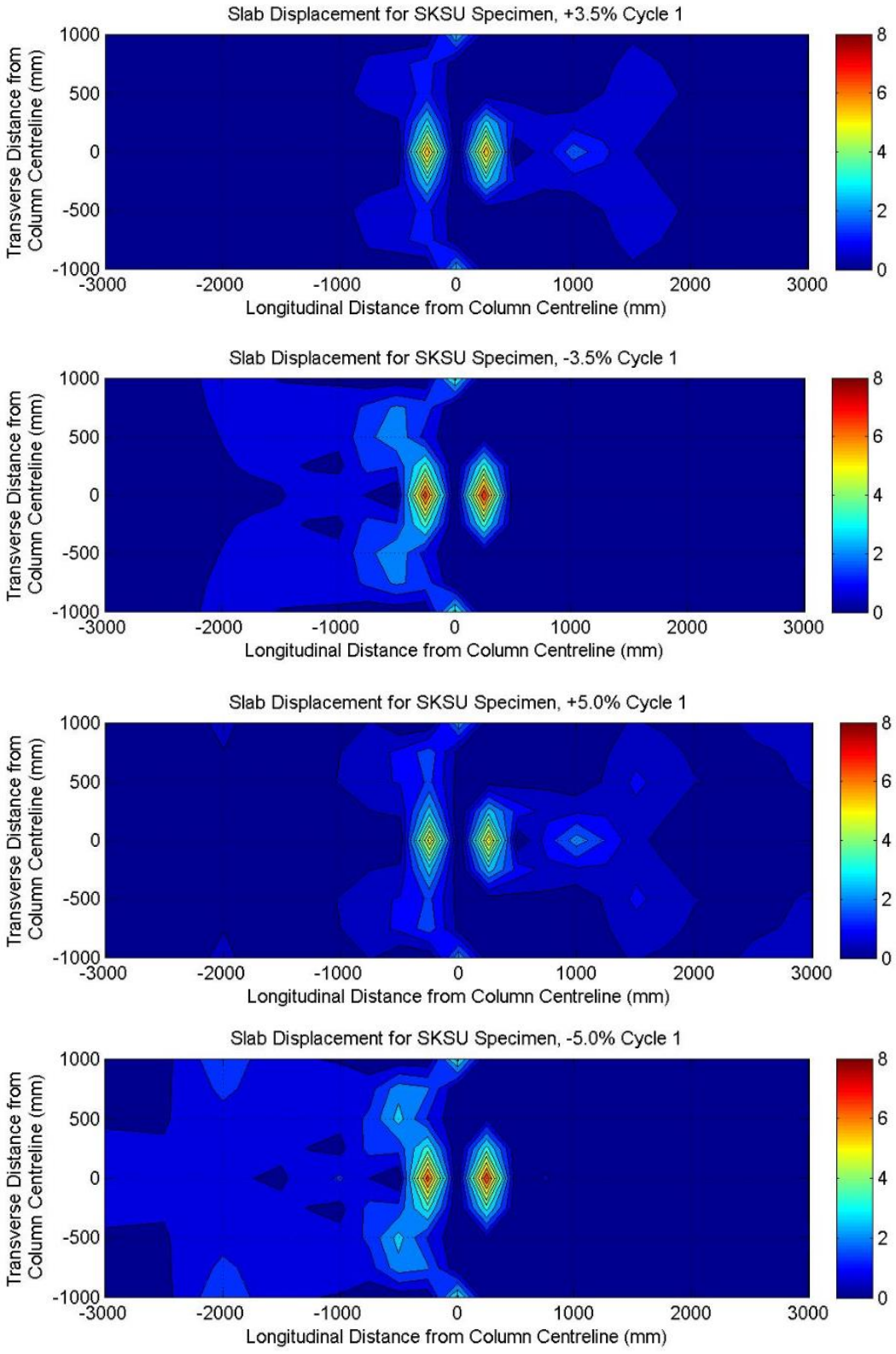

Figure D.9 - Slab Surface Deformation : SK-SU Sub-assembly

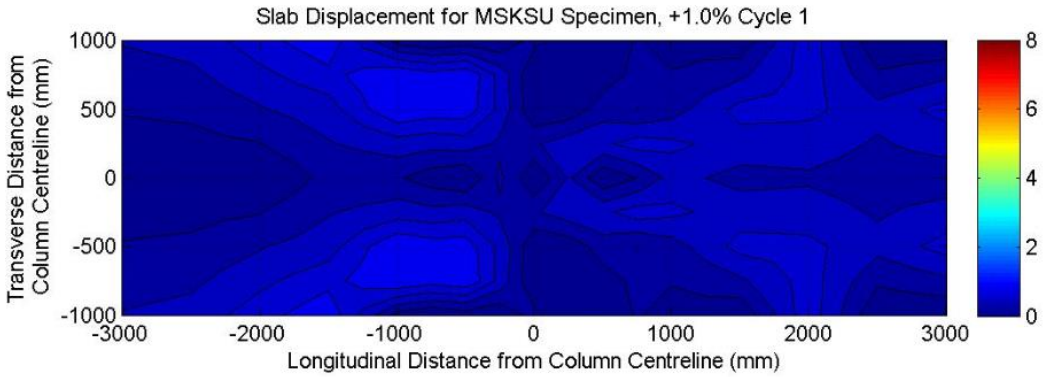
Slab Displacement for MSKSU Specimen, +1.0% Cycle 1
Transverse Distance from Column Centreline (mm)
1000
500
0
-500
-1000
-3000
-2000
-1000
0
1000
2000
3000
Longitudinal Distance from Column Centreline (mm)
8
6
4
2
0

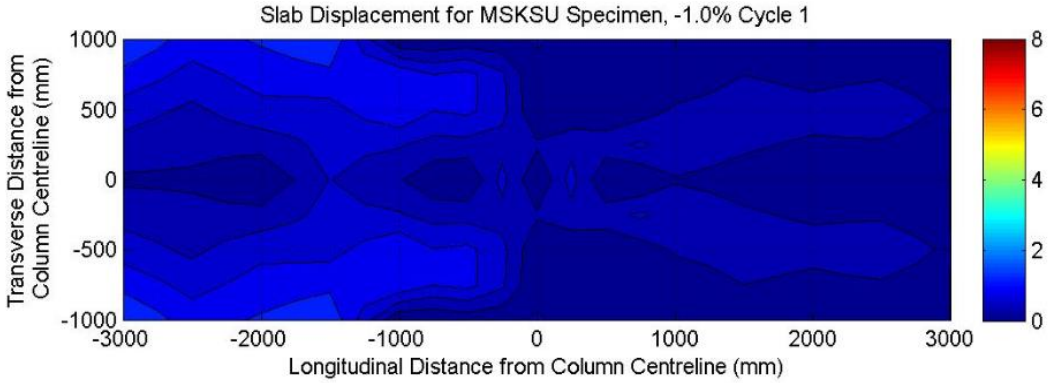
Slab Displacement for MSKSU Specimen, -1.0% Cycle 1
Transverse Distance from Column Centreline (mm)
1000
500
0
-500
-1000
-3000
-2000
-1000
0
1000
2000
3000
Longitudinal Distance from Column Centreline (mm)
8
6
4
2
0

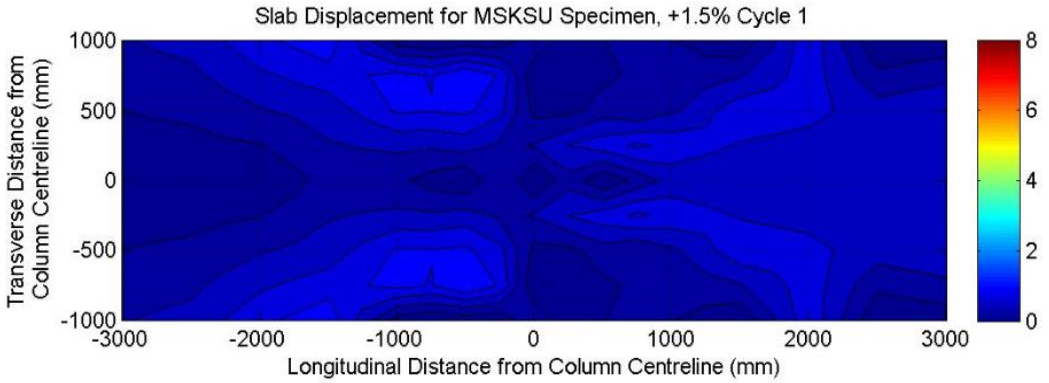
Slab Displacement for MSKSU Specimen, +1.5% Cycle 1
Transverse Distance from Column Centreline (mm)
1000
500
0
-500
-1000
-3000
-2000
-1000
0
1000
2000
3000
Longitudinal Distance from Column Centreline (mm)
8
6
4
2
0

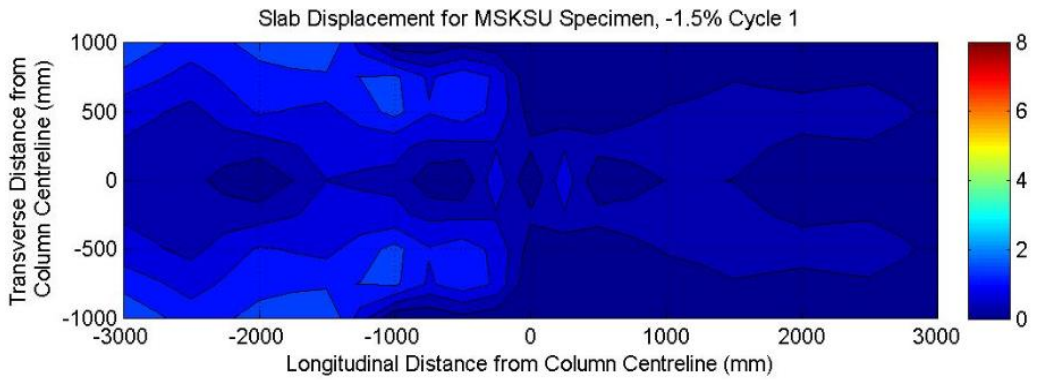
Slab Displacement for MSKSU Specimen, -1.5% Cycle 1
Transverse Distance from Column Centreline (mm)
1000
500
0
-500
-1000
-3000
-2000
-1000
0
1000
2000
3000
Longitudinal Distance from Column Centreline (mm)
8
6
4
2
0

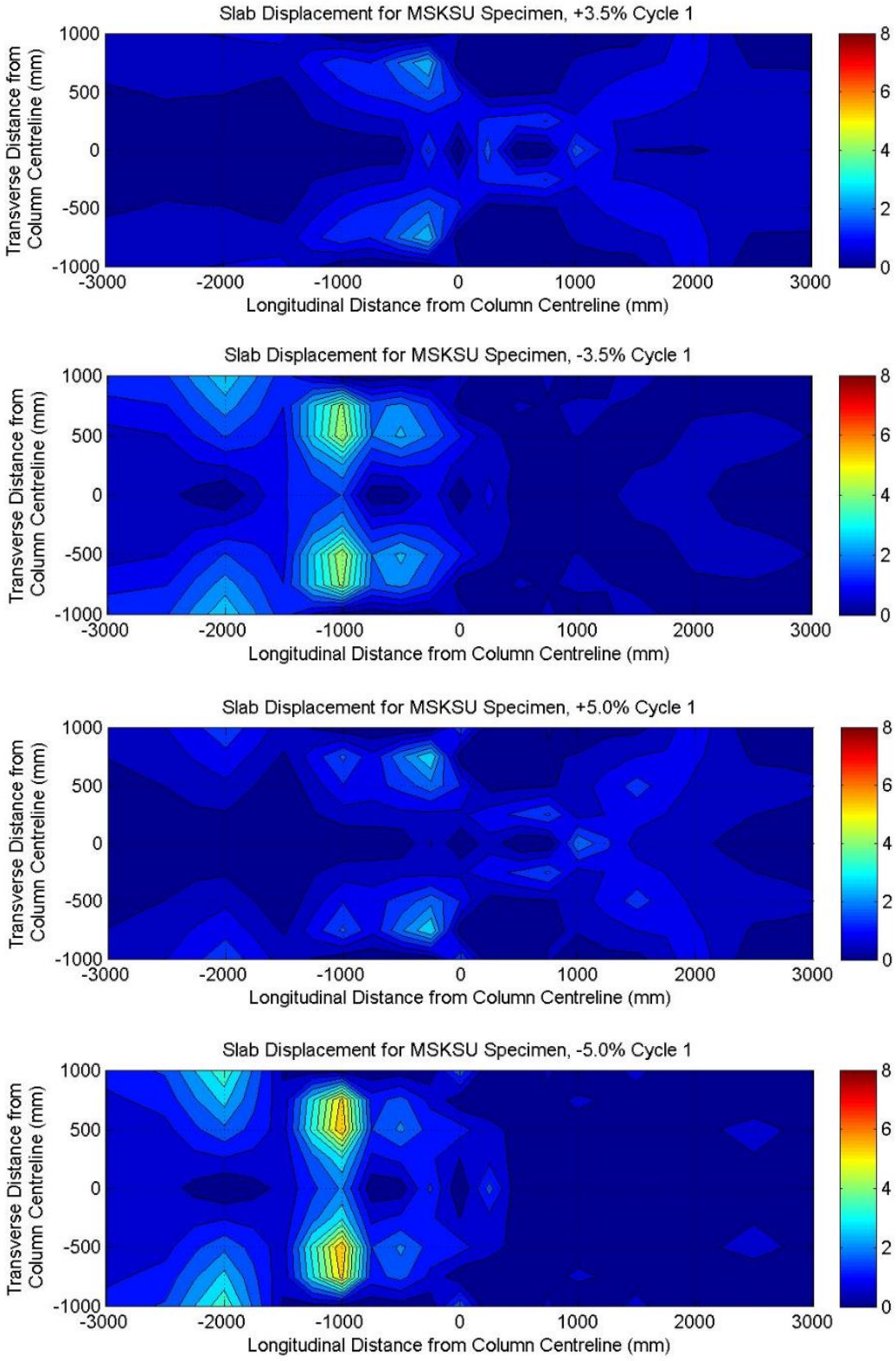

Figure D.10 - Slab Surface Deformation : MSK-SU Sub-assembly

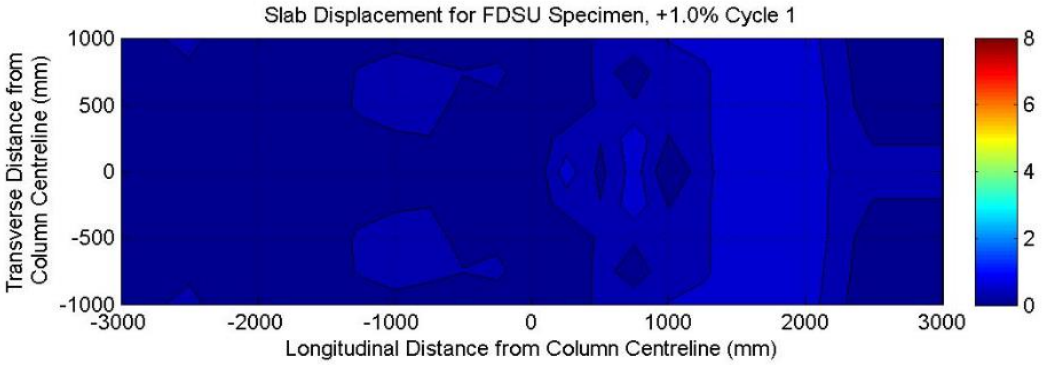
Slab Displacement for FDSU Specimen, +1.0% Cycle 1
Transverse Distance from Column Centreline (mm)
1000
500
0
-500
-1000
-3000
-2000
-1000
0
1000
2000
3000
Longitudinal Distance from Column Centreline (mm)
8
6
4
2
0

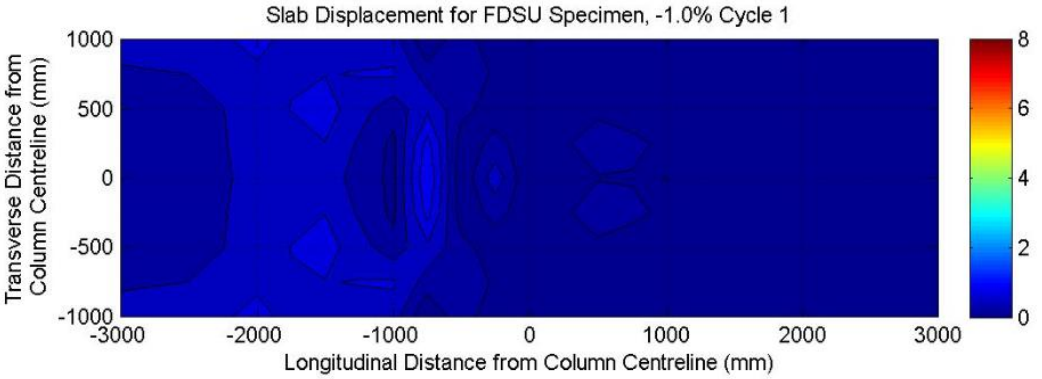
Slab Displacement for FDSU Specimen, -1.0% Cycle 1
Transverse Distance from Column Centreline (mm)
1000
500
0
-500
-1000
-3000
-2000
-1000
0
1000
2000
3000
Longitudinal Distance from Column Centreline (mm)
8
6
4
2
0

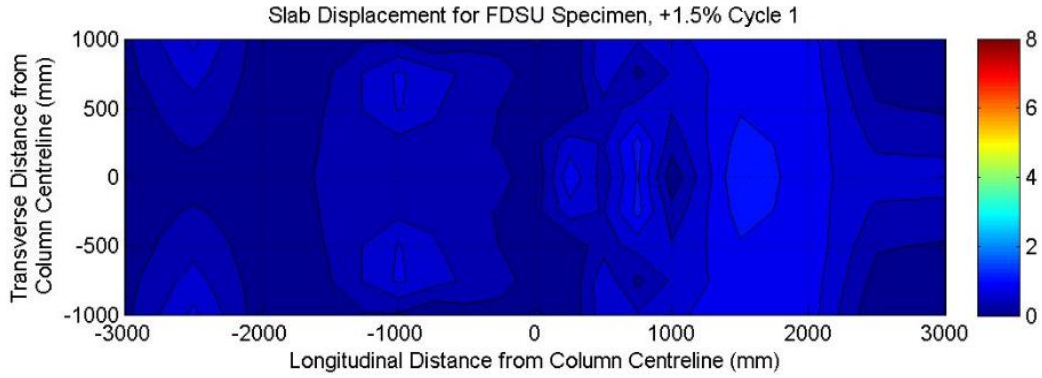
Slab Displacement for FDSU Specimen, +1.5% Cycle 1
Transverse Distance from Column Centreline (mm)
1000
500
0
-500
-1000
-3000
-2000
-1000
0
1000
2000
3000
Longitudinal Distance from Column Centreline (mm)
8
6
4
2
0

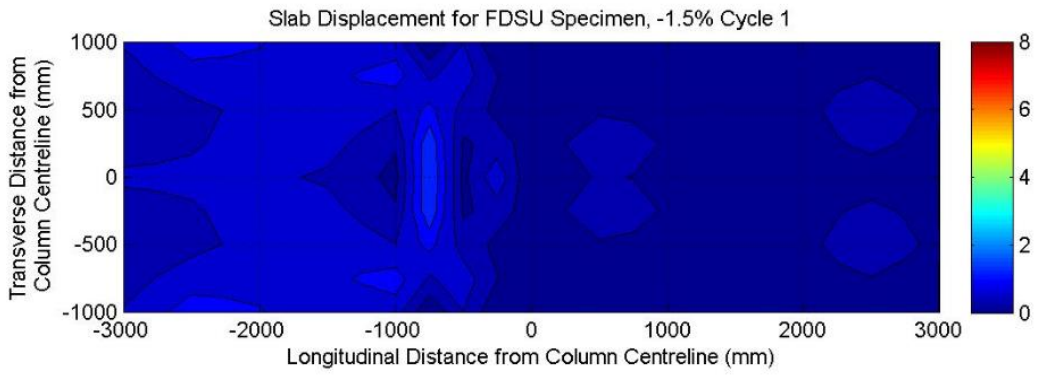
Slab Displacement for FDSU Specimen, -1.5% Cycle 1
Transverse Distance from Column Centreline (mm)
1000
500
0
-500
-1000
-3000
-2000
-1000
0
1000
2000
3000
Longitudinal Distance from Column Centreline (mm)
8
6
4
2
0

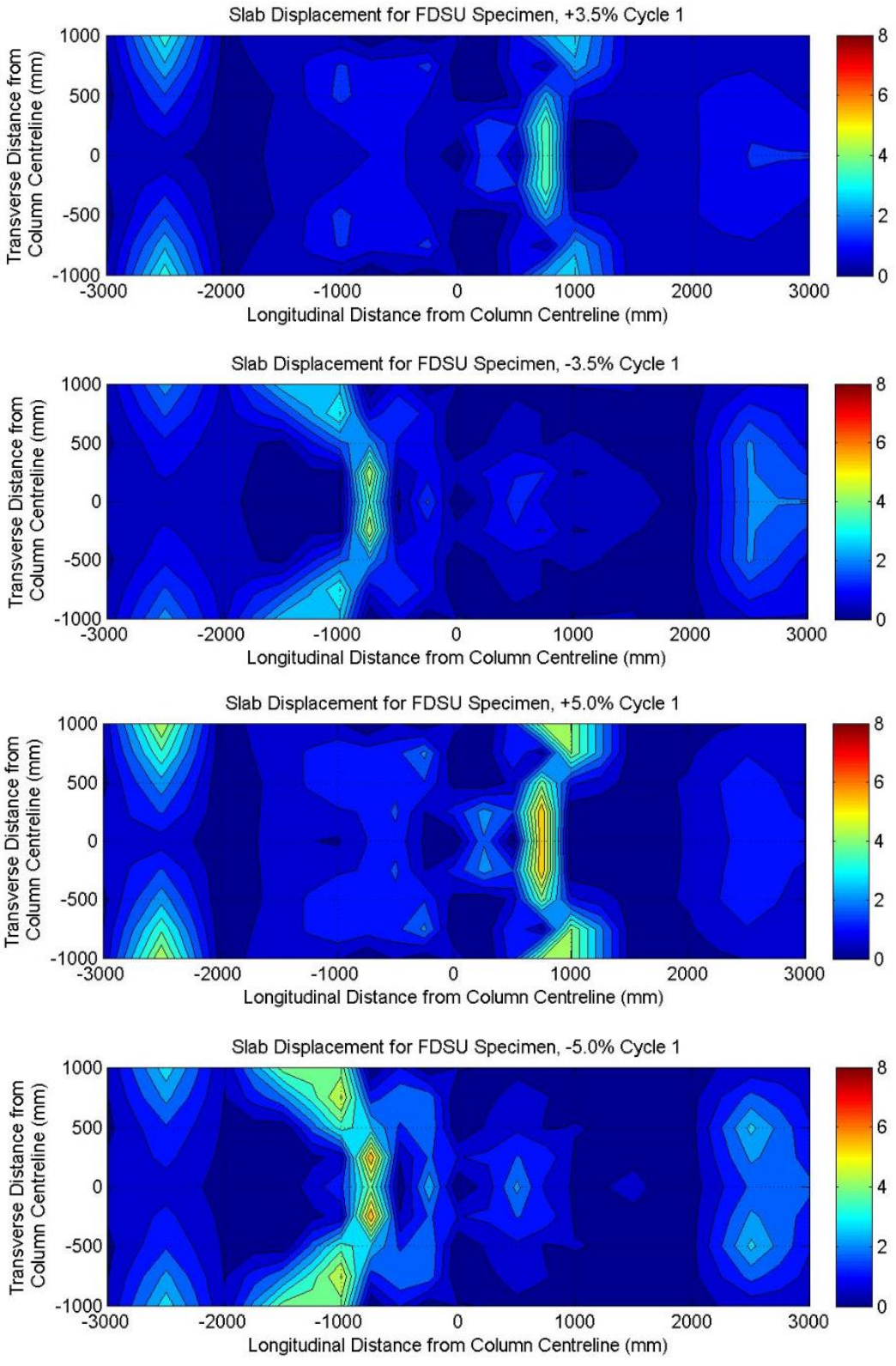

Figure D.11 - Slab Surface Deformation : FD-SU Sub-assembly

Appendix E: Calculations of Effective Moment of Area, Initial Stiffness, Equivalent Strut Area, Predicted Lateral Strength and FEA Results

This appendix provides sample calculations for determining the effective moment of area, initial stiffness as well as an example of the predicted lateral strength of the frame sub-assembly. It also discusses the additional information about beam plastic hinge formulations observed during the finite element simulation.

E.1 Calculations of Effective Moment of Inertia and Initial Stiffness

The tested frame sub-assemblies represent the interior joint of a typical steel frame building in the seismically active region. When subjected to lateral loads, results in the development of positive bending (i.e. sagging) in one beam and negative bending (i.e. hogging) in another beam, leads to a different moment of inertia for the both sagging and hogging sides. Therefore, the initial stiffness of the frame sub-assemblies with a composite slab is calculated using an equivalent moment of inertia (I_{eq}) considering the effective moment of inertia of the sagging bending and hogging bending of the composite beam. To calculate the transformed moment of inertia (I_{tr}), the location of the elastic neutral axis is calculated considering the full composite action. The effective moment of inertia (I_{eff}) of the sub-assembly considering the partial composite action is calculated based on the recommendation of NZS3404:1. A sample calculation of transformed moment of inertia, effective moment of inertia, equivalent moment of inertia and initial stiffness of SK-SU frame sub-assembly is provided here. A similar methodology is used to calculate the moment of inertia as well as the initial stiffness of the remaining subassemblies. The predicted initial stiffness of the sub-assemblies is summarised in Table E.1.

Table E.1: Predicted Initial Stiffness of Sub-assemblies

Specimen Description	Predicted Initial Stiffness (kN/m)
Bare Steel Frame **(BSF)**	5942
Fully Isolated Slab Unit **(FI-SU)**	8692
Shear Key Slab Unit **(SK-SU)**	15069
Modified Shear Key Slab Unit **(MSK-SU)**	15042
Full Depth Slab Unit **(FD-SU)**	14945
Transverse Deck Slab Unit **(TD-SU)**	16466
Longitudinal Deck Slab Unit **(LD-SU)**	16732

Calculation of Effective Moment of Inertia and Initial Stiffness:SK-SU Frame Sub-assembly

Effective thickness of concrete slab = $a := 70\,mm$

Effective width of concrete slab = $b_e := 1500\,mm$ (Ref_Based on CLNo-13.4.2.3 of NZ3404-1)

Depth of steel section = $d := 298\,mm$

Diameter of rebar mesh = $d_{bar} := 8\,mm$

Area of rebar = $A_{bar} := \frac{\pi}{4} \cdot d_{bar}^2 = 50.2655\,mm^2$

Spacing of rebar mesh = $s := 200\,mm$

no of rebars in effective width = $n := \frac{b_e}{s} + 1 = 8.5$

$n_{round} := round(n, 0) = 9$

$n_{bar} := \text{if } n_{round} < n = 9 \quad n_{round} + 1 \quad \text{else} \quad n_{round}$

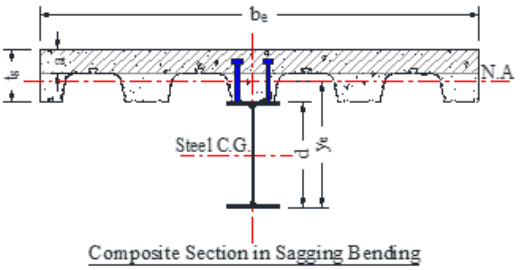

Composite Section in Sagging Bending

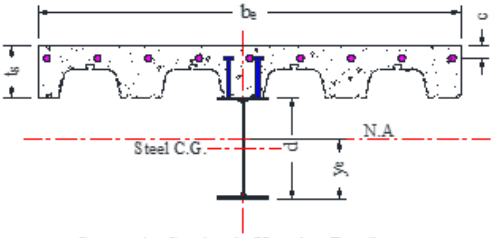

Composite Section in Hogging Bending

Concrete Compresive strength = $f'_c := 41.17\,MPa$

Yield Strength of steel = $f_y := 342.83\,MPa$

Modulus of concrete = $E_c := \left(3320 \cdot \sqrt{\frac{f'_c}{MPa}}\right) MPa + 6900\,MPa = 28202.3991\,MPa$

Modulus of steel = $E_s := 205000\,MPa$

Modular ratio = $m := \frac{E_s}{E_c} = 7.2689$

Top concrete cover to rebar mesh = $c := 35\,mm$

Total thickness of slab from slab top to beam top = $t_s := 150\,mm$

Gross area of steel beam = $A_s := 4080\,mm^2$

Momemnt of intertia of steel section = $I_{xx} := 63200000\,mm^4$

Momemnt of intertia of Column Section = $I_{xxcol} := 388000000\,mm^4$

Length of beam upto column face = $L_b := 2836\,mm$

Height of Column = $H := 2100\,mm$

Total beam Span = $L := 6000\,mm$ Depth of Beam = $D_b := 298\,mm$

Moment of Intertia for Sagging Bending

Elastic neutral axis from beam bottom =

$$y_e := \frac{\left(a \cdot b_e \cdot \left(d + t_s - \frac{a}{2}\right) + A_s \cdot m \cdot \frac{d}{2} + n_{bar} \cdot A_{bar} \cdot \left(d + t_s - c\right) \cdot m\right)}{\left(a \cdot b_e + A_s \cdot m + n_{bar} \cdot A_{bar} \cdot m\right)} = 356.2423\,mm$$

Transformed moment of inertia =

$$I_{tr} := I_{xx} + A_s \cdot \left(y_e - \frac{d}{2}\right)^2 + n_{bar} \cdot A_{bar} \cdot \left(d + t_s - c - y_e\right)^2 + \frac{1}{12 \cdot m} \cdot a^3 \cdot b_e + \frac{a}{m} \cdot b_e \cdot \left(d + t_s - \frac{a}{2} - y_e\right)^2 = 2.9232 \cdot 10^8 \, mm^4$$

Effective moment of inertia considering partial compsite action

Compression force in slab = $C_1 := 0.85 \cdot f'_c \cdot a \cdot b_e = 3.6744 \cdot 10^6 \, N$

Tension force = $T := A_s \cdot f_y = 1.3987 \cdot 10^6 \, N$

Number of shear stud actully provided = $N_p := 14$

Nominal shear capaciry of shear stud = $q_r := 47830 \, N$

Horizonatl shear based on stud strength = $R_h := N_p \cdot q_r = 6.6962 \cdot 10^5 \, N$

Design horizontal shear = $C_{min} := \min\left(\begin{bmatrix} C_1 \\ T \\ R_h \end{bmatrix}\right) = 6.6962 \cdot 10^5 \, N$

Percentage of composte action= $P_{comp} := \frac{C_{min}}{T} = 0.4787$

Effective moment of Inertia on Sagging =

$$I_{eff\_sag} := I_{xx} + 0.85 \cdot P_{comp}^{0.25} \cdot \left(I_{tr} - I_{xx}\right) = 2.252 \cdot 10^8 \, mm^4$$

Moment of Intertia for Hogging Bending

Elastic neutral axis from beam bottom = $y_{eHogg} := \frac{\left(A_s \cdot m \cdot \frac{d}{2} + n_{bar} \cdot A_{bar} \cdot \left(d + t_s - c\right) \cdot m\right)}{\left(A_s \cdot m + n_{bar} \cdot A_{bar} \cdot m\right)} = 175.3505 \, mm$

Transformed moment of inertia =

$$I_{tr} := I_{xx} + A_s \cdot \left(y_e - \frac{d}{2}\right)^2 + n_{bar} \cdot A_{bar} \cdot \left(d + t_s - c - y_{eHogg}\right)^2 = 2.6398 \cdot 10^8 \, mm^4$$

Effective moment of Inertia on Hogging =

$$I_{eff\_Hogg} := I_{xx} + 0.85 \cdot P_{comp}^{0.25} \cdot \left(I_{tr} - I_{xx}\right) = 2.0516 \cdot 10^8 \, mm^4$$

Equivalant Moment of Intertia

Equivalent Moment of Intertia = $I_{eq} := 0.6 \cdot I_{eff\_sag} + 0.4 \cdot I_{eff\_Hogg} = 2.1718 \cdot 10^8 \, mm^4$

Calculation of Initial Stiffness of Frame Subassembly

Elastic displacment of column= $\Delta_c := \frac{\left(H - D_b\right)^3}{3 \cdot E_s \cdot I_{xxcol}} = 2.4522 \cdot 10^{-5} \, \frac{s^2}{kg \, m} \, mm$

Elastic displacment of beam = $\Delta_b := 2 \cdot \frac{\left(L_b\right)^3}{3 \cdot E_s \cdot I_{eq}} \cdot \left(\frac{H}{L}\right)^2 = 4.1839 \cdot 10^{-5} \, \frac{s^2}{kg \, m} \, mm$

Initial Stiffness = $K := \frac{1}{\Delta_b + \Delta_c} = 15069.0303 \, \frac{kN}{m}$

E.2 Calculations of Equivalent Strut Area in Macro-Modelling

This section provides the calculations for the equivalent compressive strut area using in macro-model and based on the assumption that both the force transfer Mechanism-1 and Mechanism-2 act in parallel, therefore they were represented by a single compression strut with an equivalent strut area (i.e. sum of strut areas of the Mechanism-1 and Mechanism-2) and detail calculations are reported below.

Slab Span, $L := 6000\ mm$

Effective Slab Width, $B_{eff} := \frac{L}{4} = 1500\ mm$

Column Flange width, $B_c := 311\ mm$

Column Depth, $H_c := 327\ mm$

Angle of inclination of strut, $\theta := 45\ deg$

Topping Slab thickness , $t_s := 70\ mm$

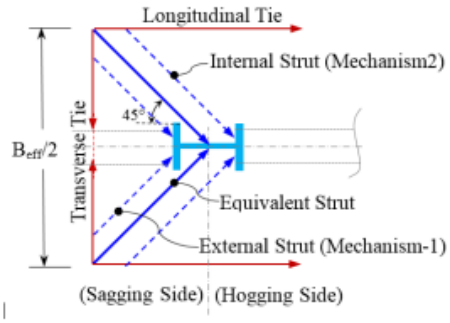

Equivalnt Strut Length based on geometry, $L_{strut} := 530\ mm$

1) For Mechanism 1: (External Strut:Bearing on column outer flange)

Strut width for Mechanism 1,

$$b1 := \frac{B_c \cdot \cos(\theta)}{2} = 109.9551\ mm$$

Area of strut for mechanism 1,

$$A1 := b1 \cdot t_s = 7696.8573\ mm^2$$

2) For Mechanism 2: (Internal Strut:Bearing on column inner flange)

Strut width for Mechanism 2, $b2 := \frac{H_c}{\sqrt{2}} = 231.2239\ mm$

Area of strut for mechnism 2,

$$A2 := b2 \cdot t_s = 16185.6742\ mm^2$$

Assuming the mechanism 1 and mechanism 2 struts are in parallel,

Equivalent area of compression strut

$$\boxed{A_e := A1 + A2 = 23882.5315\ mm^2}$$

Equivalent strut width, $b_e := \frac{A_e}{t_s} = 341.179\ mm$

E.3 Sample Calculations of Predicted Lateral Strength

This section provides the sample calculations for the predicted lateral strength of full depth frame sub-assembly based on the proposed analytical methodology depicted in Chapter 5. A similar methodology is used to calculate the lateral strength of the remaining subassemblies.

Predicted Lateral Strength Calculations for the Full Depth Speciman

Number of shear studs provided on one beam, $n_s := 14$

Characteristic Strength of Shear Studs for Two studs per rib

for Transverse Deck = $P_{rkT} := 39.45\ kN = 39450\ N$

for Longitudinal Deck = $P_{rkL} := 47.83\ kN = 47830\ N$

Yield Strength of steel = $f_y := 342.43\ MPa$ Ultimate strength of steel = $f_u := 502\ MPa$

Section modulus, $Z_e := 467000\ mm^3$

Effective concrete cover to rebar mesh = cover $:= 35\ mm$

Total thickness of slab from slab top to beam top = $D_s := 150\ mm$

Gross area of steel beam = $A_s := 4080\ mm^2$

Effective thickness of concrete slab = $t_c := 70\ mm$

Effective width of concrete slab = $b_e := 1500\ mm$

Depth of steel section = $d := 298\ mm$

Diameter of rebar mesh = $d_{bar} := 8\ mm$

Area of rebar = $A_{bar} := \frac{\pi}{4} \cdot d_{bar}^2 = 50.2655\ mm^2$

Spacing of rebar mesh = $s := 200\ mm$

no of rebars in effective width = $n := \frac{b_e}{s} + 1 = 8.5$

$n_{round} := round(n, 0) = 9$

$$n_{bar} := \begin{cases} n_{round} + 1 & \text{if } n_{round} < n = 9 \\ n_{round} & \text{else} \end{cases}$$

Yield strength of the rebar mesh = $f_{y\varphi} := 515\ MPa$

Storey height = $H := 2100\ mm$

Length of beam upto column face = $L_b := 2885\ mm$

Location of the plastic hinge from the column face = $L_p := 225\ mm$

Length of the beam upto the plastic hinge = $L_{bh} := L_b - L_p = 2660\ mm$

Column Flange width = $B_c := 311\ mm$ Column web thickness = $t_{wc} := 15.7\ mm$

Column Depth = $H_c := 327\ mm$ Depth of beam, $D_b := 298\ mm$

Angle of inclination of strut = $\theta := 45\ deg$

Width of the strut= $W_{strut} := H_c \cdot \cos(\theta) = 231.2239\ mm$

reduction factor for the shear strength of the comp strut = $\nu := 1.0$

Concrete Strength, $f'_c := 39.61\ MPa$

Shear Stud Strength = $F_{stud} := n_s \cdot P_{rkT} = 5.523 \cdot 10^5\ N$

Concrete Compressive strength = $F_{conc} := 0.85 \cdot f'_c \cdot b_e \cdot t_c = 3.5352 \cdot 10^6\ N$

Steel beam strength= $F_{steel} := A_s \cdot f_y = 1.3971 \cdot 10^6\ N$

Rebar strength = $F_{rebar} := n_{bar} \cdot A_{bar} \cdot f_{y\varphi} = 2.3298 \cdot 10^5\ N$

Sagging side slab force = $N_{sL} := \min\left(\begin{bmatrix} F_{stud} \\ F_{conc} \\ F_{steel} \end{bmatrix}\right) = 5.523 \cdot 10^5\ N$

Hogging side slab force = $N_{sR} := \min\left(\begin{bmatrix} F_{stud} \\ F_{rebar} \end{bmatrix}\right) = 2.3298 \cdot 10^5\ N$

Concrete confined strength in the interaction zone = $f'_{cc} := 47.11\ MPa$

Mechanism 1 force = $F_{rd1} := 0.85 \cdot f'_{cc} \cdot B_c \cdot D_s = 1.868 \cdot 10^6\ N$

Force in compression strut = $F_{strut} := \left(\nu \cdot 0.85 \cdot f'_{cc} \cdot W_{strut} \cdot D_s\right) = 1.3889 \cdot 10^6\ N$

Horizontal force component = $F_H := F_{strut} \cdot \cos(\theta) = 9.8207 \cdot 10^5\ N$

Vertical force component = $F_V := F_{strut} \cdot \sin(\theta) = 9.8207 \cdot 10^5\ N$

Total Nominal shear strength at the critical section

Shear resistance of concrete based on CL 7.7.4 of NZS3101:Part1:2006

Dia of shear key rebars = $D_{shear} := 12\ mm$ Number of shearkey rebars = $N_{skbars} := 4$

Shear area = $A_{vf} := N_{skbars} \cdot \frac{3.14 \cdot \left(D_{shear}^2\right)}{4} = 452.16\ mm^2$

Inclination of the shear friction reinforcemnt = $\alpha := 60\ deg$

Yiled strength of shear key = $f_{yshearkey} := 515\ MPa$

for normal density concrete, $\lambda := 1.0$

Coefficient of friction for concree cast monolithically = $\mu := 1.4 \cdot \lambda = 1.4$

Nominal Shear strength = $V_n := A_{vf} \cdot f_{yshearkey} \cdot (\mu \cdot \sin(\alpha) + \cos(\alpha)) + F_V \cdot \mu = 1.7737 \cdot 10^6\ N$

$F_{shear} := V_n = 1.7737 \cdot 10^6\ N$

Bearing force on the column internal flange=

$$F_{bearing} := 0.85 \cdot f'_{cc} \cdot \left(\frac{B_c - t_{wc}}{2}\right) \cdot D_s = 8.8686 \cdot 10^5\ N$$

Mechanism 2 force = $F_{rd2} := \min\left(2 \cdot \begin{bmatrix} F_H \\ F_{shear} \\ F_{bearing} \end{bmatrix}\right) = 1.7737 \cdot 10^6\ N$

Total interaction force at the slab-column junction

$F_{int} := F_{rd1} + F_{rd2} = 3.6418 \cdot 10^6\ N$

Force in Slab = $F_{slab} := \min\left(\begin{bmatrix} F_{int} \\ (N_{sL} + N_{sR}) \end{bmatrix}\right) = 7.8528 \cdot 10^5\ N$

Predicted strength considerding actual yield stress (lower bound)

Beam secion moment capacity = $M_b := f_y \cdot Z_e = 1.5991 \cdot 10^8\ N\,mm$

Shear demand in beam = $V_{beam} := \frac{M_b}{L_{bh}} = 60118.3496\ N$

Beam axial force in sagging beam = $N_{bL} := N_{sL} = 5.523 \cdot 10^5\ N$

Beam axial force in hogging beam = $N_{bR} := N_{sR} = 2.3298 \cdot 10^5\ N$

Modified beam moment for Sagging beam =

$$M_{pbL} := \min\left(\begin{bmatrix} 1.18 \cdot \left(1 - \frac{\left(\frac{F_{slab}}{2}\right)}{A_s \cdot f_y}\right) \cdot M_b \\ M_b \end{bmatrix}\right) = 1.3567 \cdot 10^8\ N\,mm$$

Modified beam moment for Hogging beam =

$$M_{pbR} := \min\left(\begin{bmatrix} 1.18 \cdot \left(1 - \frac{\left(\frac{F_{slab}}{2}\right)}{A_s \cdot f_y}\right) \cdot M_b \\ M_b \end{bmatrix}\right) = 1.3567 \cdot 10^8\ N\,mm$$

Total moment at the column centre =

$$M_{col\_CL} := M_{pbL} + M_{pbR} + \left(F_{slab} \cdot \left(\frac{D_b}{2} + D_s - \frac{t_c}{2}\right)\right) + 2 \cdot \left(V_{beam} \cdot \left(\frac{H_c}{2} + L_p\right)\right) = 5.2536 \cdot 10^{8}\ N\ mm$$

Predicted lateral strength at the column top =

$$V_{col\_prd\_lowerbound} := \frac{M_{col\_CL}}{H} = 250.1724\ kN$$

Predicted strength considerding actual ultimate stress (upper bound)

Beam secion moment capacity = $M_b := f_u \cdot Z_e = 2.3443 \cdot 10^{8}\ N\ mm$

Shear demand in beam = $V_{beam} := \frac{M_b}{L_{bh}} = 88133.0827\ N$

Beam axial force in sagging beam = $N_{bL} := N_{sL} = 5.523 \cdot 10^{5}\ N$

Beam axial force in hogging beam = $N_{bR} := N_{sR} = 2.3298 \cdot 10^{5}\ N$

Modified beam moment for Sagging beam =

$$M_{pbL} := \min\left(\left[1.18 \cdot \left(1 - \frac{\left(\frac{F_{slab}}{2}\right)}{A_s \cdot f_y}\right) \cdot M_b\right]\right) = 1.9889 \cdot 10^{8}\ N\ mm$$

Modified beam moment for Hogging beam =

$$M_{pbR} := \min\left(\left[1.18 \cdot \left(1 - \frac{\left(\frac{F_{slab}}{2}\right)}{A_s \cdot f_y}\right) \cdot M_b\right]\right) = 1.9889 \cdot 10^{8}\ N\ mm$$

Total moment at the column centre =

$$M_{col\_CL} := M_{pbL} + M_{pbR} + \left(F_{slab} \cdot \left(\frac{D_b}{2} + D_s - \frac{t_c}{2}\right)\right) + 2 \cdot \left(V_{beam} \cdot \left(\frac{H_c}{2} + L_p\right)\right) = 6.7357 \cdot 10^{8}\ N\ mm$$

Predicted lateral strength at the column top =

$$V_{col\_prd\_upperbound} := \frac{M_{col\_CL}}{H} = 320.7477\ kN$$

Predicted strength considerding the avarage yield stress

Beam secion moment capacity = $M_b := \left(\frac{f_y + f_u}{2}\right) \cdot Z_e = 1.9717 \cdot 10^8\ N\,mm$

Shear demand in beam = $V_{beam} := \frac{M_b}{L_{bh}} = 74125.7162\ N$

Beam axial force in sagging beam = $N_{bL} := N_{sL} = 5.523 \cdot 10^5\ N$

Beam axial force in hogging beam = $N_{bR} := N_{sR} = 2.3298 \cdot 10^5\ N$

Modified beam moment for sagging beam =

$$M_{pbL} := \min\left(\left[1.18 \cdot \left(1 - \frac{\left(\frac{F_{slab}}{2}\right)}{A_s \cdot (f_y)}\right) \cdot M_b\right]\right) = 1.6728 \cdot 10^8\ N\,mm$$

Modified beam moment for Hogging beam =

$$M_{pbR} := \min\left(\left[1.18 \cdot \left(1 - \frac{\frac{F_{slab}}{2}}{A_s \cdot (f_y)}\right) \cdot M_b\right]\right) = 1.6728 \cdot 10^8\ N\,mm$$

Total moment at the column centre =

$$M_{col\_CL} := M_{pbL} + M_{pbR} + \left(F_{slab} \cdot \left(\frac{D_b}{2} + D_s - \frac{t_c}{2}\right)\right) + 2 \cdot \left(V_{beam} \cdot \left(\frac{H_c}{2} + L_p\right)\right) = 5.9947 \cdot 10^8\ N\,mm$$

Predicted lateral strength at the column top with avarage yield stress =

$$V_{col\_prd\_avg} := \frac{M_{col\_CL}}{H} = 285.4601\ kN$$

E.4 Beam Plastic Hinge Formulation in FEA Simulation

The drift wise contour plots of the equivalent plastic strain of the different sub-assemblies are shown in the Figure E.1 to Figure E.5. It can be seen from these plots that the panel zone in all sub-assemblies remains elastic and similar observation was during the experimental investigation (reported in Chapter 5).

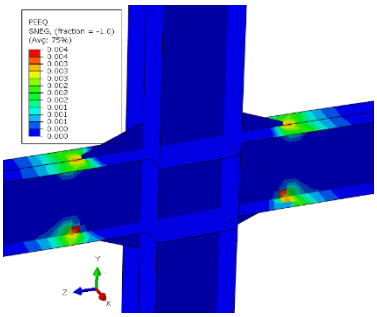

a) Equivalent Plastic Strain at 1.5% Drift

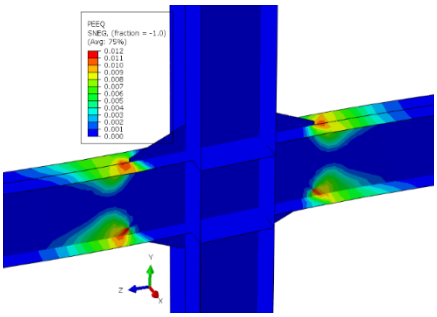

b) Equivalent Plastic Strain at 2.5% Drift

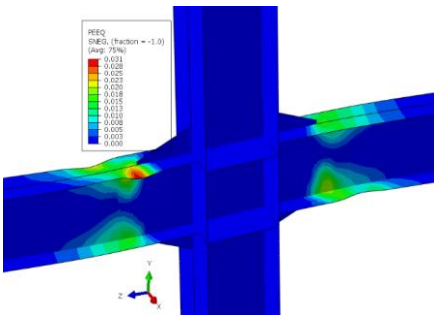

c) Equivalent Plastic Strain at 3.5% Drift

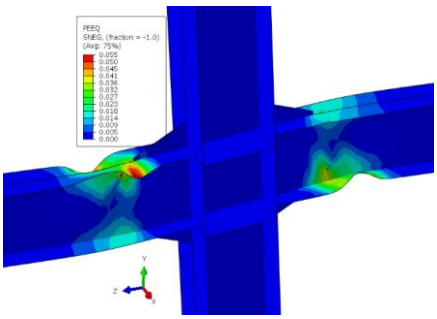

d) Equivalent Plastic Strain at 5.0% Drift

Figure E.1 - Formation of the Beam Hinges : BSF Sub-assembly

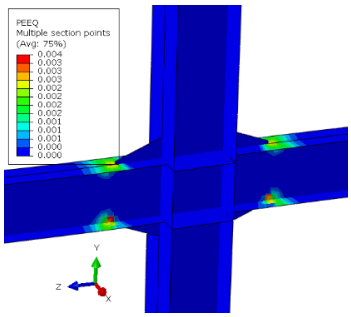

a) Equivalent Plastic Strain at 1.5% Drift

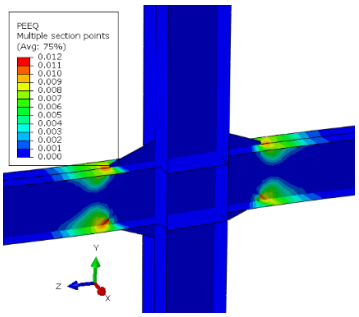

b) Equivalent Plastic Strain at 2.5% Drift

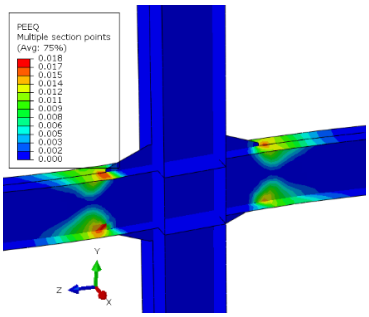

c) **Equivalent Plastic Strain at 3.5% Drift**

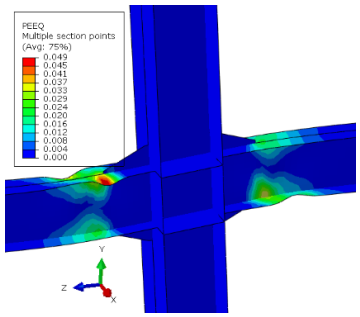

d) **Equivalent Plastic Strain at 5.0% Drift**

Figure E.2 - Formation of the Beam Hinges : FI-SU Sub-assembly

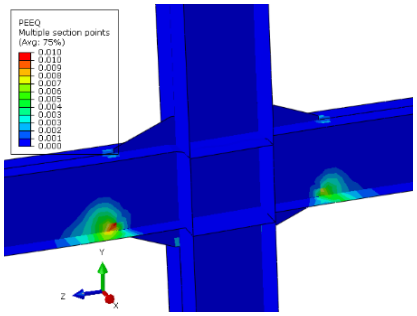

a) **Equivalent Plastic Strain at 1.5% Drift**

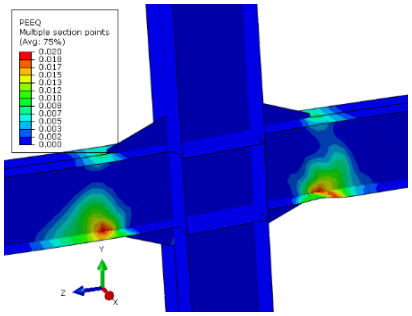

b) **Equivalent Plastic Strain at 2.5% Drift**

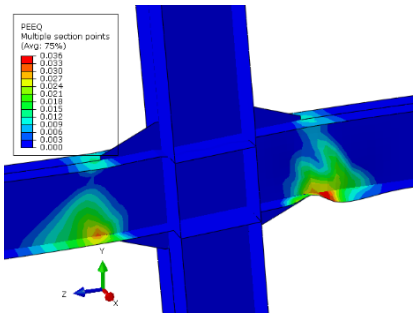

c) **Equivalent Plastic Strain at 3.5% Drift**

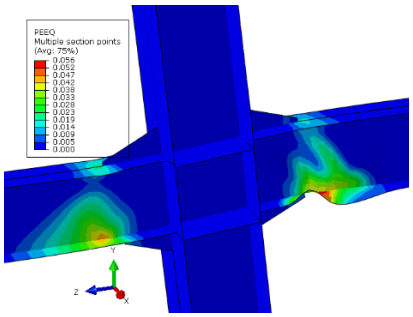

d) **Equivalent Plastic Strain at 5.0% Drift**

Figure E.3 - Formation of the Beam Hinges : SK-SU Sub-assembly

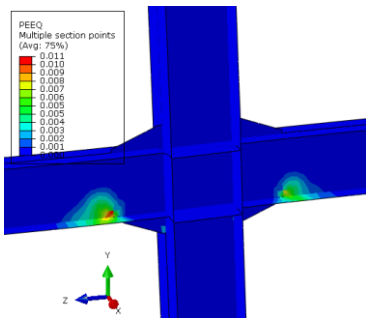

a) **Equivalent Plastic Strain at 1.5% Drift**

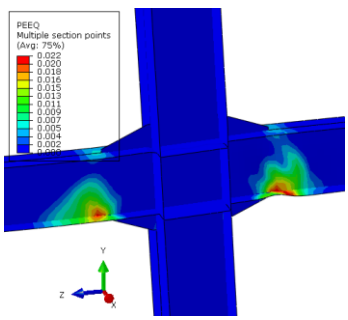

b) **Equivalent Plastic Strain at 2.5% Drift**

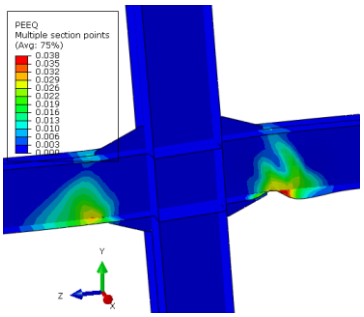

c) **Equivalent Plastic Strain at 3.5% Drift**

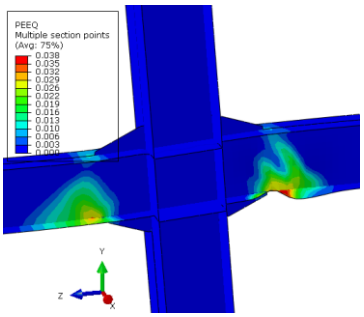

d) **Equivalent Plastic Strain at 5.0% Drift**

Figure E.4 - Formation of the Beam Hinges : MSK-SU Sub-assembly

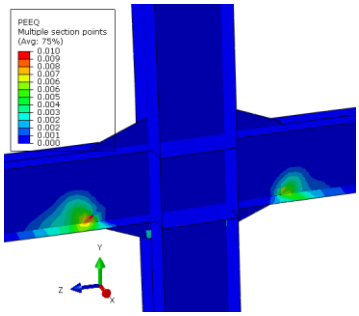

a) **Equivalent Plastic Strain at 1.5% Drift**

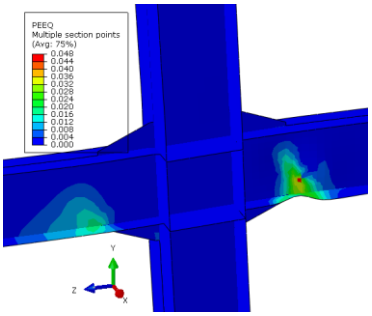

b) **Equivalent Plastic Strain at 2.5% Drift**

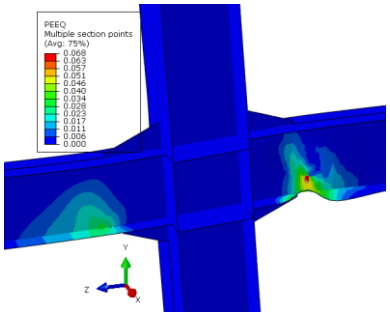

c) **Equivalent Plastic Strain at 3.5% Drift**

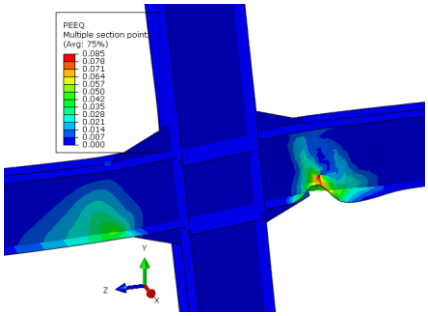

d) **Equivalent Plastic Strain at 5.0% Drift**

Figure E.5- Formation of the Beam Hinges : FD-SU Sub-assembly